The Theory of Coulomb Drag in Graphene Systems

Simon Flatres

A Thesis presented for the degree of

Doctor of Philosophy

Theoretical Physics Group

Department of Physics and Astronomy

University of Birmingham

England

September 2009

Dedicated to

my parents

The Theory of Coulomb Drag in Graphene Systems

Simon Flatres

Submitted for the degree of Doctor of Philosophy

September 2009

Abstract

This thesis addresses two similar problems that combine the theory of Coulomb drag with the emerging field of graphene physics. First, the theory of Coulomb drag between two graphene mono-layers is extended to include finite temperature. It is found that the effect is strongly enhanced at intermediate temperatures by coupled plasmon modes. This behaviour is similar to that seen between two dimensional electron gasses. In the second, we investigate the finite temperature polarisability of a graphene bilayer and apply this to the problem of Coulomb drag in a bilayer system. We find that enhancement due to coupled plasmon modes is suppressed, and dependence of the position and width of the plasmon peak on carrier density and interlayer separation is enhanced.

Declaration

The work in this thesis is based on research carried out at the University of Birmingham, England. No part of this thesis has been submitted elsewhere for any other degree or qualification and it all my own work unless referenced to the contrary in the text.

Acknowledgements

The priviledge of spending the last four years depening my understanding of the physical laws is something that I will be forever grateful for. The two people to whom I owe the deepest gratitude for making this possible are my parents, Mary and David. Without their contribution, both financially and through the childhood that has taken me along this path, it would have been impossible. I am forever in their dept.

It goes without saying that I owe a great deal of thanks to my girlfriend, Camilla Morrow, for her endless kindness and patience towards me throughout my PhD. A lesser person would have been driven to the edge of insanity.

There are two members of the Theory Group to whom I owe a great deal of thanks. To my supervisor, Dr. Robert Smith, for giving me the freedom to find my own research and for putting up with the many stupid things that have left my mouth. To Professor Ray Jones for his advice, encouragement and friendship. To both, for allowing me to lecture their mathematics course for four years. That was brave. It has been an experience that has changed me forever.

Finally, my warmest thanks go my fellow students in the Theory Group. You have been a constant source of entertainment, knowledge and laughter. I will miss you all.

Contents

Chapter 1

General Introduction

The physics of electron-electron (e-e) interaction plays a leading role in a wide range of condensed matter phenomena. These range from the fractional quantum Hall effect and high-temperature superconductivity, to Wigner crystallisation, exciton condensates and the Mott transition. In addition, the e-e interaction is central to problems involving quantum coherence since it is a leading mechanism of electron dephasing.

Despite its importance, the direct measurement of the e-e interaction through transport experiments is difficult. This is a consequence of the e-e interaction's momentum conserving nature. A scheme for doing so was first proposed in 1977 by Probrebenskii [1] and later by Price [2] in 1983. Their idea involved measuring the rate at which current, passed through one of two closely spaced conducting layers, drags charge in the other via the e-e interaction. The layers should be *uncoupled*. In other words, far enough apart so that there is no quantum mechanical tunneling between them. However, they must be close enough so that the weak drag effect can have a measurable influence and typically this equates to a layer separation of around 200Å. This effect was to become known as Coulomb drag, and from the

details one can infer something about the character of the e-e interaction.

It was not until the development of advanced semi-conductor fabrication techniques that the experimental realisation of Coulomb drag was made possible. In 1991, Gramila *et al.* [3] did just that and observed behaviour in broad agreement with theory. However, there were significant deviations from the predicted result. This led to a flurry of experimental and theoretical activity that saw Coulomb drag evolve into a field in its own right. The inconsistencies were eventually explained and this opened the door to the investigation of Coulomb drag in a number of novel experimental configurations. Although the pace of research in the field has greatly reduced, new and surprising results are still emerging. For example, the recent discovery [35] of novel universal conductance fluctuation behaviour in Coulomb drag systems.

A new and interesting opportunity arose in the field with the 2004 discovery of graphene by Novoselov *et al.* [51]. Graphene is a two dimensional crystal of carbon atoms arranged in a honeycomb lattice and it has some remarkable features. Specifically, its electronic excitations are not described by the Schrödinger equation, ubiquitous in condensed matter physics, but instead by the relativistic Dirac equation. Graphene's electrons therefore mimic the physics of quantum electrodynamics and behave as ultra-relativistic particles, with an effective speed of light around 300 times smaller than the true speed.

Although graphene's elementary properties have long been known [40], they were only used as a starting point for calculations on more readily available carbon allotropes, such as graphite. Since 2004, many new and interesting properties of graphene have been discovered, both theoretically and experimentally, and it has become the fastest growing field in the condensed matter community. There are

many interesting of graphene's unusual properties. As of 2009, graphene holds the records of being the strongest [52] material ever discovered and is approximately 200 times stronger than the strongest steel. At room temperature, it is also the most conductive, both electrically and thermally [53]. Naturally, this has led to a great deal of excitement about its potential uses. Despite theses possibilities, the difficulty in realising them comes from the inability to manufacture graphene sheets on an industrial scale and there is a great deal of work to be done in this area.

Perhaps the most exciting of graphene's potential uses is that for replacing silicon as the material of choice for building integrated circuits. As mankind reaches the physical limits of silicon, graphene may offer way to continue the trend of Moore's law. Of particular relevance to this potential application is the physics of two *coupled* graphene layers, commonly referred to as a graphene bilayer. A bilayer has the advantage of possessing a tunable band gap and as such may provide a more realistic route to viable graphene transistors.

The idea to merge the two fields of Coulomb drag and graphene is not original [106, 107]. However, to our knowledge the only calculations so far have been for two graphene monolayers, and each has used zero temperature expressions for many of the key terms. In this thesis, we will extend the theory to include a full finite temperature treatment. The primary original work of this thesis uses McCann *et al.*'s 2006 discovery [85] of the bilayer's low energy Hamiltonian as its starting point. We investigate the physics of Coulomb drag between two bilayers, deriving on the way new results for the graphene polarisation and non-linear susceptibility.

Chapter 2

Coulomb Drag

In this chapter, we give a general overview of the physics and history of Coulomb drag. This is an effect whereby charge flowing in one of two closely spaced conducting layers drag charge in the other. We begin by motivating and describing the drag effect in the context of the electron-electron (e-e) interaction and go on to describe the mathematical framework of the theory.

Following this, we discuss some of the early discrepancies between theory and experiment and how they were ultimately resolved. These led to the realisation that drag experiments exist in one of three regimes. At low temperature ($T < 0.1T_F$ where T_F is the Fermi temperature) the exchange of phonons dominates the process. In the intermediate regime ($0.1T_F < T < 0.5T_F$) the Coulomb force dominates before succumbing to the presence of coupled plasmon modes at higher temperatures ($T > 0.5T_F$).

Upon establishing the behaviour of the canonical drag experiment, we will continue by summarising some of the later developments and extensions to the field. These include the investigation of drag with correlated disorder and the discovery of novel universal conductance fluctuation behaviour.

In the final part of the chapter we will present two equivalent derivations for the drag conductivity. The first, a semi-classical approach, uses coupled Boltzmann equations to derive an expression for the interlayer momentum transfer. This method is physically transparent but is unable to capture higher order quantum effects such as weak localisation. The second, a fully microscopic approach, starts from the Kubo formula and treats the interlayer interaction as a perturbation. This is shown to be equivalent to the Boltzmann approach in the limit of weak impurity scattering.

2.1 Introduction

Perhaps the most basic type of experiments that one could hope to perform on electronic systems are those involving transport measurements. The e-e interaction has only an indirect effect on the transport properties of most condensed matter systems. This is a direct consequence of the momentum and total current conserving nature of the e-e interaction in perfectly pure, translationally invariant systems. Since transport measurements probe, for example, the average total current, this is unaffected by e-e momentum transfer where total momentum is conserved.

Despite the above argument, it is possible to measure the e-e directly by considering a system of two coupled layers. Although total momentum in the system is conserved, that within an individual layer is not. In principle momentum can be transferred between the layers via the Coulomb interaction, or indeed any other relevant interlayer interaction. It was this principle that led Probrebenskii [1] and later Price [2] to investigate an effect which was to become known as Coulomb drag. They predicted that a current passed through one of two closely spaced conducting layers (the drive layer) would drag carriers in the other (the drag layer) via interlayer

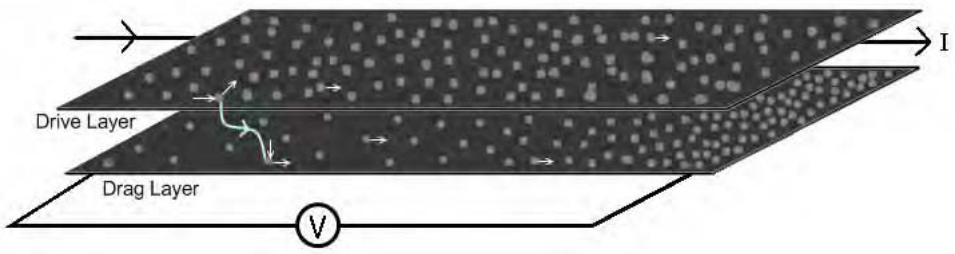

Figure 2.1: The basic configuration of a Coulomb drag experiment. A current I passing through the drive layer interacts with charge carriers in the drag layer resulting in a transfer of momentum between layers (in opposite direction for electrons and holes) A net charge builds up at one end of the drag layer as a result of electron hole asymmetry until its electric field balances the force due to Coulomb drag. Measurements of the voltage V_D along the drive layer provide information about the rate of momentum transfer.

Coulomb scattering (figure 2.1). By closely spaced it is meant that the layers are far enough apart so that quantum mechanical tunneling between the layers is negligible, but close enough so that the interlayer Coulomb interaction is strong (typically ~ 200Å).

If the drag layer is in open circuit, there will be a build up of charge at one end that will continue to increase until the electrostatic force exactly balances that due to the interlayer scattering, whereby the system is in a stationary state The voltage V_D induced across the drag layer is a direct result of the e-e interaction and in performing such experiments we may hope to learn something of its character.

It was almost 10 years between Price's 1983 theoretical prediction of Coulomb drag [2] and its first experimental observation by Gramila *et al.* in 1991 [3]. The reason for this is that the drag effect is very small and this is a direct result of quantum mechanics. The Pauli exclusion principle tells us that no two fermions can exist in the same state. Therefore, charge carriers in a drag experiment can only scatter if there is an empty state for them to scatter into. At zero temperature all states of a fermionic system are occupied up to the Fermi energy E_F. All states

above this energy are empty. The result is that Coulomb drag at zero temperature is not possible. At finite temperature however, states close to the Fermi surface become partially occupied and so interlayer scattering is allowed. Coulomb drag is therefore driven by the thermal fluctuations of the system. Because these only occur for the relatively small number of states around the Fermi surface, the effect is small. Based on this, one might suggest that the drag effect will scale as T^2 because the number of partially occupied states increases as $\sim k_B T$ for each layer. As we shall see, this is broadly correct but a more sophisticated theory is required to model the experimental results.

The drag effect is in fact even smaller than the above argument would suggest. The current passing through the drive layer consists of electrons above the Fermi energy and holes below the Fermi energy traveling in opposite directions. If one considers the electron and hole states to be symmetric, then electrons and holes in the drag layer will be dragged in the same direction and at the same rate. The result will be a zero net drag effect. The observation of a finite drag effect is therefore only possible due to the small asymmetry between electron and hole states. This asymmetry exists because the electrons and holes have slightly different energies relative to the bottom of the Fermi sea, a consequence of the band's parabolicity.

The net effect of this and of the Pauli exclusion principle is to make the drag effect very small indeed. It was not until the development of advanced semiconductor techniques that experimentalists were able to build structures with sufficient precision to observe Coulomb drag.

2.2 General Formalism

In this section, we will outline the basic mathematical framework of the theory. If the drag layer is in open circuit so that the drag current per unit width, J_D, is zero, the drag effect is characterised by the drag resistivity ρ_D (analogous to the standard transport resistivity). The drag resistivity is defined as the ratio of the induced drag electric field E_D to the drive current per unit width J_1 :

$$\rho_D = \frac{E_D}{J_1} \quad ; \quad J_D = 0, \tag{2.1}$$

where $E_D = V_D/l$. Here, l is the layer length and V_D is the voltage across the drag layer. In most theoretical treatments, the quantity most readily at hand is the drag conductivity σ_D. It is elementary to convert from one to the other by casting the resistivity for the system as a whole into the 2×2 matrix

$$\overline{\rho} = \begin{bmatrix} \rho_{11} & \rho_{12} \\ \\ \rho_{21} & \rho_{22} \end{bmatrix}, \tag{2.2}$$

where the ρ_{ii} are the in-plane layer resistivities and $\rho_{ij} \equiv \rho_D$ are the drag resistivity and, for example, the indices $1, 2$ represent the drive and drag layers respectively. From the relation $\overline{\rho} = \overline{\sigma}^{-1}$ the drag resistivities in terms of the drag conductivities are

$$\rho_D = \frac{\sigma_D}{\sigma_{11}\sigma_{22} - \sigma_{12}\sigma_{21}}. \tag{2.3}$$

The drag conductivity is typically smaller than the intralayer conductivity by a factor of 10^{-6} [7] and so a common approximation is to write

$$\rho_D \simeq \frac{\sigma_D}{\sigma_{11}\sigma_{22}}. \tag{2.4}$$

The in-plane conductivities are typically known. This leaves theoretical treatments of Coulomb drag the task of deriving an expression for σ_D in terms of the system parameters. These include temperature (T), interlayer distance (d) and the details of the interlayer interaction. A number of different approaches [3, 7, 9, 19–21] all lead to the same general expression for the drag conductivity

$$\sigma_D = \frac{1}{16\pi k_B T}\sum_q \int_0^\infty \frac{\Gamma_1(q,\omega)\Gamma_2(q,\omega)\left|U_{12}(q,\omega)\right|^2}{\sinh^2(\omega/2k_BT)}d\omega. \tag{2.5}$$

An explanation of each of the terms in (2.5) is in order. The term $U_{12}(q,\omega)$ is the effective interlayer potential. The expression above is sufficiently general so that interlayer interactions other than the Coulomb can be investigated with a suitable choice of U_{12}. In the case of the Coulomb interaction, in order to obtain agreement with experiment, it is necessary to self consistently account for the screening of charge between layers. For typical experimental parameters [3] the random phase approximation is used. This assumes that the system is in the high density limit where interactions are small and the random phase approximation is asymptotically exact. The interaction term typically results in a factor of $\sinh^{-2}(qd)$ where d is the interlayer spacing. This provides an upper cutoff to the momentum sum and is physically interpreted as fluctuations smaller than the interlayer spacing being averaged out from the point of view of the drag layer. The result is that fluctuations

with a wavelength $\ll d$ do not contribute to the drag rate.

The terms $\Gamma_i(q,\omega)$ are the non-linear response functions of the charge density in layer i to an external potential:

$$\delta\rho_i(q,\omega) = \Gamma_i(q,\omega)\phi^2(q,\omega)\,. \tag{2.6}$$

Accordingly, the drag effect can be viewed as the rectification of alternating fluctuations in the drive layer to a direct current in the drag layer. It will be shown below that for a 2DEG in the weak scattering limit, these functions are proportional to the imaginary parts of the individual layer linear susceptibilities $\chi_i(q,\omega)$. In this case (2.7) becomes

$$\sigma_D = \frac{1}{16\pi k_B T}\sum_q \int_0^\infty \frac{\mathrm{Im}\chi_1(q,\omega)\mathrm{Im}\chi_2(q,\omega)\left|U_{12}(q,\omega)\right|^2}{\sinh^2(\omega/2k_BT)}d\omega. \tag{2.7}$$

The final $\sinh^{-2}(\hbar\omega/k_BT)$ factor controls the available phase space for the charge carriers to scatter into. As described in the previous section, this arises due to the broadening of the Fermi distribution on each layer at finite temperature.

Interlayer Interaction The interlayer interaction term U_{12} is arguably the most important term in (2.5) because it is responsible for defining the character of the momentum transfer between layers. Although we will primarily consider the Coulomb interaction, it is sufficiently general so that other interactions such as phonon exchange between the layers can be investigated with an appropriate choice of U_{12}.

To get quantitative agreement with experiment, it is essential to take into account the screening of charge when constructing a Coulombic interaction term. Under the assumption that the electron gas is in the high density (weakly interacting) limit, it is

common to approximate the screened interlayer interaction using the random phase approximation (RPA) [18]. In the RPA, electrons are treated as self-consistently moving within the background electric field of the other electrons. For a single layer in the RPA, the effective intralayer interaction is given by [18]

$$U(q,\omega) = \frac{V_b(q)}{\varepsilon\,(q,\omega)} = \frac{V_b(q)}{1 + V_b(q)\chi(q,\omega)} \tag{2.8}$$

where $\varepsilon(q,\omega)$ is the dielectric function, $V_b(q) = 2\pi e^2/q$ is the bare in-plane Coulomb interaction (see appendix A) and $\chi(q,\omega)$ is the polarisability of the electron gas. The polarisability defines the response of the charge $\delta\rho(q,\omega)$ to an external potential $\psi(q,\omega)$ through

$$\delta\rho(q,\omega) = -\chi(q,\omega)\psi(q,\omega). \tag{2.9}$$

The extension to a double layer system is straightforward and requires the bare interlayer Coulomb interaction

$$U_b(q) = \frac{2\pi e^2 exp(-qd)}{q}, \tag{2.10}$$

where d is the layer separation. This is derived by considering the potential of a charge situated in one plane, as seen from the other. This is given by

$$U_b(r) = \frac{e^2}{\sqrt{r^2 + d^2}}, \tag{2.11}$$

where r, θ are the in-plane radial and angular coordinates of the observation point,

relative to the charge. Fourier transforming (2.11) we get

$$U_b(q) = \int_0^\infty r dr \int_0^{2\pi} d\theta \frac{e^2}{\sqrt{r^2+d^2}} e^{iqr\cos\theta} = 2\pi e^2 \int_0^\infty \frac{J_0(qr) r dr}{\sqrt{r^2+d^2}}, \tag{2.12}$$

where $J_n = \frac{1}{2\pi i^n}\int_0^\infty e^{iqr\cos\theta} d\theta$ is a Bessel function of the first kind. The integral over r is then performed with the aid of a standard identity [5] and yields (2.10).

The effective interlayer interaction is most conveniently expressed as a 2x2 matrix [15]

$$\widehat{U}(q,\omega) = \frac{\hat{V}_b(q)}{1+\hat{\chi}(q,\omega)\hat{V}_B(q)}, \tag{2.13}$$

where the off-diagonal elements $U_{12} = U_{21}$ are the interlayer interactions. Some straightforward algebra results in

$$U_{12}(q,\omega) = \frac{U_b(q)}{\varepsilon_{12}(q,\omega)} = \frac{U_b(q)}{[1+\chi_1][1+\chi_2] - U_b^2(q)\chi_1\chi_2}, \tag{2.14}$$

where $\chi_1 = \chi_1(q,\omega)$ and $\chi_2 = \chi_2(q,\omega)$ are the response functions for each layer. Equation (2.14) is valid for the case where the layers are treated as mathematical planes. To get quantitative agreement with experiment it is necessary to extend this result to include a finite layer thickness in which case the denominator of (2.14) acquires form factors. A standard approach [4,8] is to model each layer as an infinite square well of width L, separated by a well-centre to well-centre distance d. Under these approximations (2.14) is modified to

$$U_{12}(q,\omega) = \frac{U_b(q)}{[1+G\chi_1][1+G\chi_2] - \tilde{G}^2 U_b^2(q)\chi_1\chi_2}, \tag{2.15}$$

where

$$G = -\frac{1}{2q} e^{-qd} \left(\sinh \frac{ql}{2} \frac{8\pi^2}{ql\left(4\pi^2 + q^2L^2\right)} \right)^2, \tag{2.16}$$

$$\tilde{G} = -\frac{1}{2q} \left[\frac{2}{qL} + \frac{qL}{4\pi^2 + q^2L^2} - \left(\frac{8\pi^2}{ql\left(4\pi^2 + q^2L^2\right)} \right)^2 \sinh \frac{ql}{2} e^{-qL/2} \right]. \tag{2.17}$$

The effect of treating the layers as quantum wells and not as mathematical planes does not affect the qualitative behaviour of the Coulomb drag effect. It is necessary to do so simply to obtain precise agreement between theoretical and experimental values of the drag rate.

2.3 Early Developments

As already discussed, a naive approach to the temperature dependence of ρ_D might suggest that it should vanish as T^2 at low temperatures. This is a result of the scattering being limited by the exclusion principle to within k_BT of the Fermi surface. With the development of advanced semiconductor fabrication techniques, this prediction was first put to the test experimentally in the pioneering work of Gramilia *et al.* [3]. For the first time they were able to produce two independently contacted quantum wells that were spaced closely enough to observe Coulomb drag.

2.3.1 Double Quantum Wells

The two-dimensional electron gas, made by trapping electrons at doped semiconductor junctions, is perhaps the most prolific system in which low-dimensional electronic transport has been studied. Modern fabrication techniques and in particular molecular beam epitaxy, allow for the controlled construction of ultra high crystalline quality semiconductor structures and provide exquisite control of dopant

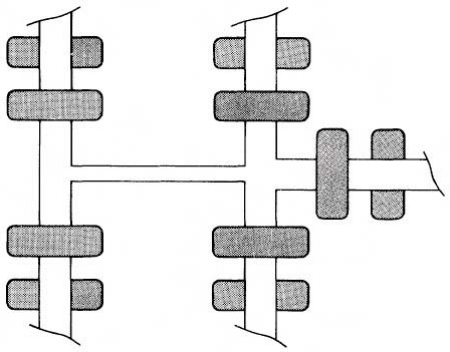

Figure 2.2: Independently contacted quantum wells. The Hall bar geometry as used by Gramila *et al.* showing upper and lower arm gates. Reproduced from [3].

levels. Modulation doping, in which the carriers are physically separated from the dopants that create them, have resulted in huge increases in the carrier mobility of these structures.

It was these techniques that allowed Gramila *et al.* [3] to construct a double quantum well (DQW) system with which to study Coulomb drag. They used a modulation doped GaAs / $Al_{0.3}Ga_{0.7}As$ heterostructure to create a system comprised of two closely spaced quantum wells, each 200Å thick and separated by $\sim$ 200Å. Carriers in the well are constrained to lie in the lowest energy level of the well but are free in the remaining two dimensions. The system therefore acts as an approximation to a two dimensional electron gas.

The key to this experiment and others like it is the ability to independently contact the quantum wells. This was achieved by creating a Hall bar geometry in which control contacts were placed on each arm above and below the DQWs. By varying the voltage applied to these gates, carriers in a given layer are locally depleted. The remaining layer is then independently contacted to that arm of the Hall bar and ordinary transport measurements can be taken from it.

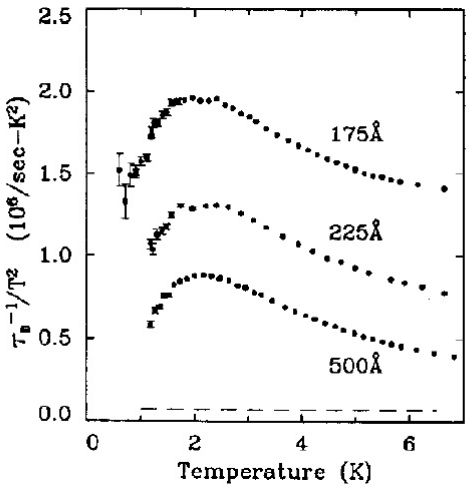

Figure 2.3: Temperature dependence of the interlayer momentum transfer rate divided by T^2 for interlayer separations of 175-, 225- and 500-Å. The dashed line shows the estimated Coulomb contribution to the 500-Å sample. For these samples the Fermi temperature is approximately $60K$. Reproduced from [3].

2.3.2 Phonons

The experiment carried out by Gramilia *et al.* [3] showed a deviation from the expected $\rho_D \sim T^2$ behaviour due to Coulomb scattering alone. Although this dependence is roughly satisfied, confirming the dominance of the e-e interaction, the experiment gave a non-monotonic ρ_D/T^2 with a maximum at $\approx 2K$ (figure 2.3). The Fermi temperature for the samples used is approximately $60K$ and the overall temperature dependence and position of the maximum are roughly similar for different layer separations. At a layer separation of 500Å, the observed ρ_D is simply too large to be the result of Coulomb scattering alone and this led Gramila *et al.* to suggest an additional interlayer interaction.

An initial clue to the nature of this interaction is that the observed scattering rate shows an extremely weak dependence on layer spacing, once Coulomb scattering is subtracted from the overall rate. This implies that the interaction is phonon mediated because low temperature acoustic phonon mean free paths in these samples

are on the order of millimetres. One would therefore not expect significant variation upon changing the layer separation by hundreds of Angstroms. Furthermore, the observed temperature dependence bears a remarkable resemblance to the well known interaction of acoustic phonons with 2D electrons [15]. The scattering rate of this interaction, τ_{ph}^{-1}, is linear in T at high temperatures, but has a much stronger temperature dependence of T^5 or T^7 at low temperatures. For samples at these densities the crossover occurs at a few Kelvin and hence the observed temperature dependence of τ_D is broadly consistent with a phonon mediated interaction.

Further evidence for a phonon mediated interaction arises when the dependence of the scattering rate on the relative electron density of each layer is considered. The phase space for back scattering diverges in a 2DEG and the phonon scattering rate is dominated by $2k_F$ phonons [18]. Therefore, a phonon in the drive layer has a much higher chance of being absorbed by the drag layer if the densities and hence the Fermi wave vectors are matched. The result is that one would a expect phonon mediated interaction to produce a peak in the interlayer scattering rate at matched densities and this is indeed observed. This argument does not hold for the Coulomb interaction between layers which, as we shall see later, is dominated by small angle scattering by the factor of e^{-qd} appearing in the interlayer interaction (2.14). Figure 2.4 shows that for the systems considered in [23], a peak at matched densities is indeed observed at 2.3K where τ_D^{-1}/T^2 is significant, but not at both higher and lower temperatures where it is small.

So far, the temperature, layer spacing and density dependence of the interlayer scattering rates strongly support a phonon mediated interaction. A problem arises when one compares the magnitude of the observed scattering rates with those obtained theoretically. It is found that the observed scattering rates are between 20

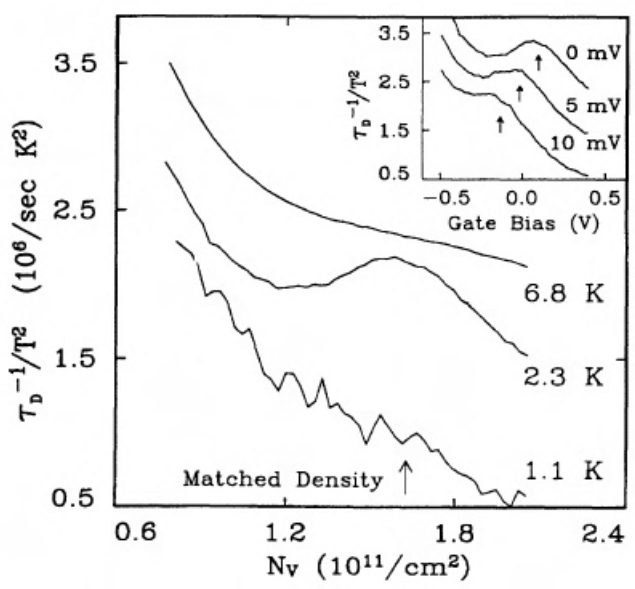

Figure 2.4: Dependence of the interlayer scatting rate on the electron density of the drag layer (N_V) for three different temperatures. The arrow indicates that the densities of the two layers are matched. Inset: drag rate at 2.3K with N_V replaced by the gate bias. Reproduced from [23].

and 100 times larger than the calculated results for real phonon exchange, despite having its characteristic temperature dependence. It was suggested [21, 22, 27] that in order to get agreement with experiment, a virtual exchange mechanism should be considered in the form of virtual phonons. Virtual phonons have the property of not obeying energy conservation and provide a much stronger interaction. This is a result of the difference in dimensionality of the electron and phonon systems. The result is that although the in-plane components of the virtual phonon's wave vector are constrained by momentum conservation, the out of plane component is not fixed by energy conservation as it is for real phonons. Therefore, for a given electronic excitation there is a line of possible excitations in phonon phase space. In comparison, for real phonons the allowed phase space for a given electronic excitation is restricted to two points.

The temperature dependence of real and virtual phonon interactions are similar

but differ in their magnitudes. It was decided by Gramila *et al.* [23] that more evidence was required to indicate virtual over real phonon exchange. They suggested that although a real phonon exchange interaction will be independent of the layer separation until it becomes comparable to the phonon mean free path, this is not true for virtual phonons. Instead, the range of virtual phonon energies able to contribute to the interaction would decrease as the interlayer distance is increased. Therefore, an observation of a reduction in τ_D^{-1} for interlayer distances well below that of the real phonon mean free path would be strong evidence in support of an additional interlayer interaction. If this interaction is due to virtual phonons it would be indicated by the fact that the temperature dependence of the virtual phonon interaction is close to that for real phonons. This was confirmed experimentally when Gramila *et al.* observed a significant decrease in interlayer scattering rate, with the appropriate temperature dependence, in a system with a layer separation of 5000Å.

2.3.3 Plasmons

Coherent, collective excitations of the electron gas, known as plasmons, play an important role in the optical properties of metals and semiconductors. The system may excite spontaneously, that is, a finite response may arise from an infinitesimal excitation, at the poles of the charge density response function. If a pole lies on the real axis then it is outside of the electron-hole (e-h) continuum ($\mathrm{Im}\chi = 0$) and so the plasmon cannot decay by electron-hole excitations. As the pole moves off the real axis and moves into the e-h continuum, the plasmon develops a finite lifetime and it may decay via excitations of e-h pairs. This process is known as Landau damping [8]. The plasmon dispersion relation is found by looking for zeros of the

dielectric function $\varepsilon(q,\omega) = 1 + V_b(q)\chi(q,\omega)$ which to lowest order in q is given by [10]

$$\omega = \begin{cases} e\left(\frac{4\pi n}{m}\right)^{\frac{1}{2}} & 3D \\ e\left(\frac{4\pi n}{m}\right)^{\frac{1}{2}} q^{\frac{1}{2}} & 2D \end{cases} \tag{2.18}$$

In the context of Coulomb drag, it was first noted by Flensberg and Hu [8, 24] that collective charge oscillations of the double layer system, that exist at the poles of the effective interlayer interaction, will enhance the drag rate at sufficiently high temperatures. For identical layers, $\chi_1 = \chi_2 \equiv \chi$, the screened interlayer interaction $U_{12}(q,\omega)$ is given by (2.3):

$$U_{12}(q,\omega) = \frac{U_b(q)}{\left[1+\chi(q,\omega)\right]^2 - U_b^2(q)\chi^2(q,\omega)}. \tag{2.19}$$

where $U_b(q) = \frac{2\pi e^2 exp(-qd)}{q}$ is the bare interlayer interaction (2.10). There are two plasmon modes, one where the charge oscillations are in phase (optic mode), and the other where they are out of phase (acoustic mode). Evidence for the symmetric (in-phase) and antisymmetric (out-of-phase) modes arises if we write (2.19) in the form

$$U_{12}(q,\omega) = \frac{1}{2}\left[\frac{V_b + U_b}{1+\chi(q,\omega)(V_b+U_b)} - \frac{V_b - U_b}{1+\chi(q,\omega)(V_b-U_b)}\right]. \tag{2.20}$$

where $V_b(q) = 2\pi e^2/q$ is the bare in-plane Coulomb interaction. At zero temperature the poles of U_{12} lie on the real ω axis. This implies that the plasmons lie outside of the e-h continuum and are therefore stable. Since the expression for the drag conductivity involves an integration over $\mathrm{Im}\{\chi(q,\omega)\}$, there can be no plasmon contribution to the drag rate at zero temperature. At finite temperature, the plasmon

poles move off the real axis and acquire a finite lifetime, decaying by excitation of e-h pairs. As the plasmon poles begin to overlap with the e-h continuum the latter contribute to, and eventually dominate, the drag rate. That the finite temperature expressions for $\chi(q,\omega)$ are required to see a contribution from plasmons explains why Jauho *et al.* [4] did not see a plasmon enhancement. At finite temperature, there is no analytic expression for $\chi(q,\omega)$ and so Flensberg and Hu [8, 24] were forced to evaluate it numerically. They did so using the following expression by Maldague [28] that expresses the finite temperature polarisation as an integral over the zero temperature expression,

$$\chi(q,\omega;\mu,T) = \int_0^\infty d\mu' \frac{\chi(q,\omega;\mu',T=0)}{4k_BT\cosh^2[(\mu-\mu')/2k_BT]}. \tag{2.21}$$

As usual the chemical potential in two dimensions is obtained via conservation of particle number and is given by [11]

$$\mu = T\ln(e^{T_F/T}-1)/T_F. \tag{2.22}$$

It is possible to obtain the small q dispersion of these plasmon modes under the assumptions of zero layer thickness and zero temperature. In this limit, the poles are close to the real axis and so we may look for zeros of the real part of (2.20). For typical drag experiments where the electronic density is high and kinetic energy dominates over potential (see section 3.3.2.3), the appropriate 2D polarisation function, $\chi(q,\omega)$, is that taken in the RPA. First calculated in 1967 by Stern [12],

it is given by

$$\chi(q,\omega) = \frac{k_F m}{\pi q}\left\{\frac{q}{k_F} - \sqrt{\left(\frac{q}{2k_F} - \frac{\omega}{qv_F}\right)^2 - 1} - \sqrt{\left(\frac{q}{2k_F} + \frac{\omega}{qv_F}\right)^2 - 1}\right\}. \quad (2.23)$$

To calculate the small q plasmon dispersion it is necessary to take $\chi(q,\omega)$ in the limits $q \ll 1$ and $\omega > q$. This region is outside of the electron-hole continuum and where the plasmon modes exits. In this limit we have

$$\chi(q,\omega) \simeq -\frac{n}{m}(\frac{q}{\omega})^2, \quad (2.24)$$

where n is the electron density and m the effective mass. In the small q limit $V_b + U_b \simeq 4\pi e^2/q$ and $V_b - U_b \simeq 4\pi e^2 d$, which when substituted into (2.20) yields the dispersions $\omega_\pm(q)$ of the two plasmon modes

$$\begin{aligned} \omega_+ &= e\left(\tfrac{4\pi n}{m}\right)^{\frac{1}{2}} q^{\frac{1}{2}} \quad \textit{Optic}, \\ \omega_- &= e\left(\tfrac{2\pi n d}{m}\right)^{\frac{1}{2}} q \quad \textit{Acoustic}. \end{aligned} \quad (2.25)$$

As the acoustic plasmon mode is lower in energy, it provides the dominant contribution to the drag rate. The plasmon dispersions at zero temperature are shown in figure 2.5 for two different values of layer separation, along with the e-h continuum. At large q the plasmon modes are not well defined because the two branches initially merge and are then Landau damped out of existence.

Flensberg and Hu [24] were able to develop an approximation for the plasmon contribution to the drag rate that is reasonably accurate up to around $0.5T_F$. By

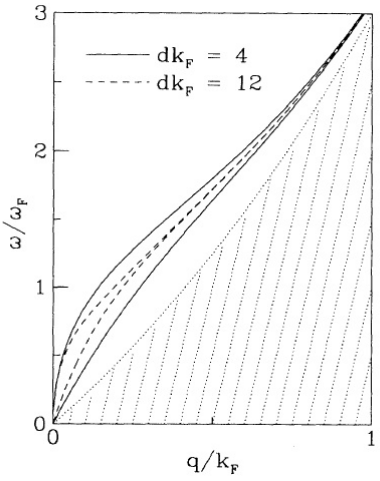

Figure 2.5: The plasmon dispersion for two coupled quantum wells for two different layer separations at zero temperature. Reproduced from [8].

expanding around the plasmon pole they obtained the expression

$$\tau_{\pm}^{-1} = \frac{\hbar^2}{8\pi enmk_BT}\int_0^{q_{c,\pm}} dqq^3 \frac{\mathrm{Im}[\chi(q,\omega_{\pm}(q))]}{4\,|\beta_{\pm}(q)|\sinh^2[\hbar\omega_{\pm}(q)\beta/2]} \tag{2.26}$$

where $\beta_{\pm}(q) = dRe[\chi(q,\omega)]/d\omega\ |_{\omega=\omega_{\pm}}$ and the parameter $q_{c,\pm}$ defines the value where the plasmon ceases to exist, i.e. when there are no more solutions to $\varepsilon\,(q,\omega) = 0$. In analysing the dependence of the plasmon contribution on the interlayer separation d, they noted that although the exponential dependence on the layer separation has dropped out of (2.26), $\tau_{\pm}$ is still d dependent through the d dependence of $\omega_{\pm}(q)$, $\beta_{\pm}(q)$ and q_c. As can be seen from figure 2.5, as d increases the slope of $\omega_{-}(q)$ increases while q_c decreases. This is counteracted by the decreasing slope of $\omega_{+}(q)$, although this is a weaker effect. The drag rate then decreases with increasing d as is expected. It is not possible to obtain an analytic expression for the d dependence of the plasmon contribution. However, Flensberg and Hu were able to determine numerically that within the range of validity of their approximation, $\tau_D^{-} \propto d^{-\alpha}$ where $\alpha \simeq 3$.

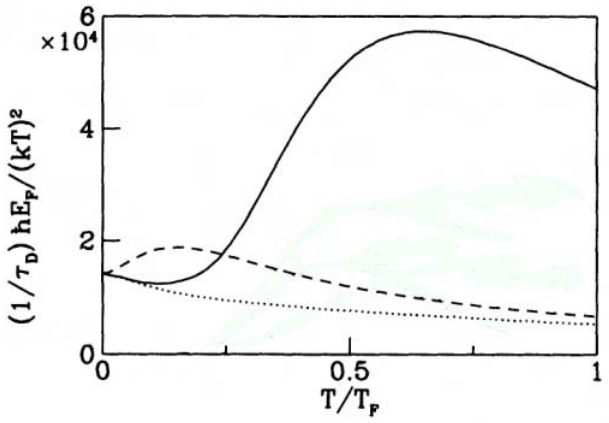

Figure 2.6: The temperature dependence of the drag rate scaled by T^2 for two identical GaAs quantum wells with densities $n = 1.5 \times 10^{11} cm^{-2}$, a well separation of $d = 375$Åand a well widths of 200Å. The full bold curve corresponds to calculations using the finite-T form of $\chi(q, \omega)$, the dotted curve to using the $T = 0$ form of χ, and the short-dashed curve is based on the static screening approximation of [4]. Reproduced from [8].

The numerical calculations of Flensberg and Hu [24] suggest that at temperatures above $0.2T_F$ the plasmons dominate the drag effect with a peak at around $0.5T_F$ (see figure 2.6). At higher temperatures, the plasmons are increasingly Landau damped and their contribution to the drag rate decreases. They also showed that the drag rate is maximised when the densities of each layer are matched which is an important experimental signature of plasmon enhancement. This peak occurs because the contribution of each layer to the plasmon enhancement is essentially determined by distance from the e-h continuum to the plasmon dispersion. These distances are minimised for matched densities.

As the temperature is increased well beyond the Fermi temperature, the 2DEG begins to behave like a gas of classical particles and is governed by the Maxwell-Boltzmann distribution. In the high temperature limit it was shown [24] that drag rate that goes as $\tau_D^{-1} \propto T^{-3/2}$, although the numerics indicated that does not occur until around $10T_F$, for a T_F of around $60K$.

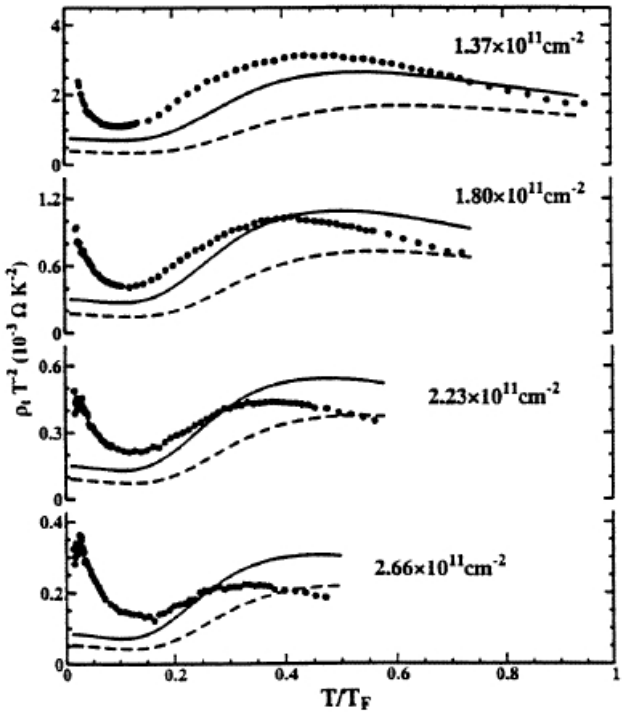

Figure 2.7: The scaled transresistivity $\rho_D T^{-2}$ verses T/T_F for different but matched densities. The dashed (solid) curves are the RPA (Hubbard) calculations of [8]. The circles are the experimental results of [30]. Reproduced from [30].

The theoretical predictions for plasmon enhancement were put to the test in experiments by Hill *et al.* [29] with good qualitative agreement. They found that the temperature required to excite the plasmons is lower than expected and that, over the majority of their temperature range, the magnitude of the drag rate was higher than the prediction. The suggestion that this indicated a failure of the RPA approximation was bolstered by several attempts [25, 26] to go beyond it. More closely matching the experimental data, they emphasised the fact that RPA is only good for very high densities. In general it overestimates the screening so that the effective interlayer interaction is weaker. The comparison with theory and experiment (figure 2.7) clearly shows that this is particularly the case at higher temperatures. In addition, Guven and Tanatar [31] studied coupled plasmon-phonon modes and found an enhancement to the drag effect.

2.3.4 Disorder

The effect of disorder on the drag rate was first investigated by Zheng and MacDonald [19]. They used the fact that in the diffusive regime ($q < 1/l$ and $\omega < 1/\tau$), the density response $\chi(q,\omega)$ is given at small frequencies and wave-vectors by

$$\chi(q,\omega) = \frac{dn}{d\mu}\frac{Dq^2}{Dq^2 - i\omega}, \tag{2.27}$$

where $D = l^2/2\tau$ is the diffusion constant, l the mean free path, $\tau = l/v_F$ the scattering time and $dn/d\mu$ the density of states. They showed that the diffusive contribution to the drag resistivity is

$$\rho_D^{Diffusive} = \frac{e^2\beta}{(k_{TF}d)^2}\int_0^{1/\tau} d\omega \frac{\omega^2}{e^{\beta\hbar\omega} + e^{-\beta\hbar\omega} - 2}\int_{(\omega/D)^{1/2}}^{1/l}\frac{dq}{q}. \tag{2.28}$$

In the low temperature, large layer separation limit they were able to obtain an analytic expression for the drag resistivity and found that

$$\rho_D \approx \frac{e^2}{(k_{TF}d)^2}T^2 logT, \tag{2.29}$$

which is valid for $l \ll d$, $T \ll T_F$ and $k_F d \gg 1$. The change in the distance dependence from d^{-4} in the ballistic case to d^{-2} in the diffusive case is a direct result of the change in the wave-vector dependence of $Im\chi$ from q^{-1} to q^{-2}. Zheng and MacDonald numerically calculated the relative correction to the interlayer scattering rate, τ_Δ/τ_B, where τ_Δ is the correction due to disorder and τ_B the ballistic contribution. These results are shown in figure 2.8 as a function of sample mobility and it can be seen that disorder dominates the drag effect at low temperatures and mobilities.

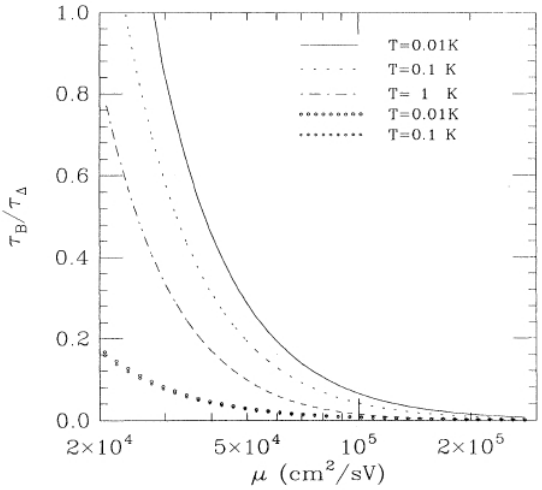

Figure 2.8: The relative correction to the interlayer scattering rate due to disorder enhancement for several temperatures as a function of sample mobility and for a layer separation of 500Å and a density of $1.5 \times 10^{11} cm^{-2}$. The last two plots are results for the case where one layer has an infinite mobility and the other a finite mobility. Reproduced from [19].

Zheng and MacDonald also estimated the crossover temperature T_c where the effect of disorder on drag becomes observable as

$$T_c \sim T_\tau exp[-3(l/d)^2/4\zeta(3)], \tag{2.30}$$

where $T_\tau = \hbar/k_B\tau$ and $\zeta(z)$ is the Riemann zeta function. No experiment has yet observed Coulomb drag in the diffusive regime. For typical drag experiments this crossover temperature is below experimentally attainable temperatures.

2.4 Further Developments

By the end of the 1990s, the physical properties of the canonical drag experiment were well established [15]. Researchers now turned their attention to some novel extensions to the theory and experiment, and in this section we review a selection of these.

2.4.1 Mesoscopic Systems

A mesoscopic system is one whose size is of the order of the coherence length, L_φ, of the charge carriers. The coherence length is the distance that the carriers travel before losing their phase coherence. These systems are essentially in between the atomic and the bulk regimes and as such the cornerstone of statistical physics (that principle that systems behave as the average over an ensemble of identical systems), is no longer applicable. An electron loses its coherence through inelastic e-e or electron-phonon scattering processes. As temperature decreases, the coherence length increases as the density of phonons decreases. In the low temperature regime, e-e scattering dominates the dephasing process [37].

In mesoscopic systems, the wave properties of electrons are observable and manifest themselves in various phenomenon such as weak localisation and universal conductance fluctuations (UCF). Weak localisation is seen in bulk samples and is the process by which coherent, diffusive electrons, traveling on time reversed paths, constructively interfere. It manifests itself in a divergence in the resistivity of mesoscopic systems, as the temperature approaches zero, and a decrease in resistance with an applied magnetic field (negative magnetoresistance). This is a result of the magnetic field interacting with the phase of the interfering electrons. It has been shown [7, 9] that weak localisation has a negligible effect on the drag resistance.

Universal conductance fluctuations are not seen in bulk samples and are small variations in the resistivity. These variations' defining characteristic is that they are *reproducible*. As parameters such as magnetic field, impurity configuration (reconfigured by heating) or carrier density are varied across a range, the resistivity will vary in a way that will be exactly duplicated if the process is repeated. This

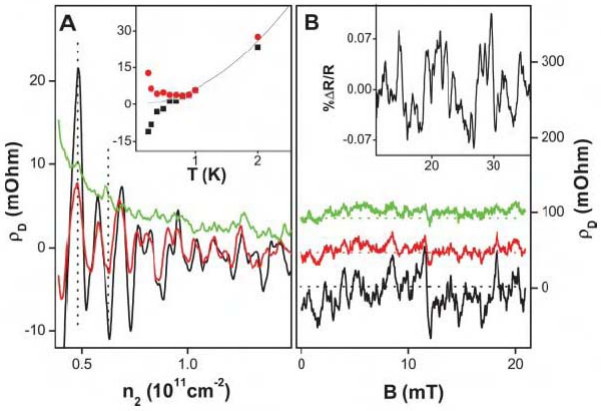

Figure 2.9: Reproducible fluctuations of the drag resistivity. The black, green, and red plots show reproduced fluctuations of the drag resistivity, each taken at a different temperature. The amplitude of the fluctuations are clearly larger at lower temperatures. (**A**) Drag resistance measured at low temperatures as a function of passive layer concentration; T = 1, 0.4 and 0.24 K, from top to bottom. (Inset) ρ_D as a function of T for two values of n_2 denoted by the dotted lines; solid line is the expected T^2 dependence of the average drag. (**B**) ρ_D as a function of B; T = 0.4, 0.35, and 0.24 K, from top to bottom. (Graphs for higher T are vertically offset for clarity.) Single-layer concentration for each layer is $5.8 \times 10^{10} cm^{-2}$. (Inset) The UCF of the single layer, with an average background resistance of 500 Ω subtracted. Reproduced from [35].

leads to concepts such as magneto-fingerprinting whereby a sample's unique and reproducible resistance fluctuations could in principle be used to identify it.

It was first suggested by Aleiner and Narozhny [36] that at low enough temperatures and for very small disordered systems, mesoscopic fluctuations may actually come to dominate the drag conductivity with the sign of the drag current becoming random. These ideas were first put to the test experimentally by Price *et al.* [35]. They explored the potential for UCF in samples larger and cleaner than theory suggested would produce significant fluctuations. Surprisingly, they found (see figure 2.9) that although the fluctuating drag resistance was small, it was still four orders of magnitude higher than predicted by theory.

The authors have provided a possible explanation for this surprising result. In mesoscopic systems it is not only the conductivity but also the local density of states

that fluctuates. In their samples, the mean free path between impurity scattering is large compared to the layer separation. This implies that only relatively large momentum transfers contribute to the drag conductivity. The uncertainty principle then demands that the interlayer interactions occur over small distances. Therefore, fluctuations in properties such as the local density of states govern the drag effect. At the relevant experimental parameters, fluctuations in the local density of states are known to be much bigger than the average of the sample. Fortunately, this particular mechanism has a very specific temperature dependence and Price *et al.* were able to show that their experiment is in good agreement with this behaviour. This experiment has provided an interesting new way to study not only just the e-e interaction, but the interplay between the e-e interaction and quantum coherence effects [37].

2.4.2 Correlated Disorder

In conventional Coulomb drag experiments, the carriers in each layer are donated by doped layers below and above the system. Because screening is effective in these systems, the carriers in each layer are only scattered by the smooth and random potential of the impurities in the closest doped layer. This is the so called independent impurity model.

Gornyi *et al.* [34] studied a correlated impurity model in which a doped layer is placed between the layers of a conventional drag experiment. There is therefore a correlation in the impurity potential experienced by the carriers of each layer. It was found that at low temperatures and in the diffusive regime, the correlated impurity model results in a significant enhancement in the drag effect. A cartoon of this effect is that because the carriers are moving within the same impurity potential,

there is an increased probability for electrons in opposite layers to follow an identical trajectory. The result is that overall there is an increase in the average time during which electrons in opposite layers can experience Coulomb scattering.

2.4.3 Tunneling Bridges

Kamenev and Oreg [32] investigated the drag effect with local tunneling links between the layers. Their particular model was to include the presence of point like bridges (places where electrons may tunnel), between the layers. Such a situation often occurs in metallic double layer systems [33]. For charge carriers of the same sign, the drag current flows in the same direction as the drive current. Kamenev and Oreg showed that in the presence of tunneling bridges, the interaction between the tunneling and the Coulomb interaction leads to a drag conductivity that is finite at zero temperature and negative for carriers of the same sign.

Two different regimes were identified in which different tunneling mechanisms cause a negative drag conductivity. If the temperature is not too small then the drag current is dominated by the following mechanism. As current passes through the drive layer, a fraction of the carriers tunnel into the drag layer and in doing so "forget" the direction of their initial momentum (a consequence of the uncertainty principle). The result is that there is no net contribution to the drag current at this stage. However, the repulsive Coulomb interaction between the remaining electron in the drive layer and the tunneled electrons cause the later to move in a direction opposite to the drive current. The net result is a negative drag conductivity. At lower temperatures the dominant process is one that involves coherent tunneling to the drag layer and back, accompanied by the Coulomb interaction. It was shown that this mechanism has a strong temperature dependence that is logarithmically

divergent as $T \to 0$.

2.5 Derivation of the Drag Conductivity

The first microscopic theoretical treatment of the drag effect was given by Jauho and Smith [4] and was based on a Boltzmann equation approach. Alternative treatments include the Green's function formalism [7, 9], presented in section 2.5.2, the memory function formalism [19] and the collective excitation approach [20]. Although studying Coulomb drag through the Boltzmann equation is semi-classical and hence unable to capture higher order quantum effects, such as weak localisation, it has the advantage of providing a transparent origin for the terms appearing in equation (2.7). With this in mind it is instructive to look at this approach in some detail.

2.5.1 The Boltzmann Equation Approach

This calculation due to Jauho *et al.* [4] is valid under the condition of weak scattering ($\omega\tau > 1$). It uses coupled, linearised Boltzmann transport equations to calculate the transfer of momentum from the drive to the drag layer. This approach is semi-classical in the sense that although the Boltzmann equation treats scattering classically, quantum mechanics enters the procedure via the de Broglie relation and the use of the Fermi equilibrium distribution function.

The calculation proceeds as follows. After obtaining the Boltzmann equation and the collision term for interlayer scattering, the resulting expression is linearised under the assumption of weak interlayer scattering. Following this, it is coupled with the in-plane Boltzmann equation for the drive layer, linearised under the assumption of weak intralayer impurity scattering. After a series of technical manipulations, the

resulting expression will be written in terms of the polarisabilities, $\chi(q,\omega)$, of each individual layer.

The Boltzmann equation describes the evolution of the non-equilibrium distribution function $f(\mathbf{r},\mathbf{k},t)$ as a function of time. It is one of the most important equations of non-equilibrium statistical mechanics. The distribution function is defined so that $f(\mathbf{r},\mathbf{k},t)\,d\mathbf{r}d\mathbf{k}$ is the number of particles that, at time t, have a position within an element $d\mathbf{r}$ about $\mathbf{r}$, and a momentum within an element $d\mathbf{k}$ about $\mathbf{k}$. In the *absence* of collisions, and in the presence of an external force $\mathbf{F}$, particle conservation demands that

$$f\left(\mathbf{r}+\frac{\mathbf{k}}{m}dt,\mathbf{k}+\mathbf{F}dt,t+dt\right)d\mathbf{r}d\mathbf{k}-f(\mathbf{r},\mathbf{k},t)\,d\mathbf{r}d\mathbf{k}=0. \tag{2.31}$$

In the presence of collisions, the resulting change in distribution function must equal (2.31),

$$f\left(\mathbf{r}+\frac{\mathbf{k}}{m}dt,\mathbf{k}+\mathbf{F}dt,t+dt\right)d\mathbf{r}d\mathbf{k}-f(\mathbf{r},\mathbf{k},t)\,d\mathbf{r}d\mathbf{k}=\left(\frac{\partial f}{\partial t}\right)_{coll}d\mathbf{r}d\mathbf{k}dt. \tag{2.32}$$

Dividing (2.32) by $d\mathbf{r}d\mathbf{k}dt$ and taking the infinitesimal limit, we arrive at the Boltzmann equation,

$$\frac{\partial f}{\partial t}+\frac{\partial f}{\partial \mathbf{r}}\cdot\mathbf{v}+\frac{d\mathbf{k}}{dt}\cdot\frac{df}{d\mathbf{k}}=\left(\frac{\partial f}{\partial t}\right)_{coll}. \tag{2.33}$$

In general, solutions to (2.33) are non-linear integro-differential equations that must be evaluated numerically. There are several approximations that are commonly used in Boltzmann equation calculations in order to make the problem more tractable. The first is to linearise the Boltzmann equation and restrict the problem to small

deviations from equilibrium. The distribution function can then be written as $f^0(\mathbf{k}) + \Delta f(\mathbf{k})$, where $f^0(\mathbf{k})$ is the equilibrium distribution function and $\Delta f(\mathbf{k})$ is small. The second commonly used technique for evaluating the Boltzmann equation is to approximate the collision term by a relaxation time form by writing,

$$\left(\frac{\partial f}{\partial t}\right)_c = -\frac{f(\mathbf{k}) - f^0(\mathbf{k})}{\tau_{\mathbf{k}}} = -\frac{\Delta f(\mathbf{k})}{\tau_{\mathbf{k}}}. \tag{2.34}$$

This implies that the collisions restore the non-equilibrium distribution function $f(\mathbf{k})$ to its equilibrium value $f^0(\mathbf{k})$ in a characteristic time $\tau_{\mathbf{k}}$. In a further simplification, the scattering time $\tau_{\mathbf{k}}$ is often taken as being momentum independent, τ. It is possible to derive an expression for the drag rate assuming a momentum dependent scattering time [38]. However, the result is not expressible in terms of the individual layer susceptibilities.

In calculating the interlayer collision rate in a Coulomb drag system it will be necessary to work with an explicit form for the collision term. For a single layer, it is straightforward to construct the collision integral by considering the phase space restrictions to scattering, along with the scattering probability $\Omega_{\mathbf{k},\mathbf{k}'}$. The probability per unit time that an electron in a state $\mathbf{k}$ will be scattered into a state with the same spin, contained in an infinitesimal element $d\mathbf{k}'$ around $\mathbf{k}'$, is $\Omega_{\mathbf{k},\mathbf{k}'} d\mathbf{k}'$. However, not all of the states in $d\mathbf{k}'$ are empty. As a consequence of the exclusion principle, the actual rate of scattering will be reduced by the fraction of occupied states, $1 - f(\mathbf{k}')$. Now, the probability per unit time $P(\mathbf{k})$ of an electron in a state $\mathbf{k}$, leaving $d\mathbf{k}$ via collisions, must be the sum over all $\mathbf{k}'$ of the probability to scatter into a state $\mathbf{k}'$:

$$P(\mathbf{k}) = \int \frac{d\mathbf{k}'}{(2\pi)^d} \Omega_{\mathbf{k},\mathbf{k}'} \left(1 - f(\mathbf{k}')\right). \tag{2.35}$$

The total number of electrons per unit time that undergo a scattering event in the infinitesimal volume $d\mathbf{k}$ around $\mathbf{k}$, and consequently leave it, is $P(\mathbf{k}) f(\mathbf{k})$. The change in the distribution function due to these collisions is therefore,

$$\left(\frac{\partial f(\mathbf{k})}{\partial t}\right)_{out} = -f(\mathbf{k}) P(\mathbf{k}) = -f(\mathbf{k}) \int \frac{d\mathbf{k}'}{(2\pi)^d} \Omega_{\mathbf{k},\mathbf{k}'} (1 - f(\mathbf{k}')) . \tag{2.36}$$

To evaluate $\left(\frac{\partial f(\mathbf{k})}{\partial t}\right)_{in}$, we note that the probability per unit time that electron in a state $\mathbf{k}'$ is scattered into $d\mathbf{k}$ around $\mathbf{k}$ is $\Omega_{\mathbf{k}',\mathbf{k}} d\mathbf{k}'$. Because only a fraction of these states are occupied, the probability is reduced by a factor $f(\mathbf{k}')$. Similarly, due to the exclusion principle, the fraction of $\mathbf{k}$ states available for scattering into reduces the scattering probability by a factor $1 - f(\mathbf{k})$. The total number of electrons per unit time scattering into $d\mathbf{k}$ is therefore,

$$\left(\frac{\partial f(\mathbf{k})}{\partial t}\right)_{in} = (1 - f(\mathbf{k})) \int \frac{d\mathbf{k}'}{(2\pi)^d} \Omega_{\mathbf{k}',\mathbf{k}} f(\mathbf{k}') . \tag{2.37}$$

The total change in f per unit time due to collisions is therefore

$$\begin{aligned} \left(\frac{\partial f(\mathbf{k})}{\partial t}\right)_c &= \left(\frac{\partial f(\mathbf{k})}{\partial t}\right)_{out} + \left(\frac{\partial f(\mathbf{k})}{\partial t}\right)_{in} \qquad (2.38) \\ &= \int \frac{d\mathbf{k}'}{(2\pi)^d} \left[\Omega_{\mathbf{k}',\mathbf{k}} (1 - f(\mathbf{k})) f(\mathbf{k}') - \Omega_{\mathbf{k},\mathbf{k}'} f(\mathbf{k}) (1 - f(\mathbf{k}'))\right] \end{aligned}$$

where, for a Coulomb drag system where each layer is taken as a mathematical plane, $d = 2$.

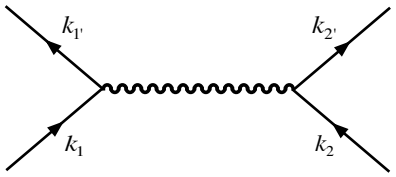

Figure 2.10: Diagram representing interlayer scattering.

2.5.1.1 Interlayer Scattering

Equation (2.38) describes the change of the distribution function as a result of scattering with impurities in a given layer. The quantity of interest in calculating the drag resistivity is the change of the distribution function as a result of scattering events between electrons in different layers. We may extend (2.38) to this case by noting that such scattering events involve two incoming and two outgoing momenta (see figure 2.10). Therefore, the scattering probability, Ω, becomes a function of four momenta and the occupancy of the two extra states must be taken into account. Enforcing energy conservation with Dirac δ functions and including spin summations, the collision term for interlayer electron-electron scattering is

$$\left(\frac{\partial f_1}{\partial t}\right)_c = \sum_{\sigma_{1'},\sigma_2,\sigma_{2'}} \int \frac{d\mathbf{k}_{1'}}{(2\pi)^2} \int \frac{d\mathbf{k}_2}{(2\pi)^2} \int \frac{d\mathbf{k}_{2'}}{(2\pi)^2} \Omega\left(1,2:1',2'\right) \tag{2.39}$$

$$\times S\left(f_1,f_2,f_{1'},f_{2'}\right)\delta\left(\mathbf{k_1}+\mathbf{k_2}-\mathbf{k_{1'}}-\mathbf{k_{2'}}\right)\delta\left(\varepsilon_1+\varepsilon_2-\varepsilon_{1'}-\varepsilon_{2'}\right)$$

where $S\left(f_1,f_2,f_{1'},f_{2'}\right) = f_{1'}f_{2'}\left(1-f_1\right)\left(1-f_2\right) - f_1 f_2\left(1-f_{1'}\right)\left(1-f_{2'}\right)$. It should be noted that in equilibrium ($f_i = f_i^0$), the detailed balance condition implies that the should be no net flow of probability around a closed cycle of states. Therefore, $S\left(f_1^0,f_2^0,f_{1'}^0,f_{2'}^0\right) = 0$. Therefore, momentum transfer to the drag layer arises because of the asymmetry of the electron distribution of one layer relative to the

other.

The delta function involving momentum in (2.39) allows us to omit a momentum integration and we may therefore write $\left(\frac{\partial f_1}{\partial t}\right)_c =$

$$\sum_{\sigma_{1'},\sigma_2,\sigma_{2'}} \int \frac{d\mathbf{k}_{1'}}{(2\pi)^2} \int \frac{d\mathbf{k}_2}{(2\pi)^2} \Omega\left(1,2:1',2'\right) S\left(f_1,f_2,f_{1'},f_{2'}\right) \delta\left(\varepsilon_1+\varepsilon_2-\varepsilon_{1'}-\varepsilon_{2'}\right), \tag{2.40}$$

where σ_i are spin variables and a dash indicates a state after a scattering event. The function $\Omega\left(1,2:1',2'\right)$ is the probability that two electrons in states $k_1\sigma_1$ and $k_2\sigma_2$ will scatter into the states $\mathbf{k}_{1'},\sigma_{1'}$ and $\mathbf{k}_{2'},\sigma_{2'}$. Time reversal symmetry is assumed so that $\Omega\left(1,2:1',2'\right) = \Omega\left(1',2':1,2\right)$.

It turns out that it is useful to recast the collision integral using terms of the form $\frac{f_i}{1-f_i}$, allowing us to exploit the identity $\frac{f_i^0}{1-f_i^0} = \exp\left(-\frac{\varepsilon_i-\mu}{k_BT}\right)$. To this end, energy conservation's demand that $\varepsilon_1+\varepsilon_2 = \varepsilon_{1'}+\varepsilon_{2'}$ allows us to write,

$$\frac{f_1^0}{1-f_1^0}\frac{f_2^0}{1-f_2^0} = \frac{f_{1'}^0}{1-f_{1'}^0}\frac{f_{2'}^0}{1-f_{2'}^0}, \tag{2.41}$$

and $S\left(f_1,f_2,f_{1'},f_{2'}\right) =$

$$= \left(1-f_1\right)\left(1-f_2\right)\left(1-f_{1'}\right)\left(1-f_{2'}\right)\left[\frac{f_{1'}f_{2'}}{\left(1-f_{1'}\right)\left(1-f_{2'}\right)} - \frac{f_1f_2}{\left(1-f_1\right)\left(1-f_2\right)}\right]. \tag{2.42}$$

Next, we linearise the distribution f_i under the assumption of weak interlayer scattering to yield,

$$f_i = f_i^0 + \Delta f_i \simeq f_i^0 + \frac{\partial f_i^0}{\partial \varepsilon}\zeta_i\left(\varepsilon\right) = f_i^0 + f_i^0\left(1-f_i^0\right)\psi_i\left(\epsilon\right), \tag{2.43}$$

and similarly,

$$\frac{f_i}{1-f_i} \simeq \frac{f_i^0}{1-f_i^0} + \frac{f_i^0}{1-f_i^0}\psi_i(\varepsilon), \tag{2.44}$$

where $\psi_i(\varepsilon) = -\zeta_i(\varepsilon)/k_BT$ is a slowly varying function of energy, ε. Substituting (2.44) , (2.41) and (2.43) into (2.42) gives for the linearised S term,

$$S(f_1, f_2, f_{1'}, f_{2'}) \simeq \left(1-f_{1'}^0\right)\left(1-f_{2'}^0\right) f_1^0 f_2^0 \left[\psi_{2'} + \psi_{1'} - \psi_2 + \psi_1\right] + O\left(\psi^2\right). \tag{2.45}$$

Substituting this into (2.40) we arrive at the linearised collision integral:

$$\left(\frac{\partial f_1}{\partial t}\right)_c = -\sum_{\sigma_{1'}\sigma_2\sigma_{2'}} \int \frac{d\mathbf{k}_{1'}}{(2\pi)^2} \int \frac{d\mathbf{k}_2}{(2\pi)^2} \Omega(1,2:1',2') \left[\psi_1 + \psi_2 - \psi_{1'} - \psi_{2'}\right]$$

$$\times {f^0}_1 {f^0}_2 \left(1-{f^0}_{1'}\right)\left(1-{f^0}_{2'}\right) \delta\left(\varepsilon_1 + \varepsilon_2 - \varepsilon_{1'} - \varepsilon_{2'}\right). \tag{2.46}$$

If we assume that impurity scattering in the drive layer (2) is weak so that the distribution function in this layer is not far from equilibrium, then the dynamics of this layer can then be described by the single layer Boltzmann equation in the relaxation time approximation:

$$e\mathbf{E}.v_{\mathbf{k}} \frac{df_2^0}{d\varepsilon} = \frac{\Delta f(\mathbf{k})}{\tau_2}, \tag{2.47}$$

where $\Delta f(\mathbf{k}) \simeq \frac{\partial f_2^0}{\partial \varepsilon}\zeta_2(\varepsilon)$ is the change in the distribution function from equilibrium. Noting that $\zeta_2(\varepsilon) = k_BT\psi_2(\varepsilon)$ and then choosing the direction of the current to be parallel to the x-axis, we can express the deviation functions ψ_2 and $\psi_{2'}$ as

$$\psi_2 = -\frac{1}{k_BT}\tau_2 e v_{2x} E_2, \qquad \psi_{2'} = -\frac{1}{k_BT}\tau_2 e v_{2x'} E_2. \tag{2.48}$$

Because no current is flowing in the drag layer the distribution function is the equilibrium one, corresponding to $\psi_1 = \psi_{1'} = 0$. Assuming that the effective masses in both layers are identical, momentum conservation gives $v_{2x} - v_{2x'} = v_{1x'} - v_{1x} = \frac{\hbar}{m}(k_{1x'} - k_{1x})$. With this in mind we substitute (2.48) into (2.46) to get

$$\left(\frac{\partial f_1}{\partial t}\right)_c = -\frac{\tau_2 e^2}{m k_B T} \sum_{\sigma_{1'}\sigma_2\sigma_{2'}} \int \frac{d\mathbf{k}_{1'}}{(2\pi)^2} \int \frac{d\mathbf{k}_2}{(2\pi)^2} \Omega\left(1,2:1',2'\right) \tag{2.49}$$

$$\times \left[k_{1x'} - k_{1x}\right] {f^0}_1 {f^0}_2 \left(1 - {f^0}_{1'}\right)\left(1 - {f^0}_{2'}\right) \delta\left(\varepsilon_1 + \varepsilon_2 - \varepsilon_{1'} - \varepsilon_{2'}\right).$$

If we multiply (2.49) by k_{1x} and integrate over momentum and spin, we get the rate of transfer of momentum from the drive to the drag layer,

$$\frac{dP}{dt} = -\frac{\tau_2 e^2}{m k_B T} \sum_{\sigma_1\sigma_{1'}\sigma_2\sigma_{2'}} \int \frac{d\mathbf{k}_1}{(2\pi)^2} \int \frac{d\mathbf{k}_{1'}}{(2\pi)^2} \int \frac{d\mathbf{k}_2}{(2\pi)^2} \Omega\left(1,2:1',2'\right) \tag{2.50}$$

$$\times k_{1x} \left[k_{1x'} - k_{1x}\right] {f^0}_1 {f^0}_2 \left(1 - {f^0}_{1'}\right)\left(1 - {f^0}_{2'}\right) \delta\left(\varepsilon_1 + \varepsilon_2 - \varepsilon_{1'} - \varepsilon_{2'}\right).$$

The summation over spins may be evaluated by noting that only two of the four variables are independent since $\sigma_1 = \sigma_{1'}$ and $\sigma_2 = \sigma_{2'}$, providing an additional factor of 4. Furthermore, the right-hand side of (2.50) may be simplified by noting the symmetry of the integrand with respect to the interchange of 1 and $1'$. This implies that $k_{1x}\left(k_{1'x} - k_{1x}\right) = k_{1'x}\left(k_{1x} - k_{1'x}\right)$ and so $k_{1x}^2 = k_{1'x}^2$. In addition, the relaxation rate is independent of whether the electric field is taken along the x or y axis. Consequently, we may average the contribution from each so that

$$\frac{1}{2}\left(k_{1'x} - k_{1x}\right)^2 \equiv \frac{1}{4}\left(\mathbf{k_{1'}} - \mathbf{k_1}\right)^2 = \frac{\mathbf{q}^2}{4}. \tag{2.51}$$

where $\mathbf{q}$ is the interlayer momentum transfer. Substituting this into (2.49) gives

$$\frac{dP}{dt} = -\frac{e\hbar E_2\tau_2}{mk_BT}\int\frac{d\mathbf{k_1}}{(2\pi)^2}\int\frac{d\mathbf{k_{1'}}}{(2\pi)^2}\int\frac{d\mathbf{k_2}}{(2\pi)^2}\Omega\left(1,2:1',2'\right) \tag{2.52}$$

$$\times q^2 {f^0}_1 {f^0}_2\left(1-{f^0}_{1'}\right)\left(1-{f^0}_{2'}\right)\delta\left(\varepsilon_1+\varepsilon_2-\varepsilon_{1'}-\varepsilon_{2'}\right).$$

If we assume that the scattering amplitude, Ω, depends only on $\mathbf{q}$ and not on the specific momentum values, the integral over $\mathbf{k_{1'}}$ can be replaced by an integral over $\mathbf{q}$ to give

$$\frac{dP}{dt} = -\frac{e\hbar E_2\tau_2}{4mk_BT}4\int\frac{d\mathbf{q}}{(2\pi)^2}\int\frac{d\mathbf{k}_1}{(2\pi)^2}\int\frac{d\mathbf{k}_2}{(2\pi)^2}\Omega\left(q\right)q^2 \tag{2.53}$$
$$\times {f^0}_1 {f^0}_2\left(1-{f^0}_{1'}\right)\left(1-{f^0}_{2'}\right)\delta\left(\varepsilon_1+\varepsilon_2-\varepsilon_{1'}-\varepsilon_{2'}\right).$$

A few more technical manipulations are now needed to cast (2.53) in terms of the layer density-density response functions. Noting the following two identities,

$$\delta\left(\varepsilon_1+\varepsilon_2-\varepsilon_{1'}-\varepsilon_{2'}\right)=\hbar\int_{-\infty}^{\infty}d\omega\delta\left(\varepsilon_1+\varepsilon_{1'}-\hbar\omega\right)\delta\left(\varepsilon_2+\varepsilon_{2'}+\hbar\omega\right), \tag{2.54}$$

$$f^0\left(\varepsilon\right)\left[1-f^0\left(\varepsilon+\hbar\omega\right)\right]=\frac{f^0\left(\varepsilon\right)-f^0\left(\varepsilon+\hbar\omega\right)}{1-e^{-\frac{\hbar\omega}{k_BT}}}, \tag{2.55}$$

we substitute these into (2.53) and use the identity

$$\left(1-e^{+\frac{\hbar\omega}{k_BT}}\right)\left(1-e^{-\frac{\hbar\omega}{k_BT}}\right)=-4sinh^2\left(\frac{\hbar\omega}{2k_BT}\right), \tag{2.56}$$

to yield

$$\begin{aligned}\frac{dP}{dt} &= \frac{e\hbar^2 E_2\tau_2}{mk_BT}\int_{-\infty}^{\infty}d\omega\int\frac{d\mathbf{q}}{(2\pi)^2}\Omega(q)\frac{q^2}{sinh^2\left(\frac{\hbar\omega}{2k_BT}\right)} \\ &\times\left\{\int\frac{d\mathbf{k}_1}{(2\pi)^2}\left(f^0(\varepsilon_1)-f^0(\varepsilon_1+\hbar\omega)\right)\delta(\varepsilon_1+\varepsilon_{1'}-\hbar\omega)\right\} \\ &\times\left\{\int\frac{d\mathbf{k_2}}{(2\pi)^2}\left(f^0(\varepsilon_2)-f^0(\varepsilon_2-\hbar\omega)\right)\delta(\varepsilon_2+\varepsilon_{2'}+\hbar\omega)\right\}.\end{aligned} \tag{2.57}$$

The terms in curly brackets in (2.57) are proportional to the imaginary part of the individual layer density-density response functions $Im\chi_1(\mathbf{q},\omega)$ and $Im\chi_2(\mathbf{q},-\omega)$. Using the oddness of $Im\chi_i(\mathbf{q},\omega)$ with respect to ω, the second of these terms may be written as $-\frac{1}{\pi}Im\chi_2(\mathbf{q},\omega)$. Observing that the integrand in (2.57) is an even function of ω, we now change the limits of the integral over ω from $\int_{-\infty}^{\infty}$to $\int_0^{\infty}$ and get,

$$\frac{dP}{dt}=\frac{e\hbar^2E_2\tau_2}{4\pi^2mk_BT}\int_0^{\infty}d\omega\int\frac{d\mathbf{q}}{(2\pi)^2}\Omega(q)\frac{q^2}{sinh^2\left(\frac{\hbar\omega}{2k_BT}\right)}Im\chi_1(q,\omega)Im\chi_2(q,\omega). \tag{2.58}$$

2.5.1.2 Drag Resistivity

In order to obtain an expression for the drag resistivity we must first invoke Newton's second law and equate the rate of momentum transfer to the drag layer, to the total force per particle on the electrons in the drag layer due to the induced electric field E_D:

$$\frac{dP}{dt}=n_2eE_D, \tag{2.59}$$

where n_2 is the carrier density of the drag layer. This is the condition for a steady state. Substituting in (2.58) we have

$$n_2 e E_D = \frac{e\hbar^2 E_2 \tau_2}{4\pi^2 m k_B T} \int_0^\infty d\omega \int \frac{d\mathbf{q}}{(2\pi)^2} \Omega(q) \frac{q^2}{sinh^2\left(\frac{\hbar\omega}{2k_B T}\right)} Im\chi_1(q,\omega) Im\chi_2(q,\omega). \tag{2.60}$$

To proceed, we write the drag resistivity ρ_D in terms of an interlayer scattering rate τ_D, in analogy with the Drude conductivity, so that

$$\rho_D = \frac{E_D}{J_1} = \frac{m}{n_2 e^2 \tau_D}. \tag{2.61}$$

Using the standard Drude expression

$$J_1 = \frac{n_2 e^2 \tau_1}{m} E_1, \tag{2.62}$$

where E_1 is the electric field across the drive layer and τ_1 the transport scattering time. We then combine (2.61) and (2.62) to yield

$$\frac{E_D}{E_1} = \frac{\tau_1}{\tau_D}. \tag{2.63}$$

Combining equations (2.60), (2.61) and (2.62) we have for the drag resistivity

$$\rho_D = \frac{1}{2\pi^2 e^2 n_1 n_2} \int_0^\infty dq \Omega(q) q^3 \int_0^\infty d\omega \frac{\beta}{4\sinh^2\left[\frac{\beta\omega}{2}\right]} Im\chi_1(q,\omega) Im\chi_2(q,\omega). \tag{2.64}$$

In general, equation (2.64) must be evaluated numerically. In order to extract an analytic result we make a number of approximations. Foremost, we assume that each layer is identical so that $Im\chi_1 = Im\chi_2 \equiv Im\chi$ and $n_1 = n_2 \equiv n$. We then

approximate the scattering probability $\Omega(q)$ using the Born approximation [4], valid under the assumption of weak scattering. The Born approximation states that the scattering probability is proportional to the square of the interaction potential so that

$$\Omega(q) = \left|eU_{12}(q, \omega = 0)\right|^2, \tag{2.65}$$

where $U_{12}(q, \omega = 0)$ is the static screened interlayer interaction (2.14). The consequence of using static screening in demonstrated in figure (2.6) where it can be seen that it overestimates the drag resistivity at intermediate temperatures. Under these approximations we have

$$\rho_D \simeq \frac{1}{2\pi^2 n^2} \int_0^\infty dq \left|U_{12}(q, \omega = 0)\right| q^3 \int_0^\infty d\omega \frac{\beta}{4 \sinh^2\left[\frac{\beta\omega}{2}\right]} Im\chi(q, \omega). \tag{2.66}$$

To obtain an analytic result, we must calculate (2.66) under the assumptions of large layer separation ($d \gg q^{-1}$) and low temperature ($T \to 0$). In the limit of large layer separation, we have for the interlayer interaction

$$U_{12}(q, \omega = 0) \simeq \frac{\pi q}{q_{TF}^2 sinh\,(qd)}. \tag{2.67}$$

The consequence of taking the low temperature limit ($T \to 0$) is that the frequency integral of (2.66) is cut off at low ω. In this limit, the imaginary part of the polarisability becomes

$$Im\chi\left(\mathbf{q}, \omega\right) \simeq \frac{m^2 \omega}{2\pi q k_F}. \tag{2.68}$$

With the use of equations (2.66), (2.67) and (2.68), the drag resistivity is now written in terms of elementary integrals. Performing these, it can be shown that in the limit

of large layer separation and low temperature, the drag resistivity reduces to

$$\rho_D = \frac{\pi k_B^2 T^2 \zeta(3)}{16 e^2 q_{TF}^2 E_F^2 k_F^2 d^4} \tag{2.69}$$

where $\zeta(z)$ is the Riemann Zeta function.

2.5.2 The Green's Function Approach

This calculation is due to Kamenev and Oreg [9] and Flensberg *et al.* [7] and uses linear response theory, starting from the Kubo formula to find the leading order Feynman diagrams that contribution to the drag conductivity. The Kubo formula for the drag conductivity is [9]

$$\sigma_D(\mathbf{Q}, \Omega) = \frac{1}{\Omega S} \int_0^\infty dt e^{i\Omega t} \langle [J_1(\mathbf{x}, t), J_2(\mathbf{x}', 0)] \rangle \tag{2.70}$$

where $\mathbf{Q}$, Ω are the wave vector and frequency of the external field, J_i is the current operator in the i'th layer and S is the area of the system.

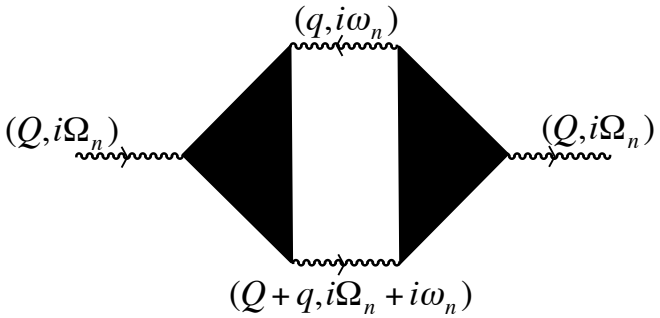

Figure 2.11: Diagram corresponding to the current-current correlation function to second order in the inter-layer Coulomb interaction. The shaded triangles corresponds to the non-linear susceptibilities, $\Gamma(q, \omega)$, appearing in (2.72).

The full Hamiltonian for the Coulomb drag system is of the general form $H = H_1 + H_2 + H_{12}$ where H_i are the individual layer Hamiltonians and H_{12} is the

interlayer contribution. The interlayer term has the form

$$H_{12}\left(\mathbf{r_1},\mathbf{r_2}\right)=\int d^3\mathbf{r_1}\int d^3\mathbf{r_2}\rho_1\left(\mathbf{r_1}\right)U_{12}(\mathbf{r_1}-\mathbf{r_2})\rho_2\left(\mathbf{r_2}\right) \tag{2.71}$$

where $U_{12}(\mathbf{r_1}-\mathbf{r_2})$ is the screened interlayer interaction. Treating H_{12} as a perturbation, they found that the leading order contribution to the drag conductivity is second order in the interlayer interaction, corresponding to the diagram in figure 2.11. In the uniform system ($Q\to 0$) and DC($\Omega\to 0$) limit, the leading contribution to drag conductivity has the form

$$\sigma_D=\frac{1}{16\pi k_BT}\sum_q\int_0^\infty d\omega\frac{\Gamma_1(q,\omega)\Gamma_2(q,\omega)\left|U_{12}(q,\omega)\right|^2}{\sinh^2\left(\hbar\omega/2k_BT\right)}. \tag{2.72}$$

The three point correlation functions, $\Gamma_i(q,\omega)$, appearing in (2.72) are the central characters in this formalism and correspond to the shaded triangles in figure 2.11. They are the non-linear susceptibilities (NLS) of layer i and can be evaluated under various levels of approximation. Here, as in [7,9], the approximation taken is that of non-interacting electrons scattering against random impurities, corresponding to the high density limit. This allows one to express the non-linear susceptibilities in terms of Green's functions. It is easier to work initially in the finite frequency Matsubara representation, before analytically continuing to real frequencies and taking the DC limit.

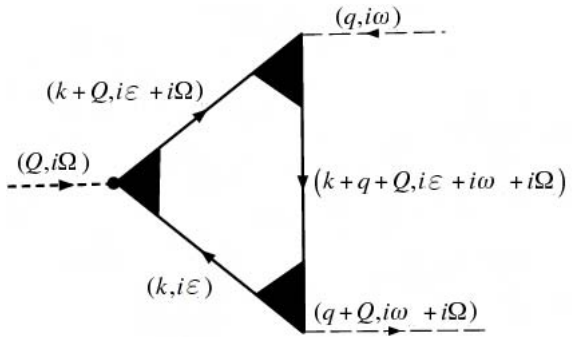

Figure 2.12: The Feynman diagram representing $\Delta(\mathbf{k}, \mathbf{q}, i\varepsilon, i\Omega, i\omega)$.

Each correlation function, Γ_i, is the sum of contributions from diagrams with clockwise and anti-clockwise propagating Green's functions (figure 2.12) and correspond to

$$\Gamma_i(\mathbf{q}; i\Omega + i\omega) = \tag{2.73}$$
$$\sum_{\mathbf{k}} \sum_{i\varepsilon} \left[\Delta(\mathbf{k}, \mathbf{q}, i\varepsilon, i\Omega, i\omega) + \Delta(\mathbf{k}, -\mathbf{q}, i\varepsilon, i\Omega, -i\omega - i\Omega)\right]$$

where

$$\Delta(\mathbf{k}, \mathbf{q}, i\varepsilon, i\Omega, i\omega) = G(\mathbf{k}, i\varepsilon)\, J(\mathbf{k})\gamma(\mathbf{k}, \mathbf{k}, i\varepsilon + i\Omega) \tag{2.74}$$
$$\times G(\mathbf{k}, i\varepsilon + i\Omega)\, \eta(\mathbf{k}, \mathbf{k}+\mathbf{q}; i\varepsilon + i\Omega, i\varepsilon + i\omega + i\Omega)$$
$$\times G(\mathbf{k}+\mathbf{q}, ik + i\Omega + i\omega)\, \eta(\mathbf{k}+\mathbf{q}, i\varepsilon; i\varepsilon + i\omega + i\Omega, i\varepsilon)$$

and the summation is over Fermi frequencies $i\varepsilon$. The functions γ and η are the current and charge vertex corrections respectively, and consist of ladder diagrams that take into account correlated *intralayer* impurity scattering. In what follows we will take the weak scattering limit, in which case charge vertex corrections can be ignored (see section 2.3.4 for a discussion of Coulomb drag in the diffusive regime). Correlated impurity scattering between the layers is also ignored. Taking these

into account would otherwise involve introducing impurity lines crossing from one triangle to the other (see section 2.4.2 for a discussion of correlated disorder). The current vertex cannot be ignored as it is important to take into account the fact that small angle scattering events contribute more to the conductivity. In general, this leads to the transport lifetime (τ_{tr}) and the impurity lifetime being (τ) being different but in the weak scattering limit $\gamma(\mathbf{k}) = \tau_{tr}(\mathbf{k})/\tau(\mathbf{k})$ [10]. In what follows we will assume that the current operator includes this correction.

The summation over Fermionic frequencies is evaluated by decomposing the Feynman diagram for (2.74) into allowed (internally consistent and non-zero) combinations of advanced (-) and retarded (+) Green's functions and then converting the summations over ik_m into contour integrals. The demand of a positive external frequency, Ω, and the interaction lines provide the first inequalities:

$$\Omega > 0;\ \omega < 0;\ \omega + \Omega > 0.$$

The only two non-zero contributions come from the triangle functions, Δ, with $\varepsilon < 0$, $\varepsilon + \Omega > 0$. This leads to two possible combinations Δ_1 and Δ_2 where,

$\Delta_1 =$ 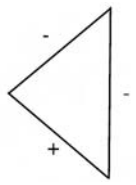

$$\varepsilon < 0,\ \varepsilon + \Omega > 0,\ \varepsilon + \omega + \Omega > 0$$
$$\therefore -\omega - \Omega < \varepsilon < 0$$

$\Delta_2 =$ 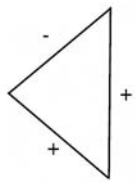

$$\varepsilon < 0,\ \varepsilon + \Omega > 0,\ \varepsilon + \omega + \Omega < 0$$
$$\therefore -\Omega < \varepsilon < -\omega - \Omega$$

The other two possibilities have three Green's functions of the same type and so

contribute nothing because their poles are on same side of the real axis. Writing Δ_1 and Δ_2 out explicitly and summing over $\mathbf{k}$ and ε we have,

$$\sum_{\mathbf{k},\varepsilon}\Delta_1 = -\sum_{\mathbf{k}}\sum_{-\omega-\Omega<\varepsilon<0} G^a_{\mathbf{k}}(i\varepsilon)J(\mathbf{k})G^r_{\mathbf{k}}(i\varepsilon+i\Omega)G^r_{\mathbf{k+q}}(i\varepsilon+i\Omega+i\omega), \quad (2.75)$$

$$\sum_{\mathbf{k},\varepsilon}\Delta_2 = -\sum_{\mathbf{k}}\sum_{0<\varepsilon<-\omega-\Omega} G^a_{\mathbf{k}}(i\varepsilon)J(\mathbf{k})G^r_{\mathbf{k}}(i\varepsilon+i\Omega)G^a_{\mathbf{k+q}}(i\varepsilon+i\Omega+i\omega). \quad (2.76)$$

We now convert the above summations into contour integral, following the standard prescription [10] of making the replacement

$$\beta^{-1}\sum_{i\varepsilon} f(i\varepsilon) = -\frac{1}{2\pi i}\oint dz n_F(z)f(z) \quad (2.77)$$

where n_F is the Fermi distribution function. After performing the contour integral, we analytically continue back to real frequencies and take the DC ($\Omega \to 0$) limit to yield,

$$\sum_{\mathbf{k},\varepsilon}\Delta_1 = \textstyle\sum_{\mathbf{k}}\int_{\infty}^{\infty}\frac{n_F(\varepsilon)d\varepsilon}{2\pi i} \left\{G^a_{\mathbf{k}}(\varepsilon)J(\mathbf{k})G^r_{\mathbf{k}}(\varepsilon)G^r_{\mathbf{k+q}}(\varepsilon+\omega)\right. \quad (2.78)$$
$$\left. -G^a_{\mathbf{k}}(\varepsilon-\omega)J(\mathbf{k})G^r_{\mathbf{k}}(\varepsilon-\omega)G^r_{\mathbf{k+q}}(\varepsilon)\right\},$$

$$\sum_{\mathbf{k},\varepsilon}\Delta_2 = \textstyle\sum_{\mathbf{k}}\int_{\infty}^{\infty}\frac{n_F(\varepsilon)d\varepsilon}{2\pi i} \left\{G^a_{\mathbf{k}}(\varepsilon-\omega)J(\mathbf{k})G^r_{\mathbf{k}}(\varepsilon-\omega)G^a_{\mathbf{k+q}}(\varepsilon)\right. \quad (2.79)$$
$$\left. -G^a_{\mathbf{k}}(\varepsilon)J(\mathbf{k})G^r_{\mathbf{k}}(\varepsilon)G^a_{\mathbf{k+q}}(\varepsilon+\omega)\right\}.$$

Summing (2.78) and (2.79) gives, for the first of the two triangle functions in (2.73),

$\sum_{\mathbf{k}}\sum_{i\varepsilon}\Delta\left(\mathbf{k},\mathbf{q},i\varepsilon,i\Omega,i\omega\right)=\sum_{\mathbf{k},\varepsilon}\Delta_1+\sum_{\mathbf{k},\varepsilon}\Delta_2$

$$\begin{aligned}=\ & \frac{1}{2\pi i}\sum_{\mathbf{k}}\int_{\infty}^{\infty}n_F(\varepsilon)d\varepsilon\left\{G^a_{\mathbf{k}}(\varepsilon)J(\mathbf{k})G^r_{\mathbf{k}}(\varepsilon)\left[G^r_{\mathbf{k+q}}(\varepsilon+\omega)-G^a_{\mathbf{k+q}}(\varepsilon+\omega)\right]\right. \\ & \left.-G^a_{\mathbf{k}}(\varepsilon-\omega)J(\mathbf{k})G^r_{\mathbf{k}}(\varepsilon-\omega)\left[G^r_{\mathbf{k+q}}(\varepsilon)-G^a_{\mathbf{k+q}}(\varepsilon)\right]\right\}.\end{aligned} \tag{2.80}$$

Now, making a change of variables $\varepsilon\rightarrow\varepsilon+\omega$ in the second term of (2.80) yields,

$\sum_{\mathbf{k}}\sum_{i\varepsilon}\Delta\left(\mathbf{k},\mathbf{q},i\varepsilon,i\Omega,i\omega\right)=$

$$\frac{1}{2\pi i}\int_{\infty}^{\infty}d\varepsilon\left[n_F(\varepsilon+\omega)-n_F(\varepsilon)\right]G^a_{\mathbf{k}}(\varepsilon)J(\mathbf{k})G^r_{\mathbf{k}}(\varepsilon)\left[G^r_{\mathbf{k+q}}(\varepsilon+\omega)-G^a_{\mathbf{k+q}}(\varepsilon+\omega)\right]. \tag{2.81}$$

Recalling (2.73), $\Gamma\left(\mathbf{q};i\Omega+i\omega\right)=\sum_{\mathbf{k},i\varepsilon}\left[\Delta\left(\mathbf{k},\mathbf{q},i\varepsilon,i\Omega,i\omega\right)+\Delta\left(\mathbf{k},-\mathbf{q},i\varepsilon,i\Omega,-i\omega-i\Omega\right)\right]$, in the DC limit the second term can be obtained from the first by setting $\mathbf{q}\rightarrow-\mathbf{q}$ and $\omega\rightarrow-\omega$. With this in mind we have our final Green's function expression for $\Gamma(q,\omega)$:

$$\begin{aligned}\Gamma(\mathbf{q},\omega)\ =\ & \frac{1}{2\pi i}\int_{\infty}^{\infty}d\varepsilon\left[n_F(\varepsilon+\omega)-n_F(\varepsilon)\right]G^a_{\mathbf{k}}(\varepsilon)J(\mathbf{k})G^r_{\mathbf{k}}(\varepsilon)\left[G^r_{\mathbf{k+q}}(\varepsilon+\omega)-G^a_{\mathbf{k+q}}(\varepsilon+\omega)\right] \\ & +\{q\rightarrow-q,\quad\omega\rightarrow-\omega\}.\end{aligned} \tag{2.82}$$

This expression is extremely important as it forms the basis for deriving the NLS for graphene monolayers and bilayers.

Derivation of the Boltzmann Equation Result We proceed to derive the Boltzmann equation result for the drag resistivity (2.64) by employing the identities [10] $G^r\left(\mathbf{k},\omega\right)-G^a\left(\mathbf{k},\omega\right)=-iA(k,\omega)$ and $G^r\left(\mathbf{k},\omega\right)G^a\left(\mathbf{k},\omega\right)=\tau A\left(\mathbf{k},\omega\right)$ and

substituting in the momentum operator $J(\mathbf{k}) = \mathbf{k}/m$. With these, (2.82) becomes

$$\begin{aligned}\Gamma(\mathbf{q},\omega) &= \frac{-\tau}{2\pi m}\mathbf{k}\sum_{\mathbf{k}}\int_{-\infty}^{\infty} d\varepsilon\left[n_F(\varepsilon+\omega)-n_F(\varepsilon)\right]A(\mathbf{k}+\mathbf{q},\varepsilon+\omega)\,A(\mathbf{k},\epsilon)\\ &\quad +\{q\to -q,\quad \omega\to-\omega\}.\end{aligned} \tag{2.83}$$

We now perform a change of variables $k \to k+q$ in the second term of (2.83) and swap the order of the Fermi functions. This yields

$$\Gamma(\mathbf{q},\omega) = \frac{\tau}{2\pi m}\mathbf{q}\sum_{\mathbf{k}}\int_{-\infty}^{\infty} d\varepsilon\left[n_F(\varepsilon+\omega)-n_F(\varepsilon)\right]A(\mathbf{k}+\mathbf{q},\varepsilon+\omega)\,A(\mathbf{k},\epsilon) \tag{2.84}$$

In the weak scattering limit the full impurity Green functions become free Green functions since the self energy vanishes in the non-interacting case. Furthermore, the use of free Green functions implies that the spectral functions reduce to δ functions so that

$$A(\mathbf{k},\varepsilon) = 2\pi\delta(\epsilon_{\mathbf{k}}). \tag{2.85}$$

Employing the identity $\int_{-\infty}^{\infty} d\epsilon\delta(\varepsilon+\omega-\xi_{\mathbf{k+q}})\,\delta(\varepsilon-\xi_{\mathbf{k}}) = \delta(\xi_{\mathbf{k}}+\omega-\xi_{\mathbf{k+q}})$ and $\frac{1}{\alpha\pm i\delta} = C\frac{1}{\alpha}\mp i\pi\delta(\alpha)$, equation (2.83) takes the form

$$\Gamma(\mathbf{q},\omega) = \frac{2\tau}{m}\mathbf{q}\sum_{\mathbf{k}} Im\left\{\frac{n_F(\xi_{\mathbf{k+q}})-n_F(\xi_{\mathbf{k}})}{\xi_{\mathbf{k+q}}-\xi_{\mathbf{k}}-\omega-i\delta}\right\} \tag{2.86}$$

after which it is trivial to see that (2.86) may be written in terms of the layer susceptibility function as

$$\Gamma(\mathbf{q},\omega) = \frac{2\tau}{m}\mathbf{q}Im\chi(\mathbf{q},\omega). \tag{2.87}$$

It is convenient for calculating the transresistivity to write (2.87) in terms of the in plane conductivity via the usual Drude result $\sigma_{ii} = e^2 n_i \tau_i / m$ so that (reintroducing system labels)

$$\Gamma_i(\mathbf{q},\omega) = \frac{2\sigma_{ii}}{e^2 n_i}\mathbf{q} Im\chi_i(\mathbf{q},\omega). \tag{2.88}$$

Substituting (2.88) into the transconductivity (2.72) yields,

$$\sigma_D = \frac{-2\sigma_{11}\sigma_{22}}{e^2 n_1 n_2}\sum_{\mathbf{q}} q^2 \left|U_{12}(q)\right|^2 \int_{-\infty}^{\infty}\frac{d\omega}{2\pi}\left[\partial_\omega n_B(\omega)\right] Im\chi_1(\mathbf{q},\omega) Im\chi_2(\mathbf{q},\omega) \tag{2.89}$$

where the fact that $Im\chi(\mathbf{q},\omega)$ is odd in both $\mathbf{q}$ and ω has been used. Therefore,

$$\begin{aligned}\rho_D &= \frac{2}{e^2 n_1 n_2}\sum_{\mathbf{q}} q^2 \left|U_{12}(\mathbf{q})\right|^2 \int_{-\infty}^{\infty}\frac{d\omega}{2\pi}\left[\partial_\omega n_B(\omega)\right] Im\chi_1(\mathbf{q},\omega) Im\chi_2(\mathbf{q},\omega) \\ &= \frac{-4}{e^2 n^2 k_B T}\sum_{\mathbf{q}} q^2 \left|U_{12}(\mathbf{q})\right|^2 \int_0^{\infty}\frac{d\omega}{2\pi}\frac{Im\chi(\mathbf{q},\omega)^2}{4sinh^2\left[\frac{\beta\omega}{2}\right]}\end{aligned} \tag{2.90}$$

where in the second line it has been assumed that the layers are identical. Finally, agreement with the Boltzmann transport calculation (2.64) is achieved by converting the sum over $\mathbf{q}$ to an integral to give

$$\rho_D = \frac{1}{2\pi^2 n_1 n_2}\int_0^{\infty} dq \left|U_{12}(\mathbf{q})\right|^2 q^3 \int_0^{\infty} d\omega \frac{\beta}{4sinh^2\left[\frac{\beta\omega}{2}\right]}\left[Im\chi(\mathbf{q},\omega)\right]^2. \tag{2.91}$$

Since the above calculation ignores all higher order (quantum-mechanical) processes, such was weak localisation, it is perhaps not surprising that the same result was obtainable via the Boltzmann transport approach.

Chapter 3

Graphene

In this chapter, we give a general overview of the history and physical properties of graphene, a potentially revolutionary two dimensional crystal within which electrons take on the characteristics of ultra-relativistic particles. After a brief introduction, we discuss the reason for its relatively recent discovery, despite long standing theoretical knowledge of its properties. In order for graphene to exists, it must overcome the predictions of the Mermin-Wagner theorem which states that it is impossible for macroscopically large two dimensional crystals to exit. Graphene overcomes this by rippling in the third dimension, whilst retaining the two dimensional character of its electronic properties. In addition, we discuss the technique that allows graphene to be searched for and classified with an optical microscope. The interference effect at its heart is responsible for catalysing this emerging field.

In the second half of the chapter, we discuss some of the electronic properties of graphene, primarily the unusual chiral Dirac fermion quasiparticles that characterise graphene physics. These are the result of the electron's interactions with the background lattice, leading to low energy excitations that have a linear dispersion, and are best described using the two dimensional Dirac equation. Details of graphene's

band structure, demonstrating why it is classified as a gap-less semiconductor, are given. Following this, we move on to the basic electronic properties of a graphene bilayer and highlight the essential differences with a monolayer. In particular, the retention of the property of pseudospin and the restoration of a quadratic quasiparticle spectrum.

In the final section, we discuss the open question of graphene's minimum conductivity. This is an effect whereby conductivity of undoped graphene is quantized, despite the fact that at zero doping the electronic density of states vanishes. It remains perhaps the biggest unsolved problem in graphene physics.

3.1 Introduction

On Earth, carbon is arguably the most important of all elements in the periodic table. The flexibility of its bonds make it the central component of life, all of organic chemistry and of course our hydrocarbon based society. It is able to form an unlimited number of different structures of varying dimensionality and displays an array of interesting phenomena. Three dimensional structures consisting of only carbon atoms are familiar in everyday life in the form of diamond and graphite (see figure 3.1). Less familiar are the lower dimensional allotropes of carbon such as graphene. Graphene is a one atom thick layer of carbon atoms arranged in a honeycomb lattice. It plays a leading role in understanding the physical properties of carbon nanotubes and fullerenes (commonly known as Buckyballs) because it forms the basis of their structures.

Carbon nanotubes are made by rolling up graphene along a given axis and reconnecting the carbon bonds. They can be modeled as one dimensional structures and

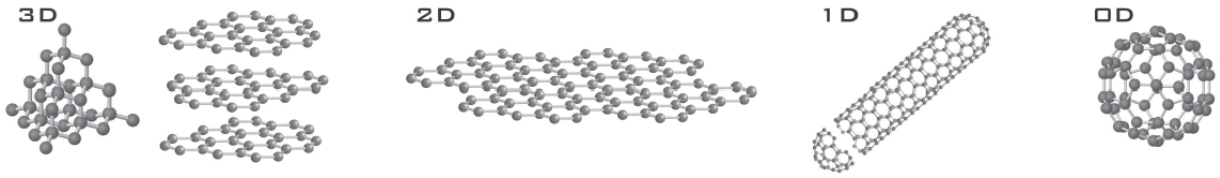

Figure 3.1: Carbon allotropes of varying dimensionality. From left to right; diamond, graphite, graphene, nanotubes, fullerenes. Reproduced from [41].

have been the subject of a great deal of theoretical and experimental interest [39]. Fullerenes are carbon atoms arranged into a sphere and may be treated as zero dimensional objects with discrete energy levels. To make fullerenes from graphene, it is necessary to introduce pentagons into the structure.

Although the basic properties of graphene, such as its band structure and unusual semi-metallic behaviour, have long been known [40], its actual realisation was for a long time considered improbable. Its properties were instead used as a starting point to study graphite (from the Greek word "graphein", to draw, to write), first discovered in a mine near Borrowdale in Cumbria in the 16th century, and an important material in the post-war era for its use in the nuclear fission industry. Experimental and theoretical interest in graphene was revitalised when in 2004 a group at Manchester university, led by Andre Geim, succeeded for the first time in isolating a graphene flake [51]. Graphene physics is currently the fastest expanding area of condensed matter physics, and graphene's highly unusual mechanical and electronic properties hold promise for a staggering number of technological applications.

As of 2009, graphene holds the records of being the strongest [52] material ever discovered and is approximately 200 times stronger than the strongest steel. At room temperature, it is also the most conductive, both electrically and thermally [53]. For example, it is approximately 30% more electrically conductive than silver, previously the most conductive material at room temperature. Many of its unique properties

can be traced to its unusual low energy excitations that are massless, chiral, Dirac fermions (see section 3.3). In undoped graphene, the electronic dispersion mimics the physics of quantum electrodynamics, but with an *effective* speed of light that is 300 times smaller than c. Indeed, many of the unusual properties of quantum electrodynamics show up in graphene, but at much smaller speeds where their magnitude is enhanced [43].

3.2 Fabrication

The early history of graphene is full of many surprises, starting with the fact that for many years it was thought that it could not exist in an isolated form. The reason for this pessimism originated with an argument put forward more than seventy years ago by Landau and Peierls [46–48], and later extended by Mermin [49] into what is now known as the Mermin-Wagner theorem. They argued that a strictly 2D crystal would be thermodynamically unstable due to a divergence in the density of long wavelength phonons. At finite temperature, this would lead to displacements comparable to the lattice spacing. This argument was supported by experimental evidence showing that the melting temperature of thin films rapidly decreases with decreasing thickness [50, 63].

It came a surprise then when in 2004, Novoselov *et al.* [51] reported the discovery of graphene. A year later they reported the discovery of other free standing two dimensional atomic crystals such as single layer boron nitride [55]. What was also surprising was that these crystals displayed a remarkable high crystal quality, especially so in the case of graphene. With the benefit of hindsight, the existence of graphene has been reconciled [56] with the earlier arguments that it should not

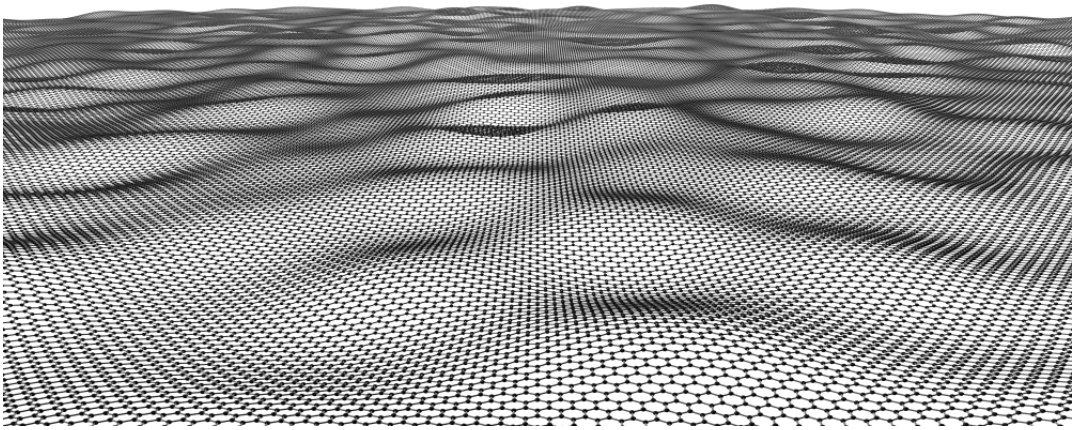

Figure 3.2: Stability in two dimensions. An artist's impression of ripples in a graphene sheet. Reproduced from [86].

exist. The suggestion is that graphene avoids the divergence in the phonon density of states by forming ripples on a scale of $\approx 10nm$ in the third dimension. Although this increases the elastic energy, it is more than compensated for by the suppression of the thermal vibrations.

Consequently, it could be argued that graphene is not a truly two dimensional crystal. However, it should be remembered that broadly speaking, the graphene is still no more three dimensional than the surface of an apple is to an ant. Although there may be effects of moving over a curved surface, both still have only two spatial degrees of freedom. In fact, it has been shown that rippled graphene retains its characteristic electronic properties where, for ripples that change slowly on the lattice scale, the curvature can be recast as an effective magnetic field [57]. In the opposite case they are equivalent to potential scatterers and are screened in the normal way [58]. That graphene is inherently curved has led some to make analogies of Dirac fermions propagating on a locally curved surface, to problems of quantum gravity [59]. The question remains however as to what extent two, three, or more graphene layers should be considered two dimensional crystals. The question is, as more layers are added, when does the system resemble the bulk behaviour of

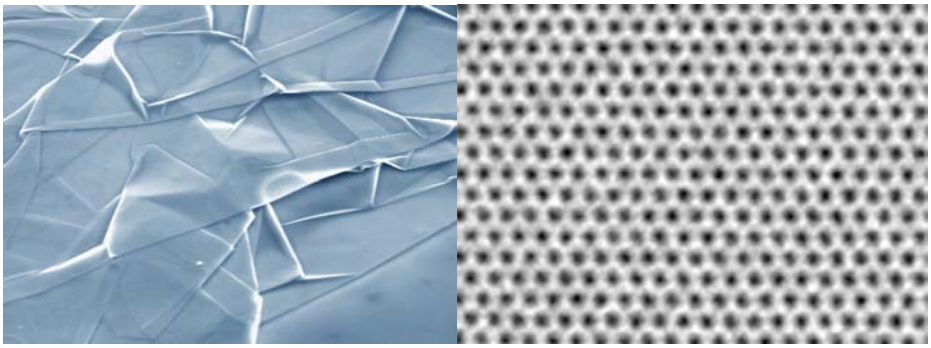

Figure 3.3: Left: Scanning electron microscope image of a strongly crumpled graphene sheet on a Si wafer. The image width is $20\mu m$. The Si wafer can be seen in the bottom right corner. Image reproduced from [86]. Right: Transmission electron microscope image of a graphene layer with a resolution of $\sim$ 1Å (atoms appear white). Reproduced from [87].

graphite? In fact it is known that the electronic properties of graphene layers change quickly as layers are added with the system behaving as bulk graphite approaching ten layers [60]. Already for a bilayer, the behaviour is markedly changed. Although many of the important features of monolayer graphene, such as pseudospin and zero band gap, (sec. 3.3.3) remain. As more layers are added, many of the distinguishing features of graphene's electronic properties disappear and it can be argued that one, two, and more layers should be identified as three different types of 2D crystals [45]. From the point of view of screening, this distinction is sensible because the screening length in graphite is approximately 5Å, equating to less than two layers' thickness. For systems larger than this, a distinction must be made between the surface and the bulk.

The technique that Novoselov *et al.* [51] used to create their graphene samples is technically known as micro-mechanical cleavage. Initially, they were applying adhesive tape to graphite and transferring the residue to a SiO_2 substrate (figure 3.3). The technique has since been refined. In hindsight, every time that a pencil is used some graphene is created. This should not be surprising because graphite

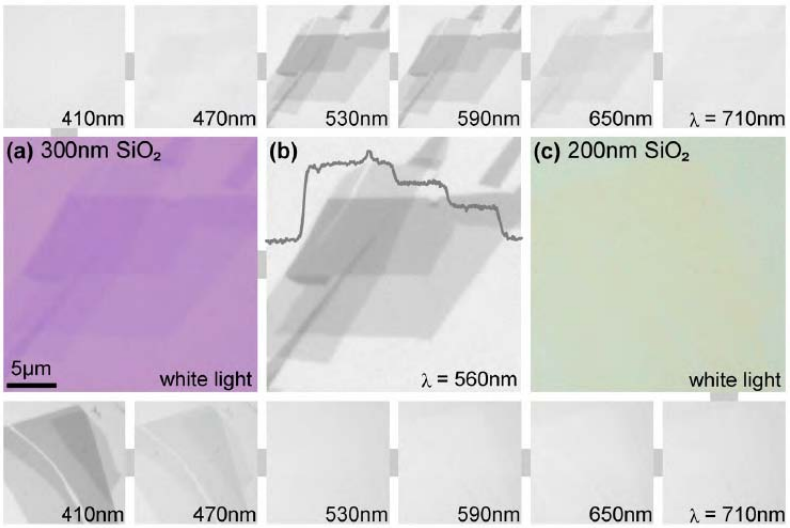

Figure 3.4: Graphitic samples on SiO_2 substrates of varying thickness and illuminated with a range of sources. (a) A 300nm SiO_2 substrate illuminated by white light. Graphene is visible as the lightest areas set against the background substrate. (b) Another 300nm substrate but illuminated with green light at 560nm showing a marked improvement in contrast over white light. (c) A 200nm substrate illuminated with white light. Even three layers of graphene are not distinguishable. Reproduced from [64]

is composed of stacks of weakly bonded graphene sheets. In fact, this is the reason that graphite is so useful as a writing material. The real breakthrough of Novoselov *et al.* [51] was to develop a method of finding single graphene flakes amongst a sea of graphitic flakes.

3.2.1 Making Graphene Visible

It was not possible to search for graphene flakes using established techniques, such as atomic force or electron microscopy, because they do not provide a strong enough signature of a monolayer and are slow at searching micrometer length scales. Remarkably, the technique that Novoselov *et al.* [51] used to search for graphene flakes used an optical microscope and the human brain's image processing capability.

By placing the graphitic sample onto a thin ($\sim 100nm$) SiO_2 layer, itself on top of

a Si substrate, they were able to exploit an interference effect that is strong enough to distinguish between one and two layers of graphene. By carefully choosing the SiO_2 layer thickness, the effect was maximised. Graphene monolayers then appeared under the microscope as areas darker than the background substrate but lighter than the surrounding multilayered graphitic pieces.

The nature of this interference effect was studied theoretically by Blake *et al.* [64] who showed that graphene's opacity was in part responsible for the effect's extreme sensitivity. In fact, not only is the opacity of graphene staggeringly high for a one atom thick layer, but it also has a startlingly simple value of $\pi\alpha \approx 2.3\%$, where $\alpha = e^2/\hbar c \approx 1/137$ is the fine structure constant (c is the real speed of light). It is unusual in condensed matter physics to find phenomena that are defined only by fundamental constants and not a material's properties. Other examples include the quantum of resistivity, h/e^2, that appears in universal conductance fluctuations and various transport experiments, and the magnetic flux quantum, $h/2e$, that appears in superconductivity. What is particularly unusual in this case is that an *unsophisticated* quantity such as opacity is defined in terms of a constant that is usually associated with quantum electrodynamics. The fine structure constant describes the coupling between relativistic electrons and light and is an empirical parameter in the standard model of particle physics.

Blake *et al.* [64] were able to derive theoretically the contrast between a graphene flake and the substrate, as a function of wavelength and SiO_2 thickness (figure 3.5). It was shown that given a suitable choice of monochromatic source, graphene can be found on any thickness of SiO_2. It was clear however that a thickness of $100nm$ produces the greatest contrast for visible searching. They applied the same approach to other insulating substrates and were able to find, for example, graphene on $50nm$

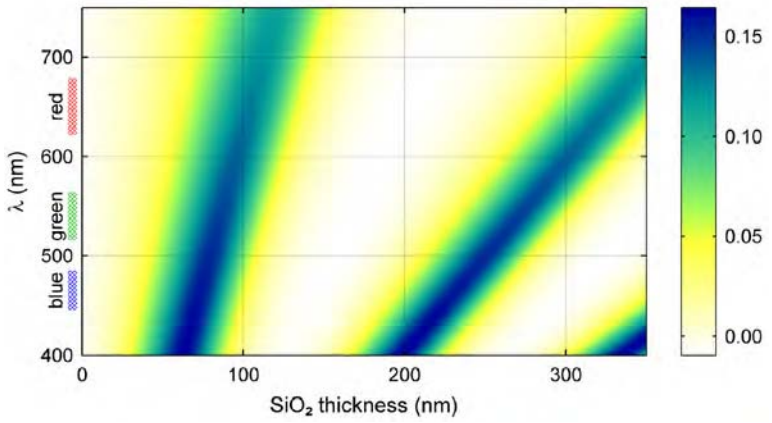

Figure 3.5: Plot showing the contrast of a graphene flake and the substrate as a function of SiO_2 thickness and wavelength. The colour scale on the right shows the expected contrast. A thickness of 100nm is clearly the best choice for searching for graphene with white light. Reproduced from [64].

Si_3N_4 using blue light.

3.2.2 Macroscopic Graphene

The development of a reliable way to make macroscopic quantities of graphene is one of the major obstacles yet to be overcome on the way to real world applications of graphene. As it stands, graphene is currently the most expensive material known to man with 1mg costing the equivalent of the gross domestic product of the USA. There are now many methods of producing graphene in small and often uncontrolled quantities, ranging from epitaxial growth [68], to cutting open carbon nanotubes [67]. Macroscopic scale graphene sheets have been chemically derived from graphite crystals and graphene oxides, but the purity of these samples is in serious doubt. One of the most promising recent attempts [66] at making large scale, patterned, graphene films involves using chemical vapour deposition on nickel layers. The authors were then able to transfer their graphene onto a substrate and demonstrated that its quality was comparable to that of micro-mechanically cleaved samples.

3.3 Electronic Properties

In the following section, we present the elementary electronic properties of monolayer and bilayer graphene. From a tight binding description, first investigated in 1947 by Wallace [40], we shall see that the elementary excitations of both systems have the properties of pseudospin and chirality but have different low energy dispersions. For an excellent review of the electronic properties of graphene, the reader is referred to Novoselov *et al.* [43].

3.3.1 The Carbon Atom

As the 6th element in the periodic table, carbon consists if six electrons, six protons. Nuclei with six or seven neutrons form the stable isotopes ^{12}C and ^{13}C respectively. The isotope ^{12}C is by far the most abundant in nature, making up around 99% of all carbon atoms, with much of the remaining 1% consisting of ^{13}C. However, a small number (approximately 1 in 10^{12}) are ^{14}C, a radioactive isotope that $\beta-$decays into ^{14}N with a half life of ≈ 5700 years. Despite its relative rarity, ^{14}C is an important isotope because it concentrates in organic materials, allowing one to approximate a sample's age through the abundance of ^{14}C [44].

Carbon's six electrons have a $1s^2 2s^2 2p^2$ orbital configuration in the ground state. The two electrons in the $1s$ orbital form a deep valence band and are therefore irrelevant to chemical reactions. The remaining 4 electrons occupy the $2p$ ($2p_x$,$2p_y$ and $2p_z$) and $2s$ orbitals. For an isolated carbon atom, it is energetically favourable to put two electrons in the $2s$ orbital and two in the $2p$ orbitals because the $2p$ orbitals are $4eV$ higher in energy. In the presence of other atoms, the situation is different and it is instead favourable to excite a $2s$ electron to the third $2p$ orbital to

form covalent bonds with the other atoms. This excited state then consists of four quantum-mechanical states, $|2s\rangle$, $|2p_x\rangle$, $|2p_y\rangle$ and $|2p_z\rangle$, and a quantum mechanical superposition of the $|2s\rangle$ state with n $|2p_i\rangle$ states is known as sp^n hydridisation. These superpositions are critical to the understanding of carbon physics.

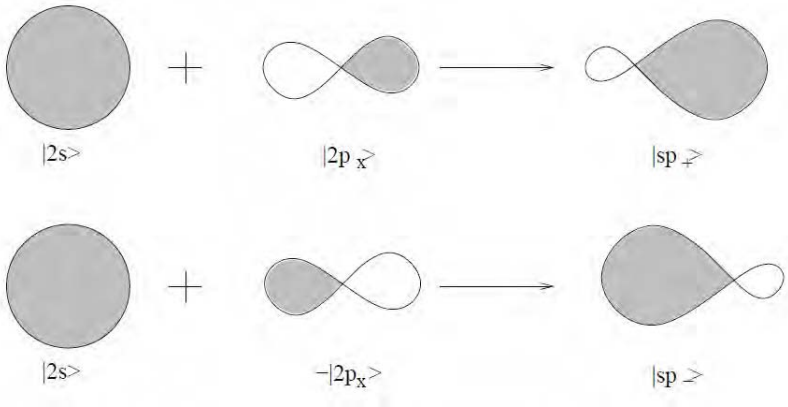

Figure 3.6: Schematic view of the sp^1 hybridisation. The figure shows on the l.h.s. the electronic density of the $|2s\rangle$ and $|2p_x\rangle$ orbitals and on the r.h.s. that of the hybridised ones. Reproduced from [44].

3.3.1.1 sp^1 Hydridisation

In sp^1 hybridisation (commonly referred to as simply sp hybridisation), the $|2s\rangle$ state forms a superposition with a $2p$ orbital ($|2p_x\rangle$ for example), leaving the others unaffected. For a superposition in which each original state has an equal weight, we have the symmetric ($|sp_+\rangle$) and anti-symmetric ($|sp_-\rangle$) combinations [44]

$$\begin{aligned} |sp_+\rangle &= \frac{1}{\sqrt{2}}\left(|2s\rangle + |2p_x\rangle\right), \\ |sp_-\rangle &= \frac{1}{\sqrt{2}}\left(|2s\rangle - |2p_x\rangle\right). \end{aligned} \tag{3.1}$$

The electronic density of these hybridised states form a shape resembling an asymmetric lemniscate (figure 3.6), with the larger of the two lobes in the $+x$ ($-x$)

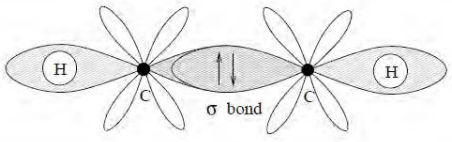

Figure 3.7: Schematic view of the acetylene molecule.The propeller-like $2p_y$ and $2p_z$ orbitals of the two C atoms strengthen the covalent σ bond by forming two π bonds (not shown). Reproduced from [44].

direction for the $|sp_-\rangle$ ($|sp_-\rangle$) states. This form of hybridisation is responsible for the acetylene molecule in which overlapping sp^1 orbitals form a strong covalent (σ) bond (see figure 3.7). In addition, the remaining unhybridised $2p$ orbitals form two additional (π) bonds that are weaker than the σ bond.

3.3.1.2 sp^2 Hydridisation

This form of hybridisation is central to the physics of the graphitic allotropes and consists of a superposition of the $2s$ orbital and two $2p$ orbitals. Choosing these to be the $|2p_x\rangle$ and $|2p_y\rangle$ states, the result is three states in the $xy-$plane separated by 120° and given by [44]

$$\begin{aligned}
\left|sp_1^2\right\rangle &= \frac{1}{\sqrt{3}}\left(|2s\rangle - \sqrt{\frac{2}{3}}\,|2p_y\rangle\right), \\
\left|sp_2^2\right\rangle &= \frac{1}{\sqrt{3}}\,|2s\rangle + \sqrt{\frac{2}{3}}\left(\frac{\sqrt{3}}{2}\,|2p_x\rangle + \frac{1}{2}\,|2p_y\rangle\right), \\
\left|sp_3^2\right\rangle &= -\frac{1}{\sqrt{3}}\,|2s\rangle + \sqrt{\frac{2}{3}}\left(-\frac{\sqrt{3}}{2}\,|2p_x\rangle + \frac{1}{2}\,|2p_y\rangle\right).
\end{aligned} \tag{3.2}$$

The remaining unhybridised $2p_z$ orbital lies perpendicular to the $xy-$plane. Their combined electronic density resembles a three lobed rose curve. (figure 3.8).

In graphene, each carbon atom is σ bonded to its three neighbouring carbon

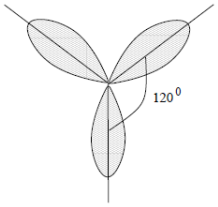

Figure 3.8: Schematic view of the sp^2 hybridisation. The orbitals form angles of 120°. Reproduced from [44].

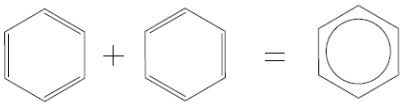

Figure 3.9: The quantum-mechanical ground state of the benzene ring is a superposition of the two configurations which differ by the position of the π bonds. The π electrons are therefore delocalised over the ring. Reproduced from [44].

atoms making six σ bonds per hexagonal unit cell. In addition to these, the remaining $2p_z$ pair up to form 3 π bonds that strengthen half of the carbon-carbon (C-C) bonds. Naively, one would expect this to result in a distorted hexagon since the double bond C-C distance (0.135 nm) is shorter than that for a single bond (0.142 nm). However, the measured C-C distance for all of the bonds is roughly the average of these two distances at 0.142 nm.

This puzzle was solved in 1931 by Pauling [42] in the context of the benzene ring (a hexagon of carbon atoms with hydrogen bound to the remaining in-plane, sp^2 states). He showed that the ground state consisted of a quantum mechanical superposition of the two possible configurations, a single and a double bond (figure 3.9). When applied to a graphene sheet, one sees that the ground state is a superposition of all possible combinations of single and double bonds with the π electrons are delocalised over the entire lattice. This explains the good conduction properties of graphitic allotropes.

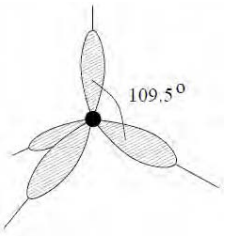

Figure 3.10: sp^3 hybridisation with an angle of 109.5° between the four orbitals. Reproduced from [44].

3.3.1.3 sp^3 Hybridisation

We mention for completeness this third class of hybridisation that involves the superposition of the $2s$ orbital and all three of the $2p$ orbitals, known as sp^3 hybridisation. The consideration of sp^3 hybridisation is important in understanding the structure of diamond. The resulting electron density consists of four club-like orbitals, separated by 109.5°, that form a corner of a tetrahedron (see figure 3.10). The fact that all four valence electrons form σ bonds explains not only the hardness and high thermal conductivity of diamond, but also its electrically insulating character.

3.3.2 Monolayer Graphene

As shown in figure 3.11, graphene consists of carbon atoms arranged hexagonally. The lattice is not Bravais but can be viewed as two intersecting triangular lattices, with a basis of two atoms per unit cell. The nearest neighbour vectors are given by

$$\delta_1 = \frac{a}{2}(1, \sqrt{3}), \quad \delta_2 = \frac{a}{2}(1, -\sqrt{3}), \quad \delta_3 = -a(1, 0). \tag{3.3}$$

and the lattice vectors by

$$a_1 = \frac{a}{2}(3, \sqrt{3}), \qquad a_2 = \frac{a}{2}(3, -\sqrt{3}), \tag{3.4}$$

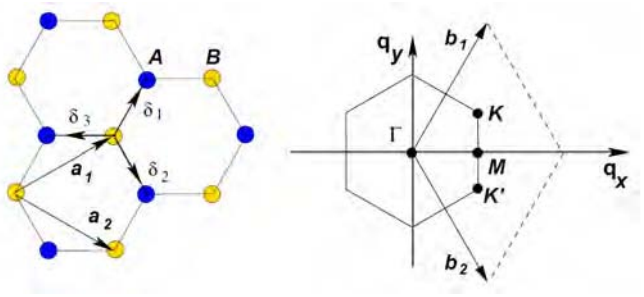

Figure 3.11: Left: Lattice structure of graphene, made out of two interpenetrating triangular lattices (a_1 and a_2 are the lattice unit vectors, and δ_i, $i = 1, 2, 3$ are the nearest neighbour vectors); Right: corresponding Brillouin zone. The Dirac cones sit at the K and K' points. Reproduced from [43].

where $a \approx 1.42$Å is the distance between carbon atoms. From these, the reciprocal lattice vectors are

$$b_1 = \frac{2\pi}{3a}(1, \sqrt{3}), \qquad b_2 = \frac{2\pi}{3a}(1, -\sqrt{3}). \tag{3.5}$$

At the corners of the Brillouin zone lie the two high symmetry points K and K'. For reasons outlined below, these are known as the Dirac points but are sometimes referred to as the charge neutrality points. In momentum space they have the coordinates

$$K = \frac{2\pi}{3a}(1, \frac{1}{\sqrt{3}}), \qquad K' = \frac{2\pi}{3a}(1, -\frac{1}{\sqrt{3}}). \tag{3.6}$$

We now investigate the low energy dynamics of graphene by considering a tight-binding Hamiltonian that takes into account nearest neighbour and next nearest neighbour hopping:

$$H = -t \sum_{\langle i,j \rangle, \sigma} \left(a^\dagger_{\sigma,i} b_{\sigma,i} + h.c. \right) - t' \sum_{\langle\langle i,j \rangle\rangle, \sigma} \left(a^\dagger_{\sigma,i} b_{\sigma,i} + h.c. \right). \tag{3.7}$$

where the operators $a^\dagger_{\sigma,i}$ and $a_{\sigma,i}$ respectively create and destroy an electron of spin σ on site $\mathbf{R_i}$ of sublattice A. The $b^\dagger_{\sigma,i}$ and $b_{\sigma,i}$ operators are equivalent to these but

for sublattice B. The energies t ($\approx 2.8eV$) and t' ($\approx 0.1eV$) [69] are the nearest neighbour and next nearest neighbour hopping energies respectively. A nearest neighbour hop takes the electron between sublattices, while a next nearest neighbour hop takes it onto the same sublattice. This Hamiltonian leads to the energy bands [40]

$$\begin{aligned} E_{\pm}(\mathbf{q}) &= \pm t\sqrt{3+f(\mathbf{q})} - t'f(\mathbf{q}) \\ f(\mathbf{q}) &= 2\cos\left(\sqrt{3}q_y a\right) + 4\cos\left(\frac{\sqrt{3}}{2}q_y a\right)\cos(\frac{3}{2}q_x a), \end{aligned} \tag{3.8}$$

where the $\dot{+}(-)$ refers to the upper (lower) band. In the absence of t', the dispersion is clearly symmetric around zero energy and in figure 3.12 we show the band structure according to (3.8), with and without $t' = 0$. The two bands meet at the Dirac points with zero gap and it is for this reason that graphene is classed as a zero gap semiconductor. In fact, at zero doping the Fermi energy passes through the Dirac points and so the carrier type can be tuned continuously between p- and n-type with the appropriate application of an electric field. This is known as an ambipolar field effect [45].

The cones that surround each Dirac point are known in the literature as valleys and, as discussed previously, there are two such valleys within the Brillouin zone. If one assumes that the physics in each valley is equivalent, then the effect of both may be taken in account by including an extra valley degeneracy of 2, in addition to the usual spin degeneracy.

It is possible to obtain the dispersion close to the Dirac points, (3.6), by setting $\mathbf{q} = \mathbf{K} + \mathbf{k}$ where $|\mathbf{k}| \ll |\mathbf{K}|$. Expanding up to second order in $\mathbf{k}$, the dispersion has

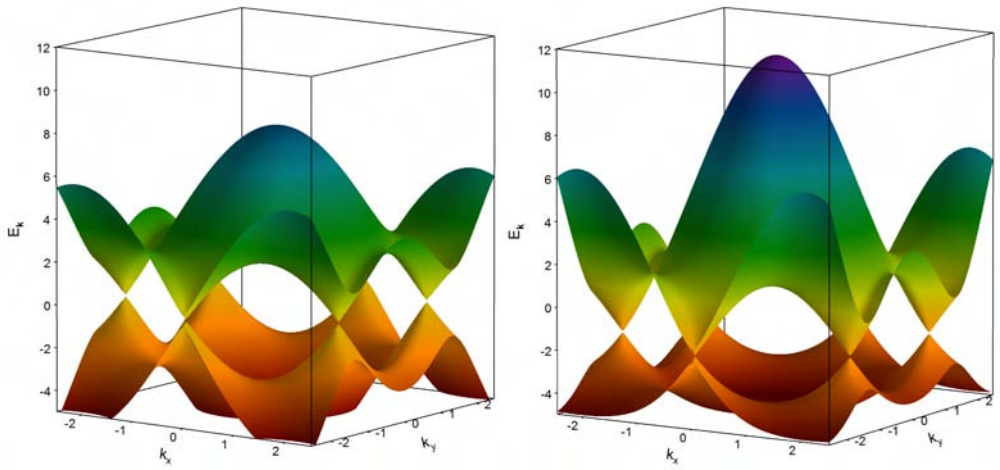

Figure 3.12: Left: Energy spectrum for $t = 2.7eV$ and $t' = 0$ showing the that bands are symmetric around the Dirac point. Right: Energy spectrum for $t' = 0.2t$. The bands are no longer symmetric and the Dirac point has shifted down in energy.

the form

$$E_{\pm}(\mathbf{k}) \approx \pm v_F |\mathbf{k}| + O(\mathbf{k}^2). \tag{3.9}$$

This dispersion is clearly conical and has the rather unusual feature of a photon like, momentum independent, Fermi velocity, $v_F = 3ta/2 \approx 1 \times 10^6 m/s \approx c/300$ [40], where c is the real speed of light. This is in contrast to the usual $v_F = k/m$. Graphene's linear spectrum at the Dirac points has been confirmed by experiments using angle resolved photo emission spectroscopy (ARPES) [77].

Including next nearest neighbour hopping (t'), the position of the Dirac point is shifted and particle-hole symmetry is broken, the two bands becoming asymmetric. Up to second order in $\mathbf{k}$ and including t', the dispersion takes the form [43],

$$E_{\pm}(\mathbf{q}) \approx 3t' \pm v_F |\mathbf{k}| - \left(\frac{9t'a^2}{4} \pm \frac{3ta^2}{8} \sin(3\theta_{\mathbf{k}}) \right) |\mathbf{k}|^2 , \tag{3.10}$$

where $\theta_{\mathbf{k}} = \tan^{-1}(k_y/k_x)$. The term in $\sin(3\theta_{\mathbf{k}})$ gives a three fold symmetry to the electronic spectrum as we move away from the Dirac point (figure 3.13). This feature

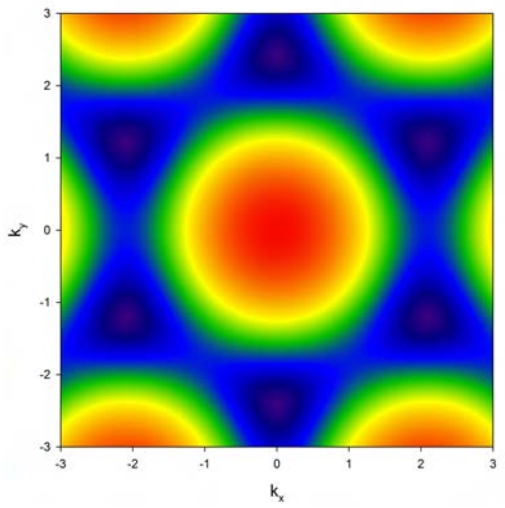

Figure 3.13: Contour plot of the positive energy band clearly showing the three fold symmetry of trigonal warping.

of the spectrum has become known in the literature as trigonal warping [71, 72].

It is possible to obtain an analytic expression for the graphene density of states per unit cell, but only in the case of $t' = 0$ [73] (see figure 3.14). In this case it is given by [43]

$$\rho(E) = \frac{4}{\pi^2}\frac{|E|}{t^2}\frac{1}{\sqrt{Z_0}}F\left(\frac{\pi}{2}, \sqrt{\frac{Z_1}{Z_0}}\right) \tag{3.11}$$

$$Z_0 = \begin{cases} \left(1 + \left|\frac{E}{t}\right|\right)^2 - \frac{\left(\left(\frac{E}{t}\right)^2 - 1\right)^2}{4} & ; \quad -t \leq E \leq t \\ 4\left|\frac{E}{t}\right| & ; \quad -3t \leq E \leq -t, \ \ or \ \ t \leq E \leq 3t \end{cases}$$

$$Z_0 = \begin{cases} 4\left|\frac{E}{t}\right| & ; \quad -t \leq E \leq t \\ \left(1 + \left|\frac{E}{t}\right|\right)^2 - \frac{\left(\left(\frac{E}{t}\right)^2 - 1\right)^2}{4} & ; \quad -3t \leq E \leq -t, \ \ or \ \ t \leq E \leq 3t \end{cases}$$

Close to the Dirac points the density of states $D(\varepsilon)$ is given by [43]

$$D(\varepsilon) = \frac{g_s g_v |\varepsilon|}{2\pi \upsilon_F^2}, \tag{3.12}$$

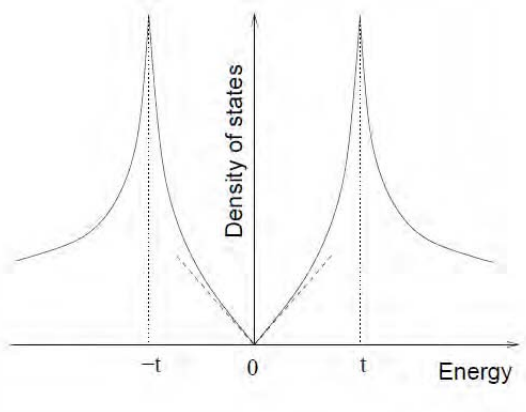

Figure 3.14: Schematic plot of the density of states for electrons in graphene in the absence of next nearest neighbour hopping. The dashed line indicates the density of states obtained at linear order (equation 3.12). The divergences at $\pm t$ are known as *van-Hove singularities* and are due to the saddle points at the borders of the Brillouin zone. Reproduced from [44].

where $g_s = 2$ and $g_v = 2$ are the spin and valley degeneracies respectively. At the Dirac points it is clear that the density of states vanishes and as a result there is no screening there.

3.3.2.1 Dirac fermions

The linear, mass independent dispersion of graphene is reminiscent of ultra-relativistic particles and it is a key feature of physics close to the Dirac point. This analogy deepens when one considers the effective Hamiltonian close to the Dirac points. Here, one finds that the electron's interactions with the two equivalent sublattices leads to quasiparticles that are more naturally described in terms of the (2+1)-dimensional Dirac equation, as opposed to the Schrödinger equation that is so ubiquitous in condensed matter physics. These quasiparticles are formally known as massless Dirac fermions and as the name suggests behave as massless, relativistic spin-$\frac{1}{2}$ particles. They may also be viewed as being equivalent to neutrinos that have gained an electronic charge, although given their origins it is perhaps the former description that

is more natural.

At **K**, these low energy quasiparticles are formally described by the following Dirac like Hamiltonian [40, 74]

$$\hat{H}_{\mathbf{K}} = \upsilon_F \begin{pmatrix} 0 & k_x - ik_y \\ k_x + ik_y & 0 \end{pmatrix} = \upsilon_F \underline{\sigma} \cdot \mathbf{k}, \tag{3.13}$$

where $\mathbf{k}$ is the quasiparticle momentum and $\underline{\sigma} = (\sigma_x, \sigma_y)$ is a 2D vector of Pauli matrices. As we have already established (3.9), the above Hamiltonian has eigenenergies $E = \pm \upsilon_F |\mathbf{k}|$, with the momentum independent Fermi velocity acting as an effective speed of light. The Hamiltonian of the remaining Dirac point is the same as above, but with σ replaced by σ^*. It is important to realise that these Pauli matrices are not acting in spin space but instead on the sublattice degrees of freedom. The result is that the eigenstates of (3.13) are themselves two component vectors in sublattice space (spinors). The similarity of the sublattice index (A, B) to spin index (up, down) has led to the sublattice degree of freedom becoming referred to as pseudospin.

The eigenstates of $\hat{H}_{\mathbf{K}}$, labeled by $\psi_{\pm,\mathbf{K}}(\mathbf{k})$, have contributions from both sublattices and are given by

$$\psi_{\pm,\mathbf{K}}(\mathbf{k}) = \frac{1}{\sqrt{2}} \begin{pmatrix} e^{-i\theta_{\mathbf{k}}/2} \\ \pm e^{i\theta_{\mathbf{k}}/2} \end{pmatrix}, \tag{3.14}$$

with $\theta_{\mathbf{k}} = \tan^{-1}(k_y/k_x)$. For the remaining Dirac point $\mathbf{K}'$, $\psi_{\pm,\mathbf{K}'}(\mathbf{k}) = \psi^*_{\pm,\mathbf{K}}(\mathbf{k})$. An interesting feature of these eigenfunctions is that if the phase $\theta_{\mathbf{k}}$ is rotated by 2π then the eigenfunction changes sign, indicating an overall change in phase of π.

This feature is a characteristic of spinors known as a Berry's phase and leads to some interesting phenomena in graphene such as weak anti-localisation [57, 75].

Because the eigenfunctions (3.14) are composed of contributions from both sublattices, it follows that the sublattice index is not a good quantum number. Instead, quasiparticles near to the Dirac points exist in states of definite chirality, defined as the projection of σ onto the direction of motion $\mathbf{k}$. This may be seen by first defining the quantum mechanical operator for chirality $\hat{h}$:

$$\hat{h} = \underline{\sigma} \cdot \frac{\mathbf{k}}{|\mathbf{k}|}. \tag{3.15}$$

Acting this operator on (3.13) shows that the eigenstates (3.14) are also eigenstates of $\hat{h}$ with eigenvalues ± 1. This demonstrates that electrons (holes) exist in states of definite positive (negative) chirality, with the components of pseudospin projected parallel (antiparallel) to momentum. A similar relation holds for states near $\mathbf{K}'$ but with opposite chirality and projection (see figure 3.15). This situation with chirality is similar to the conjugated electron and hole states that appear in QED. The fundamental reason for this in graphene is that the k electron and the $-k$ hole states are connected because they originate from the same sublattices and are governed by the same Dirac equation. This is quite different to the situation that normally arises in condensed matter physics where electrons and holes are described by independent Schrodinger equations, with independent effective masses. This is a consequence of the Seitz sum rule [76].

Chirality, as well as pseudospin, are important concepts in graphene physics because many of its unusual electronic properties arise from them. It should be remembered however that chirality only exists as a good quantum number so long

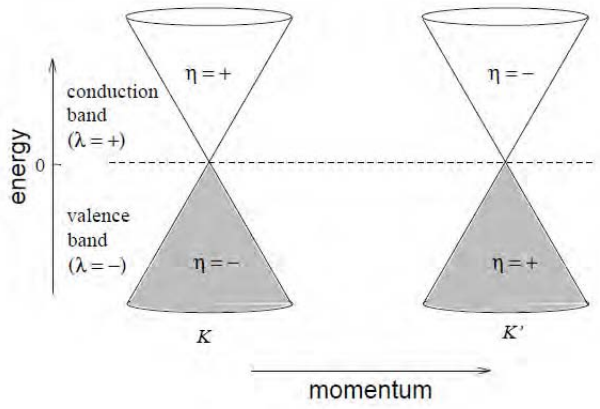

Figure 3.15: Relation between band index λ, valley (K,K'), and chirality η in graphene. Reproduced from [44].

as the Hamiltonian (3.13) is valid. It is therefore an asymptotic property of graphene approaching the Dirac points.

3.3.2.2 Is graphene a Fermi liquid?

As discussed elsewhere (Section 2.1), information about the character of a material's electron-electron interactions is important because it determines many of its physical properties. The question as to whether or not graphene's Dirac fermion quasiparticles fit into the normal Fermi liquid picture is of particular importance because Fermi liquid theory allows one to greatly simplify calculations involving the interacting electron liquid.

First put forward by Landau [80], the central premise in Fermi liquid theory is that as interactions are adiabatically turned on between free electrons, the quantum numbers of the system are preserved, unless there is a phase transition. The single particle excitations of the non-interacting fermions are replaced by incoherent collective excitations of the electron liquid, known as quasiparticles. The quasiparticles preserve the spin, charge and momentum of the non-interacting case, but with a renormalised (effective) mass.

Quantities such as specific heat and compressibility show the same qualitative behaviour in a Fermi liquid, but often with different magnitudes. These can be used to indicate whether or not a system is behaving as a Fermi liquid and furthermore, measurements of, for example, the specific heat can be used to estimate the effective mass.

That the physics of the Fermi liquid can be described within the framework of the free Fermi gas, with a renormalised mass, immediately raises an issue when investigating graphene close to the Dirac points. This is because the quasiparticles there behave as massless particles. It has been shown [79] that close to the Dirac points, the quasiparticles acquire an effective velocity, as opposed to an effective mass. Furthermore, it has been confirmed [78] by ARPES experiments that the quasiparticle picture is preserved.

In undoped graphene, when the Fermi energy lies exactly at the Dirac point, Das Sarma *et al.* [79] showed that the system behaves as *marginal* Fermi liquid. Using diagrammatic perturbation theory, they were able to show that the quasiparticle lifetime scales linearly in energy but that unphysically, the renormalised Fermi velocity diverges logarithmically at the Dirac points. The result is that the step in the Fermi function vanishes, whereby the concept of a Fermi surface no longer applies.

At finite doping, it was shown that graphene displays ordinary Fermi liquid behaviour with the Fermi velocity renormalising in a similar fashion to an ordinary 2DEG. This is a result of the emergence of intraband and plasmon excitations, as well as the return of a finite density of states, restoring Fermi liquid behaviour. It has been shown more recently [81], that the specific heat of doped graphene has normal Fermi liquid, linear in temperature behaviour. Very far away from the Dirac points it is not surprising that the system should behave as a Fermi

liquid because the system has as ordinary quadratic dispersion and is composed of ordinary "Schrödinger" fermions. There as yet exists no robust theory for describing the presumably smooth crossover between this regime and the pseudo-relativistic behaviour close to the Dirac points.

Even for experiments involving undoped graphene, there will inevitably be a finite Fermi energy due to either charge from a substrate and / or rippling of the graphene itself [58]. As we will see in section 3.4, there is evidence that undoped graphene splits into puddles of positively and negatively doped regions, within which the Fermi liquid picture holds. In almost all realistic situations it is therefore reasonable to treat graphene as a normal Fermi liquid.

3.3.2.3 Screening and Plasmons

Of particular interest to studies of Coulomb drag is the nature of screening and plasmons in graphene close to the Dirac points. In the majority of 2DEG drag experiments and theoretical treatments, screening has been taken in the random phase approximation. This approximation is valid in the high density limit where kinetic energy dominates over potential. It is critical to understand whether or not this approximation is appropriate for use in graphene systems. In an interacting electron system, the quantity that paramaterises the ratio (R_E) of the average potential energy to the average kinetic energy is the Wigner-Seitz radius (r_s), defined as the mean electronic separation;

$$r_s = \begin{cases} \left(\frac{3}{4\pi n}\right)^{\frac{1}{3}} & \text{3D} \\ \left(\frac{\pi}{n}\right)^{\frac{1}{2}} & \text{2D}, \end{cases} \tag{3.16}$$

where n is the electronic density. The average potential energy is

$$\langle \text{Potential Energy} \rangle \approx \frac{1}{2}\frac{e^2}{\kappa r_s}, \tag{3.17}$$

where κ is the background dielectric constant. Using the graphene dispersion (3.9), the average kinetic energy is

$$\langle \text{Kinetic Energy} \rangle \approx \frac{2\pi v_F}{\lambda} \approx \frac{v_F \pi}{r_s}, \tag{3.18}$$

and therefore we have for the ratio (R_E) of the potential to the kinetic energy,

$$\frac{\langle \text{Potential Energy} \rangle}{\langle \text{Kinetic Energy} \rangle} = \frac{e^2}{\kappa \pi v_F} \tag{3.19}$$

which is clearly independent of r_s and therefore the density, n. This constant relationship is markedly different to the usual 2D $\left(R_E \backsim n^{-1/2}\right)$ and 3D $\left(R_E \backsim n^{-1/3}\right)$ case for electron liquids, where interaction effects increase with increasing density n. It should however be remembered that (3.19) only holds close to the Dirac point where the quasiparticle spectrum is linear. It will therefore fail at high enough doping. An estimate for R_E can be obtained for experimentally relevant systems by assuming that the graphene substrate used in SiO_2 so that $\kappa = 4$ and therefore $R_E \sim 0.5$. This shows that graphene is a weakly interacting system for all carrier densities. The RPA is asymptotically exact in the $R_E \ll 1$ limit and so it is an excellent approximation for graphene [84].

Treating screening in the RPA, the dynamical screening function (or dielectric

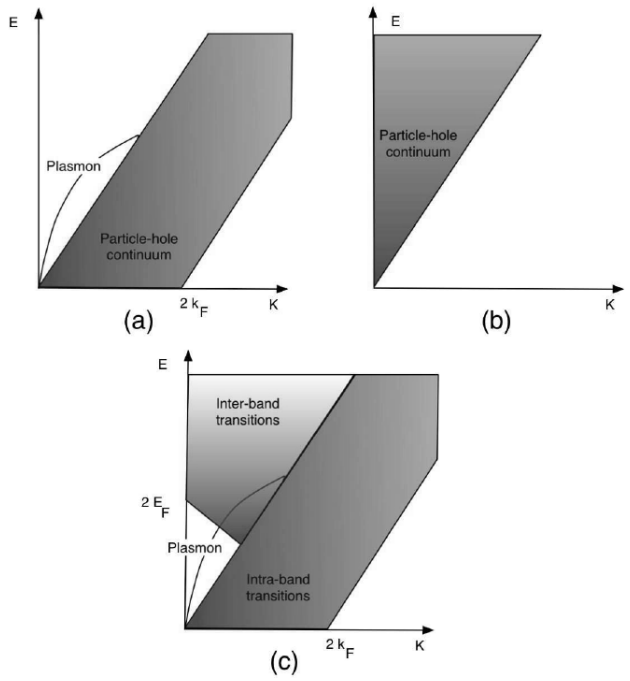

Figure 3.16: Particle-hole continuum and collective modes of: (a) 2DEG; (b) undoped graphene; (c) doped graphene. Reproduced from [43].

function) is given by [18]

$$\varepsilon(q,\omega) = 1 + \upsilon(q)\chi(q,\omega), \tag{3.20}$$

where $\upsilon(q) = 2\pi e^2/\kappa q$ is the bare 2D coulomb interaction and $\chi(q,\omega)$ is the 2D polarisability. The polarisability is calculated as usual from the bare bubble diagram and is given by (see section 5.2) [82]

$$\chi(\mathbf{q},\omega) = \sum_{\lambda,\lambda'=\pm}\sum_{\mathbf{k}}(1+\lambda\lambda'\cos\theta_+)\frac{n_F(\varepsilon_{\mathbf{k},\lambda'}) - n_F(\varepsilon_{\mathbf{k}+\mathbf{q},\lambda})}{\omega + \varepsilon_{\mathbf{k},\lambda'} - \varepsilon_{\mathbf{k}+\mathbf{q},\lambda} + i\delta}. \tag{3.21}$$

For undoped (intrinsic) graphene at zero temperature we have $n_F(\varepsilon_{\mathbf{k},-}) = 1$ and $n_F(\varepsilon_{\mathbf{k},+}) = 0$. Therefore, there are no *intraband* transitions, only *interband* transitions between the upper and lower cones are allowed. As these have a relatively

high energy cost, intrinsic graphene does not support any electron-hole excitations at low energy and at zero temperature. The polarisability (3.21) has been evaluated in this case and found to have the simple analytic form [83]

$$\chi(q,\omega) = \frac{q^2}{4\sqrt{v_F^2 q^2 - \omega^2}}. \tag{3.22}$$

In doped (extrinsic) graphene, where $n_F(\varepsilon_{\mathbf{k},\lambda}) = [exp\{\beta(\varepsilon_{\mathbf{k},\lambda} - \mu) + 1\}]$, *intraband* transitions are allowed. An analytic form for the polarisability has been found [82] that is a great deal more complicated than (3.22) and the reader is referred to [82] for details. However, it is worth mentioning a few limiting cases. In the long wavelength ($q \to 0$) limit it has been shown that [82]

$$\chi(q,\omega) \approx \begin{cases} \frac{D(E_F)v_F^2 q^2}{2\omega^2}\left[1 - \frac{\omega^2}{4E_F^2}\right], & v_F q < \omega < 2E_F, \\ D(E_F)\left[1 + i\frac{\omega}{v_F q}\right], & \omega < v_F q, \end{cases} \tag{3.23}$$

and for the static ($\omega = 0$) case,

$$\chi(q) \approx \begin{cases} D(E_F), & q < 2k_F, \\ D(E_F)\left[1 + \frac{\pi q}{8k_F} - \frac{1}{2}\sqrt{1 - \frac{4k_F^2}{q^2}} - \frac{q}{4k_F}\sin^{-1}\frac{2k_F}{q}\right], & q > 2k_F, \end{cases} \tag{3.24}$$

where $D(E_F) = 2k_F/\pi v_F$ is the graphene density of states at the Fermi energy. By looking for the zeros of the dielectric function, (3.20), they were able to determine the plasmon mode dispersion of doped monolayer graphene (figure 3.16). They found that in the $q \to 0$ limit, the plasmon dispersion has the form

$$\omega_p(q \to 0) = \omega_0\sqrt{q} \tag{3.25}$$

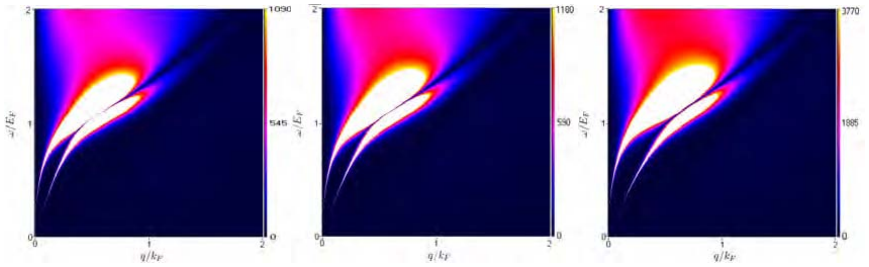

Figure 3.17: $Im\left[\varepsilon_{12}^{-1}(q,\omega,T)\right]$ plotted at $0.1T_F$ and for three different layer separations. From left to right $3.5k_F^{-1}$, $2.5k_F^{-1}$ and $1.5k_F^{-1}$. As the layer separation decreases the plasmon modes are seen to move further apart.

where $\omega_0 = \sqrt{2e^2E_F/\kappa}$. This leading order behaviour has exactly the same $q^{1/2}$ form as for a normal 2D plasmon. The difference however is in the density dependence of the plasma frequency, which goes as $n^{1/4}$ compared to $n^{1/2}$ in a 2DEG. This is a direct consequence of the graphene's relativistic dispersion.

Ramezanali *et al.* [81] were able to derive a semi-analytic expression for the finite temperature polarisability, $\chi(q,\omega,T)$, of doped graphene, given by $\chi(q,\omega,T) = \mathrm{Re}\chi(q,\omega,T) + \mathrm{Im}\chi(q,\omega,T)$ with

$$\begin{aligned}\mathrm{Im}\chi(q,\omega,T) &= \frac{1}{\pi}\sum_{\alpha=\pm}\Bigg\{\theta(v_Fq-\omega)q^2f(v_Fq,\omega)\left[G_+^{(\alpha)}(q,\omega,T)-G_-^{(\alpha)}(q,\omega,T)\right]\\ &\quad+\theta(\omega-v_Fq)q^2f(\omega,v_Fq)\left[-\frac{\pi}{2}\delta_{\alpha,-}+H_+^{(\alpha)}(q,\omega,T)\right]\Bigg\}, \qquad (3.26)\end{aligned}$$

$$\begin{aligned}\mathrm{Re}\chi(q,\omega,T) &= \frac{1}{\pi}\sum_{\alpha=\pm}\Bigg\{\frac{-2k_BT\ln\left[1+e^{\alpha\mu(T)/k_BT}\right]}{v_F^2}+\theta(\omega-v_Fq)\\ &\quad\times q^2f(\omega,v_Fq)\left[G_-^{(\alpha)}(q,\omega,T)-G_+^{(\alpha)}(q,\omega,T)\right]\\ &\quad+\theta(vq-\omega)q^2f(v_Fq,\omega)\left[-\frac{\pi}{2}\delta_{\alpha,-}+H_-^{(\alpha)}(q,\omega,T)\right]\Bigg\}, \qquad (3.27)\end{aligned}$$

where,

$$f(x,y) = \frac{1}{2\sqrt{x^2 - y^2}}, \tag{3.28}$$

$$G_{\pm}^{(\alpha)}(q,\omega,T) = \int_1^{\infty} du \frac{\sqrt{u^2-1}}{\exp\left(\frac{|v_F q u \pm \omega| - 2\alpha\mu(T)}{2k_B T}\right) + 1}, \tag{3.29}$$

$$H_{\pm}^{(\alpha)}(q,\omega,T) = \int_{-1}^{1} du \frac{\sqrt{1-u^2}}{\exp\left(\frac{|v_F q u \pm \omega| - 2\alpha\mu(T)}{2k_B T}\right) + 1}. \tag{3.30}$$

Their numerical results (figure 3.17) showed that although, as expected, the intralayer region of the e-h continuum is bounded by $\omega \leq q$, the interlayer region acquires a significant weight at small ω and q, even for temperatures as low as $T = 0.2T_F$.

3.3.3 Bilayer Graphene

A great deal of theoretical and experimental activity stemmed from the 2004 fabrication of graphene monolayers. More recently, graphene bilayers have become the subject of intense research, primarily because they offer the possibility of opening up a band gap, while retaining many of the properties associated with chiral quasiparticles. A graphene bilayer is simply two parallel graphene monolayers close enough so that they are coupled by interlayer tunneling. The distance between them is essentially identical to the graphite interlayer spacing [43].

McCann *et al.* [85] were the first to investigate the low energy Hamiltonian of a graphene bilayer and their findings were later confirmed by several other authors [88–90]. They did so by employing a tight binding approach to two graphene monolayers arranged according to Bernal stacking. With four atoms per unit cell, if A, B and $\tilde{A}$, $\tilde{B}$ are the sublattices of the bottom and top layers respectively, Bernal $(\tilde{A} - B)$

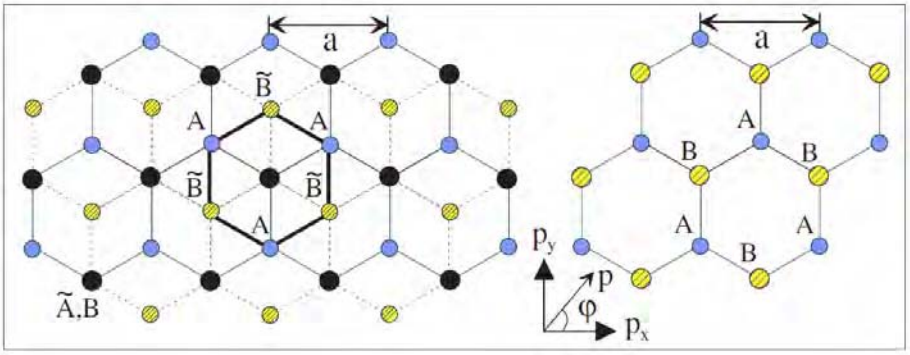

Figure 3.18: Left: Schematic of the bilayer lattice (bonds in the bottom layer A, B are indicated by solid lines and in the top layer $\tilde{A}$, $\tilde{B}$ by dashed lines) containing four sites in the unit cell: A (blue circles), $\tilde{B}$ (yellow hashed), $\tilde{A}$B dimer (solid). Right: the lattice of a monolayer. Reproduced from [85].

stacking has every B site directly below an $\tilde{A}$ site, but the A and $\tilde{B}$ sites do not sit directly above or below another site (figure 3.18).

The bilayer lattice shares some features of its hexagonal Brillouin zone with a graphene monolayer and has two inequivalent corners $\mathbf{K}$ ($\xi = 1$) and $\mathbf{K}'$ ($\xi = -1$) that form two valleys and are labeled by $\xi = \pm$. Like the monolayer, the Fermi energy lies at these points for an undoped system. The bilayer Hamiltonian forms four bands (figure 3.21), two low energy gap-less bands ($\varepsilon_{\pm}^{(1)}$) and two high energy bands ($\varepsilon_{\pm}^{(2)}$). The starting point for the tight binding calculation is the second quantized Hamiltonian [43],

$$\begin{aligned} \hat{H} &= \gamma_0 \sum_{\langle i,j \rangle} \sum_{m,\sigma} \left(a^{\dagger}_{m,i,\sigma} b_{m,j,\sigma} + h.c. \right) - \gamma_1 \sum_{j,\sigma} \left(a^{\dagger}_{1,j,\sigma} a_{2,j,\sigma} + h.c. \right) \\ &- \gamma_3 \sum_{j,\sigma} \left(a^{\dagger}_{1,j,\sigma} b_{2,j,\sigma} + a^{\dagger}_{2,j,\sigma} b_{1,j,\sigma} + h.c. \right) - \gamma_4 \sum_{j,\sigma} \left(b^{\dagger}_{1,j,\sigma} b_{2,j,\sigma} + h.c. \right). \end{aligned} \tag{3.31}$$

The above Hamiltonian is characterised by several parameters that relate to the amplitudes or both in-plane and out-of-plane hopping. The parameter $\gamma_0 \equiv \gamma_{AB} = \gamma_{\tilde{A}\tilde{B}} \simeq 2.8eV$ controls the nearest in-plane neighbour hopping and is identical to

the nearest neighbour hopping amplitude t (3.7) that appears in the monolayer system. The strongest interlayer coupling forms a dimer and comes from hopping between the directly opposite sites $\tilde{A}$ and B. It is controlled by the parameter $\gamma_1 \equiv \gamma_{\tilde{A}B} \simeq 0.39eV$ and forms the two higher energy bands ($\varepsilon_{\pm}^{(2)}$), with energy $\geq \gamma_1$. The weakest coupling taken into account in [85] is $A - \tilde{B}$ hopping, controlled by the parameter $\gamma_3 \equiv \gamma_{A\tilde{B}} \simeq 0.315eV$. In principle one should take into account hopping between sites B and $\tilde{B}$ with an energy $\gamma_4 \simeq 0.2eV$. Taking into account higher order hopping introduces a negligible overlap between the low energy bands.

One of the most interesting features of bilayer graphene is the ability to open up a gap, Δ, between the two bands ($\varepsilon_{\pm}^{(1)}$) via asymmetric doping of the layers. It is this feature in particular that may lead the the bilayer becoming important for graphene electronics devices. At the corners of the Brillouin zone, at either **K** ($\xi = 1$) or **K′** ($\xi = -1$) the Hamiltonian has the form [85]

$$\hat{H} = \xi \begin{pmatrix} \frac{1}{2}\Delta & \upsilon_3\pi & 0 & \upsilon\pi^\dagger \\ \upsilon_3\pi^\dagger & -\frac{1}{2}\Delta & \upsilon\pi & 0 \\ 0 & \upsilon\pi^\dagger & -\frac{1}{2}\Delta & \xi\gamma_1 \\ \upsilon\pi & 0 & \xi\gamma_1 & \frac{1}{2}\Delta \end{pmatrix}, \tag{3.32}$$

where $\pi = k_x + ik_y$, $\pi^\dagger = k_x - ik_y$, and the in-plane (υ) and out-of-plane (υ_3) velocities are given by $\upsilon = \left(\sqrt{3}/2\right) a\gamma_0/\hbar$ and $\upsilon_3 = \left(\sqrt{3}/2\right) a\gamma_3/\hbar$ respectively (a is the lattice constant and $\upsilon_3 \simeq 0.1\upsilon$). The in-plane velocity, υ, is the same as that appearing in the monolayer calculation. Just as the monolayer Hamiltonian (3.13) acts on the subspace of sites A and B, the bilayer Hamiltonian (3.32) acts on the subspace of sites A, B, $\tilde{A}$ and $\tilde{B}$. The band structure near the **K** points (figure

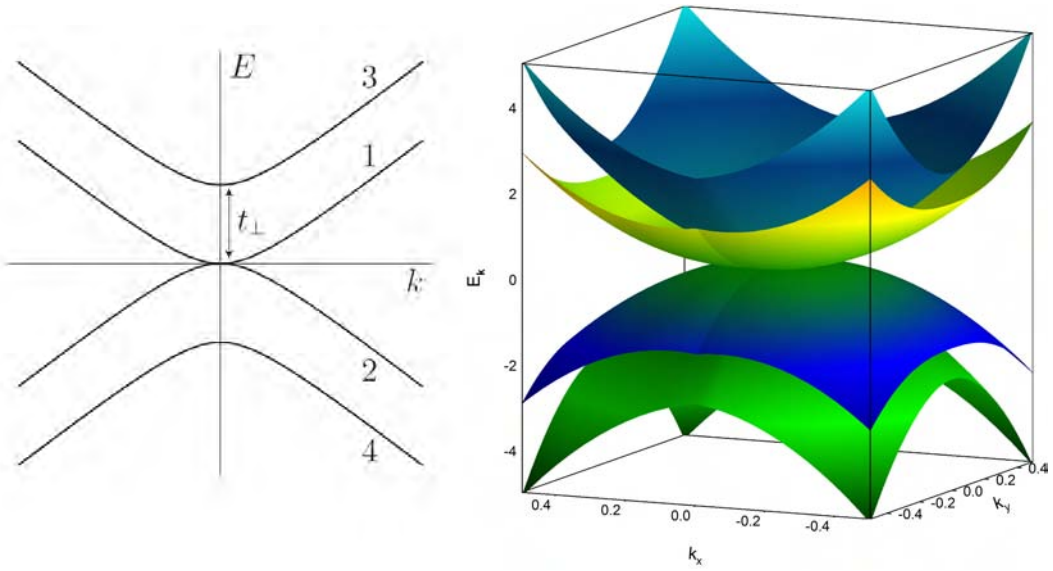

Figure 3.19: Left: 2D band dispersion near to one of the **K** points ($t_\perp \equiv \gamma_1$). Reproduced from [88]. Right: 3D bands structure of bilayer graphene near to one of the **K** points as plotted from (3.33).

3.21) is given by

$$\mp\varepsilon_{\pm}^{\alpha}(\mathbf{k}) = \frac{\gamma_1^2}{2} + \frac{\Delta^2}{2} + \left(v^2 + \frac{v_3^2}{2}\right)|\mathbf{k}|^2 + (-1)^{\alpha}\left[\frac{\left(\gamma_1^2 - v_3^2|\mathbf{k}|^2\right)^2}{4} + v^2|\mathbf{k}|^2\left[\gamma_1^2 + u^2 + v_3^2|\mathbf{k}|^2\right] + 2\xi\gamma_1 v_3 v^2|\mathbf{k}|^3\cos 3\theta_{\mathbf{k}}\right]^{\frac{1}{2}}, \quad (3.33)$$

where $\alpha = 1, 2$ labels the bands high and low energy bands respectively (figure 3.19) and $\theta_{\mathbf{k}} = \tan^{-1}(k_y/k_x)$. Equation (3.33) describes the four bands, two low energy bands (ε_+^1, ε_-^1) that meet with zero gap (for $\Delta = 0$) at zero energy, and two higher energy bands (ε_+^2, ε_-^2) with $\left|\varepsilon_{\pm}^2\right| > \gamma_1$.

In the low energy regime, where only the low energy bands ($\varepsilon_{\pm}^1$) are relevant, electrons are mostly localised on the A and $\tilde{B}$ sites (those not directly opposite a site in the adjacent layer). This is demonstrated [88, 90] by real space electron density calculations that show a triangular structure for the bilayer (figure 3.20). This is in contrast to the monolayer case where the electrons are evenly distributed between

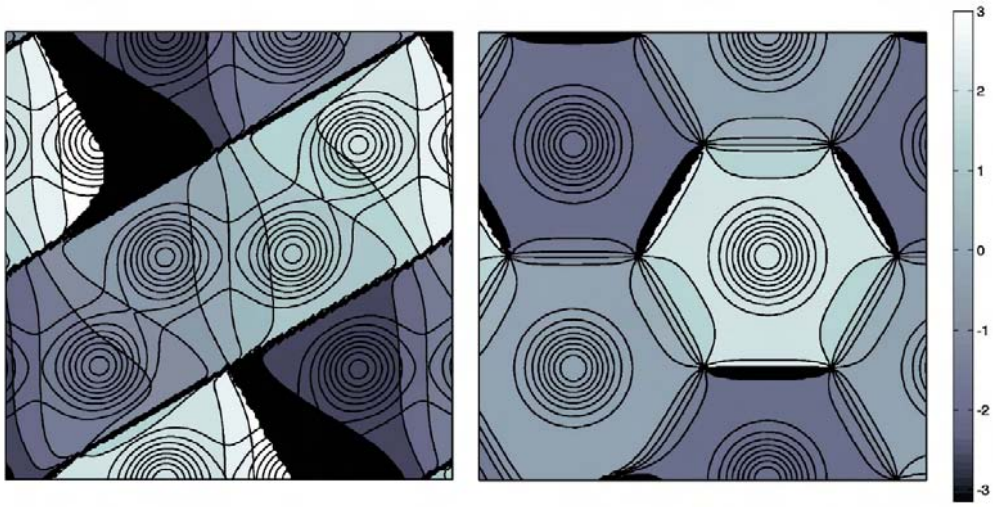

Figure 3.20: The phase (using grey colouring with the corresponding scale to the far right) of one of the two degenerate wave functions at the **K** point for (Left) monolayer and (Right) bilayer graphene with a contour plot of the electron density superimposed (both calculated at 1Å above the surface). The monolayer electron density is shared between the A and B sites forming the usual hexagonal pattern. For the bilayer this pattern is missing as the electron density is confined to the A (or equivalently $\tilde{B}$) sublattice forming a triangular pattern. Reproduced from [90].

the sublattices and the expected hexagonal structure is seen. Consequently, the low energy dynamics of a bilayer can be described by a 2×2 Hamiltonian acting in the A, $\tilde{B}$ subspace. Valid within the energy range $|\varepsilon| < \frac{1}{4}\gamma_1$, it was shown [85] that the low energy states of a bilayer are described by the following Hamiltonian, $\hat{H} =$

$$\frac{1}{2m}\begin{pmatrix} 0 & \left(\pi^\dagger\right)^2 \\ \pi^2 & 0 \end{pmatrix} + \xi\upsilon_3 \begin{pmatrix} 0 & \pi \\ \pi\dagger & 0 \end{pmatrix} + \xi\Delta\left[\frac{1}{2}\begin{pmatrix} 1 & 0 \\ 0 & -1 \end{pmatrix} - \frac{\upsilon^2}{\gamma_1^2}\begin{pmatrix} \pi^\dagger\pi & 0 \\ 0 & -\pi\pi^\dagger \end{pmatrix}\right]. \tag{3.34}$$

The first term, quadratic in $\mathbf{k}$, describes $A \leftrightharpoons \tilde{B}$ hopping via the dimer state formed between $\tilde{A}$ and B. The second term (linear in $\mathbf{k}$) is the bilayer equivalent of trigonal warping and describes direct $A \leftrightharpoons \tilde{B}$ hopping. The third term takes into account the effect of a gap, Δ, that as previously stated, is induced via asymmetric doping of the bilayer.

In contrast to monolayer graphene, the trigonal warping term for the bilayer has a

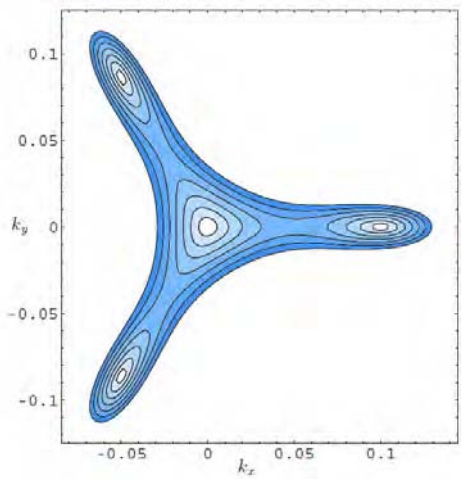

Figure 3.21: Constant energy lines (in units of γ_1) of the graphene bilayer dispersion relation (3.33). Shown for the positive eigenvalues in the (k_x,k_y) plane around the K point of the Brillouin zone (at the origin in this figure). The asymmetry of the Fermi line at the K' valley is inverted. Reproduced from [61].

profound effect on the band dispersion at very low energies $\left(|\varepsilon| < \frac{1}{2}\gamma_1 \left(\upsilon_3/\upsilon\right)^2 \simeq 2 \times 10^{-3} eV\right)$, where it dominates. This corresponds to a charge density $n \leq 1 \times 10^{-11} cm^{-2}$. Its effect is to change the topology of the band from parabolic into four pockets, one circular "central" pocket and three satellite elliptical "leg" parts (figure 3.21). At zero energy these legs meet, forming cones with a linear spectrum.

For intermediate energies $\left(\frac{1}{2}\gamma_1 \left(\upsilon_3/\upsilon\right)^2 < |\varepsilon| < \frac{1}{4}\gamma_1\right)$ the first term of (3.34) dominates and the quasiparticles behave as chiral fermions with a Hamiltonian

$$\hat{H} = \frac{1}{2m} \begin{pmatrix} 0 & [k_x - ik_y]^2 \\ [k_x + ik_y]^2 & 0 \end{pmatrix}, \tag{3.35}$$

and a parabolic dispersion

$$\varepsilon = \pm \frac{|\mathbf{k}|^2}{2m}. \tag{3.36}$$

The quasiparticles' effective mass $m = \gamma_1/2\upsilon^2$ is estimated [85] to be light at $m \simeq 0.054 m_e$ and, in contrast to the monolayer, have a Berry's phase of 2π.

At yet higher energies, $|\varepsilon| > \frac{1}{4}\gamma_1 \simeq 0.1eV$, the Hamiltonian (3.34) does not hold and the dispersion again becomes linear [85] . In the crossover between the parabolic and linear dispersion at high energies, and before the lower band is reached ($|\varepsilon| = \gamma_1$), the dispersion can be approximated by [85]

$$\varepsilon_{\pm}^{1} \approx \pm\gamma_1 \left[\sqrt{1 + \frac{4\upsilon\,|\mathbf{k}|^2}{\gamma_1^2}} - 1\right]. \tag{3.37}$$

The crossover occurs at $|\mathbf{k}| \simeq \gamma_1/\upsilon$ and corresponds to a carrier density $n \approx 4.36 \times 10^{12}$. This is below the density at which the upper bands $\left(\varepsilon_{\pm}^{2}\right)$ become occupied, estimated to be $n \approx 3.49 \times 10^{13}$.

In principle, calculations of the low energy properties of the bilayer should use a Hamiltonian describing all of the above regimes. The theoretical framework to describe the effects of chirality in the complicated crossover regimes remains to be developed. Fortunately, for most experimental systems of interest, the relevant Hamiltonian is the one describing chiral fermions with a quadratic spectrum (3.35). It has been estimated [62] that charged impurities from the substrate will induce a residual charge density that corresponds to $\varepsilon \geq 0.01eV$. This is above the range at which the trigonal warping term dominates. Furthermore, typical experimental systems induce charge densities below, or comparable to, the high energy crossover from a parabolic to a linear dispersion ($n \approx 4.36 \times 10^{12}$). Therefore, as long as the system in question has a charge density in the range

$$1 \times 10^{-11} cm^{-2} < n < 4.36 \times 10^{12} cm^{-2}, \tag{3.38}$$

or equivalently energy in the range

$$2 \times 10^{-3} eV < |\varepsilon| < 0.1 eV, \tag{3.39}$$

it is justifiable to make the simplifying assumption that the system may be described by (3.35).

3.3.3.1 Screening and Plasmons

The full details of screening and plasmons in bilayer graphene is an area yet to be explored in the literature and will form part of the original work of this thesis. The case of static screening has been considered at zero temperature [92]. From the bare bubble (RPA) diagram, the dynamic polarisability is found to be (see for example Section 5.2)

$$\chi(q,\omega) = \sum_{\lambda,\lambda'=\pm} \sum_{\mathbf{k}} (1 + \lambda\lambda' \cos 2\theta_+) \frac{n_F(\varepsilon_{\mathbf{k},\lambda'}) - n_F(\varepsilon_{\mathbf{k}+\mathbf{q},\lambda})}{\omega + \varepsilon_{\mathbf{k},\lambda'} - \varepsilon_{\mathbf{k}+\mathbf{q},\lambda} + i\delta}. \tag{3.40}$$

In the static limit, this reduces to

$$\chi(q) = \sum_{\lambda,\lambda'=\pm} \sum_{\mathbf{k}} (1 + \lambda\lambda' \cos 2\theta_+) \frac{n_F(\varepsilon_{\mathbf{k},\lambda'}) - n_F(\varepsilon_{\mathbf{k}+\mathbf{q},\lambda})}{\varepsilon_{\mathbf{k},\lambda'} - \varepsilon_{\mathbf{k}+\mathbf{q},\lambda}}. \tag{3.41}$$

For an intrinsic (undoped) bilayer, it was shown that the static polarisability (arising from interband transitions) equals a constant for all $\mathbf{k}$ and is given by

$$\chi(q) = D(E_F) \ln 4, \tag{3.42}$$

where $D(E_F)$ is the density of states at the Fermi surface, given by $2m/\pi$. This is quite different from both the 2DEG and single layer graphene case. The former is a factor of 4 smaller and only constant for $q \leq 2k_F$. For a graphene monolayer the static polarisability is proportional to k and given by $\chi_{SLG}(q) = q/4\upsilon_F$.

In the extrinsic (doped) case the static polarisability was shown to have the form

$$\begin{aligned}\frac{\chi(q)}{D(E_F)} &= \frac{2k_F^2+q^2}{2k_F^2 q}\sqrt{q^2-4k_F^2} + \ln\frac{q-\sqrt{q^2-4k_F^2}}{q+\sqrt{q^2-4k_F^2}} \\ &- \theta(q-2k_F)\left(\frac{\sqrt{4k_F^4+q^4}}{2k_F^2} - \ln\left[\frac{k_F^2-\sqrt{k_F^4+q^4/4}}{2k_F^2}\right]\right). \qquad (3.43)\end{aligned}$$

3.4 Minimum Conductivity

One of the most intriguing properties of graphene is its finite minimal conductivity at the Dirac points that is of the order of the conductance quantum e^2/h per valley/spin. Note that it is *conductivity* quantization and not *conductance* quantization (often associated with transport through quantum wires). This is essentially conductivity without charge carriers since the density of states vanishes at the Dirac points. This feature of graphene is potentially important for electronic application. The experimental results [93] indicate that the conductivity approaches its quantized value for an ideal crystal and is therefore independent of scattering (figure 3.22). This is completely at odds with conventional transport theory where, at low temperatures, conductivity *is* limited by impurity scattering.

There has been a great deal of theoretical activity trying to explain the precise value of the minimum conductivity, for example [94–97]. None so far has succeeded, with most predicting a minimum conductivity of $4e^2/h\pi$. This is approximately π times smaller than the experimental value and has led to the problem becoming

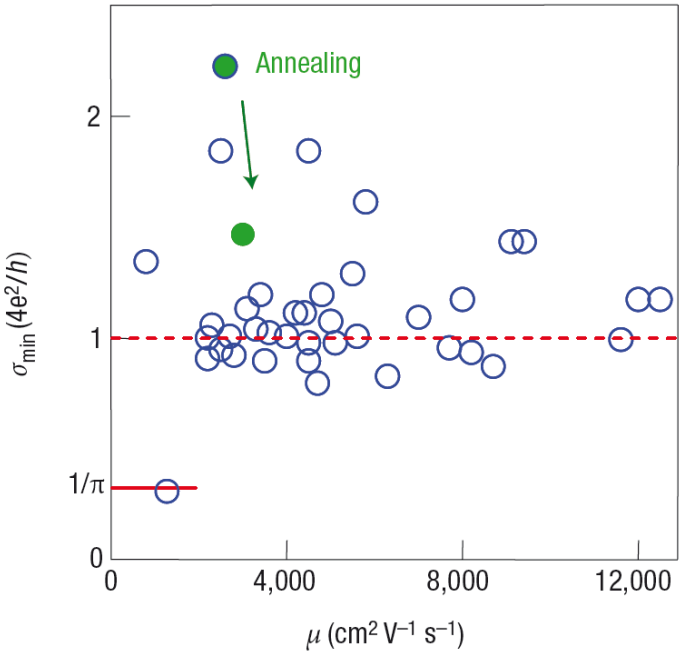

Figure 3.22: Minimum conductivity of graphene. Independent of their carrier mobility μ, different graphene devices exhibit approximately the same conductivity at the neutrality point (open circles) with most data clustering around $\approx 4e^2/h$ indicated for clarity by the dashed line (A.K.G. and K.S.N., unpublished work; includes the published data from [93]). The high-conductivity tail is attributed to macroscopic inhomogeneity. By improving the homogeneity of the samples, σ_{min} generally decreases, moving closer to $\approx 4e^2/h$. The green arrow and symbols show one of the devices that initially exhibited an anomalously large value of σ_{min} but after thermal annealing at $\approx 400K$ its σ_{min} moved closer to the rest of the statistical ensemble. Most of the data are taken in the bend resistance geometry where the macroscopic inhomogeneity plays the least role. Reproduced from [45].

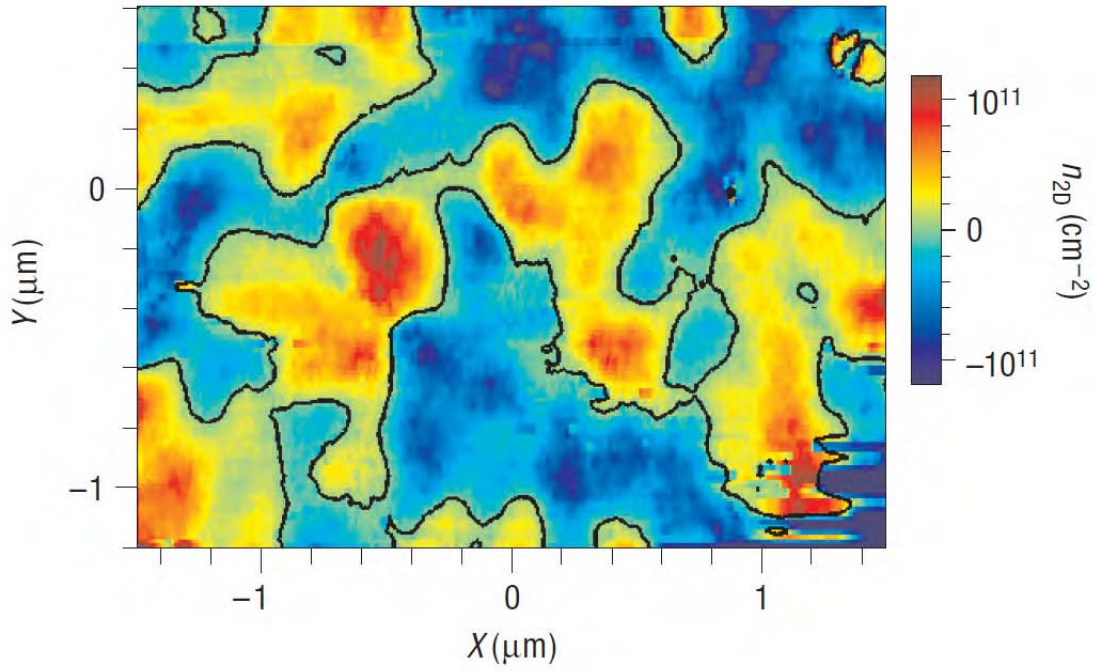

Figure 3.23: Spatial density fluctuations and electron/hole puddles. Colour map of the spatial density variations in the graphene flake extracted from surface potential measurements at high density and when the average carrier density is zero. The blue regions correspond to holes and the red regions to electrons. The black contour marks the zero density contour. Reproduced from [45, 100].

known as "the mystery of the missing pi". It is one of the great outstanding problems in graphene physics. Many of the theories so far rely on the linear spectrum and hence the vanishing density of states of graphene. However, experiments on graphene bilayers [98,99] also indicate a minimum conductivity of e^2/h per valley/spin. This suggests than the minimum conductivity is an effect of chirality and not the linear spectrum. It is not clear at this point whether or not the discrepancy between experiment and theory is due to inaccurate approximations about electron scattering in graphene, or because experiments so far have only probed a limited set of sample parameters e.g. length to width ratios [95].

In attempts to solve the mystery, there has been a great deal of interest in the effects of microscopic inhomogeneities in graphene. Although pure, undoped

graphene has its Fermi energy at the Dirac points, it is reasonable to suggest that in a realistic sample, disorder, ripples or dopants will shift the local Fermi energy away from the Dirac points. The result will be the formation of "puddles" of electron and hole carrier regions. It has been shown that this is indeed the case, except that these puddles are an intrinsic property of graphene, not related to the substrate. [100]. It is not at first obvious how this relates to minimum conductivity as the sample average carrier density will still be zero. However, modeling the carrier puddles as a random network of resistors [101], through which the current percolates has resulted in good agreement with experiment. The boundaries of the electron and hole regions can be seen as conventional p-n junctions, forming a potential barrier through which a carrier may tunnel.

It is here than an interesting feature of relativistic particles known as the Klein paradox comes into play. The Klein paradox in relativistic quantum mechanics, and consequently graphene, states that for particular angles of incidence, a carrier may tunnel through an arbitrary high barrier without a reduction in amplitude. In fact, only for an infinitely high potential does the transparency become perfect and in general the tunneling probability is only weakly dependent on the barrier height. In non-relativistic quantum mechanics such tunneling would result in a reduction of the wave-function's amplitude. It is not yet known whether this relativistic effect, or indeed any other, holds the key to solving issues surrounding the minimum conductivity.

Chapter 4

Graphene Monolayer Systems

In this chapter, we perform a full finite temperature calculation of Coulomb drag between two graphene mono-layers. After a brief introduction, we will derive a semi-analytic expression for the graphene non-linear susceptibility, representing the first original work of this thesis.

Following this, we will use a semi-analytic expression for the finite temperature graphene polarisability (derived in [81]) to study, for the first time, the behaviour of finite temperature plasmons modes in the double layer graphene system.

In the final original calculation of this chapter, we will combine the above results to calculate the finite temperature drag resistivity at various carrier densities and interlayer spacings. Our results show that the drag effect is dominated by plasmons at around $0.2T_F$ (approximately room temperature) and should therefore be experimentally accessible. This is in contrast to a prediction made elsewhere [106] that suggests that none will be seen until $T \approx T_F$. For comparison, the plasmon contribution to drag between two dimensional electron gasses peaks at around $0.5T_F$ [8]. We will then discuss the behaviour of the drag resistivity at very small interlayer distances (≈ 30Å) where the plasmon enhancement is weak due to a competition

between phase space terms, and the strength and position of the plasmon peaks.

4.1 Introduction

There are several differences between graphene and a two dimensional electron gas (2DEG) that make it an intriguing system in which to study the Coulomb drag effect. Foremost, its linear dispersion and chiral properties may be expected to lead to some novel drag effects with which to probe direct interactions between Dirac Fermions. There is some precedence for this since other transport properties of graphene show unusual features such as weak localisation and minimum conductivity (see chapter 3). As we shall see, an effect of the linear dispersion is that the non-linear susceptibility (NLS) is not simply proportional to the imaginary part of the individual layer polarisability, as is the case for a 2DEG system in the weak scattering limit. Furthermore, interband transitions, as well as the more usual intraband ones, need to be accounted for. This is not normally the case in a 2DEG semiconductor system because its band gap prevents low energy interband transitions.

Another important difference between these two systems is that it should be possible to study the drag effect in graphene at much smaller interlayer distances than in a conventional drag system. This is because interlayer tunneling will not occur between graphene layers until the out of plane π orbitals begin to overlap at approximately 3.5Å [106]. Below this distance the system will begin to behave as a single graphene bilayer (section 3.3.3).

As an extremely clean and strictly two dimensional system, the added complications of modeling disorder and a finite well width are no longer as relevant to a graphene monolayer drag system, and in a sense we might expect to observe a

purer drag effect. As yet, there have been no actual drag experiments performed in graphene systems although, it is understood that some groups are investigating such experiments. [105]

Perhaps disappointingly, a 2007 theoretical investigation by Das Sarma *et al.* [106] of Coulomb drag in graphene, performed with zero temperature expressions for the NLS and polarisation, showed strikingly similar behaviour at finite doping to that of a 2DEG system. At zero doping they showed that the symmetry of the system around the Dirac point precludes a drag effect, so long as one does not include the effects of trigonal warping or strong disorder [107]. Away from the Dirac point one sees the same d^{-4}, T^2 behavior of the drag resistivity in the limit of low temperature and large interlayer spacing, although the strength of the effect typically an order of magnitude greater. Interestingly, the fact that graphene's Fermi temperature is typically an order of magnitude higher than that of a $GaAs$ 2DEG means that this low temperature behaviour should be observable up to a higher absolute temperature.

The calculation of Das Sarma *et al.* only included temperatures up to $0.2T_F$ and displayed conservative behaviour, with the drag resistivity decreasing slightly faster than T^2 away from zero temperature. The calculation showed no evidence of any plasmon enhancement up to this temperature and in fact the authors put forward an argument that that there will be no such enhancement in a graphene system until one approaches the Fermi temperature. Their argument was primarily based on the fact that (see section 4.2) the graphene intraband excitations are strictly bound to a region $\omega < v_F q$. The result is that as temperature is increased, intraband excitations never acquire a weight in the region containing the plasmon dispersions. This is in contrast to the case of a 2DEG system where, at finite temperatures, the migration

of electron-hole (e-h) excitations into the path of the plasmons dispersions drives the plasmon enhancement to the drag effect. Therefore, the only possible source of a plasmon enhancement to graphene drag come from the interband region of the e-h continuum. Das Sarma *et al.* predicted that this would not happen until approximately the Fermi temperature, at around $1000K$. This is clearly outside of typical experiment parameters. As we shall show in this chapter, this is not the case and interband transitions enhance the drag effect at much lower temperatures.

4.2 The Non-Linear Susceptibility

As usual, the central quantity in the drag calculation is the non-linear susceptibility (NLS), $\Gamma_i(q,\omega)$, appearing in the general expression for the drag conductivity (2.72)

$$\sigma_D = \frac{1}{16\pi k_B T}\sum_{\mathbf{q}}\int_0^\infty d\omega \frac{\Gamma_1(q,\omega)\Gamma_2(q,\omega)\left|U_{12}(q,\omega)\right|^2}{\sinh^2\left(\hbar\omega/2k_BT\right)}. \tag{4.1}$$

where i labels the layer. As we have already seen (section 2.5.2), the 2DEG NLS in the weak scattering limit is proportional to the individual layer polarisabilities. This is not the case in graphene and it is a direct consequence of the fact that the graphene current operator is not directly proportional to momentum, itself a consequence of its linear dispersion. In this section, we will derive a semi-analytic expression for the finite temperature NLS. Following that, we will state the small q and ω limit of the zero temperature expression for the NLS, originally derived by Das Sarma *et al.* [106], allowing us to reproduce an analytic expression for the drag resistivity in the limit of large interlayer spacing and $T \to 0$.

We will not derive the general expression for general form of the graphene NLS

in this chapter as the structure of the calculation is broadly similar to that presented in the next chapter for bilayer graphene. It can be shown [106] that the graphene NLS in the weak scattering limit has the form

$$\Gamma(q,\omega) = \tau \sum_{\lambda,\lambda'=\pm} \sum_{\mathbf{k}'} \left[J_{\lambda\lambda}^{\mathbf{k}'+\mathbf{q}} - J_{\lambda'\lambda'}^{\mathbf{k}'} \right] \mathrm{Im} \left\{ (1+\lambda\lambda'\cos\theta_+) \frac{n_F(\varepsilon_{\mathbf{k}'\lambda'}) - n_F(\varepsilon_{\mathbf{k}'+\mathbf{q},\lambda})}{\omega + \varepsilon_{\mathbf{k}'\lambda'} - \varepsilon_{\mathbf{k}'+\mathbf{q},\lambda} + i\delta} \right\} \tag{4.2}$$

where $\theta_+ = \phi_{\mathbf{k}'+\mathbf{q}} - \phi_{\mathbf{k}}$ is the scattering angle from momentum $\mathbf{k}$ to $\mathbf{k}+\mathbf{q}$, λ, λ' label the bands, $\varepsilon_{k\lambda} = \lambda v_F |\mathbf{k}'|$ and $\omega > 0$. The impurity dressed charge-current operator, expressed in the chiral basis which diagonalises the problem, is [106]

$$J_{\lambda\lambda}^{\mathbf{k}} = \lambda(\frac{\tau_{tr}}{\tau}) v_F \cos\phi_{\mathbf{k}'}. \tag{4.3}$$

The non-linear susceptibility can be broken into two parts, an interband ($\lambda \neq \lambda'$) and an intraband ($\lambda = \lambda'$) term so that

$$\Gamma(q,\omega) = \Gamma_{\lambda\neq\lambda'}^{inter}(q,\omega) + \Gamma_{\lambda=\lambda'}^{intra}(q,\omega). \tag{4.4}$$

The intraband term corresponds to low energy electron-hole conduction band excitations bounded by $\omega < v_F q$. The interband contributions are in general an order $O(q^2)$ smaller than the intraband contribution at zero temperature [106].

4.2.1 Coulomb Drag in Intrinsic Graphene

For the case where *at least* one of the layers is undoped, with the Fermi energy passing exactly through the Dirac point, there is no net drag effect ($\sigma_D = 0$). As we have discussed previously (section 2.1), a consequence of electron-hole symmetry

is that the momentum transfer from each works in opposite directions, resulting in a zero net drag effect. This is precisely the case at the Dirac point where there is a mirror symmetry from one side to the other. If the drive layer is doped and the drag layer is undoped, equal numbers of electrons and holes are dragged resulting in a zero drag current. Similarly, if the drive layer is undoped and the drag layer is doped, there are equal number of electrons and holes driving the drag current [106].

It has been suggested that this fact may be used to ones advantage when looking for non-linearities in the graphene spectrum at the Dirac point. Sources of these non-linearities are effects such as corrections due to next nearest neighbour hopping, impurity scattering and trigonal warping. It was shown [107] that there will be a finite drag conductivity at the Dirac point due to trigonal warping. Furthermore, it was argued that it could be distinguished from the other mechanisms mentioned above by its dependence on system parameters such as the layer separation. In this thesis we will only consider the case of drag in doped graphene systems, under the assumption that the strength of the drag caused by subtle non-linearities will be small compare to the conventional drag effect.

4.2.2 Finite Temperature *Intraband* NLS

We will now manipulate (4.2) into a form that lends itself to explicit calculation and do so under the assumption of electron doping. Consequently, at zero temperature $n_F(\varepsilon_{\mathbf{k},-}) = 1$ and $n_F(\varepsilon_{\mathbf{k}',+}) = \theta(k_F - k)$, whereas at finite temperature we have

$$n_F(\varepsilon_{\mathbf{k}',\lambda}) = \left[\exp\left(\beta\left(\lambda\varepsilon_{\mathbf{k}'} - \mu\right)\right) + 1\right]^{-1}. \tag{4.5}$$

From (4.2), we have for the intraband contribution ($\Gamma^{Intra} = \Gamma^{\lambda,\lambda'=+} + \Gamma^{\lambda,\lambda'=-}$)

$$\Gamma^{Intra} = -\pi\tau \sum_{\mathbf{k}',\lambda=\pm} \left[J^{\lambda\lambda}_{\mathbf{k}'+\mathbf{q}} - J^{\lambda\lambda}_{\mathbf{k}'}\right] (1+\cos\theta_+) \left[n_F(\varepsilon_{\mathbf{k}',\lambda}) - n_F(\varepsilon_{\mathbf{k}'+\mathbf{q},\lambda})\right] \delta(\omega+\varepsilon_{\mathbf{k}',\lambda}-\varepsilon_{\mathbf{k}'+\mathbf{q},\lambda}). \tag{4.6}$$

We will first calculate the $\lambda = \lambda' = +$ term, Γ^{++}, where

$$\Gamma^{++} = -\pi\tau \sum_{\mathbf{k}'} \left[J^{++}_{\mathbf{k}'+\mathbf{q}} - J^{++}_{\mathbf{k}'}\right] (1+\cos\theta_+) \left[n_F(\varepsilon_{\mathbf{k}',+}) - n_F(\varepsilon_{\mathbf{k}'+\mathbf{q},+})\right] \delta(\omega+\varepsilon_{\mathbf{k}',+}-\varepsilon_{\mathbf{k}'+\mathbf{q},+}). \tag{4.7}$$

The calculation can be simplified somewhat by noting that the current operators are even with respect to $\phi_{\mathbf{k}} \to \phi_{-\mathbf{k}}$. Therefore, we may make a change of variables $\mathbf{k} \to -\mathbf{k} - \mathbf{q}$ in the term of (4.7) involving the Fermi function $n_F(\varepsilon_{\mathbf{k}'+\mathbf{q},+})$ and thereby write

$$\Gamma^{++} = -\pi\tau \sum_{\mathbf{k}'} \left[J^{++}_{\mathbf{k}'+\mathbf{q}} - J^{++}_{\mathbf{k}'}\right] (1+\cos\theta_+) n_F(\varepsilon_{\mathbf{k}',+}) \delta(\omega+\varepsilon_{\mathbf{k}',+}-\varepsilon_{\mathbf{k}'+\mathbf{q},+}) - \{\omega \to -\omega\}\,. \tag{4.8}$$

To evaluate this expression, we will need to write the ϕ dependent terms as functions of the θ, the angle between the vectors $\mathbf{k}'$ and $\mathbf{q}$. We proceed by noting that since the angles $\phi_{\mathbf{k}'}$ and $\phi_{\mathbf{k}'+\mathbf{q}}$, which are measured with respect to an axis parallel to the current direction, are integrated over and so for convenience we may choose the vector $\mathbf{q}$ to be parallel to that axis. This gives

$$J^{++}_{\mathbf{k}'+\mathbf{q}} - J^{++}_{\mathbf{k}'} = \frac{\tau_{tr}}{\tau} e v_F \left(\frac{k'\cos\theta + q}{\sqrt{k'^2 + q^2 + 2k'q\cos\theta}} - \cos\theta \right) \tag{4.9}$$

The case for $1+\cos\theta_+$ is more simple. We have

$$1+\cos\theta_+ \;=\; 1+\cos(\phi_{\mathbf{k}'+\mathbf{q}}-\phi_{\mathbf{k}}) = 1+\frac{q\cos\theta+k'}{\sqrt{k'^2+q^2+2k'q\cos\theta}}. \qquad (4.10)$$

Returning to (4.8) and writing the sum over momentum as an integral, we have for the non-linear intraband susceptibility

$$\Gamma^{++} \;=\; -4\frac{\pi\tau_{tr}ev_F}{(2\pi)^2}\int_0^\infty k'dk'\int_0^{2\pi}d\theta\left[\frac{k'cos\theta+q}{Q}-cos\theta\right]\left[1+\frac{q\cos\theta+k'}{Q}\right]$$

$$\times n_F(\varepsilon_{\mathbf{k}',+})\delta(\omega+\varepsilon_{\mathbf{k}',+}-\varepsilon_{\mathbf{k}'+\mathbf{q},+})-\{\omega\to-\omega\}\,, \qquad (4.11)$$

where $Q=\sqrt{k^2+q^2+2kqcos\theta}$ and we have taken into account the 2×2 spin and valley degeneracy. Introducing $\varepsilon_{k,\lambda}=\lambda v_F k$ explicitly,

$$\Gamma^{++} \;=\; -\frac{\tau_{tr}ev_F}{\pi}\int_0^\infty k'dk'\int_0^{2\pi}d\theta\left[\frac{k'cos\theta+q}{Q}-cos\theta\right]\left[1+\frac{q\cos\theta+k'}{Q}\right]$$

$$\times n_F(\varepsilon_{\mathbf{k}',+})\delta(\omega+v_Fk'-v_FQ)-\{\omega\to-\omega\}\,. \qquad (4.12)$$

It is convenient at this stage to introduce the dimensionless variables $k=k'/k_F$, $x=q/k_F$ and $y=\omega/E_F$. Making use of the identity $\delta(\alpha x)=\frac{1}{|\alpha|}\delta(x)$ and noting

that $E_F = \upsilon_F k_F$ we then have

$$\Gamma^{++} = -2\alpha \int_0^\infty kdk \int_0^{2\pi} d\theta \left[\frac{kcos\theta + x}{Q} - cos\theta\right]\left[1 + \frac{x\cos\theta + k}{Q}\right]$$

$$\times n_F(\varepsilon_{\mathbf{k},+})\delta(y + k - Q) - \{\omega \to -\omega\}\,, \tag{4.13}$$

where $Q = \sqrt{k^2 + x^2 + 2kxcos\theta}$ and $\alpha = \frac{\tau_{tr} e k_F}{2\pi}$. The angular integration can be carried out via the delta function which provides the conditions

$$k > \frac{x - y}{2} \quad \& \quad y \leq x. \tag{4.14}$$

Making the change of variable $Q = \sqrt{k^2 + x^2 + 2kxcos\theta}$ so that

$$d\theta = \frac{QdQ}{\sqrt{4k^2x^2 - (Q^2 - k^2 - x^2)^2}}, \quad \cos\theta = \frac{Q^2 - k^2 - x^2}{2kx}, \tag{4.15}$$

equation (4.14) becomes

$$\Gamma^{++} = -\frac{\alpha}{x}\int_{\frac{x-y}{2}}^\infty kdk \int QdQ \left[\frac{Q^2 - k^2 + x^2}{Q} - \frac{Q^2 - k^2 - x^2}{k}\right] \tag{4.16}$$

$$\times \left[1 + \frac{Q^2 + k^2 - x^2}{2kQ}\right] \frac{n_F(\varepsilon_{\mathbf{k},+})\delta(y + k - Q)}{\sqrt{4k^2x^2 - (Q^2 - k^2 - x^2)^2}}\theta(x - y) - [\omega \to -\omega]\,.$$

Evaluating the integrand at $Q = y + k$,

$$\Gamma^{++} = -\frac{\alpha}{x}\int_{\frac{x-y}{2}}^{\infty} kdk\left[\frac{(y+k)^2-k^2+x^2}{y+k}-\frac{(y+k)^2-k^2-x^2}{k}\right] \tag{4.17}$$

$$\times\left[1+\frac{(y+k)^2+k^2-x^2}{2k\,(y+k)}\right]\frac{n_F(\varepsilon_{\mathbf{k},+})\,(y+k)\,\theta(x-y)}{\sqrt{4k^2x^2-\left((y+k)^2-k^2-x^2\right)^2}}-\{y\to -y\}\,.$$

The term in the square root factorises into $\sqrt{(x^2-y^2)(2k-x+y)(2k+x+y)}$. We then have,

$$\Gamma^{++} = -\frac{\alpha}{x\sqrt{x^2-y^2}}\int_{\frac{x-y}{2}}^{\infty} kdk\left[\frac{2yk+y^2+x^2}{y+k}-\frac{2yk+y^2-x^2}{k}\right] \tag{4.18}$$

$$\times\left[1+\frac{2k^2+2yk+y^2-x^2}{2k\,(y+k)}\right]\frac{n_F(\varepsilon_{\mathbf{k},+})\,(y+k)}{\sqrt{(2k-x+y)(2k+x+y)}}\theta(x-y)-\{y\to -y\}\,.$$

Putting the terms in square brackets over common denominators

$$\Gamma^{++} = -\frac{\alpha}{x\sqrt{x^2-y^2}}\int_{\frac{x-y}{2}}^{\infty} kdk\left[\frac{(x^2-y^2)\,(2k+y)}{k(k+y)}\right]\left[\frac{(2k-x+y)(2k+x+y)}{2k(k+y)}\right]$$

$$\times\frac{n_F(\varepsilon_{\mathbf{k},+})\,(y+k)}{\sqrt{(2k-x+y)(2k+x+y)}}\theta(x-y)-[y\to -y]\,, \tag{4.19}$$

and then tidying up a little yields

$$\Gamma^{++} = -\frac{\alpha\sqrt{x^2-y^2}}{2x}\int_{\frac{x-y}{2}}^{\infty} dk n_F(\varepsilon_{\mathbf{k},+})\left[\frac{(2k+y)\sqrt{(2k-x+y)(2k+x+y)}}{k(k+y)}\right]\theta(x-y)-\{y\to -y\} \tag{4.20}$$

We proceed by making the substitution $u=\frac{2k}{x}+\frac{y}{x}$ so that $k=(xu-y)/2$ and

$dk = \frac{x}{2}du$. This gives

$$\Gamma^{++} = -\alpha\sqrt{x^2-y^2}\int_1^\infty du n_F(\varepsilon_{\mathbf{u},+})\frac{xu\sqrt{(xu-x)(xu+x)}}{(xu-y)(xu+y)}\theta(x-y) - \{y \to -y\}$$

Expanding the denominator we have our final form for the finite temperature Γ^{Intra}

$$\Gamma^{++}(x,y,T) = -\alpha\sqrt{x^2-y^2}\int_1^\infty du n_F(\varepsilon_{\mathbf{u},+})\frac{u\sqrt{u^2-1}}{u^2-\frac{y^2}{x^2}}\theta(x-y) - \{y \to -y\}\,, \quad (4.21)$$

where $\alpha = \frac{\tau_{tr}ek_F}{2\pi}$.

Moving on to the $\lambda = \lambda' = -$ term, Γ^{--}, we have

$$\Gamma^{--} = -\pi\tau\sum_{\mathbf{k}'}\left[J_{--}^{\mathbf{k}'+\mathbf{q}} - J_{--}^{\mathbf{k}'}\right](1+\cos\theta_+)\left[n_F(\varepsilon_{\mathbf{k}',-}) - n_F(\varepsilon_{\mathbf{k}'+\mathbf{q},-})\right]\delta(\omega+\varepsilon_{\mathbf{k}',-}-\varepsilon_{\mathbf{k}'+\mathbf{q},-}), \quad (4.22)$$

which as we have already seen can be written as

$$\Gamma^{--} = -\pi\tau\sum_{\mathbf{k}'}\left[J_{--}^{\mathbf{k}'+\mathbf{q}} - J_{--}^{\mathbf{k}'}\right](1+\cos\theta_+)n_F(\varepsilon_{\mathbf{k}',-})\delta(\omega+\varepsilon_{\mathbf{k}',-}-\varepsilon_{\mathbf{k}'+\mathbf{q},-}) - [\omega \to -\omega]. \quad (4.23)$$

Making use of the identities $J_{\lambda\lambda}^{\mathbf{k}'} = -J_{-\lambda-\lambda}^{\mathbf{k}'}$, $\varepsilon_{\mathbf{k}',\lambda} = -\varepsilon_{\mathbf{k}',-\lambda}$ and $\delta(ax) = \frac{1}{|a|}\delta(x)$ yields,

$$\Gamma^{--} = +\pi\tau\sum_{\mathbf{k}'}\left[J_{++}^{\mathbf{k}'+\mathbf{q}} - J_{++}^{\mathbf{k}'}\right](1+\cos\theta_+)n_F(\varepsilon_{\mathbf{k}',-})\delta(-\omega+\varepsilon_{\mathbf{k}',+}-\varepsilon_{\mathbf{k}'+\mathbf{q},+}) - \{\omega \to -\omega\}\,. \quad (4.24)$$

Therefore, we have shown that

$$\Gamma^{--} = \Gamma^{++}\frac{n_F(\varepsilon_{\mathbf{k}',-})}{n_F(\varepsilon_{\mathbf{k}',+})}. \quad (4.25)$$

Applying (3.11) to (2.3), we have for Γ^{--},

$$\Gamma^{--} = -\frac{\alpha\sqrt{x^2-y^2}}{2x}\theta(x-y)\int_{\frac{x-y}{2}}^{\infty} dk n_F(\varepsilon_{\mathbf{k},-})\left[\frac{(2k+y)\sqrt{(2k-x+y)(2k+x+y)}}{k(k+y)}\right] - \{y\to -y\}\,. \tag{4.26}$$

Repeating the steps that led up to (2.47) we have finally for both intraband terms,

$$\Gamma^{--} = -\alpha\sqrt{x^2-y^2}\theta(x-y)\int_1^{\infty} du n_F(\varepsilon_{\mathbf{u},-})\frac{u\sqrt{u^2-1}}{u^2-\frac{y^2}{x^2}} - [y\to -y]\,, \tag{4.27}$$

$$\Gamma^{++} = -\alpha\sqrt{x^2-y^2}\theta(x-y)\int_1^{\infty} du n_F(\varepsilon_{\mathbf{u},+})\frac{u\sqrt{u^2-1}}{u^2-\frac{y^2}{x^2}} - [y\to -y]\,, \tag{4.28}$$

with

$$n_F(\varepsilon_{\mathbf{u},\lambda}) = \left[\exp\left(\frac{\lambda\,|xu-y|-2\mu'}{2T'}\right)+1\right],^{-1} \tag{4.29}$$

where $\mu' = \mu/E_F$ is the dimensionless chemical potential and $T^{'} = T/T_F$ the dimensionless temperature. Defining a function

$$M_{\pm}^{\lambda}(x,y,T') = \int_1^{\infty}\frac{u\sqrt{u^2-1}}{[u^2-y^2x^{-2}]\left[\exp\left(\frac{\lambda|xu\pm y|-2\mu'}{2T'}\right)+1\right]}du, \tag{4.30}$$

we can write Γ^{Intra} in the compact form

$$\Gamma^{Intra} = -\alpha\sum_{\lambda=\pm}\sqrt{x^2-y^2}\theta(x-y)\left[M_{+}^{\lambda}(x,y,T') - M_{-}^{\lambda}(x,y,T')\right], \tag{4.31}$$

where $\alpha = \frac{\tau_{tr}ek_F}{2\pi}$.

4.2.3 Finite Temperature *Interband* NLS

From (4.2) we have for the intraband contribution ($\lambda \neq \lambda'$), $\Gamma^{Inter} = \Gamma_{\lambda=1,\lambda'=-1} + \Gamma_{\lambda=-1,\lambda'=1}$

$$= -\pi\tau \sum_{\mathbf{k}'} \left[J_{++}^{\mathbf{k}'+\mathbf{q}} - J_{--}^{\mathbf{k}'} \right] (1-\cos\theta_+) \left[n_F(\varepsilon_{\mathbf{k}',-}) - n_F(\varepsilon_{\mathbf{k}'+\mathbf{q},+}) \right] \delta(\omega + \varepsilon_{\mathbf{k}',-} - \varepsilon_{\mathbf{k}'+\mathbf{q},+}) \tag{4.32}$$

$$-\pi\tau \sum_{\mathbf{k}'} \left[J_{++}^{\mathbf{k}'+\mathbf{q}} - J_{--}^{\mathbf{k}'} \right] (1-\cos\theta_+) \left[n_F(\varepsilon_{\mathbf{k}',+}) - n_F(\varepsilon_{\mathbf{k}'+\mathbf{q},-}) \right] \delta(\omega + \varepsilon_{\mathbf{k}',+} - \varepsilon_{\mathbf{k}'+\mathbf{q},-}).$$

The second term in (4.32) is zero because every term in its δ function is always positive. Therefore,

$$\Gamma^{Inter} = -\pi\tau \sum_{\mathbf{k}'} \left[J_{++}^{\mathbf{k}'+\mathbf{q}} - J_{--}^{\mathbf{k}'} \right] (1-\cos\theta_+) \left[n_F(\varepsilon_{\mathbf{k}',-}) - n_F(\varepsilon_{\mathbf{k}'+\mathbf{q},+}) \right] \delta(\omega+\varepsilon_{\mathbf{k}',-}-\varepsilon_{\mathbf{k}'+\mathbf{q},+}). \tag{4.33}$$

Changing variables $\mathbf{k}' \to -\mathbf{k}'-\mathbf{q}$ in the second of (4.33) involving $n_F(\varepsilon_{\mathbf{k}'+\mathbf{q},+})$, which we shall call $\Gamma_{(2)}$, we have

$$\Gamma_{(2)} = -\pi\tau \sum_{\mathbf{k}'} \left[J_{++}^{-\mathbf{k}'} - J_{--}^{-\mathbf{k}'-\mathbf{q}} \right] (1-\cos\theta_+) n_F(\varepsilon_{-\mathbf{k}',+}) \delta(\omega+\varepsilon_{-\mathbf{k}'-\mathbf{q},-}-\varepsilon_{-\mathbf{k}',+}) \tag{4.34}$$

Using the fact that $J^{-\mathbf{k}'} = J^{\mathbf{k}'}$ and $\varepsilon_{-\mathbf{k}'\lambda} = \varepsilon_{\mathbf{k}'\lambda}$ we have,

$$\Gamma_{(2)} = \pi\tau \sum_{\mathbf{k}'} \left[J_{++}^{\mathbf{k}'} - J_{--}^{\mathbf{k}'+\mathbf{q}} \right] (1-\cos\theta_+) n_F(\varepsilon_{\mathbf{k}',+}) \delta(\omega + \varepsilon_{\mathbf{k}'+\mathbf{q}-}, -\varepsilon_{\mathbf{k}',+}) \tag{4.35}$$

which, using $\varepsilon_{\mathbf{k}',-\lambda} = -\varepsilon_{\mathbf{k}',\lambda}$ we can write as

$$\Gamma_{(2)} = \pi\tau \sum_{\mathbf{k}'} \left[J_{++}^{\mathbf{k}'} - J_{--}^{\mathbf{k}'+\mathbf{q}} \right] (1-\cos\theta_+) n_F(\varepsilon_{\mathbf{k}',+}) \delta(\omega + \varepsilon_{\mathbf{k}',-} - \varepsilon_{\mathbf{k}'+\mathbf{q}+},). \tag{4.36}$$

Using $J^{\mathbf{k}}_{\lambda\lambda} = -J^{\mathbf{k}}_{-\lambda-\lambda}$,

$$\Gamma_{(2)} = \pi\tau \sum_{\mathbf{k}'} \left[J^{\mathbf{k}'+\mathbf{q}}_{++} - J^{\mathbf{k}'}_{--} \right] (1 - \cos\theta_+) n_F(\varepsilon_{\mathbf{k}',+}) \delta(\omega + \varepsilon_{\mathbf{k}',-} - \varepsilon_{\mathbf{k}'+\mathbf{q}+,}). \quad (4.37)$$

Therefore, we have for Γ^{Inter},

$$\Gamma^{Inter} = -\pi\tau \sum_{\mathbf{k}'} \left[J^{\mathbf{k}'+\mathbf{q}}_{++} - J^{\mathbf{k}}_{--} \right] (1-\cos\theta_+) \left[n_F(\varepsilon_{\mathbf{k}',-}) - n_F(\varepsilon_{\mathbf{k}',+}) \right] \delta(\omega+\varepsilon_{\mathbf{k}',-}-\varepsilon_{\mathbf{k}'+\mathbf{q},+}). \quad (4.38)$$

As before, we now write the ϕ dependent terms as functions of θ. For the current operators we have,

$$J^{\mathbf{k}'+\mathbf{q}}_{++} - J^{\mathbf{k}'}_{--} = \frac{\tau_{tr}}{\tau} e v_F \left(\frac{k' \cos\theta + q}{\sqrt{k'^2 + q^2 + 2k'q\cos\theta}} + \cos\theta \right), \quad (4.39)$$

and for $1 - \cos\theta_+$,

$$1 - \cos\theta_+ \;=\; 1 - \cos(\phi_{\mathbf{k}'+\mathbf{q}} - \phi_{\mathbf{k}'}) = 1 - \frac{q\cos\theta + k'}{\sqrt{k'^2 + q^2 + 2k'q\cos\theta}}. \quad (4.40)$$

Returning to (4.33) and writing the sum over momentum as an integral, we have for the non-linear interband susceptibility

$$\Gamma^{Inter} \;=\; -4\frac{\pi\tau_{tr} e v_F}{(2\pi)^2} \int_0^\infty k'dk' \int_0^{2\pi} d\theta \left[\frac{k'\cos\theta + q}{Q} + \cos\theta \right] \left[1 - \frac{q\cos\theta + k'}{Q} \right]$$

$$\times \left[n_F(\varepsilon_{\mathbf{k}',-}) - n_F(\varepsilon_{\mathbf{k}',+}) \right] \delta(\omega + \varepsilon_{\mathbf{k}',-} - \varepsilon_{\mathbf{k}'+\mathbf{q},+}), \quad (4.41)$$

where $Q = \sqrt{k'^2 + q^2 + 2k'q\cos\theta}$ and we have included the 2×2 spin and valley degeneracy. Introducing $\varepsilon_{k',\lambda} = \lambda \upsilon_F k'$ explicitly,

$$\Gamma^{Inter} = -\frac{\tau_{tr} e \upsilon_F}{\pi} \int_0^\infty k' dk' \int_0^{2\pi} d\theta \left[\frac{k'\cos\theta + q}{Q} + cos\theta\right] \left[1 - \frac{q\cos\theta + k'}{Q}\right]$$

$$\times \left[n_F(\varepsilon_{\mathbf{k}',-}) - n_F(\varepsilon_{\mathbf{k}',+})\right] \delta(\omega - \upsilon_F k' - \upsilon_F Q). \tag{4.42}$$

We now once again introduce the dimensionless variables $k = k'/k_F$, $x = q/k_F$ and $y = \omega/E_F$. Making use of the identity $\delta(\alpha x) = \frac{1}{|\alpha|}\delta(x)$ and noting that $E_F = \upsilon_F k_F$ we have

$$\Gamma^{Inter} = -2\alpha \int_0^\infty k dk \int_0^{2\pi} d\theta \left[\frac{k\cos\theta + x}{Q} + cos\theta\right] \left[1 - \frac{x\cos\theta + k}{Q}\right]$$

$$\times \left[n_F(\varepsilon_{\mathbf{k},-}) - n_F(\varepsilon_{\mathbf{k},+})\right] \delta(y - k - Q), \tag{4.43}$$

where $Q = \sqrt{k^2 + x^2 + 2kx\cos\theta}$ and $\alpha = \frac{\tau_{tr} e k_F}{2\pi}$. The angular integration can be carried out via the delta function which provides the conditions

$$\frac{y - x}{2} < k < \frac{y + x}{2} \qquad\qquad x \leq y. \tag{4.44}$$

Making the change of variables $Q = \sqrt{k^2 + x^2 + 2kxcos\theta}$ so that

$$d\theta = \frac{QdQ}{\sqrt{4k^2x^2 - (Q^2 - k^2 - x^2)^2}}, \quad \cos\theta = \frac{Q^2 - k^2 - x^2}{2kx}, \tag{4.45}$$

equation (4.14) becomes

$$\Gamma^{Inter} = -\frac{\alpha}{x}\int_{\frac{y-x}{2}}^{\frac{y-x}{2}} kdk \int QdQ \left[\frac{Q^2-k^2+x^2}{Q}+\frac{Q^2-k^2-x^2}{\tilde{k}}\right] \tag{4.46}$$

$$\times\left[1-\frac{Q^2+k^2-x^2}{2kQ}\right]\frac{\left[n_F(\varepsilon_{\mathbf{k},-})-n_F(\varepsilon_{\mathbf{k},+})\right]\theta(y-x)}{\sqrt{4k^2x^2-(Q^2-k^2-x^2)^2}}\delta(y-k-Q).$$

Evaluating the integrand at $Q=y-k$,

$$\Gamma^{Inter} = -\frac{\alpha}{x}\int_{\frac{y-x}{2}}^{\frac{y+x}{2}} kdk \left[\frac{\left(y-\tilde{k}\right)^2-\tilde{k}^2+x^2}{y-\tilde{k}}+\frac{\left(y-\tilde{k}\right)^2-\tilde{k}^2-x^2}{\tilde{k}}\right] \tag{4.47}$$

$$\times\left[1-\frac{(y-k)^2+k^2-x^2}{2k\,(y-k)}\right]\frac{n_F(\varepsilon_{\mathbf{k},-})\,(y-k)\,\theta(y-x)}{\sqrt{4kx^2-\left((y-k)^2-k^2-x^2\right)^2}},$$

the term in the square root factorises into $\sqrt{(y^2-x^2)(x+y-2k)(2k+x-y)}$ and we have

$$\Gamma^{Inter} = -\frac{\alpha}{x\sqrt{y^2-x^2}}\int_{\frac{y-x}{2}}^{\frac{y+x}{2}} kdk \left[\frac{y^2+x^2-2yk}{y-k}+\frac{y^2-x^2-2yk}{k}\right] \tag{4.48}$$

$$\times\left[1-\frac{2k^2-2yk+y^2-x^2}{2k\,(y-k)}\right]\frac{\left[n_F(\varepsilon_{\mathbf{k},-})-n_F(\varepsilon_{\mathbf{k},+})\right](y-k)\,\theta(y-x)}{\sqrt{(x+y-2k)(2k+x-y)}}.$$

Putting the terms in square brackets over common denominators,

$$\Gamma^{Inter} = -\frac{\alpha}{x\sqrt{y^2-x^2}}\int_{\frac{y-x}{2}}^{\frac{y+x}{2}} k\left[\frac{(y^2-x^2)(y-2k)}{k\,(k-y)}\right] \tag{4.49}$$

$$\times\left[\frac{(x+y-2k)(2k+x-y)}{2k\,(y-k)}\right]\frac{\left[n_F(\varepsilon_{\mathbf{k},-})-n_F(\varepsilon_{\mathbf{k},+})\right](y-k)\,\theta(y-x)}{\sqrt{(x+y-2k)(2k+x-y)}}d\tilde{k}.$$

Tidying up a little,

$$\Gamma^{Inter} = -\frac{\alpha\sqrt{y^2-x^2}}{2x}\int_{\frac{y-x}{2}}^{\frac{y+x}{2}} dk\left[\frac{y-2k}{k\,(k-y)}\right]\sqrt{(x+y-2k)(2k+x-y)}$$

$$\times\left[n_F(\varepsilon_{\mathbf{k},-}) - n_F(\varepsilon_{\mathbf{k},+})\right]\theta(y-x). \tag{4.50}$$

We proceed by making the substitution $u = \frac{2k}{x} - \frac{y}{x}$ so that $k = (xu+y)/2$ and $dk = \frac{x}{2}du$. This gives

$$\Gamma^{Inter} = +\alpha\sqrt{y^2-x^2}\int_{-1}^{1}\left[\frac{xu\sqrt{(x-xu)(x+xu)}}{(xu+y)(xu-y)}\right]$$

$$\times\left[n_F(\varepsilon_{\mathbf{u},-}) - n_F(\varepsilon_{\mathbf{u},+})\right]\theta(y-x)du. \tag{4.51}$$

Expanding out the terms in round brackets, we have for our final form for Γ^{Inter}

$$\Gamma^{Inter} = -\alpha\sqrt{y^2-x^2}\int_{-1}^{1}\left[\frac{u\sqrt{1-u^2}}{u^2-\frac{y^2}{x^2}}\right]\left[n_F(\varepsilon_{\mathbf{u},+}) - n_F(\varepsilon_{\mathbf{u},-})\right]\theta(y-x)du. \tag{4.52}$$

with

$$n_F(\varepsilon_{\mathbf{u},\lambda}) = \left[\exp\left(\frac{\lambda\,|xu-y| - 2\mu'}{2T'}\right)+1\right]^{-1}, \tag{4.53}$$

where $\mu' = \mu/E_F$ is the dimensionless chemical potential and $T' = T/T_F$ the dimensionless temperature. Defining a function

$$N_{\pm}^{\lambda}(x,y,T') = \int_{-1}^{1}\frac{u\sqrt{1-u^2}}{\left[u^2-y^2x^{-2}\right]\left[\exp\left(\frac{\lambda|xu\pm y|-2\mu'}{2T'}\right)+1\right]}du \tag{4.54}$$

we can write Γ^{Intra} in the compact form

$$\Gamma^{Inter} = -\alpha \sum_{\lambda=\pm} \sqrt{y^2 - x^2}\theta(y-x)\lambda N_+^\lambda(x, y, T'). \tag{4.55}$$

4.2.4 Summary and Discussion

We have shown that the graphene finite temperature non-linear susceptibility$\Gamma(x, y, T') = \Gamma^{Intra} + \Gamma^{Inter}$ is

$$\Gamma(x, y, T) = -\alpha \sum_{\lambda=\pm} \left\{ \theta(x-y) f(x, y) \left[M_+^\lambda - M_-^\lambda \right] + \lambda \theta(y-x) f(y, x) N_+^\lambda \right\}, \tag{4.56}$$

$$M_\pm^\lambda(x, y, T') = \int_1^\infty \frac{u\sqrt{u^2-1}}{[u^2 - y^2x^{-2}]\left[\exp\left(\frac{\lambda|xu \pm y| - 2\mu'}{2T'}\right) + 1\right]} du,$$

$$N_\pm^\lambda(x, y, T') = \int_{-1}^1 \frac{u\sqrt{1-u^2}}{[u^2 - y^2x^{-2}]\left[\exp\left(\frac{\lambda|xu \pm y| - 2\mu'}{2T'}\right) + 1\right]} du,$$

$$f(x, y) = \sqrt{x^2 - y^2},$$

and where $k = k'/k_F$, $x = q/k_F$, $y = \omega/E_F$, $T' = T/T_F$, $\mu' = \mu/E_F$, and $\alpha = \frac{\tau_{tr} e k_F}{2\pi}$. Equation (4.56) represents the first original work of this thesis. It is evaluated numerically for three difference temperature in figure 4.1, clearly showing that the intralayer contribution ($\omega > \upsilon_F q$) migrates toward the origin as the temperature increase. As we will see, this is crucial to driving the plasmon enhancement to the drag effect as it quickly overlaps with the plasmon dispersions.

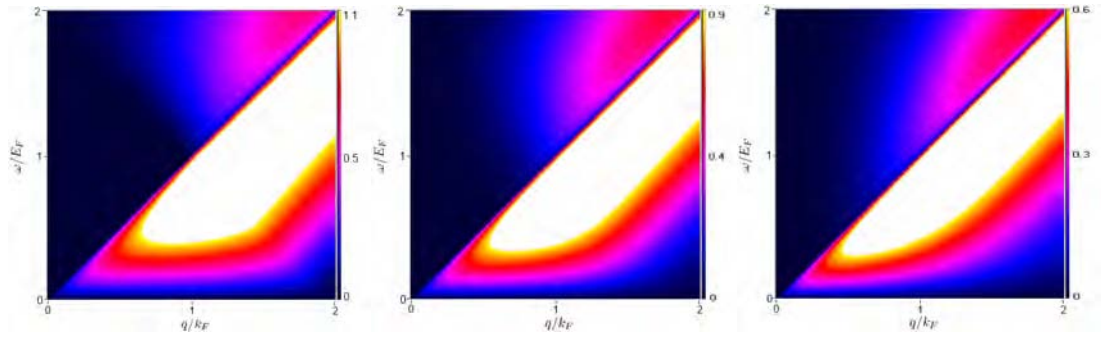

Figure 4.1: The finite temperature graphene non-linear susceptibility. Density plots of $|\Gamma(q/k_F, \omega/E_F, T)|/\alpha$ as a function of ω and q for three different temperatures. From left to right $0.01T_F$, $0.1T_F$ and $0.2T_F$. The colour scale shows the value of the non-linear susceptibility in units of $\alpha = \frac{\tau_{tr} e k_F}{2\pi}$. The intraband contribution is restricted to the region $\omega < v_F q$ and the interband contribution to $\omega > v_F q$. The interband contribution is seen to migrate toward the origin with increasing temperature.

4.2.5 Zero Temperature

The zero temperature graphene non-linear susceptibility was first derived by Das Sarma *et al.* [106]. At zero temperature and for electron doping, the lower band the Fermi function $n_F(\varepsilon_{\tilde{\mathbf{k}},-}) = 1$ whereas $n_F(\varepsilon_{\tilde{\mathbf{k}},+}) = \theta\left(k_F - \tilde{k}\right)$. The result is that for the intraband contribution the Fermi functions of (4.2) cancel and we are left with only one intraband term, Γ^{++}, given by equation (4.20) with an upper momentum cutoff of 1. The calculation is now reduced to a series of elementary integrals and after some straightforward but tedious algebra one arrives at

$$\begin{aligned}\Gamma^{Intra}_{T=0} &= -\frac{\alpha\,(x^2-y^2)}{x}\theta(x-y)\theta(2-x-y)\left\{2\frac{\sqrt{(y+x-2)(y-x-2)}}{\sqrt{x^2-y^2}}\right. \\ &\left. -\left[\tan^{-1}\left(\frac{\sqrt{(y+x-2)(y-x-2)}\sqrt{x^2-y^2}}{x^2-2-(y-2)y}\right)-\pi\theta\left[y(y-2)-x^2+2\right]\right]\right\}\end{aligned} \tag{4.57}$$

$-\{y \to -y\}$, where $\alpha = \frac{\tau_{tr} e k_F}{2\pi}$. Similarly, for the intraband contribution (4.32) the difference of the two Fermi functions gives a lower momentum cutoff of 1. This leads

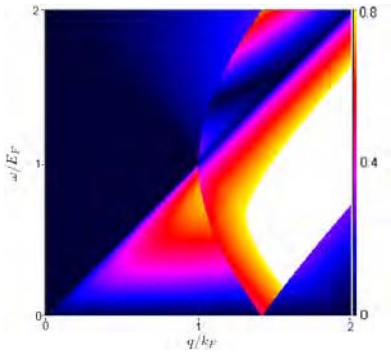

Figure 4.2: The absolute value of the zero temperature non-linear susceptibility $\Gamma(q,\omega) = \Gamma^{Intra}_{T=0}(q,\omega) + \Gamma^{Inter}_{T=0}(q,\omega)$ (as derived in [106]) as a function of $\omega$and q. The colour scale shows the value of the non-linear susceptibility in units of $\alpha = \frac{\tau_{tr} e k_F}{2\pi}$.

to

$$\Gamma^{Inter}_{T=0} = -\frac{\alpha\,(y^2-x^2)}{x}\theta(y-x)\theta(x+y-2)\theta(x-y+2)\left\{2\frac{\sqrt{(x+y-2)(x-y-2)}}{\sqrt{y^2-x^2}}\right. \tag{4.58}$$
$$\left. -\left[\tan^{-1}\left(\frac{\sqrt{(x+y-2)(x-y-2)}\sqrt{y^2-x^2}}{x^2-2-(y-2)y}\right)-\pi\theta\left[x^2-2-y(y-2)\right]\right]\right\}.$$

A plot of the zero temperature NLS is shown in figure 4.2, showing clearly that the interband contribution ($y > x$) resides high up on the y axis and therefore has no weight to contribute to the drag effect as zero temperature.

It will be useful in deriving the analytic result of section 4.4 to give an expression for the small y and x limit of $\Gamma(x$,y). In this case, the interband contribution has no weight and (4.57) reduces to

$$\Gamma(x,y) = \Gamma^{Intra}_{T=0}(x,y) \approx \frac{4e\tau_{tr}k_F y}{E_F\pi} = \frac{4e\tau_{tr}\omega}{v_F\pi} \quad x,y \ll 1 \tag{4.59}$$

where $\omega = E_F y$. This expression will be useful in deriving a result for the drag rate that is valid in the limit of lower temperature ($T \ll T_F$) and large interlayer spacing ($k_F d \ll 1$).

4.3 Screening and Plasmons

As we have already discussed (section 3.3.2.3), the random phase approximation (RPA) is an excellent choice for graphene as it is a weakly interacting system. In the RPA the screened *intralayer* potential is given by (2.8)

$$U(q,\omega) = \frac{U_b(q)}{1+\chi(q,\omega)} \equiv \frac{U_b(q)}{\varepsilon(q,\omega)} \tag{4.60}$$

where $U_b(q) = 2\pi e^2 exp(-qd)/q$ is the bare interlayer Coulomb interaction and $\chi(q,\omega)$ is the graphene polarisability. We showed in section 2.2 that under the RPA and treating the graphene layers as identical, the screened *interlayer* interaction (2.19)

$$U_{12}(q,\omega) = \frac{U_b(q)}{[1+\chi(q,\omega)]^2 - U_b^2(q)\chi^2(q,\omega)} \equiv \frac{U_b(q)}{\varepsilon_{12}(q,\omega)}. \tag{4.61}$$

Das Sarma *et al.* [82] were the first to derive an analytic expression for the finite frequency polarisability at zero temperature and finite doping. Its form is formidable and so it will not be stated here. It will be useful in deriving the analytic result of section 4.4 to give the zero temperature, large layer separation expression ($d^{-1} \ll q, k_F, q_{TF}$) limit of (4.61). In this limit we have

$$U_{12}(q,\omega) \approx \frac{q}{4\pi e^2 \sinh(qd)\chi^2(q,\omega)}. \tag{4.62}$$

As $T \to 0$, the integral governing the drag conductivity (2.7) is restricted to small frequencies ω by the $\sinh^2(\omega/2k_B)$ appearing in the denominator. Consequently, we may take the static limit of the polarisability where it is real and equals the

graphene density of states (3.24). We have

$$\chi(q,\omega\to 0)\approx\frac{2k_F}{\pi v_F}. \tag{4.63}$$

Substituting this into (4.62), the large d, small ω limit of the interlayer interaction is

$$U_{12}(q,\omega)\approx\frac{\pi e^2 q}{q_{TF}^2\sinh qd} \tag{4.64}$$

where $q_{TF}=4e^2k_F/v_F$ is the Thomas Fermi Screening wave-vector for graphene [106].

The finite temperature graphene polarisability was first considered by Ramezanali *et al.* (2009, [81]). They were able to derive a semi-analytic expression and showed that it has real and imaginary parts given by

$$\begin{aligned}\mathrm{Im}\chi(q,\omega,T) &= \frac{1}{\pi}\sum_{\alpha=\pm}\Bigg\{\theta(v_Fq-\omega)q^2f(v_Fq,\omega)\left[G_+^{(\alpha)}(q,\omega,T)-G_-^{(\alpha)}(q,\omega,T)\right]\\ &\quad+\theta(\omega-v_Fq)q^2f(\omega,v_Fq)\left[-\frac{\pi}{2}\delta_{\alpha,-}+H_+^{(\alpha)}(q,\omega,T)\right]\Bigg\},\end{aligned} \tag{4.65}$$

$$\begin{aligned}\mathrm{Re}\chi(q,\omega,T) &= \frac{1}{\pi}\sum_{\alpha=\pm}\Bigg\{\frac{-2k_BT\ln\left[1+e^{\alpha\mu(T)/k_BT}\right]}{v_F^2}+\theta(\omega-v_Fq)\\ &\quad\times q^2f(\omega,v_Fq)\left[G_-^{(\alpha)}(q,\omega,T)-G_+^{(\alpha)}(q,\omega,T)\right]\\ &\quad+\theta(vq-\omega)q^2f(v_Fq,\omega)\left[-\frac{\pi}{2}\delta_{\alpha,-}+H_-^{(\alpha)}(q,\omega,T)\right]\Bigg\},\end{aligned} \tag{4.66}$$

where,

$$f(x,y)=\frac{1}{2\sqrt{x^2-y^2}}, \tag{4.67}$$

$$G_\pm^{(\alpha)}(q,\omega,T)=\int_1^\infty du\frac{\sqrt{u^2-1}}{\exp\left(\frac{|v_Fqu\pm\omega|-2\alpha\mu(T)}{2k_BT}\right)+1}, \tag{4.68}$$

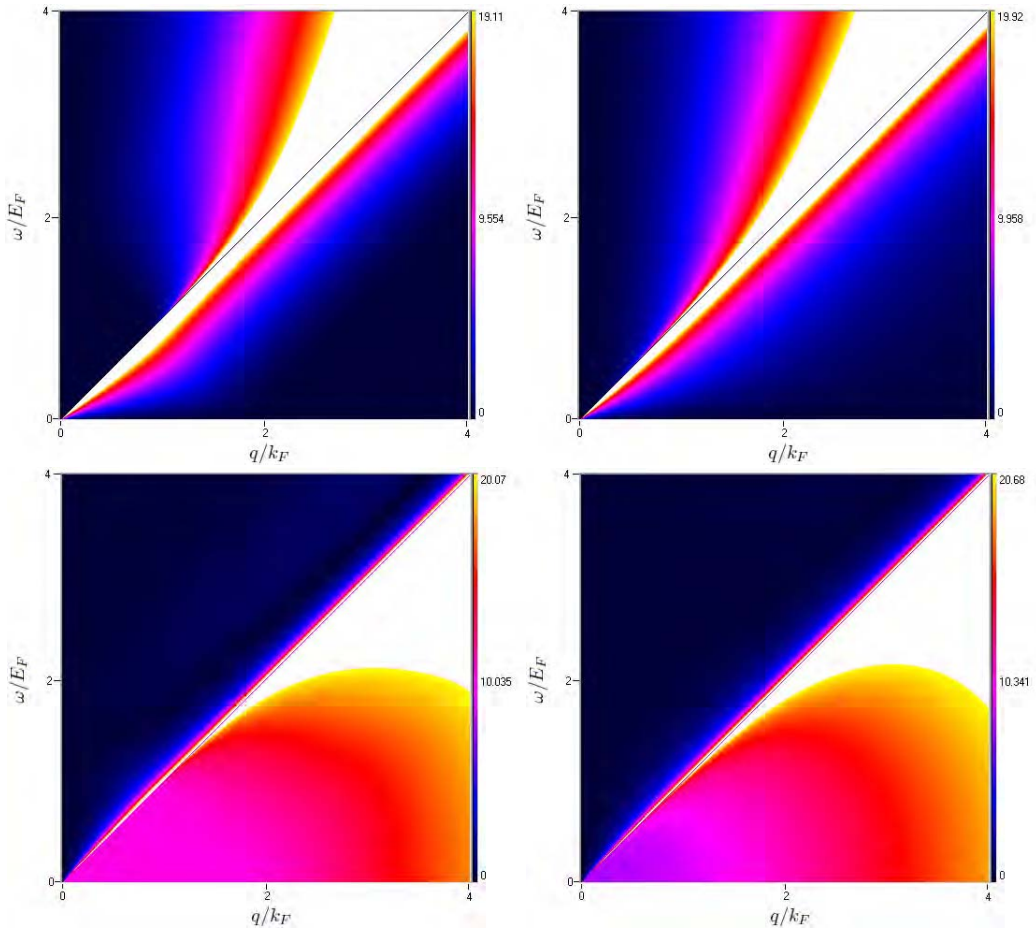

Figure 4.3: The finite temperature graphene polarisability showing the imaginary (upper) and real (lower) parts for temperatures $0.05T_F$ (left) and $0.5T_F$ (right). The imaginary part, which represents the electron-hole continuum, is seen to migrate toward the origin although it is only the interband ($\omega > v_F q$) region that does so. In real part has most of its weight in the region $\omega < v_F q$.

$$H_{\pm}^{(\alpha)}(q,\omega,T)\int_{-1}^{1} du \frac{\sqrt{1-u^2}}{\exp\left(\frac{|v_F q u \pm \omega| - 2\alpha\mu(T)}{2k_B T}\right)+1}. \tag{4.69}$$

As for the NLS, the intraband contribution is restricted to the region where $\omega < v_F q$ and the interband contribution to $\omega > v_F q$. The real and imaginary parts of the polarisation are plotted separately in figure 4.3 at two different temperatures.

Das Sarma *et al.* [82] showed that the plasmon dispersion in a single graphene layer has the familiar q dependence

$$\omega_p(q \to 0) = \omega_0\sqrt{q} \tag{4.70}$$

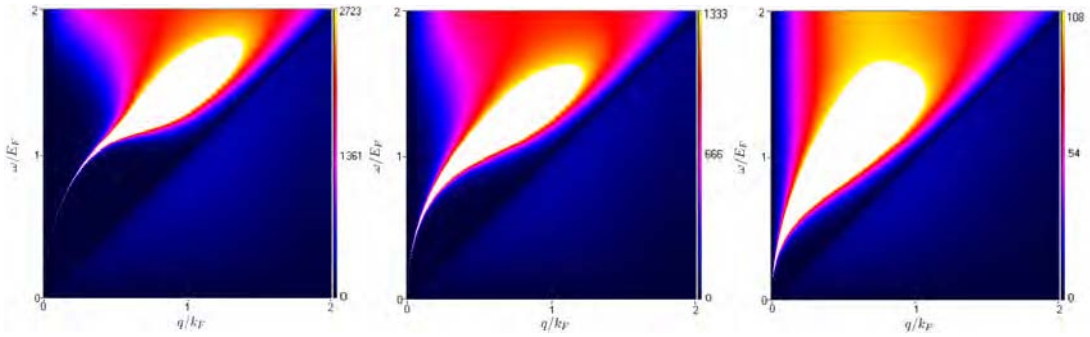

Figure 4.4: $\mathrm{Im}\,[\varepsilon^{-1}(x, y, T)]$ plotted for three different temperatures, from left to right $0.05T_F$, $0.1T_F$ and $0.2T_F$. As the temperature increases, the interband e-h continuum ($\omega > v_F q$) migrates towards the origin, progressively damping the single layer plasmon with dispersion $\omega \propto \sqrt{q}$.

in the $q \to 0$ limit where $\omega_0 = \sqrt{2e^2 E_F/\kappa}$. The plasmon dispersion is found to lie outside of the intraband particle hole continuum and as such the plasmon cannot decay via intraband excitations. Instead, as temperature increases the interband contribution migrates down towards the origin and as it does so overlaps with the plasmon mode. This is best illustrated by plotting the imaginary part of the reciprocal of the dielectric function $\mathrm{Im}\,[\varepsilon^{-1}(q, \omega, T)]$ (figure 4.4). The dielectric function has peaks at the plasmon dispersion but it is also proportional to $\mathrm{Im}\chi(q, \omega)$. It therefore provides a measure of the weight of particle-hole excitations available to the plasmon. At the lowest temperature ($T = 0.05T_F$), there is little overlap with the electron-hole continuum. Consequently, the plasmon is lightly damped, giving a large magnitude over a small area that follows the dispersion. As the temperature increases, the plasmon acquires a lifetime (width) as it overlaps with the continuum and it can decay via particle hole excitations. This process is know as Landau damping. The result is a lower maximum amplitude, spread over a wider region of the plane.

The issue of plasmons in the double graphene layer system was considered by Das Sarma *et al.* [82] at zero temperature. By finding the poles of the interlayer

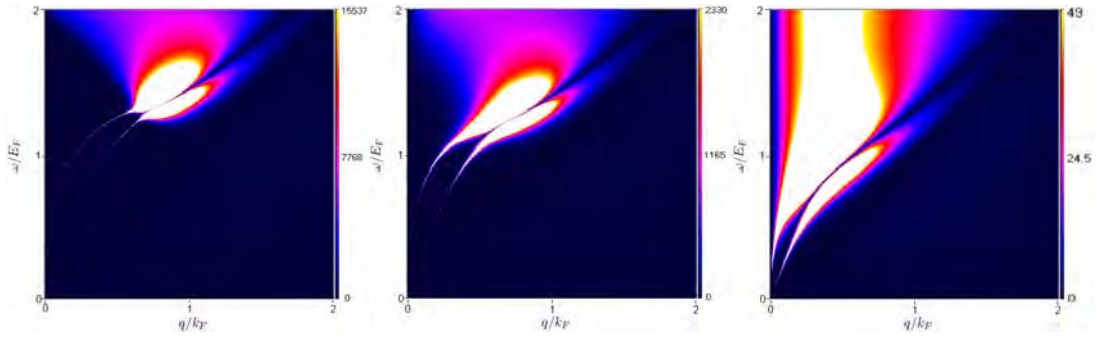

Figure 4.5: A density plot of Im $\left[\varepsilon_{12}^{-1}(q,\omega,T)\right]$ plotted at $k_F d = 2.5$ and for three different temperatures. From left to right $0.01T_F$, $0.5T_F$ and $0.2T_F$. As the temperature increases, the interband e-h continuum ($\omega > v_F q$) migrates towards the origin, progressively damping the coupled interlayer acoustic (out of phase) and optic (in phase) plasmons modes.

interaction (4.61), they found that at small q the plasmon dispersions have the form

$$\omega_+(\mathrm{q}) \approx \omega_0\sqrt{2q} \tag{4.71}$$

$$\omega_-(\mathrm{q}) \approx 2\omega_0\sqrt{d}q \tag{4.72}$$

where $\omega_0 = \sqrt{2e^2E_F/2\kappa}$ and $\omega_+(q)$, $\omega_-(q)$ are the optical (in phase) and acoustic (out of phase) plasmon modes, respectively. These show the same qualitative behaviour as plasmons in a 2DEG drag system (2.25).

To our knowledge, the case of finite temperature is yet to be considered and we do so now. Following the same path as above, in figure 4.5 we plot the imaginary part of the reciprocal of the interlayer dielectric function Im $\left[\varepsilon_{12}^{-1}(q,\omega,T)\right]$, the results of which are shown in the figure for three different temperatures at $k_F d = 2.5$. As for the single layer, as the temperature is increased the interband contribution migrates towards the origin, progressively damping both plasmon modes.

Of particular relevance to the drag effect is the way in which the plasmon modes vary as the interlayer distance changes. To this end, we show in figure 4.6 the function Im $\left[\varepsilon_{12}^{-1}(q,\omega,T)\right]$ for three difference layer separations d, at $T = 0.1T_F$. As

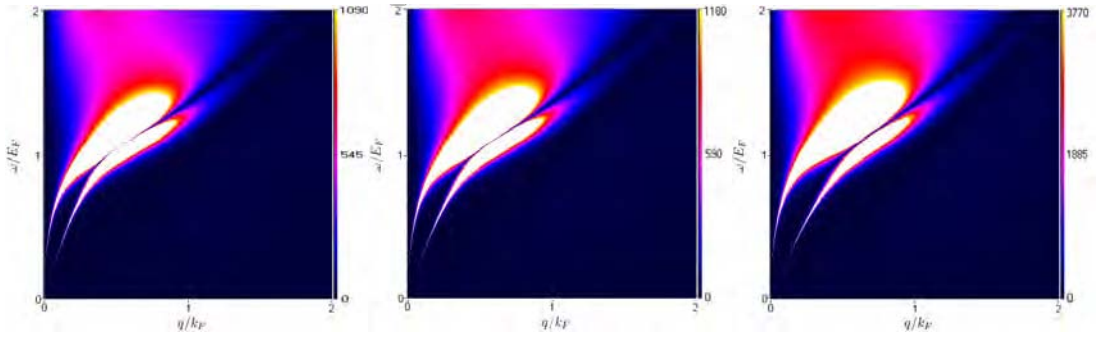

Figure 4.6: A density plot of $\mathrm{Im}\left[\varepsilon_{12}^{-1}(q,\omega,T)\right]$ plotted at $0.1T_F$ and for three different layer separations. From left to right $3.5k_F^{-1}$, $2.5k_F^{-1}$ and $1.5k_F^{-1}$. As the layer separation decreases the plasmon modes are seen to move further apart.

the layer separation increases, the acoustic plasmon mode is seen to move further away from the optical mode.

4.4 Limit of Low Temperature and Large Interlayer Spacing

In general, calculations of the drag resistivity must be carried out numerically. However, it is possible to obtain an analytic result in the limit of low temperature ($T \to 0$) and large interlayer spacing ($d^{-1} \ll k_F, q_{TF}$). In this limit, the dominant contribution to the drag resistivity comes from a region with small q and ω. To this end we recall the expression for the NLS in this limit (4.59)

$$\Gamma(q,\omega) \simeq \frac{4\tau_{tr} e\omega}{\pi v_F} \tag{4.73}$$

as well as that for the interlayer interaction (4.64)

$$U_{12}(q,\omega) \simeq \frac{\pi e^2 q}{q_{TF}^2 \sinh qd}. \tag{4.74}$$

We will now work toward an analytic expression for the drag resistivity by substituting (4.73) and (4.74) into the general expression for the drag conductivity (4.1)

$$\sigma_D = \frac{1}{16\pi k_B T} \sum_q \int_0^\infty \frac{\Gamma_1 \Gamma_2 \left|U_{12}(q,\omega)\right|^2}{\sinh^2(\omega/2k_BT)} d\omega. \tag{4.75}$$

Doing so, as well as converting the summation into an integral yields

$$\sigma_D = \frac{\tau_{tr}^2 e^6}{2k_BT q_{TF}^4 \pi^2 \upsilon_F^2} \int_0^\infty \int_0^\infty \frac{q^2\omega^2}{\sinh^2(qd)\sinh^2\left(\frac{\omega}{2k_BT}\right)} dq d\omega \tag{4.76}$$

Making use of the identity

$$\int_0^\infty \frac{x^p}{4\sinh^2\left(\frac{x}{2}\right)} dx = p!\zeta(p) \tag{4.77}$$

where $\zeta(p)$ is the Riemann Zeta function, we may perform the integrals over ω and q to give

$$\int_0^\infty \frac{\omega^2}{\sinh^2\left(\frac{\omega}{2k_BT}\right)} d\omega = \frac{8}{6}\pi^2 k_B^3 T^3 \tag{4.78}$$

and

$$\int_0^\infty \frac{q^3}{\sinh^2 qd} dq = \frac{6}{4d^4}\zeta(3). \tag{4.79}$$

Putting this all together yeids the final expression of the drag conductivity in the low temperature limit;

$$\sigma_D = \frac{\tau_{tr}^2 e^2 k_B^2 T^2 \zeta(3)}{\pi q_{TF}^4 \upsilon_F^2 d^4} \tag{4.80}$$

To convert (4.80) into a resistivity we must make use of the relation (2.4)

$$\rho_D \simeq -\frac{\sigma_D}{\sigma_{L1}\sigma_{L2}},$$

where σ_{L1} and σ_{L2} are the longitudinal conductivities given by [106]

$$\sigma_{11} = \sigma_{22} = \frac{e^2 E_F \tau_{tr}}{\pi}.$$

Reintroducing Plank's constant and writing the final expression in terms of q_{TF} we have for the drag resistivity

$$\rho_D = \frac{\hbar \pi e^2 k_B^2 T^2 \zeta(3)}{q_{TF}^4 \upsilon_F^2 d^4}. \tag{4.81}$$

To get agreement with [106], we expand two of the Thomas-Fermi wave-vectors by making the replacement $q_{TF}^2 = \left(4e^2 k_F/\upsilon_F\right)^2$. This yields,

$$\rho_D = \frac{\pi k_B^2 T^2 \zeta(3)}{16 e^2 q_{TF}^2 E_F^2 k_F^2 d^4}. \tag{4.82}$$

The drag resistivity in this limit therefore displays the same dependence on temperature ($\sim T^2$), layer separation ($\sim d^{-4}$) and density ($\sim n^{-3}$) as that of a 2DEG system (2.69), but is smaller in magnitude.

4.5 Numerical Results

Das Sarma *et al.* [106] numerically evaluated the zero temperature drag conductivity for a range of system parameters (figure 4.7). Their results showed qualitatively similar behaviour to a 2DEG system but with an order of magnitude increase in the strength of the drag conductivity. Calculating up to $0.2T_F$, they discovered no plasmon enhancement and indeed argued that none should be seen until $T \approx T_F$. Their argument was that since the intraband excitations are bounded by $\omega < \upsilon_F q$,

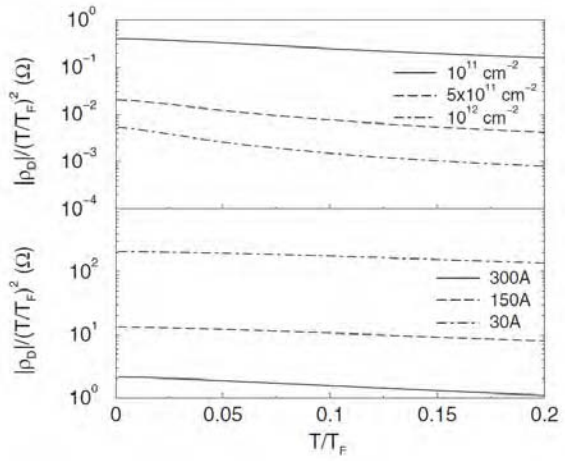

Figure 4.7: $|\rho_D|/(T/T_F)^2$ vs T/T_F for higher values of T up to $0.2T_F$. **Upper panel:** for fixed interlayer distance $d = 500\mathring{A}$ and different values of density $n = 10^{11}cm^{-2}$ (solid line), $5 \times 10^{11}cm^{-2}$ (dashed line), $10^{12}cm^{-2}$ (dot-dashed line), corresponding to $T_F = 431$, 963, 1361 K, respectively; **Lower panel**: for fixed density $n = 10^{11}cm^{-2}$ and different values of interlayer distance $d = 300\mathring{A}$ (solid line), $150\mathring{A}$ (dashed line), and $30\mathring{A}$ (dot-dashed line). Reproduced from [106].

any plasmons excitations would have to come from the intraband excitations. That these reside above an energy $\omega \approx E_F$ mean that there are only accessible by the drag integral (4.1) at temperatures approaching the Fermi energy.

We believe that this argument is flawed because it underestimates the rate at which the interband continuum migrates toward the origin with increasing temperature and therefore the extent to which the integrand acquires weight from the plasmon modes. As we can see from figure 4.1, by $0.2T_F$ it has weight well below $\omega = E_F$. Although relatively small, it is sufficient to pick up the plasmon modes strongly. In figure 4.8, we plot the full finite temperature integrand for five temperatures. It is clear that at $0.08T_F$ the finite temperature integrand has a significant enhancement from the plasmon modes, in contrast to the zero temperature result (figure 4.7). By $0.2T_F$ the modes are fully exposed, after which they are progressively Landau damped.

The above suggests that the drag rate will demonstrate a plasmon enhancement,

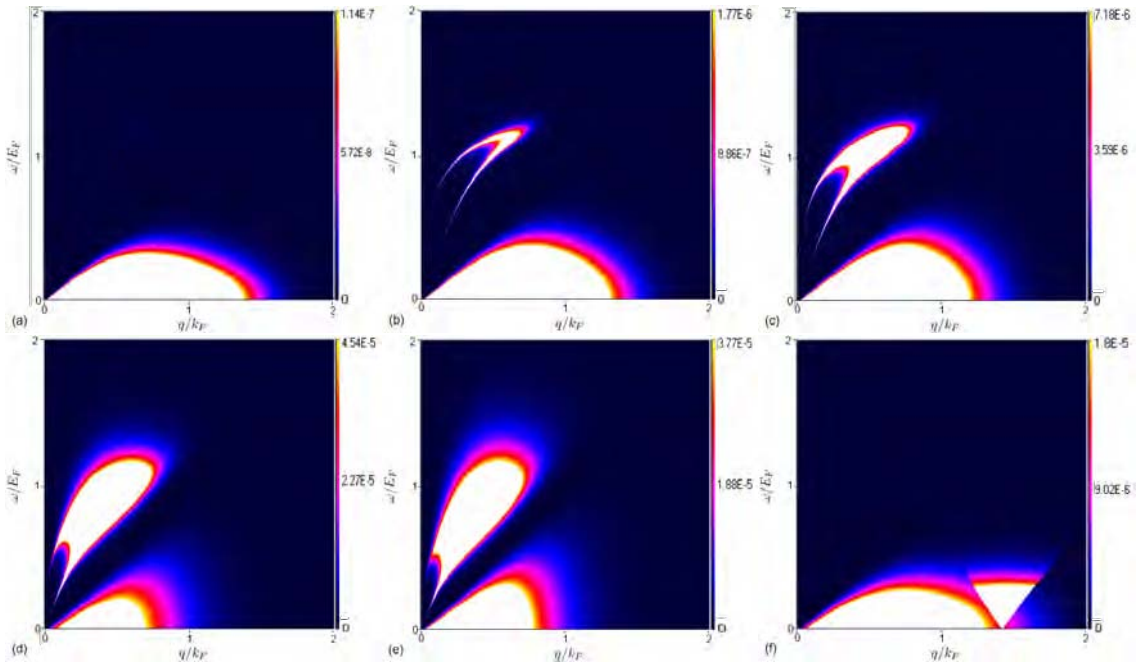

Figure 4.8: The *dimensionless* integrand of the drag conductivity (4.1) for $n = 1.5 \times 10^{-11} cm^{-2}$ and $d = 375$Å. (**a**)-(**e**): The full finite temperature integrand at $T = 0.06, 0.08, 0.1, 0.2, 0.3T_F$ respectively. (**f**): The zero temperature susceptibility and polarisation integrand of [106] at $T = 0.08T_F$. The full finite temperature integrand has a weight from the plasmon modes starting at around $0.08T_F$. By $0.2T_F$ the modes are fully exposed. In contrast, the integrand of [106], (**f**), that has almost no plasmon weighting at $0.08T_F$.

in contrast to the zero temperature prediction. Indeed, this is what we find and in figure 4.9 we numerically evaluate the drag conductivity, divided by T^2, for a range of carrier densities n and interlayer distances d. The enhancement of the drag effect due to plasmons is clearly demonstrated with a peak in the drag rate at approximately $0.2T_F$. This is in contrast to 2DEG drag which shows a plasmon peak at approximately $0.5T_F$ (figure 2.6). Since $0.2T_F$ corresponds to approximately room temperature, the plasmon enhancement to the graphene drag rate should be experimentally observable.

Of particular interest are the results plotted for a range of interlayer spacings (figure 4.9 (**a**)). As the distance is decreased, the plasmon peak decreases in relative height above the $T = 0$ level. By $d = 30$Å it does not rise above it. The drag resistivity integrand at $d = 30$Å is plotted in figure 4.10 for several temperatures. There are several key differences between these and those plotted for $d = 375$Å in figure 4.8. Foremost, at $d = 30$Å the dimensionless interlayer distance $k_F d = 0.53$ compared to $k_F d = 2.57$ at $d = 375$Å. The result is that the momentum cutoff of the drag integral (4.1) is much higher for $d = 30$Å and consequently we see that the integrand extends much further along the q axis. Consequently, when the plasmon modes are activated their contribution to the drag integrand is smaller relative to whole.

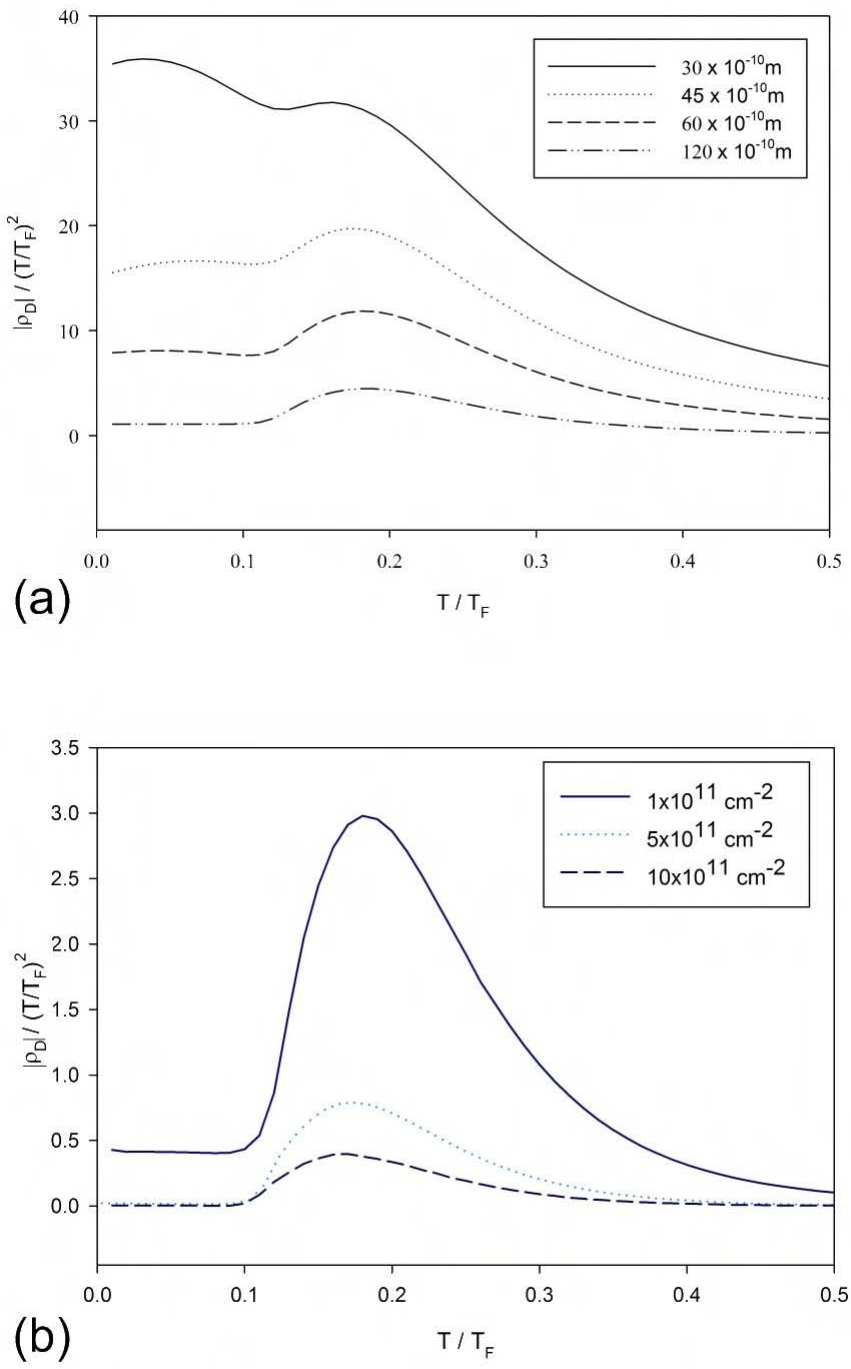

Figure 4.9: $|\rho_D| / (T/T_F)^2$ vs T/T_F. (**a**) Fixed density $n = 10^{12} cm^{-2}$ and several interlayer distances. The dominance of the plasmon peak is seen to decrease with decreasing interlayer distance. (**b**) Fixed interlayer distance $d = 500$Å and several densities. The plasmon enhancement is seen to increase with decreasing density. Both plots show a peak due to plasmon enhancement at $\approx 0.2T_F$ compared to $0.5T_F$ for 2DEG drag .

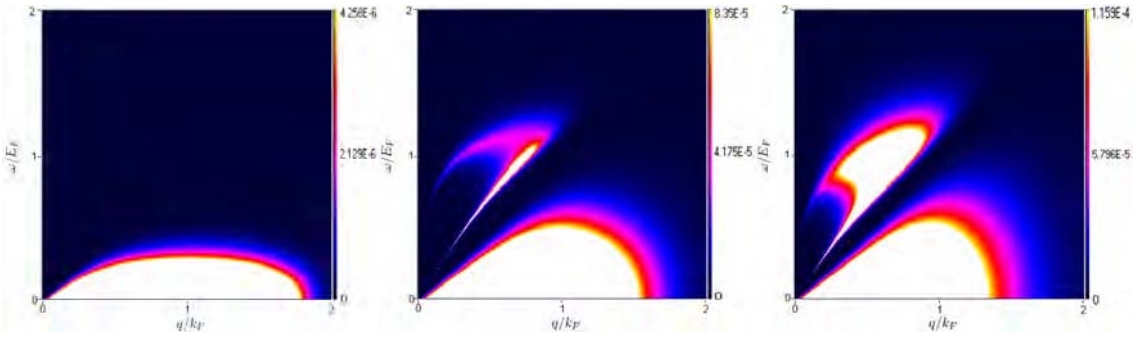

Figure 4.10: The *dimensionless* integrand of the drag conductivity (4.1) for $d = 30$Å ($k_F d = 0.53$) for three different temperatures. From left to right $0.05T_F$, $0.125T_F$, $0.2T_F$. The integrand extends far along the q axis at this distance. By $0.125T_F$, the acoustic plasmon is the dominant mode but its relative contribution to the overall integrand is less than for larger interlayer distances.

The second reason for this behaviour can be seen from figure 4.11 which shows several plots of the interlayer potential and non-linear susceptibility, at fixed ω. As the interlayer distance is decreased, the position and magnitude of the right (acoustic) mode moves to higher values of q and decreases rapidly in magnitude. The result of its decrease in magnitude is a decrease in its contribution to the drag rate. Conversely, by moving to higher values of q the plasmon enters a region of increasing non-linear susceptibility weight (see figure 4.11 (**f**)), thereby increasing its contribution to the drag rate. There is therefore a competition between the weight of the non-linear susceptibility at higher q and the decreasing plasmon magnitude there. This is in addition to the decrease in the plasmon's relative contribution to the drag integrand already mentioned. This explains the results at $d = 30$Å where the plasmons are much less dominant. Indeed, one would expect that for still smaller interlayer distances the plasmon contribution could become undetectable.

4.6 Conclusion

In this chapter, we performed a full finite temperature calculation of Coulomb drag between two graphene mono-layers. After a brief introduction, we derived a semi-analytic expression for the graphene non-linear susceptibility, representing the first original work of this thesis.

Following this, we used a semi-analytic expression for the finite temperature graphene polarisability (derived in [81]) to study, for the first time, the behaviour of finite temperature plasmons modes in the double layer graphene system.

In the final original calculation of this chapter, we combined the above results to calculate the finite temperature drag resistivity at various carrier densities and interlayer spacings. Our results showed that the drag effect is dominated by plasmons at around $0.2T_F$ (approximately room temperature) and should therefore be experimentally accessible. This is in contrast to a prediction made elsewhere [106] that suggests that none will be seen until $T \approx T_F$. For comparison, the plasmon contribution to drag between two dimensional electron gasses peaks at around $0.5T_F$ [8]. We then discussed the behaviour of the drag resistivity at very small interlayer distances (≈ 30Å) where the plasmon enhancement is weak, due to a competition between phase space terms and the strength and position of the plasmon peaks.

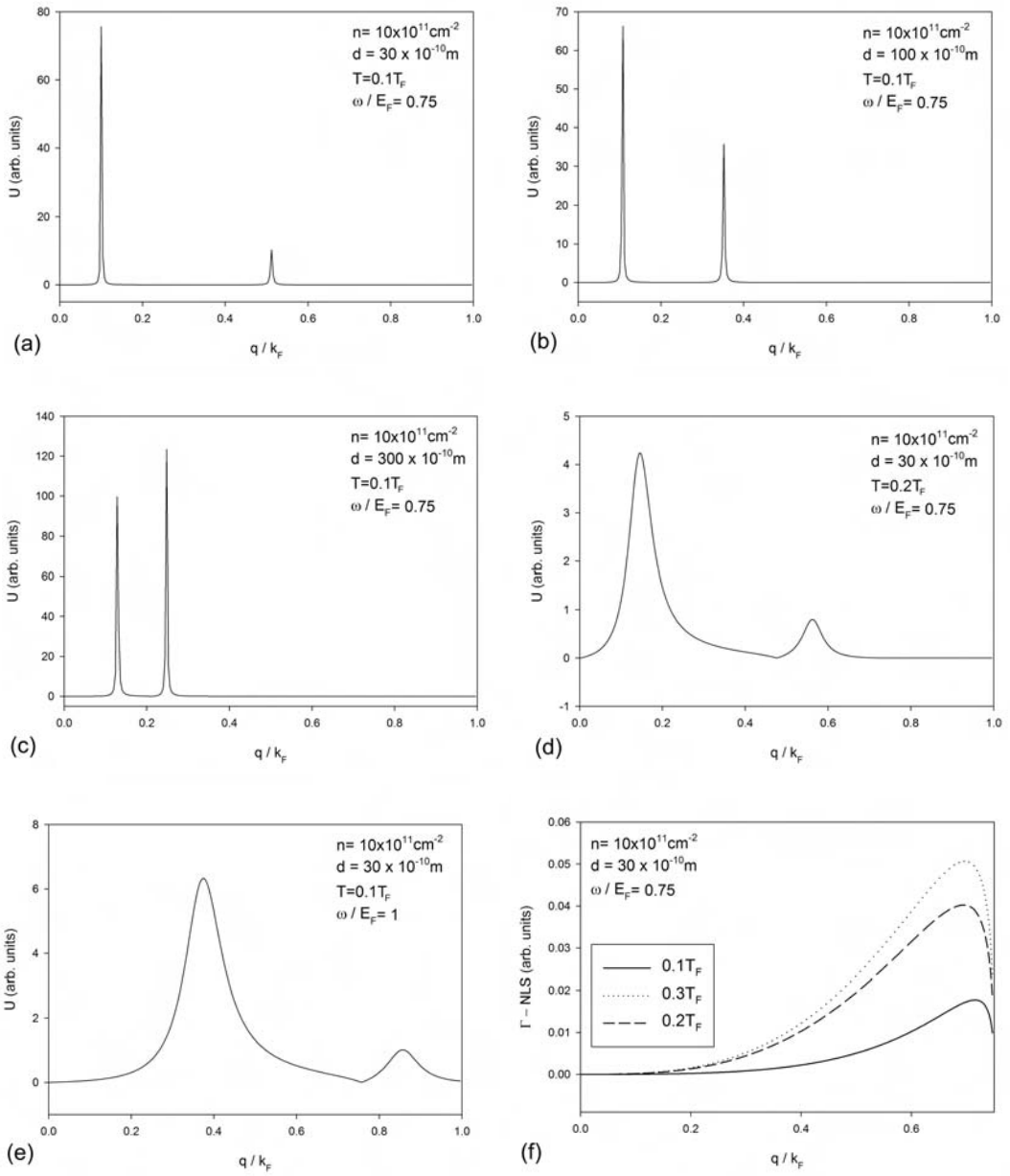

Figure 4.11: (**a**)-(**e**): The interlayer potential at fixed values of ω/E_F for several interlayer distances and temperatures. As the interlayer distance is increased the right plasmon mode is seen to exist at lower values of q and increase in magnitude relative to the left mode. As ω/E_F and T/T_F is increased the modes broaden as they are Landau damped. (**f**) The non-linear susceptibility at fixed ω/E_F for several temperatures. Most of the weight is at large q in the region of the left plasmon mode and is seen to increase as the temperature is increased.

Chapter 5

Graphene Bilayer Systems

In this chapter we investigate Coulomb drag between two graphene bilayers, arranged far enough apart so that there is no coupling between them. Throughout, we remain in the regime within which the low energy Hamiltonian of McCann *et al.* [85] is valid. Before numerically evaluating the drag conductivity itself we will perform two preliminary calculations, each an original work.

First, we will derive a semi-analytic expression for the finite temperature polarisability, re-deriving on the way the general expression of Das Sarma *et al.* [62]. We investigate both the single layer and coupled layer plasmon modes and upon numerical evaluation find them to be within the intra-band continuum, even at zero temperature. This is in contrast to the mono-layer case and will be key to interpreting the Coulomb drag results.

Second, with equation 2.82 as our starting point, we derive a general expression for the bilayer non-linear susceptibility (NLS). We arrive at a form identical to that for a mono-layer, but with the bilayer Berry's phase of 2π. This will lead us to derive a semi-analytic expression for the bilayer NLS which we evaluate numerically.

Following these preliminary calculation, we proceed by numerically evaluating

the drag resistivity of two graphene bilayers. We find that the low temperature behaviour is similar ($\sim T^2$) to that for 2DEGs and monolayers. However, in contrast to these the plasmon enhancement at intermediate temperature is strongly suppressed by Landau damping of the plasmon modes. This is a result of the plasmon modes being within the e-h continuum, even at zero temperature. We also find that the density and interlayer separation dependence of the position and width of the plasmon peak is stronger than for the 2DEG and monolayer systems. An explanation for this is suggested.

5.1 Introduction

The Coulomb drag effect between graphene bilayers is in some sense an intermediate case between the standard 2DEG and monolayer systems. With bilayers, we have a system within which the electronic spectrum is quadratic, as for a 2DEG. The difference of course is that the bilayer quasiparticles are chiral and one would expect this fact to result in a significant departure from the standard 2DEG behaviour. However, in contrast to the 2DEG system, it is not necessary to take into account a finite layer thickness and this simplifies the calculations somewhat. In addition, it is possible to study bilayer drag at the same small interlayer separations that were possible in the monolayer system. This is because the out of plane π orbitals no not begin to overlap until approximately 3.5Å [106]. Below this distance, the system will start to behave as a graphene quad-layer with properties more similar to that of bulk graphite.

A naive analysis of the system would suggest that compared to the monolayer system, the strength of the drag effect will be smaller with bilayers. The reason for

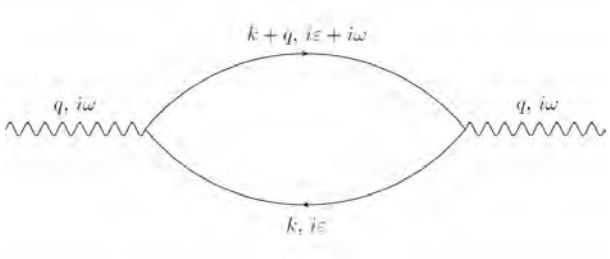

Figure 5.1: Feynman Diagram: The imaginary time polarisation bubble.

its size in the monolayer system can largely be traced to the vanishing density of states at the Dirac point, implying weak screening of the interlayer potential. This does not apply to the bilayer.

Throughout this chapter, we restrict ourselves to the regime in which the low energy Hamiltonian of McCann *et al.* [85] is valid. This amounts to restricting the range of electronic densities (n) to

$$1 \times 10^{-11} cm^{-2} < n < 4.36 \times 10^{12} cm^{-2}. \tag{5.1}$$

(see section 3.3.3). Fortunately, this range is typical to experiments on both 2DEG, monolayer and bilayer systems.

5.2 Polarisability

In the random phase approximation, the graphene bilayer polarisability is given by the bare bubble diagram (figure 5.1) [92]. Working in the finite temperature, imaginary frequency Matsubara formalism, the Feynman rules [17] give us for the polarisability,

$$\chi(q, i\omega) = -\sum_{\mathbf{k}} T \sum_{\varepsilon} \mathrm{tr} \left\{ \tilde{G}_{\mathbf{k}} (i\varepsilon) \tilde{G}_{\mathbf{k+q}} (i\varepsilon + i\omega) \right\}, \tag{5.2}$$

where T is the temperature $tr\{\}$ is the trace and the minus sign is from the Fermion loop. The Green's functions $G_{\mathbf{k}}(i\varepsilon) = (i\varepsilon - \hat{H}_{\mathbf{k}})^{-1}$ are 2×2 matrices in sub-lattice space, where $\hat{H}$ is the bilayer Hamiltonian (3.35). The calculation is greatly simplified by transforming to a basis in which the Hamiltonian and hence the Green's functions, are diagonal. As for the monolayer, the bilayer Hamiltonian is diagonal in the chiral basis, i.e eigenstates of the Hamiltonian are states of definite chirality and not pseudospin. The unitary matrix that transforms from the pseudospin to chiral basis is

$$U_{\mathbf{k}}^{\dagger} = \frac{1}{\sqrt{2}} \begin{pmatrix} e^{i2\phi_{\mathbf{k}}} & 1 \\ e^{i2\phi_{\mathbf{k}}} & -1 \end{pmatrix}, \tag{5.3}$$

where $\phi_{\mathbf{k}} = \tan^{-1}(k_y/k_x)$. We can therefore express (5.2) in the chiral basis as,

$$\chi(q, i\omega) = -\sum_{\mathbf{k}} T \sum_{\varepsilon} \mathrm{tr}\left\{ U_{\mathbf{k}}^{\dagger} G_{\mathbf{k}}(i\varepsilon)\, U_{\mathbf{k}} U_{\mathbf{k+q}}^{\dagger} G_{\mathbf{k+q}}(i\varepsilon + i\omega)\, U_{\mathbf{k+q}} \right\}. \tag{5.4}$$

Using the fact that the trace is invariant under cyclic permutations, we can write (5.4) as

$$\chi(q, i\omega) = -\sum_{\mathbf{k}} T \sum_{\varepsilon} \mathrm{tr}\left\{ G_{\mathbf{k}}(i\varepsilon)\, U_{\mathbf{k}} U_{\mathbf{k+q}}^{\dagger} G_{\mathbf{k+q}}(i\varepsilon + i\omega)\, U_{\mathbf{k+q}} U_{\mathbf{k}}^{\dagger} \right\}. \tag{5.5}$$

This allows us to define the operators

$$U_{+} = U_{\mathbf{k}} U_{\mathbf{k+q}}^{\dagger} = \frac{1}{2} \begin{pmatrix} e^{-i2\theta_{+}} + 1 & e^{-i2\theta_{+}} - 1 \\ e^{-i2\theta_{+}} - 1 & e^{-i2\theta_{+}} + 1 \end{pmatrix}, \tag{5.6}$$

$$U_{+}^{\dagger} = U_{\mathbf{k+q}} U_{\mathbf{k}}^{\dagger} = \frac{1}{2} \begin{pmatrix} e^{i2\theta_{+}} + 1 & e^{i2\theta_{+}} - 1 \\ e^{i2\theta_{+}} - 1 & e^{i2\theta_{+}} + 1 \end{pmatrix} \tag{5.7}$$

where $\theta_+ = \phi_{\mathbf{k+q}} - \phi_{\mathbf{k}}$ is the scattering angle. Expressing (5.5) in terms of these operators yields

$$\chi(q, i\omega) = -\sum_{\mathbf{k}} T \sum_{\varepsilon} \mathrm{tr}\left\{ G_{\mathbf{k}}\left(i\varepsilon\right) U_+ G_{\mathbf{k+q}}\left(i\varepsilon + i\omega\right) U_+^\dagger \right\}. \tag{5.8}$$

Employing the more compact notation $G^{ij}_{\mathbf{k+q}}(i\varepsilon + i\omega) \equiv G_1^{ij}$ and $G^{ij}_{\mathbf{k}}(i\varepsilon) \equiv G_2^{ij}$, where i and j label the rows and columns respectively, we will now calculate the trace explicitly by taking each term in turn from the right. Remembering that the Green's functions are now diagonal we have,

$$G_1 U_+^\dagger = \frac{1}{2}\begin{pmatrix} \left(e^{i2\theta_+}+1\right) G_1^{11}, & \left(e^{i2\theta_+}-1\right) G_1^{11} \\ \left(e^{i2\theta_+}-1\right) G_1^{22}, & \left(e^{i2\theta_+}+1\right) G_1^{22} \end{pmatrix}, \tag{5.9}$$

$$U_+ G_1 U_+^\dagger = \frac{1}{4}\begin{pmatrix} 2(1+\cos 2\theta_+)G_1^{11}+2(1-\cos 2\theta_+)G_1^{22}, & 2i\sin\theta_+ G_1^{11} - 2i\sin\theta_+ G_1^{22} \\ -2i\sin\theta_+ G_1^{11}+2i\sin\theta_+ G_1^{22}, & 2(1-\cos 2\theta_+)G_1^{11}+2(1+\cos 2\theta_+)G_1^{22} \end{pmatrix}, \tag{5.10}$$

$$G_2 U_+ G_1 U_+^\dagger = \frac{1}{2}\begin{pmatrix} (1+\cos 2\theta_+)G_2^{11}G_1^{11}+(1-\cos 2\theta_+)G_2^{11}G_1^{22} & - \\ - & (1-\cos 2\theta_+)G_2^{22}G_1^{11}+(1+\cos 2\theta_+)G_2^{22}G_1^{22} \end{pmatrix}. \tag{5.11}$$

Finally, taking the trace of (5.11) yields

$$\mathrm{tr}\left\{ G_2 U_+ G_1 U_+^\dagger \right\} = -\frac{1}{2}\sum_{\lambda\lambda'=\pm} G_{k+q,\lambda'}(i\varepsilon) G_{k+q,\lambda}(i\varepsilon + i\omega), \tag{5.12}$$

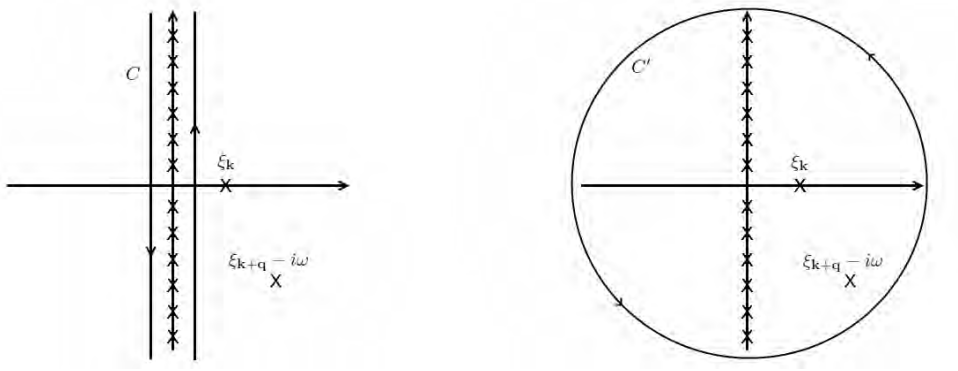

Figure 5.2: Contours in the complex frequency (ε) plane, C and C', used to calculate the energy summation of equation (5.13).

where we have used the notation $G^{11}_{\mathbf{k}}(i\varepsilon) \equiv G_{\mathbf{k},+}(i\varepsilon)$ and $G^{22}_{\mathbf{k}}(i\varepsilon) \equiv G_{\mathbf{k},-}(i\varepsilon)$. Substituting this into (5.8), the polarisation takes the form

$$\chi(q, i\omega) = -\frac{1}{2} \sum_{\lambda\lambda'=\pm} \sum_{\mathbf{k}} (1 + \lambda\lambda' \cos 2\theta)\, T \sum_{\varepsilon} G_{\mathbf{k},\lambda'}(i\varepsilon) G_{\mathbf{k}+\mathbf{q},\lambda}(i\varepsilon + i\omega). \qquad (5.13)$$

The summation over the frequency is evaluated using the standard techniques [17] of complex analysis, as follows. With polarisation now in terms of Green's functions of the form $G_{\mathbf{k}\lambda}(i\varepsilon) = (i\varepsilon - \xi_{\mathbf{k}\lambda})^{-1}$, we have

$$T \sum_{\varepsilon} G_{\mathbf{k},\lambda'}(i\varepsilon) G_{\mathbf{k}+\mathbf{q},\lambda}(i\varepsilon + i\omega) = T \sum_{\varepsilon} \frac{1}{(i\varepsilon - \xi_{\mathbf{k}\lambda'})\,(i\varepsilon + i\omega - \xi_{\mathbf{k}+\mathbf{q}\lambda})}. \qquad (5.14)$$

Note that the complex Fermi function, $n_F(z) = [\exp(z/T) + 1]^{-1}$, has poles at $z = i\varepsilon = i(2n+1)\pi T$, where n is an integer. Each pole has a residue $-T$, the result of which is to be able to write (5.14) via the residue theorem as

$$-T \sum_{\varepsilon} \frac{1}{(i\varepsilon - \xi_{\mathbf{k}\lambda'})\,(i\varepsilon + i\omega - \xi_{\mathbf{k}+\mathbf{q}\lambda})} = \frac{1}{2\pi i} \oint_C \frac{n_F(z)}{(z - \xi_{\mathbf{k}\lambda'})\,(z + i\omega - \xi_{\mathbf{k}+\mathbf{q}\lambda})}, \qquad (5.15)$$

where C is a contour enclosing the imaginary axis (figure 5.2). We now consider a new contour C', also shown in figure 5.2. It not only encloses the poles along the imaginary axis but also the two poles at $z_1 = \xi_{\mathbf{k}+\mathbf{q}\lambda} - i\omega$ and $z_2 = \xi_{\mathbf{k}\lambda'}$. The sum of the residues of these two poles is simply

$$\frac{n_F(\xi_{\mathbf{k},\lambda})}{\xi_{\mathbf{k}\lambda'} + i\omega - \xi_{\mathbf{k}+\mathbf{q}\lambda}} + \frac{n_F(\xi_{\mathbf{k}+\mathbf{q},\lambda} - i\omega)}{\xi_{\mathbf{k}\lambda'} + i\omega - \xi_{\mathbf{k}+\mathbf{q}\lambda}} = \frac{n_F(\xi_{\mathbf{k},\lambda}) - n_F(\xi_{\mathbf{k}+\mathbf{q},\lambda})}{i\omega + \xi_{\mathbf{k},\lambda'} - \xi_{\mathbf{k}+\mathbf{q},\lambda}}, \quad (5.16)$$

where in the last line we have used the fact that $n_F(\xi_{\mathbf{k}+\mathbf{q},\lambda} - i\omega) = n_F(\xi_{\mathbf{k}+\mathbf{q},\lambda})$ (the $-i\omega$ just adds an extra factor of $e^{-2\pi m i} = 1$ to the exponential in the denominator). Using (5.16), and the fact that as $C' \to \infty$ the contour $\oint_{C'} = 0$, we may once again use the residue theorem to write

$$\oint_{C'} F(z) n_F(z) = 0 = \frac{n_F(\xi_{\mathbf{k},\lambda}) - n_F(\xi_{\mathbf{k}+\mathbf{q},\lambda})}{i\omega + \xi_{\mathbf{k},\lambda} - \xi_{\mathbf{k}+\mathbf{q},\lambda}} - T \sum_{\varepsilon} \frac{1}{(i\varepsilon - \xi_{\mathbf{k}\lambda'})\,(i\varepsilon + i\omega - \xi_{\mathbf{k}+\mathbf{q}\lambda})}. \quad (5.17)$$

Therefore, we have

$$T \sum_{\varepsilon} \frac{1}{(i\varepsilon - \xi_{\mathbf{k}\lambda'})\,(i\varepsilon + i\omega - \xi_{\mathbf{k}+\mathbf{q}\lambda})} = \frac{n_F(\xi_{\mathbf{k},\lambda'}) - n_F(\xi_{\mathbf{k}+\mathbf{q},\lambda})}{i\omega + \xi_{\mathbf{k},\lambda'} - \xi_{\mathbf{k}+\mathbf{q},\lambda}}. \quad (5.18)$$

Substituting (5.18) into (5.13) gives

$$\chi(q, i\omega) = -\frac{1}{2} \sum_{\lambda\lambda'=\pm} \sum_{\mathbf{k}} (1 + \lambda\lambda' \cos 2\theta)\, \frac{n_F(\xi_{\mathbf{k},\lambda'}) - n_F(\xi_{\mathbf{k}+\mathbf{q},\lambda})}{i\omega + \xi_{\mathbf{k},\lambda'} - \xi_{\mathbf{k}+\mathbf{q},\lambda}}. \quad (5.19)$$

Finally, we analytically continue to real frequencies, $i\omega \to \omega + i\delta$, to yield

$$\chi(q, \omega) = -\frac{1}{2} \sum_{\lambda\lambda'=\pm} \sum_{\mathbf{k}} (1 + \lambda\lambda' \cos 2\theta)\, \frac{n_F(\xi_{\mathbf{k},\lambda'}) - n_F(\xi_{\mathbf{k}+\mathbf{q},\lambda})}{\omega + \xi_{\mathbf{k},\lambda'} - \xi_{\mathbf{k}+\mathbf{q},\lambda} + i\delta}. \quad (5.20)$$

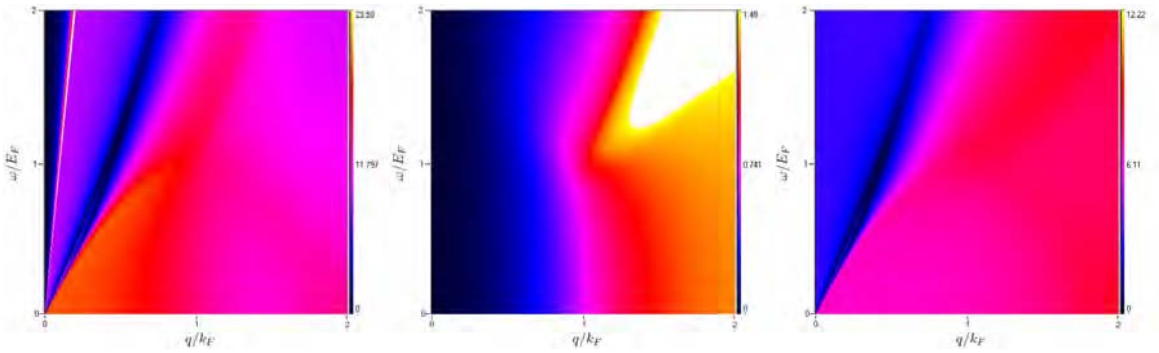

Figure 5.3: Three density plots showing the real part of the graphene bilayer polarisability $\mathrm{Re}\chi(q,\omega)$ as a function of ω and q, at $T = 0.05T_F$. **Left**: The intraband contribution. **Centre**: The interband contribution. **Right**: The combined contribution. The colour scale shows the value of $\mathrm{Re}\chi(q,\omega)$ in units of $N(E_F)$, where $N(E_F)$ is the density of states at the Fermi energy.

5.2.1 Finite Temperature Evaluation

In appendix C, we derive semi-analytic expressions for the finite temperature polarisability (5.20). The result is composed of intraband ($\lambda = \lambda'$) and interband ($\lambda \neq \lambda'$) parts, and is given by

$$\chi(x,y) = \chi^{Intra}(x,y) + \chi^{Inter}(x,y) \tag{5.21}$$

where

$$\mathrm{Im}\chi(x,y) = \mathrm{Im}\chi^{Intra} + \mathrm{Im}\chi^{Inter}, \qquad \mathrm{Re}\chi(x,y) = \mathrm{Re}\chi^{Inter}(x,y) + \mathrm{Re}\chi^{Inter}(x,y) \tag{5.22}$$

and

$$\mathrm{Im}\chi^{Intra} = \frac{m}{2\pi}\int_0^\infty dk \frac{[n_F(\xi_{\mathbf{k}-}) - n_F(\xi_{\mathbf{k}+})]\,(\eta_- + 2k^2)^2}{k\,(k^2+y)\,\sqrt{4k^2x^2 - \eta_-^2}}\theta(k^2 - s_-) - \{y \to y\}\,, \tag{5.23}$$

$$\mathrm{Im}\chi^{Inter} = \frac{m}{2\pi}\int_0^\infty dk\,[n_F(\xi_{\mathbf{k},-}) - n_F(\xi_{\mathbf{k},+})]\,\frac{\sqrt{(\eta_- + 2kx - 2k^2)(2k^2 + 2kx - \eta_-)}}{k\,(k^2 - y)}, \tag{5.24}$$

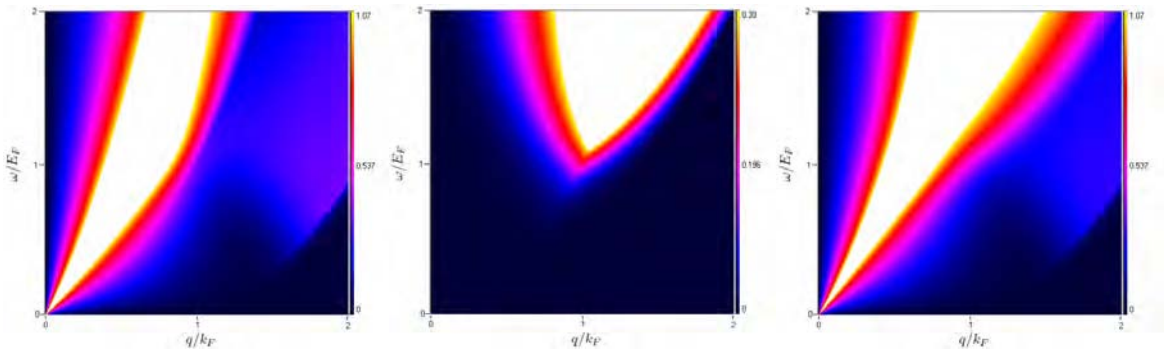

Figure 5.4: Three density plots showing the imaginary part of graphene bilayer polarisability, $\mathrm{Im}\chi(q,\omega)$, as a functon of ω and q at $T = 0.01T$. **Left**: The intraband contribution. **Centre**: The interband contribution. **Right**: The combined contribution. The fact that the contributions overlap is the main difference with the monolayer, where the individual contributions to the NLS occupy independent areas of the $q-\omega$ plane. The colour scale shows the value of $\mathrm{Im}\chi(q,\omega)$ in units of $N(E_F)$, where $N(E_F)$ is the density of states at the Fermi energy.

$$\mathrm{Re}\chi^{Intra} = \frac{m}{\pi}\int_0^\infty \frac{[n_F(\xi_{\mathbf{k}+}) - n_F(\xi_{\mathbf{k}-})]}{k\,(k^2+y)}\left[k^2 + y - \left|k^2 - x^2\right| - \frac{sgn(\eta_-)\theta\,(s_- - k^2)\,(2k^2+\eta_-)^2}{2x\sqrt{s_- - k^2}}\right] dk + \{y \to -y\}\,, \tag{5.25}$$

$$\mathrm{Re}\chi^{Inter} = \frac{m}{\pi}\int_0^\infty \frac{[n_F(\xi_{\mathbf{k}+}) - n_F(\xi_{\mathbf{k}-})]}{k(k^2+y)}\left[k^2 + y + \left|k^2 - x^2\right| - \frac{(2k^2-2k+\eta_+)\,(2k^2+2k+\eta_+)}{\sqrt{(2k^2+\eta_+)^2 - 4k^2x^2}}\theta\left(\left|2k^2+\eta\right| - 2kx\right)\right] dk + \{y \to -y\}\,. \tag{5.26}$$

In figure 5.3, we have numerically evaluated the real part of bilayer polarisability at $0.05T_F$. We have created density plots of the intraband, interband and combined contributions. Little information of use can be extracted from these as the real part's primary contribution to the drag effect is in its control over the plasmon dispersions.

Of greater interest are the density plots of the imaginary part of the polarisability (figure 5.4). These are important as they define the electron-hole continuum through which plasmons may decay. The bilayer continuum is quite different that of both the monolayer and 2DEG. The primary difference that the intraband and interband

contributions are not restricted to their own regions, as they were in the monolayer. The consequences of this are twofold. First, the intraband continuum may migrate over a wider are so that it is more likely to pick up a plasmon mode. Second, since the intraband and interband regions overlap, a plasmon mode decaying via electron-hole excitation within this region may do so simultaneously via both. This feature was missing in the monolayer and could result in increased Landau damping. The most immediate difference between the bilayer and 2DEG continuum is the existence of interband excitation which do not exist for a 2DEG.

5.3 The Non-Linear Susceptibility

As with any Coulomb drag calculation, the central quantity is the nonlinear susceptibility (NLS). In this section we will derive the graphene bilayer nonlinear susceptibility, starting from the general expression (2.82) in terms of Green's functions, derived in chapter 2. Following this, we will evaluate the angular part of the NLS and obtain a semi-analytic expression for finite temperature.

5.3.1 Derivation

The derivation presented in this section will lead us to the following expression for the graphene bilayer nonlinear susceptibility;

$$\Gamma(\mathbf{q},\omega) = \tau \sum_{\lambda,\lambda'=\pm} \sum_{\mathbf{k}} \left[J^{\mathbf{k}+\mathbf{q}}_{\lambda\lambda'} - J^{\mathbf{k}}_{\lambda\lambda'} \right] Im \left\{ (1+\lambda\lambda'\cos 2\theta_+) \frac{n_F(\varepsilon_{\mathbf{k},\lambda'}) - n_F(\varepsilon_{\mathbf{k}+\mathbf{q},\lambda})}{\omega + \varepsilon_{\mathbf{k},\lambda'} - \varepsilon_{\mathbf{k}+\mathbf{q},\lambda} + i\delta} \right\}, \tag{5.27}$$

where $\theta_+ = \phi_{\mathbf{k}+\mathbf{q}} - \phi_{\mathbf{k}}$ is the scattering angle and $J^{\mathbf{k}}_{\lambda,\lambda'}$ is the impurity dressed current operator in the chiral basis. Interestingly, the only difference between this

and the monolayer susceptibility is the argument of cos which is just θ_+ for the monolayer. The starting point of the derivation is the expression (2.82) for the nonlinear susceptibility in terms of advanced and retarded Green's functions;

$$\Gamma(\mathbf{q},\omega) = \frac{-1}{2\pi i}\sum_{\mathbf{k}}\int_{-\infty}^{\infty} d\varepsilon \left[n_F^{\varepsilon+\omega} - n_F^{\varepsilon}\right] \widetilde{G}^a_{\mathbf{k}}(\varepsilon)\widetilde{J}_{\mathbf{k}}\widetilde{G}^r_{\mathbf{k}}(\varepsilon)\left[\widetilde{G}^a_{\mathbf{k+q}}(\varepsilon+\omega) - \widetilde{G}^r_{\mathbf{k+q}}(\varepsilon+\omega)\right]$$

$$+ \{\mathbf{q}\to-\mathbf{q}, \omega\to-\omega\}\,. \tag{5.28}$$

The fact that the graphene bilayer Hamiltonian is a 2×2 matrix in pseudospin means that the corresponding Green's functions and operators are themselves 2×2 matrices. When calculating its nonlinear susceptibility we must therefore take the trace over the resulting matrix so that

$$\Gamma(\mathbf{q},\omega) = \frac{-1}{2\pi i}\sum_{\mathbf{k}}\int_{-\infty}^{\infty} d\varepsilon \left[n_F^{\varepsilon+\omega} - n_F^{\varepsilon}\right] tr\left\{\widetilde{G}^a_{\mathbf{k}}(\varepsilon)\widetilde{J}_{\mathbf{k}}\widetilde{G}^r_{\mathbf{k}}(\varepsilon)\left[\widetilde{G}^a_{\mathbf{k+q}}(\varepsilon+\omega) - \widetilde{G}^r_{\mathbf{k+q}}(\varepsilon+\omega)\right]\right\}$$

$$+ \{\mathbf{q}\to-\mathbf{q}, \omega\to-\omega\}\,. \tag{5.29}$$

The algebra involved in deriving (5.29) is greatly simplified by transforming to a basis in which the Hamiltonian and hence the Green's functions are diagonal (note that the current operator is not diagonal in this basis). Again, as for the monolayer the bilayer Hamiltonian is diagonal in the chiral basis, i.e eigenstates of the Hamiltonian are states of definite chirality and not pseudospin. The unitary matrix that transforms

from the pseudospin to chiral basis is

$$U_{\mathbf{k}}^{\dagger} = \frac{1}{\sqrt{2}} \begin{pmatrix} e^{i2\phi_{\mathbf{k}}} & 1 \\ e^{i2\phi_{\mathbf{k}}} & -1 \end{pmatrix} \tag{5.30}$$

where $\phi_{\mathbf{k}} = \tan^{-1}(k_y/k_x)$. We can therefore express (5.29) in the chiral basis by making the replacements

$$\widetilde{G}_{\mathbf{k}}(\varepsilon) = U_{\mathbf{k}}^{\dagger} G_{\mathbf{k}}(\varepsilon) U_{\mathbf{k}} \tag{5.31}$$

$$\widetilde{J}_{\mathbf{k}} = U_{\mathbf{k}}^{\dagger} J_{\mathbf{k}} U_{\mathbf{k}} \tag{5.32}$$

$$\widetilde{G}_{\mathbf{k}}(\varepsilon) - \widetilde{G}_{\mathbf{k}}(\varepsilon) = U_{\mathbf{k}}^{\dagger} \left[G_{\mathbf{k}}(\varepsilon) - G_{\mathbf{k}}(\varepsilon) \right] U_{\mathbf{k}} \tag{5.33}$$

so that

$$\begin{aligned} \Gamma(\mathbf{q},\omega) = \frac{-1}{2\pi i} \sum_{\mathbf{k}} \int_{-\infty}^{\infty} d\varepsilon \left[n_F^{\varepsilon+\omega} - n_F^{\varepsilon} \right] tr \Big\{ & U_{\mathbf{k}}^{\dagger} G_{\mathbf{k}}^{a}(\varepsilon) U_{\mathbf{k}} U_{\mathbf{k}}^{\dagger} J_{\mathbf{k}} U_{\mathbf{k}} U_{\mathbf{k}}^{\dagger} G_{\mathbf{k}}^{r}(\varepsilon) U_{\mathbf{k}} \\ & \times U_{\mathbf{k}+\mathbf{q}}^{\dagger} \left[G_{\mathbf{k}+\mathbf{q}}^{a}(\varepsilon+\omega) - G_{\mathbf{k}+\mathbf{q}}^{r}(\varepsilon+\omega) \right] U_{\mathbf{k}+\mathbf{q}} \Big\} + \{\mathbf{q} \to -\mathbf{q}, \omega \to -\omega\}. \end{aligned} \tag{5.34}$$

Making use of the fact that the trace is invariant under cyclic permutations of the operators and that by definition $U_{\mathbf{k}} U_{\mathbf{k}}^{\dagger} = \mathbf{I}$, we can write (5.34) as $\Gamma(\mathbf{q},\omega) = -\frac{1}{2\pi i} \sum_{\mathbf{k}} \int_{-\infty}^{\infty} d\varepsilon$

$$\begin{aligned} \times \quad & \Big(\left[n_F^{\varepsilon+\omega} - n_F^{\varepsilon} \right] \mathrm{tr} \Big\{ U_{\mathbf{k}} U_{\mathbf{k}+\mathbf{q}}^{\dagger} \left[G_{\mathbf{k}+\mathbf{q}}^{a}(\varepsilon+\omega) - G_{\mathbf{k}+\mathbf{q}}^{r}(\varepsilon+\omega) \right] U_{\mathbf{k}+\mathbf{q}} U_{\mathbf{k}}^{\dagger} G_{\mathbf{k}}^{a}(\varepsilon) J_{\mathbf{k}} G_{\mathbf{k}}^{r}(\varepsilon) \Big\} \\ + \quad & \left[n_F^{\varepsilon-\omega} - n_F^{\varepsilon} \right] \mathrm{tr} \Big\{ U_{\mathbf{k}} U_{\mathbf{k}-\mathbf{q}}^{\dagger} \left[G_{\mathbf{k}-\mathbf{q}}^{a}(\varepsilon-\omega) - G_{\mathbf{k}-\mathbf{q}}^{r}(\varepsilon-\omega) \right] U_{\mathbf{k}-\mathbf{q}} U_{\mathbf{k}}^{\dagger} G_{\mathbf{k}}^{a}(\varepsilon) J_{\mathbf{k}} G_{\mathbf{k}}^{r}(\varepsilon) \Big\} \Big) \end{aligned} \tag{5.35}$$

where we have explicitly written the second $\{\mathbf{q} \to -\mathbf{q}, \omega \to -\omega\}$ term. It is convenient at this stage to define two new operators U_+ and U_- where

$$U_+ = U_{\mathbf{k}} U^\dagger_{\mathbf{k+q}} = \frac{1}{2} \begin{pmatrix} e^{-i2\theta} + 1 & e^{-i2\theta} - 1 \\ e^{-i2\theta} - 1 & e^{-i2\theta} + 1 \end{pmatrix} \tag{5.36}$$

$$U_- = U_{\mathbf{k}} U^\dagger_{\mathbf{k-q}} = \frac{1}{2} \begin{pmatrix} e^{+i2\theta} + 1 & e^{+i2\theta} - 1 \\ e^{+i2\theta} - 1 & e^{+i2\theta} + 1 \end{pmatrix} \tag{5.37}$$

where $\theta = \phi_{\mathbf{k+q}} - \phi_{\mathbf{k}}$ is the scattering angle. It will be useful to note that $U_- = U_+^\dagger$. In terms of these new operators, (5.40) becomes

$$\Gamma(\mathbf{q},\omega) = -\tfrac{1}{2\pi i} \textstyle\sum_{\mathbf{k}} \int_{-\infty}^{\infty} d\varepsilon \Big(\big[n_F^{\varepsilon+\omega} - n_F^{\varepsilon} \big] tr \big\{ U_+ \big[G^a_{\mathbf{k+q}}(\varepsilon+\omega) - G^r_{\mathbf{k+q}}(\varepsilon+\omega) \big] \tag{5.38}$$

$$\times \quad U_+^\dagger G^a_{\mathbf{k}}(\varepsilon) J_{\mathbf{k}} G^r_{\mathbf{k}}(\varepsilon) \big\} + \big[n_F^{\varepsilon-\omega} - n_F^{\varepsilon} \big] tr \big\{ U_- \big[G^a_{\mathbf{k-q}}(\varepsilon-\omega) - G^r_{\mathbf{k-q}}(\varepsilon-\omega) \big] U_-^\dagger G^a_{\mathbf{k}}(\varepsilon) J_{\mathbf{k}} G^r_{\mathbf{k}}(\varepsilon) \big\} \Big)$$

We can simplify this expression somewhat by performing a change of variables $\varepsilon \to \varepsilon + \omega$ in the second term. This yields

$$\Gamma(\mathbf{q},\omega) = \frac{-1}{2\pi i} \sum_{\mathbf{k}} \int_{-\infty}^{\infty} d\varepsilon \left[n_F^{\varepsilon+\omega} - n_F^{\varepsilon} \right] \Big[tr \left\{ U_+ \left[G^a_{\mathbf{k+q}}(\varepsilon+\omega) - G^r_{\mathbf{k+q}}(\varepsilon+\omega) \right] \right. \tag{5.39}$$

$$\left. \times \quad U_+^\dagger G^a_{\mathbf{k}}(\varepsilon) J_{\mathbf{k}} G^r_{\mathbf{k}}(\varepsilon) \right\} - \mathrm{tr} \left\{ U_- \left[G^a_{\mathbf{k-q}}(\varepsilon) - G^r_{\mathbf{k-q}}(\varepsilon) \right] U_-^\dagger G^a_{\mathbf{k}}(\varepsilon+\omega) J_{\mathbf{k}} G^r_{\mathbf{k}}(\varepsilon+\omega) \right\} \Big] .$$

Furthermore, we can introduce the spectral function $A_{\mathbf{k}}(\omega)$, which is in fact a diagonal matrix, via the identity [10]

$$G^a_{\mathbf{k}}(\omega) - G^r_{\mathbf{k}}(\omega) = iA_{\mathbf{k}}(\omega) \tag{5.40}$$

so that

$$\begin{aligned}\Gamma &= -\frac{1}{2\pi}\sum_{\mathbf{k}}\int_{-\infty}^{\infty} d\varepsilon \left[n_F^{\varepsilon+\omega} - n_F^{\varepsilon}\right]\Big[\mathrm{tr}\left\{U_+ A_{\mathbf{k}+\mathbf{q}}(\varepsilon+\omega)U_+^\dagger G^a_{\mathbf{k}}(\varepsilon) J_{\mathbf{k}} G^r_{\mathbf{k}}(\varepsilon)\right\} \\ &\quad -\mathrm{tr}\left\{U_- A_{\mathbf{k}-\mathbf{q}}(\varepsilon)U_-^\dagger G^a_{\mathbf{k}}(\varepsilon+\omega) J_{\mathbf{k}} G^r_{\mathbf{k}}(\varepsilon+\omega)\right\}\Big].\end{aligned} \tag{5.41}$$

The next stage is to evaluate the trace. After some lengthy algebra that is nonetheless greatly simplified by the use of the chiral basis, we arrive at

$$\Gamma = -\frac{1}{2\pi}\sum_{\mathbf{k}}\int_{-\infty}^{\infty} d\varepsilon \left[n_F^{\varepsilon+\omega} - n_F^{\varepsilon}\right]\left[T_1 + T_2 - T_3 - T_4\right] = \tag{5.42}$$

where

$$\begin{aligned}4T_1 &= A^{11}_{\mathbf{k}-\mathbf{q}}(\varepsilon)\left\{\left[e^{i2\theta}+1\right]\left[e^{-i2\theta}+1\right]J^{11}_{\mathbf{k}} G^{11,a}_{\mathbf{k}}(\varepsilon+\omega) G^{11,r}_{\mathbf{k}}(\varepsilon+\omega) + \left[e^{i2\theta}+1\right]\left[e^{-i2\theta}-1\right]J^{12}_{\mathbf{k}} G^{22,a}_{\mathbf{k}}(\varepsilon+\omega) G^{11,r}_{\mathbf{k}}(\varepsilon+\omega)\right\} \\ &\quad + A^{22}_{\mathbf{k}-\mathbf{q}}(\varepsilon)\left\{\left[e^{i2\theta}-1\right]\left[e^{-i2\theta}-1\right]J^{11}_{\mathbf{k}} G^{11,a}_{\mathbf{k}}(\varepsilon+\omega) G^{11,r}_{\mathbf{k}}(\varepsilon+\omega) + \left[e^{i2\theta}-1\right]\left[e^{-i2\theta}+1\right]J^{21}_{\mathbf{k}} G^{22,a}_{\mathbf{k}}(\varepsilon+\omega) G^{11,r}_{\mathbf{k}}(\varepsilon+\omega)\right\},\end{aligned}$$

$$4T_2 = A^{11}_{\mathbf{k-q}}(\varepsilon)\Big\{\big[e^{i2\theta}-1\big]\big[e^{-i2\theta}+1\big]J^{21}_{\mathbf{k}}G^{11,a}_{\mathbf{k}}(\varepsilon+\omega)G^{22,r}_{\mathbf{k}}(\varepsilon+\omega)+\big[e^{i2\theta}-1\big]\big[e^{-i2\theta}-1\big]J^{22}_{\mathbf{k}}G^{22,a}_{\mathbf{k}}(\varepsilon+\omega)G^{22,r}_{\mathbf{k}}(\varepsilon+\omega)\Big\}$$

$$+A^{22}_{\mathbf{k-q}}(\varepsilon)\Big\{\big[e^{i2\theta}+1\big]\big[e^{-i2\theta}-1\big]J^{21}_{\mathbf{k}}G^{11,a}_{\mathbf{k}}(\varepsilon+\omega)G^{22,r}_{\mathbf{k}}(\varepsilon+\omega)+\big[e^{i2\theta}+1\big]\big[e^{-i2\theta}+1\big]J^{22}_{\mathbf{k}}G^{22,a}_{\mathbf{k}}(\varepsilon+\omega)G^{22,r}_{\mathbf{k}}(\varepsilon+\omega)\Big\},$$

$$4T_3 = A^{11}_{\mathbf{k+q}}(\varepsilon+\omega)\Big\{\big[e^{-i2\theta}+1\big]\big[e^{i2\theta}+1\big]J^{11}_{\mathbf{k}}G^{11,a}_{\mathbf{k}}(\varepsilon)G^{11,r}_{\mathbf{k}}(\varepsilon)+\big[e^{-i2\theta}+1\big]\big[e^{+i2\theta}-1\big]J^{12}_{\mathbf{k}}G^{22,a}_{\mathbf{k}}(\varepsilon)G^{11,r}_{\mathbf{k}}(\varepsilon)\Big\}$$

$$+A^{22}_{\mathbf{k+q}}(\varepsilon+\omega)\Big\{\big[e^{-i2\theta}-1\big]\big[e^{+i2\theta}-1\big]J^{11}_{\mathbf{k}}G^{11,a}_{\mathbf{k}}(\varepsilon)G^{11,r}_{\mathbf{k}}(\varepsilon)+\big[e^{-i2\theta}-1\big]\big[e^{i2\theta}+1\big]J^{21}_{\mathbf{k}}G^{22,a}_{\mathbf{k}}(\varepsilon)G^{11,r}_{\mathbf{k}}(\varepsilon)\Big\},$$

$$4T_4 = A^{11}_{\mathbf{k+q}}(\varepsilon+\omega)\Big\{\big[e^{-i2\theta}-1\big]\big[e^{i2\theta}+1\big]J^{21}_{\mathbf{k}}G^{11,a}_{\mathbf{k}}(\varepsilon)G^{22,r}_{\mathbf{k}}(\varepsilon)+\big[e^{i2\theta}-1\big]\big[e^{-i2\theta}-1\big]J^{22}_{\mathbf{k}}G^{22,a}_{\mathbf{k}}(\varepsilon)G^{22,r}_{\mathbf{k}}(\varepsilon)\Big\}$$

$$+A^{22}_{\mathbf{k+q}}(\varepsilon+\omega)\Big\{\big[e^{-i2\theta}+1\big]\big[e^{i2\theta}-1\big]J^{21}_{\mathbf{k}}G^{11,a}_{\mathbf{k}}(\varepsilon)G^{22,r}_{\mathbf{k}}(\varepsilon)+\big[e^{-i2\theta}+1\big]\big[e^{i2\theta}+1\big]J^{22}_{\mathbf{k}}G^{22,a}_{\mathbf{k}}(\varepsilon)G^{22,r}_{\mathbf{k}}(\varepsilon)\Big\}.$$

To proceed, we take the high density, non-interacting limit by replacing the spectral functions with δ functions so that

$$A^{ii}_{\mathbf{k}}(\varepsilon) \equiv 2\pi\delta(\varepsilon - \xi_{\mathbf{k},i}), \tag{5.43}$$

where $\xi_{\mathbf{k},\lambda} = \lambda v_F k$ is the bilayer dispersion. We can do likewise with the Green's

function products by employing the useful identity [?]

$$G^{ii,a}_{\mathbf{k}}(\omega)G^{jj,r}_{\mathbf{k}}(\omega) = \quad 2\tau\delta(\varepsilon - \xi_{\mathbf{k}}) \quad i = j \tag{5.44}$$

$$= \quad 2\tau\delta(\varepsilon - \xi_{\mathbf{k},i})\delta(\xi_{\mathbf{k},i} - \xi_{\mathbf{k},j}) \quad i \neq j, \tag{5.45}$$

where τ is the impurity scattering rate. The consequence of (5.45) is that since $\xi_{\mathbf{k},i} = \xi_{\mathbf{k},j}$ only at $k = 0$, and we are ultimately integrating over $\mathbf{k}$, terms proportional to products of Green's functions where $i \neq j$ vanish. These terms all involve off-diagonal elements of the current operator and so, perhaps surprisingly, only diagonal elements of the current operator contribute to the non-linear susceptibility. Employing the notation $\xi_{\mathbf{k},1} \equiv \xi_{\mathbf{k},+}$, $\xi_{\mathbf{k},2} \equiv \xi_{\mathbf{k},-}$ and making use of the following identities

$$\left[e^{i2\theta} + 1\right]\left[e^{-i2\theta} + 1\right] = 2\left(1 + \cos 2\theta\right), \tag{5.46}$$

$$\left[e^{i2\theta} - 1\right]\left[e^{-i2\theta} - 1\right] = 2\left(1 - \cos 2\theta\right), \tag{5.47}$$

the above considerations give for the non-linear susceptibility

$$\Gamma = -\tau \sum_{\mathbf{k}} \int_{-\infty}^{\infty} d\varepsilon \left[n_F^{\varepsilon+\omega} - n_F^{\varepsilon}\right]\left[T_1 + T_2 - T_3 - T_4\right], \tag{5.48}$$

where

$$T_1 \quad = \quad (1 + \cos 2\theta)\, J^{+}_{\mathbf{k}}\delta(\varepsilon - \xi_{\mathbf{k}-\mathbf{q},+})\delta(\varepsilon + \omega - \xi_{\mathbf{k}+}) + (1 - \cos 2\theta)\, J^{+}_{\mathbf{k}}\delta(\varepsilon - \xi_{\mathbf{k}-\mathbf{q},-})\delta(\varepsilon + \omega - \xi_{\mathbf{k}+})$$

$$T_2 = (1-\cos 2\theta)\, J_{\mathbf{k}}^{-}\delta(\varepsilon-\xi_{\mathbf{k}-\mathbf{q},+})\delta(\varepsilon+\omega-\xi_{\mathbf{k}-}) + (1-\cos 2\theta)\, J_{\mathbf{k}}^{-}\delta(\varepsilon-\xi_{\mathbf{k}-\mathbf{q},+})\delta(\varepsilon+\omega-\xi_{\mathbf{k}-})$$

$$T_3 = (1+\cos 2\theta)\, J_{\mathbf{k}}^{+}\delta(\varepsilon+\omega-\xi_{\mathbf{k}+\mathbf{q},+})\delta(\varepsilon-\xi_{\mathbf{k}+}) + (1-\cos 2\theta)\, J_{\mathbf{k}}^{+}\delta(\varepsilon+\omega-\xi_{\mathbf{k}+\mathbf{q},-})\delta(\varepsilon-\xi_{\mathbf{k}+})$$

$$T_4 = (1-\cos 2\theta)\, J_{\mathbf{k}}^{-}\delta(\varepsilon+\omega-\xi_{\mathbf{k}+\mathbf{q},+})\delta(\varepsilon-\xi_{\mathbf{k}-}) + (1+\cos 2\theta)\, J_{\mathbf{k}}^{-}\delta(\varepsilon+\omega-\xi_{\mathbf{k}+\mathbf{q},-})\delta(\varepsilon-\xi_{\mathbf{k}-})$$

We now evaluate the energy integral of (5.48) via the identity [5]

$$\int_{-\infty}^{\infty} d\varepsilon \delta\left(\varepsilon-\alpha\right)\delta\left(\varepsilon-\beta\right) f\left(\varepsilon\right) = \delta\left(\alpha-\beta\right) f(\varepsilon).$$

This yields

$$\Gamma = -\tau \sum_{\mathbf{k}} \left[T_1 + T_2 - T_3 - T_4\right], \tag{5.49}$$

where

$$\begin{aligned} T_1 &= \left[n_F\left(\xi_{\mathbf{k},+}\right) - n_F\left(\xi_{\mathbf{k}-\mathbf{q},+}\right)\right] C_+ J_{\mathbf{k}}^{+}\delta(\omega-\xi_{\mathbf{k},+}+\xi_{\mathbf{k}-\mathbf{q},+}) \\ &+ \left[n_F\left(\xi_{\mathbf{k},+}\right) - n_F\left(\xi_{\mathbf{k}-\mathbf{q},-}\right)\right] C_- J_{\mathbf{k}}^{+}\delta(\omega-\xi_{\mathbf{k},+}+\xi_{\mathbf{k}-\mathbf{q},-}) \end{aligned}$$

$$\begin{aligned} T_2 &= \left[n_F\left(\xi_{\mathbf{k},-}\right) - n_F\left(\xi_{\mathbf{k}-\mathbf{q},+}\right)\right] C_- J_{\mathbf{k}}^{-}\delta(\omega-\xi_{\mathbf{k},-}+\xi_{\mathbf{k}-\mathbf{q},+}) \\ &+ \left[n_F\left(\xi_{\mathbf{k},-}\right) - n_F\left(\xi_{\mathbf{k}-\mathbf{q},+}\right)\right] C_- J_{\mathbf{k}}^{-}\delta(\omega-\xi_{\mathbf{k},-}+\xi_{\mathbf{k}-\mathbf{q},+}) \end{aligned}$$

$$\begin{aligned} T_3 &= \left[n_F\left(\xi_{\mathbf{k}+\mathbf{q},+}\right) - n_F\left(\xi_{\mathbf{k},+}\right)\right] C_+ J_{\mathbf{k}}^{+}\delta(\omega+\xi_{\mathbf{k},+}-\xi_{\mathbf{k}+\mathbf{q},+}) \\ &+ \left[n_F\left(\xi_{\mathbf{k}+\mathbf{q},-}\right) - n_F\left(\xi_{\mathbf{k},+}\right)\right] C_- J_{\mathbf{k}}^{+}\delta(\omega+\xi_{\mathbf{k},+}-\xi_{\mathbf{k}+\mathbf{q},-}) \end{aligned}$$

$$\begin{aligned} T_4 &= \left[n_F\left(\xi_{\mathbf{k}+\mathbf{q},+}\right) - n_F\left(\xi_{\mathbf{k},-}\right)\right] C_- J^-_{\mathbf{k}} \delta(\omega + \xi_{\mathbf{k},-} - \xi_{\mathbf{k}+\mathbf{q},+}) \\ &+ \left[n_F\left(\xi_{\mathbf{k}+\mathbf{q},-}\right) - n_F\left(\xi_{\mathbf{k},-}\right)\right] C_+ J^-_{\mathbf{k}} \delta(\omega + \xi_{\mathbf{k},-} - \xi_{\mathbf{k}+\mathbf{q},-}). \end{aligned}$$

and $C_\pm = 1 \pm \cos 2\theta$. Proceeding by making a change of variables $\mathbf{k} \to -\mathbf{k} - \mathbf{q}$ in T_1 and T_2, and making us of the symmetries $\xi_{\mathbf{k}\lambda} = \xi_{-\mathbf{k},\lambda}$ and $J_{\mathbf{k}} = J_{-\mathbf{k}}$, we have

$$\begin{aligned} T_1 &= \left[n_F\left(\xi_{\mathbf{k}+\mathbf{q},+}\right) - n_F\left(\xi_{\mathbf{k},+}\right)\right] (1 + \cos 2\theta)\, J^+_{\mathbf{k}+\mathbf{q}} \delta(\omega + \xi_{\mathbf{k},+} - \xi_{\mathbf{k}+\mathbf{q},+}) \\ &+ \left[n_F\left(\xi_{\mathbf{k}+\mathbf{q},+}\right) - n_F\left(\xi_{\mathbf{k},-}\right)\right] (1 - \cos 2\theta)\, J^+_{\mathbf{k}+\mathbf{q}} \delta(\omega + \xi_{\mathbf{k},-} - \xi_{\mathbf{k}+\mathbf{q},+}) \quad (5.50) \end{aligned}$$

$$\begin{aligned} T_2 &= \left[n_F\left(\xi_{\mathbf{k}+\mathbf{q},-}\right) - n_F\left(\xi_{\mathbf{k},+}\right)\right] (1 - \cos 2\theta)\, J^-_{\mathbf{k}} \delta(\omega + \xi_{\mathbf{k},+} + \xi_{\mathbf{k}+\mathbf{q},-}) \\ &+ \left[n_F\left(\xi_{\mathbf{k}+\mathbf{q},-}\right) - n_F\left(\xi_{\mathbf{k},+}\right)\right] (1 - \cos 2\theta)\, J^-_{\mathbf{k}} \delta(\omega + \xi_{\mathbf{k},+} + \xi_{\mathbf{k}-\mathbf{q},-}). \quad (5.51) \end{aligned}$$

We can now write the non-linear susceptibility in the compact form

$$\Gamma(\mathbf{q},\omega) = \tau \sum_{\lambda,\lambda'=\pm} \sum_{\mathbf{k}} \left[J^{\mathbf{k}+\mathbf{q}}_{\lambda} - J^{\mathbf{k}}_{\lambda}\right] \mathrm{Im}\left\{(1 + \lambda\lambda' \cos 2\theta) \frac{n_F(\varepsilon_{\mathbf{k},\lambda'}) - n_F(\varepsilon_{\mathbf{k}+\mathbf{q},\lambda})}{\omega + \varepsilon_{\mathbf{k},\lambda'} - \varepsilon_{\mathbf{k}+\mathbf{q},\lambda} + i\delta}\right\}, \quad (5.52)$$

where $J^{\mathbf{k}}_{\lambda,\lambda'} = 2\lambda \frac{\tau_{tr}}{\tau} e v_F \cos\phi_{\mathbf{k}}$ is the impurity dressed current operator in the chiral basis.

5.3.2 Evaluation

We will now partially evaluate the bilayer nonlinear susceptibility and obtain a semi-analytic expression for finite temperature. Our starting point is equation 5.52;

$$\Gamma(\mathbf{q},\omega) = \tau \sum_{\lambda,\lambda'=\pm} \sum_{\mathbf{k}} \left[J_{\lambda}^{\mathbf{k+q}} - J_{\lambda'}^{\mathbf{k}} \right] \mathrm{Im} \left\{ (1+\lambda\lambda' \cos 2\theta) \frac{n_F(\varepsilon_{\mathbf{k},\lambda'}) - n_F(\varepsilon_{\mathbf{k+q},\lambda})}{\omega + \varepsilon_{\mathbf{k},\lambda'} - \varepsilon_{\mathbf{k+q},\lambda} + i\delta} \right\} \tag{5.53}$$

where $\theta = \phi_{\mathbf{k+q}} - \phi_{\mathbf{k}}$ is the scattering angle and $J_{\lambda}^{\mathbf{k}} \equiv J_{\lambda,\lambda'}^{\mathbf{k}} \delta_{\lambda\lambda'} = 2\lambda \frac{\tau_{tr}}{\tau} e v_F \cos\phi_{\mathbf{k}}$. The angles $\phi_{\mathbf{k}}$ and $\phi_{\mathbf{k+q}}$ are measured with respect to an axis parallel to the current direction, which we shall choose as the x-axis. Since we are summing over $\mathbf{k}$, we may for convenience choose the vector $\mathbf{q}$ to be parallel to that axis so that

$$\cos\phi_{\mathbf{k+q}} = \frac{(\mathbf{k}+\mathbf{q})\cdot\hat{\mathbf{x}}}{|\mathbf{k}+\mathbf{q}|} \equiv \frac{(\mathbf{k}+\mathbf{q})\cdot\mathbf{q}}{|\mathbf{k}+\mathbf{q}|\,|\mathbf{q}|} = \frac{k\cos\theta + q}{\sqrt{k^2+q^2+2kq\cos\theta}}, \tag{5.54}$$

$$\cos\phi_{\mathbf{k}} = \frac{\mathbf{k}\cdot\hat{\mathbf{x}}}{|\mathbf{k}|} \equiv \frac{\mathbf{k}\cdot\mathbf{q}}{|\mathbf{k}|\,|\mathbf{q}|} = \cos\theta. \tag{5.55}$$

The difference of current operators in (5.53) can therefore be written in terms of θ as

$$J_{\lambda}^{\mathbf{k+q}} - J_{\lambda}^{\mathbf{k}} == 2e\lambda v_F \frac{\tau_{tr}}{\tau} \left(\frac{\sqrt{k^2+q^2+2kq\cos\theta}\,(k\cos\theta+q)}{\sqrt{k^2+q^2+2kq\cos\theta}} - k\cos\theta \right) = 2e\lambda v_F \frac{\tau_{tr}}{\tau} q \tag{5.56}$$

$$J_{\lambda}^{\mathbf{k+q}} - J_{-\lambda}^{\mathbf{k}} = 2e\lambda v_F \frac{\tau_{tr}}{\tau} \left(\frac{\sqrt{k^2+q^2+2kq\cos\theta}\,(k\cos\theta+q)}{\sqrt{k^2+q^2+2kq\cos\theta}} + k\cos\theta \right) = 2e\lambda v_F \frac{\tau_{tr}}{\tau} (q+2k\cos\theta) \tag{5.57}$$

5.3.2.1 Intraband

For the intraband contribution ($\lambda = \lambda'$) we have

$$\Gamma^{Intra}(q,\omega) = \frac{2\tau_{tr}eq}{m}\sum_{\lambda=\pm}\sum_{\mathbf{k}}\lambda \mathrm{Im}\left\{(1+\cos 2\theta)\frac{n_F(\varepsilon_{\mathbf{k},\lambda}) - n_F(\varepsilon_{\mathbf{k}+\mathbf{q},\lambda})}{\omega + \varepsilon_{\mathbf{k},\lambda} - \varepsilon_{\mathbf{k}+\mathbf{q},\lambda} + i\delta}\right\}. \quad (5.58)$$

It is clear that (5.58) is closely related to the imaginary part of intraband contribution of the polarisability (5.20)

$$\chi(q,\omega) = -\frac{1}{2}\sum_{\lambda\lambda'=\pm}\sum_{\mathbf{k}}(1+\lambda\lambda'\cos 2\theta)\,\frac{n_F(\xi_{\mathbf{k},\lambda'}) - n_F(\xi_{\mathbf{k}+\mathbf{q},\lambda})}{\omega + \xi_{\mathbf{k},\lambda'} - \xi_{\mathbf{k}+\mathbf{q},\lambda} + i\delta}. \quad (5.59)$$

via

$$\Gamma^{Intra}(q,\omega) = -4\frac{\tau_{tr}e}{m}q\left\{\mathrm{Im}\chi^{++}(q,\omega) - \mathrm{Im}\chi^{--}(q,\omega)\right\} \quad (5.60)$$

where, as before,

$$\chi^{\lambda\lambda'}(q,\omega) = -\frac{1}{2}\sum_{\mathbf{k}}(1+\lambda\lambda'\cos 2\theta)\,\frac{n_F(\xi_{\mathbf{k},\lambda'}) - n_F(\xi_{\mathbf{k}+\mathbf{q},\lambda})}{\omega + \xi_{\mathbf{k},\lambda'} - \xi_{\mathbf{k}+\mathbf{q},\lambda} + i\delta}. \quad (5.61)$$

Using (C.0.61),

$$\mathrm{Im}\chi^{Intra} = \frac{m}{2\pi}\int_0^\infty dk\frac{\left[n_F(\xi_{\mathbf{k}-}) - n_F(\xi_{\mathbf{k}+})\right]\left(\eta_- + 2k^2\right)^2}{k\left(k^2+y\right)\sqrt{4k^2x^2-\eta_-^2}}\theta(k^2-s_-) - \{y\to y\}, \quad (5.62)$$

Γ^{Intra} may be written in the semi-analytic form

$$\Gamma^{Intra}(x,y) = -\gamma x\int_0^\infty dk\frac{\left[n_F(\xi_{\mathbf{k}-}) + n_F(\xi_{\mathbf{k}+})\right]\left(\eta_- + 2k^2\right)^2}{k\left(k^2+y\right)\sqrt{4k^2x^2-\eta_-^2}}\theta(k^2-s_-) - \{y\to y\}. \quad (5.63)$$

where $x = q/k_F$ $y = \omega/E_F$ and $\gamma = \frac{2\tau_{tr}ek_F}{\pi}$

5.3.2.2 Interband

For the intraband contribution ($\lambda \neq \lambda'$), the situation is slightly more complicated. We have

$$\Gamma^{Inter}(q,\omega) = 2\tau_{tr} e v_F \sum_{\lambda \neq \lambda'} \sum_{\mathbf{k}} \lambda(q+2k\cos\theta) \mathrm{Im}\left\{ (1+\cos 2\theta) \frac{n_F(\varepsilon_{\mathbf{k},\lambda}) - n_F(\varepsilon_{\mathbf{k}+\mathbf{q},\lambda})}{\omega + \varepsilon_{\mathbf{k},\lambda} - \varepsilon_{\mathbf{k}+\mathbf{q},\lambda} + i\delta} \right\}. \tag{5.64}$$

The terms proportional to the q and $2k\cos\theta$, which we shall label $\Gamma^{Inter}_{(1)}$ and $\Gamma^{Inter}_{(2)}$ respectively, will again be closely related to the polarisability. We find that

$$\begin{aligned} \Gamma^{Inter}_{(1)}(q,\omega) &= 2\tau_{tr} e v_F \sum_{\lambda \neq \lambda'} \sum_{\mathbf{k}} \lambda q \mathrm{Im}\left\{ (1+\cos 2\theta) \frac{n_F(\varepsilon_{\mathbf{k},\lambda}) - n_F(\varepsilon_{\mathbf{k}+\mathbf{q},\lambda})}{\omega + \varepsilon_{\mathbf{k},\lambda} - \varepsilon_{\mathbf{k}+\mathbf{q},\lambda} + i\delta} \right\} & (5.65) \\ &= -4\tau_{tr} e v_F q \left\{ \mathrm{Im}\chi^{+-}(q,\omega) - \mathrm{Im}\chi^{-+}(q,\omega) \right\}, & (5.66) \end{aligned}$$

where, as before,

$$\chi^{\lambda\lambda'}(q,\omega) = -\frac{1}{2} \sum_{\mathbf{k}} (1 + \lambda\lambda' \cos 2\theta) \frac{n_F(\xi_{\mathbf{k},\lambda'}) - n_F(\xi_{\mathbf{k}+\mathbf{q},\lambda})}{\omega + \xi_{\mathbf{k},\lambda'} - \xi_{\mathbf{k}+\mathbf{q},\lambda} + i\delta}. \tag{5.67}$$

The $\mathrm{Im}\chi^{-+}$ term vanishes identically because all terms in its δ functions are positive. Therefore, we only need to consider $\mathrm{Im}\chi^{+-}$,

$$\mathrm{Im}\chi^{+-} = \frac{m}{2\pi} \int_0^\infty dk \left[n_F(\xi_{\mathbf{k},-}) - n_F(\xi_{\mathbf{k},+}) \right] \frac{\sqrt{(\eta_- + 2kx - 2k^2)(2k^2 + 2kx - \eta_-)}}{k\,(k^2 - y)}, \tag{5.68}$$

we have

$$\Gamma^{Inter}_{(1)}(x,y) = -\gamma x \int_0^\infty dk\,[n_F(\xi_{\mathbf{k},-}) - n_F(\xi_{\mathbf{k},+})]\,\frac{\sqrt{(\eta_- + 2kx - 2k^2)(2k^2 + 2kx - \eta_-)}}{k\,(k^2 - y)}, \tag{5.69}$$

where $\gamma = \frac{2m\tau_{tr}ek_F v_F}{\pi}$.

We now calculate

$$\Gamma^{Inter}_{(2)}(q,\omega) = 2\tau_{tr}ev_F \sum_{\lambda\neq\lambda'}\sum_{\mathbf{k}} \lambda \mathrm{Im}\left\{2k\cos\theta(1+\cos 2\theta)\frac{n_F(\varepsilon_{\mathbf{k},\lambda}) - n_F(\varepsilon_{\mathbf{k}+\mathbf{q},\lambda})}{\omega + \varepsilon_{\mathbf{k},\lambda} - \varepsilon_{\mathbf{k}+\mathbf{q},\lambda} + i\delta}\right\}, \tag{5.70}$$

by noting that in appendix C we calculated the angular integral by first making the substitution $Q = 2k^2 + 2kx\cos\theta$ and then evaluating the integrand at $y - x^2$. Under these operations

$$2k\cos\theta = \frac{Q - 2k^2}{x} = \frac{y - x^2 - 2k^2}{x} \equiv \frac{\eta_- - 2k^2}{x}. \tag{5.71}$$

Noting that once more the $\mathrm{Im}\chi^{-+}$ term vanishes, we simply multiply (5.69) by (5.71) to get

$$\Gamma^{Inter}_{(2)}(x,y) = -\frac{\gamma}{x}\int_0^\infty dk\,[n_F(\xi_{\mathbf{k},-}) - n_F(\xi_{\mathbf{k},+})]\left(\eta_- - 2k^2\right)\frac{\sqrt{(\eta_- + 2kx - 2k^2)(2k^2 + 2kx - \eta_-)}}{k\,(k^2 - y)}. \tag{5.72}$$

Summing (5.69) and (5.72) together to give for the interband contribution to yield

$$\Gamma^{Inter}(x,y) = \frac{\gamma}{x}\int_0^\infty dk\,[n_F(\xi_{\mathbf{k},-}) - n_F(\xi_{\mathbf{k},+})]\left(2k^2 - y\right)\frac{\sqrt{(\eta_- + 2kx - 2k^2)(2k^2 + 2kx - \eta_-)}}{k\,(k^2 - y)}, \tag{5.73}$$

where $\gamma = \frac{2m\tau_{tr}ek_F v_F}{\pi}$.

5.3.2.3 Summary and Discussion

We have shown that the graphene bilayer susceptibility is closely related to the imaginary part of the polarisability Imχ, more so than for a monolayer because the bilayer current operator is proportional to k. The reason that it is not direction proportional to Imχ, as it is for a 2DEG, is a consequence of the chirality. Overall, we have shown that

$$\Gamma^{Intra}(x,y) = \Gamma^{Intra}(x,y) + \Gamma^{Intra}(x,y) \tag{5.74}$$

with

$$\Gamma^{Intra}(x,y) = -\gamma x \int_0^\infty dk \frac{\left[n_F(\xi_{\mathbf{k}-}) + n_F(\xi_{\mathbf{k}+})\right]\left(\eta_- + 2k^2\right)^2}{k\left(k^2+y\right)\sqrt{4k^2x^2-\eta_-^2}}\theta(k^2-s_-) - \{y \to y\}\,. \tag{5.75}$$

$$\Gamma^{Inter}(x,y) = \frac{\gamma}{x}\int_0^\infty dk \left[n_F(\xi_{\mathbf{k},-}) - n_F(\xi_{\mathbf{k},+})\right]\left(2k^2-y\right)\frac{\sqrt{(\eta_- + 2kx - 2k^2)(2k^2+2kx-\eta_-)}}{k\left(k^2-y\right)}, \tag{5.76}$$

where $x = q/k_F$ $y = \omega/E_F$ and $\gamma = \frac{2\tau_{tr}ek_F v_F}{\pi}$.

In figure 5.5 we numerically evaluate the NLS and show density plots for the intraband, interband and combined contributions. As was the case for the imaginary part of the polarisability (figure 5.4), the two contributions overlap. Of particular not is the rich structure of the full NLS. This results from the relative sign of the intraband and interband contributions and is not seen in either a 2DEG or monolayer.

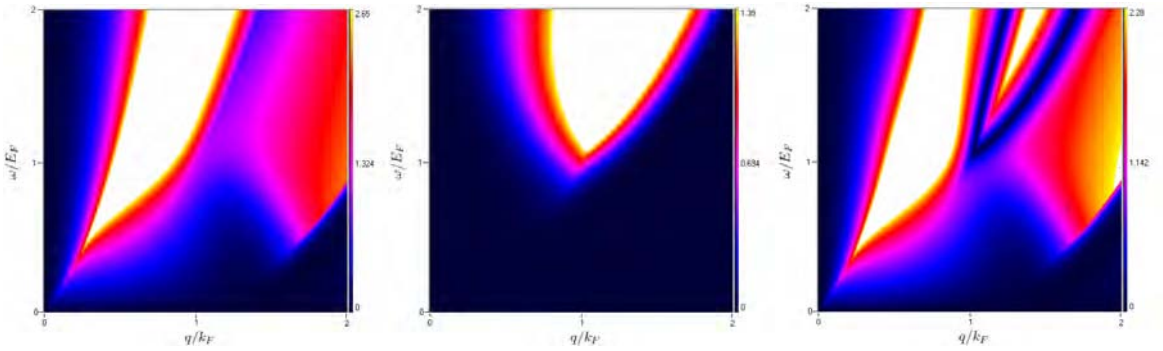

Figure 5.5: Three density plots showing the graphene bilayer nonlinear susceptibility (5.74), at $T = 0.1T_F$. **Left**: The intraband contribution. **Middle**: The interband contribution. **Right**: The combined contribution. The rich structure of the combined contribution arises because of their relative sign. This highlights the main difference with the monolayer, where the individual contributions to the NLS occupy independent areas of the $q - \omega$ plane. The colour scale shows the value of the nonlinear susceptibility in units of $\gamma = \frac{2\tau_{tr} e k_F v_F}{\pi}$.

5.4 Plasmons

Key to the analysis of the drag effect is an understanding of a system's plasmon modes. Since we have not obtained a fully analytic zero temperature expression for the polarisability, it is not possible to find the low q dispersions. However, as we did for the monolayer, we may investigate their dependence on temperature and interlayer distance by analysing the imaginary part of the inverse dielectric function $\mathrm{Im}\left[\varepsilon^{-1}(x, y, T)\right]$. To this end, in figure 5.6 we show a density plot of $\mathrm{Im}\left[\varepsilon^{-1}(x, y, T)\right]$ for a single bilayer at $T = 0.01T_F$. Surprisingly, the plasmon mode lies completely within the continuum. This implies that a non-decaying plasmon can not exist within this regime since it will immediately decay via Landau damping.

Of importance to the Coulomb drag system is the question of where the coupled plasmon modes begin to overlap with the e-h continuum. This will determine to what extent the drag effect is enhanced by them. In figure 5.7 we show density plots of $\mathrm{Im}\left[\varepsilon_{12}^{-1}(x, y, T)\right]$, where ε_{12} is the effective interlayer dielectric constant, for a range of temperatures and interlayer spacings, with a density of $10^{11} cm^{-1}$. Again, the

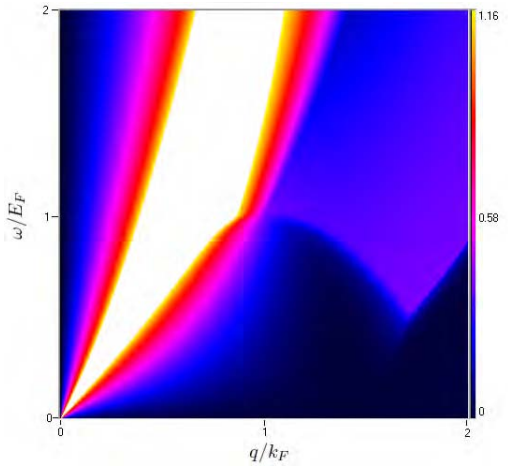

Figure 5.6: The bilayer plasmon mode. The density plot shows $Im\left[\varepsilon^{-1}(q,\omega,T)\right]$, where $\varepsilon(q,\omega,T)$ is the dielectric function, at $T = 0.01T_F$. The plasmon mode lies completely within the e-h continuum, implying that any plasmon will quickly decay via Landau damping.

plasmon modes are immediately well within the electron hole continuum, implying heavy Landau damping. In addition, the position of the modes appear to be more weakly dependent on the interlayer separation than for a monolayer and have a quite different shape (figure 4.6). By $0.5T_F$, the modes have completely merged.

5.5 The Drag Conductivity

Combining the result obtained so far, we now calculate the bilayer system drag density for a range of variables. In figure 5.8 we plot $|\rho_D|/(T/T_F)^2$ vs T/T_F for a fixed carrier density of $n = 10^{11}cm^{-2}$ and a range interlayer distances. There is very little plasmon enhancement to the drag resistivity as might have been expected from the result for the polarisability and NLS. In addition, the plasmon peak is seen to drift to higher temperatures and broaden, as the interlayer distance is decreased. Although this effect is present in the monolayer, is it is much more pronounced here. At very low temperatures, the drag rate appears to go as T^2, as it does for the 2DEG

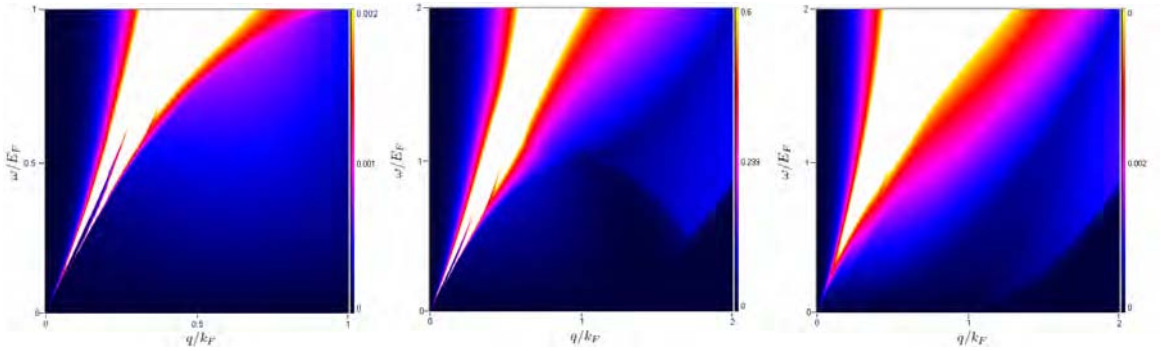

Figure 5.7: Coupled plasmon modes. Three plots showing the inverse interlayer dielectric constant $\mathrm{Im}\left[\varepsilon_{12}^{-1}(q,\omega,T)\right]$, at a carrier density of $n = 10^{11}cm^{-2}$, and for several temperatures and interlayer spacings d. **Left**: $T = 0.001T_F$, $d = 1000$Å. **Centre**: $T = 0.001T_F$, $d = 100$Å. **Right**: $T = 0.05T_F$, $d = 100$Å. Both modes are well within the e-h continuum, implying heavy Landau damping. The modes appear to be more weakly dependent on layer separation that their monolayer counterparts. Already by $0.5T_F$ the modes have merged.

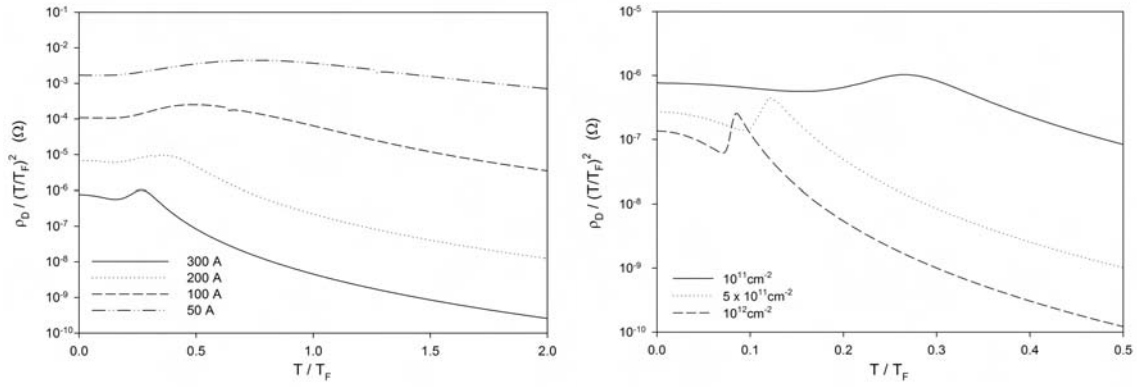

Figure 5.8: $|\rho_D|/(T/T_F)^2$ vs T/T_F **Left:** A fixed carrier density of $n = 10^{11}cm^{-2}$ and a range interlayer distances. **Right:** A fixed interlayer spacing of 300Åand a range of carrier densities. The peak due to plasmon enhancement is far less pronounced than it is for the monolayer system, a consequence of Landau damping. Unlike the monolayer system, the plasmon peak is seen to drift to higher temperatures and broaden as the interlayer distance and / or density is decreased.

and monolayer systems.

A similar description holds for the density dependence. In figure 5.8 we also plot $|\rho_D| / (T/T_F)^2$ vs T/T_F for an interlayer spacing of 300Å and a range of carrier densities. Again, little plasmon enhancement is seen as a result of heavy Landau damping and the drag rate appears to go as T^2 at low temperatures. The plasmon peak is seen to drift to higher temperatures and broaden, as the interlayer density is decreased.

The general behaviour appear to be for the plasmon enhancement peak to shift to higher temperatures and broaden as the interlayer distance or density is decreased. This is illustrated in figure 5.9, showing density plots of the drag integrand (2.91). The two density plots are for systems with carrier densities of $n = 10\dot{1}^{1}cm^{-2}$and $n = 10^{12}cm^{-2}$, corresponding to Fermi temperatures of $51K$ and $514K$ respectively. The higher density system is dominated by the damped plasmon modes at this temperature, whereas the lower density system is not. This is a consequence of both the relatively weak plasmon modes and the difference in Fermi temperatures. That the plasmon peaks are much weaker than in the monolayer system can be seen by comparing the interlayer potential of the bilayer and monolayer at fixed ω, as shown in figure 5.10. The monolayer plasmon peak is seen to be an order of magnitude higher and they are much more clearly defined. The broadening in the bilayer case is evidence for Landau damping..

The observed behaviour may be explained as follows. The consequence of the large difference in Fermi temperatures is to make far more of the ω axis available to the higher density system. This is due to the $\sinh^{-1}(\hbar\omega/k_BT)$ term in the denominator of the drag integral (2.91) restricting the region of integration to a few T_F. This results in the higher density system being able to pick up the region contain-

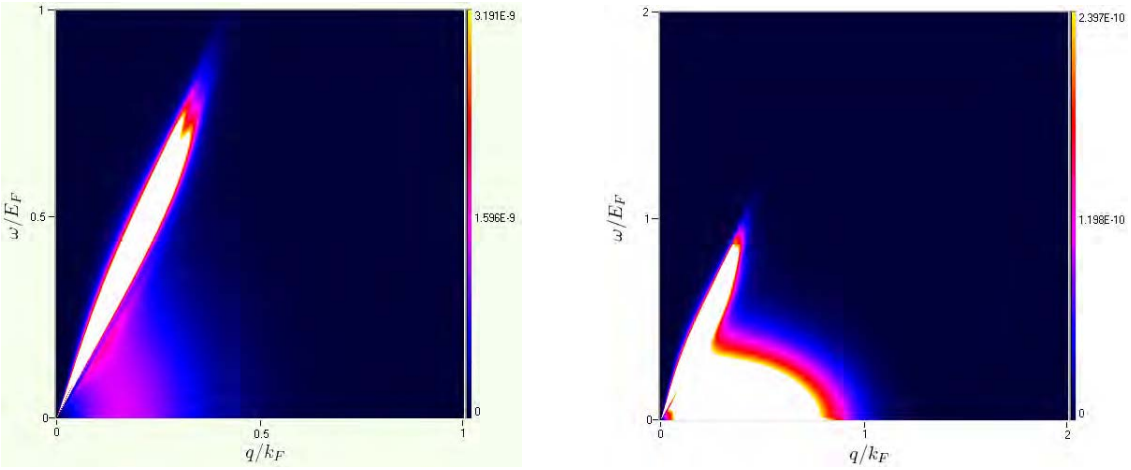

Figure 5.9: Density plots of the *dimensionless* integrand of equation (2.91) at $T = 0.08T_F$ and $d = 300$Å, and carrier densities of $10^{12}cm^{-2}$ (**left**) and $10^{11}cm^{-2}$ (**right**). The higher density system is clearly dominated by the plasmon modes in comparison to the low density system.

ing the plasmon modes, and become dominated by them, more quickly. Although this applies equally to the monolayer system, the fact that the plasmon modes here are weaker means that the system must capture more of the ω axis in order to be dominated by plasmons. Therefore the trend for lower plasmon peak temperatures with increasing density is enhanced in the bilayer system. A similar argument holds for increasing interlayer distances.

5.6 Conclusion and Further Work

In this chapter, we have studied Coulomb drag in a double graphene bilayer system. This has led us to derive semi-analytic finite temperature expressions for both the bilayer polarisability and non-linear susceptibility. Both of these calculations represent original work. Using these results, we have calculated the drag resistivity and found that the plasmon enhancement in a bilayer system is strongly suppressed by Landau damping in comparison to 2DEG and monolayer systems. This is a con-

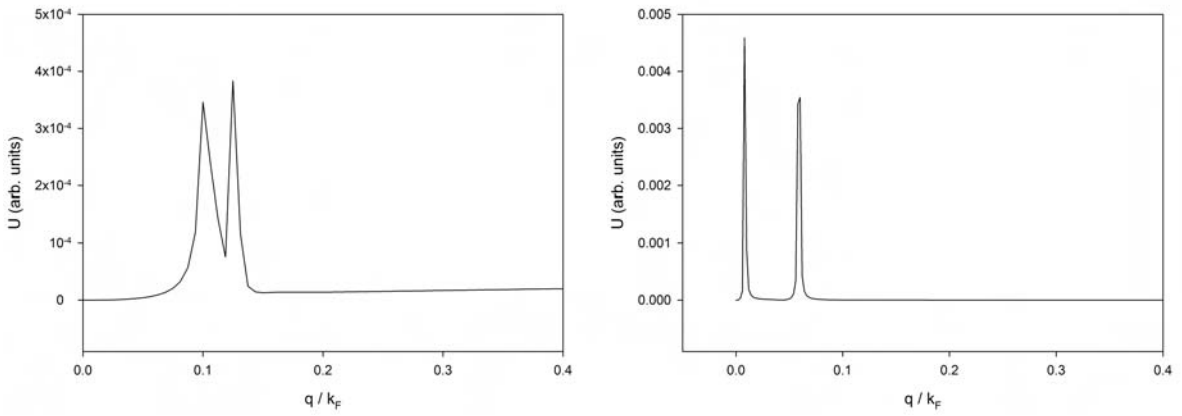

Figure 5.10: The interlayer potential for a bilayer (**left**) and a monolayer (**right**) at $\omega/E_F = 0.25$ and $T = 0.08T_F$. The monolayer's peaks are an order of magnitude higher and much more clearly defined. This is evidence for early Landau damping in the bilayer system.

sequence of the plasmon modes being entirely within the e-h continuum, even at low temperature. In the low temperature limit, is it noted that the system seems to have the usual T^2 behaviour. We have also suggested an explanation for the observation that the position and width of the plasmon peak is more strongly density and interlayer distance dependent than for the other systems.

There are many possible improvement to be made to this work and ways in which it could be extended. Foremost, fully analytic expressions for the polarisability and NLS would allow one to calculate the low-q plasmon modes and attempt to find an analytic result for the drag resistivity in the low temperature, large interlayer separation limit. This would allow more a more rigorous comparison to the monolayer and 2DEG system.

Perhaps a more natural extension would be to use the existing machinery to look at Coulomb drag between composite systems. That is to say, Coulomb drag between any combination of a bilayer, monolayer or 2DEG. No new calculations would need to be performed as it would only be a matter of adapting the numerics. From the

result obtained so far, it seems likely that such systems would display relatively conservative behaviour.

It would also be interesting to extend the theory outside of the range of validity of McCann *et al.*'s low energy Hamiltonian. There could be interesting effects related to the crossover regimes of the full bilayer Hamiltonian. It is probable that this would represent a formidable technical challenge. More simply, one could look the drag effect between bilayers in which a band gap has been opened. Of course it goes without saying that all of the above may be extended to include magnetic fields, disorder and phonons.

In conclusion, it remains to be seen which aspects of Coulomb drag in graphene systems contains the richest new physics. However, it is clear that there is a great deal of new ground to explore.

Chapter 6

Thesis Summary

This thesis began with two introductory chapters. The first gave a general overview of the field of Coulomb drag, discussing both the nomenclature and history of the subject. The second chapter introduced the physical properties of graphene, and particular attention was payed to its electronic properties.

Following this, the first of this thesis' projects was presented in chapter 3. Here, the finite temperature graphene nonlinear susceptibility was derived, representing the first original work of this thesis. This was used, in combination with previously known results, to calculate the drag rate between two graphene layers. It was found that the drag rate is enhanced by coupled plasmon modes at around $0.2T_F$, in disagreement with an earlier prediction by Das Sarma [106].

The final chapter of this thesis studied Coulomb drag between two graphene bilayers. Expressions for both the finite temperate polarisability and nonlinear susceptibility of a graphene bilayer were derived. These were combined to calculate the drag rate between two graphene bilayers. It was found that in contrast to the single layer case, plasmon enhancement at intermediate temperature is strongly suppressed by Landau damping.

Appendix A

Two Dimensional Fourier Transform of the Electron Potential

The potential in real space is

$$\phi(\mathbf{r}) = \frac{e}{r}. \tag{A.0.1}$$

It follows that the two-dimensional Fourier transform of A.0.1 is

$$\phi(\mathbf{p}) = e \int \frac{1}{r} e^{i\mathbf{q}\cdot\mathbf{r}} d\mathbf{r}. \tag{A.0.2}$$

Converting to polar coordinates,

$$\phi(\mathbf{p}) = e \int_0^\infty dr \int_0^{2\pi} e^{iqrcos\theta} d\theta. \tag{A.0.3}$$

With the use of Bessel's first integral [5],

$$J_n(z) = \frac{1}{2\pi i^n} \int_0^{2\pi} e^{izcos\theta} e^{in\theta} d\theta, \tag{A.0.4}$$

we have

$$\phi(\mathbf{p}) = 2\pi e \int_0^\infty J_0(qr)\, dr. \tag{A.0.5}$$

This is in the form of a Hankel transform [5]

$$H_p(y) = \int_0^\infty x h(x) J_p(xy)\, dx \tag{A.0.6}$$

of order $p = 0$. A property of Hankel transforms is that for $h(x) = \frac{1}{x}$, $H_0(y) = \frac{1}{y}$.

Finally,

$$\phi(\mathbf{p}) = \frac{2\pi e}{q}. \tag{A.0.7}$$

Appendix B

The Linear Response Theory of Coulomb Drag

This calculation is due to Kamenev and Oreg [9] and Flensberg *et al.* [7], and uses field theoretic techniques to evaluate the transresistivity. In the original papers, the authors demonstrated the power of this approach by extending the analysis to the case of disorder and localisation. The calculation will proceed as follows. Working with the drag conductivity σ_{21} and the Kubo formula in the Matsubara formalism, the interaction representation will be employed in order to expand the S-matrix in powers of the interlayer interaction. Following this, the lowest non-vanishing order in the dc limit will be evaluated and analytically continued back to real frequencies. It will be shown that in the ballistic (weak scattering) limit this reproduces (2.64).

B.0.1 The Kubo Formula

The starting point of the calculation is the Kubo formula [10], that expresses the drag conductivity in terms of the retarded current-current correlation function $\Pi_{ij}^{\alpha\beta}$.

In momentum and frequency space

$$\sigma_{ij}^{\alpha\beta}(Q;\Omega) = \frac{1}{\Omega S}\Pi_{ij}^{\alpha\beta}(Q;\Omega), \tag{B.0.1}$$

where α, β label the Cartesian coordinates, Ω is the frequency and S the system area. The subscripts i, j label the subsystems and for the drag conductivity $i \neq j$. The retarded current-current correlation function Π_{ij}^{r} is then defined in the time domain as

$$\Pi_{ij}(\mathbf{x}-\mathbf{x}';t-t') = -i\theta(t-t')\left\langle[j_i(\mathbf{x},t), j_j(\mathbf{x}',t')]\right\rangle. \tag{B.0.2}$$

where the i, j subscripts denote the layer, $j_i(\mathbf{x}, t)$ is the usual current operator and $\hbar = 1$.

The current-current correlation function is most conveniently evaluated via the imaginary time (Matsubara) formalism; the fundamental concept of which is to take zero temperature field theory and make the transformation

$$t \to -i\tau. \tag{B.0.3}$$

The task now is to express equation (B.0.1) as an expansion in powers of the interaction between the layers and then evaluate the most relevant terms. The quantity with which it is easiest to do this is the imaginary time, time ordered correlation function,

$$\Pi_{ij}(\mathbf{x}-\mathbf{x}';\tau-\tau') = -\left\langle T_\tau\{j_i(\mathbf{x},\tau)j_j(\mathbf{x}',\tau')\}\right\rangle. \tag{B.0.4}$$

where the operator T_τ time orders the τ terms. Equation (B.0.4) is related to (B.0.2)

via their frequency domain representations by the analytic continuation

$$\Pi^r_{ij}(\mathbf{x}-\mathbf{x}';\Omega) = \lim_{i\Omega_n\to\Omega+i\delta}\Pi(\mathbf{x}-\mathbf{x}';i\Omega_n) \tag{B.0.5}$$

where

$$\Pi_{ij}(\mathbf{x}-\mathbf{x}';i\Omega_n) = \int_0^\beta d\tau e^{i\Omega_n\tau}\Pi_{ij}(\mathbf{x}-\mathbf{x}';\tau) \tag{B.0.6}$$

$$\Pi_{ij}(\mathbf{x}-\mathbf{x}';\tau) = \frac{1}{\beta}\sum_n e^{-i\Omega_n\tau}\Pi_{ij}(\mathbf{x}-\mathbf{x}';i\Omega_n) \tag{B.0.7}$$

and $\beta = \frac{1}{k_B T}$. Using the above relations, the following will evaluate the leading order terms of a perturbative expansion of $\Pi_{ij}(\mathbf{x}-\mathbf{x}';\tau)$ via the Matsubara technique and where necessary analytically continue back to real frequencies to obtain their contribution to the drag conductivity.

B.0.2 Perturbative Expansion

Consider now the full system Hamiltonian $H = H_1 + H_2 + H_{12}$ where H_i are the individual layer Hamiltonians and H_{12} is the interaction between them, given by

$$H_{12}(\mathbf{r_1},\mathbf{r_2}) = \int d\mathbf{r_1}\int d\mathbf{r_2}\rho_1(\mathbf{r_1})\,U_{12}(\mathbf{r_1}-\mathbf{r_2})\rho_{\mathbf{2}}(\mathbf{r_2}) \tag{B.0.8}$$

Where $\mathbf{r_i}$ is a coordinate in the i'th layer and ρ_i is the charge density. In (B.0.4) the τ dependence of the current operator is determined by the full Hamiltonian. To develop a perturbative expansion in powers of the interaction term H_{12} it must be isolated by transforming to the interaction representation, upon which [10]

$$\Pi_{ij}(\mathbf{x}-\mathbf{x}',\tau-\tau') = -\frac{\langle T_\tau\{S(\beta)j_1(\mathbf{x},\tau)j_2(\mathbf{x}',\tau)\}\rangle}{\langle S(\beta)\rangle}. \tag{B.0.9}$$

The τ dependence of the current operators is now determined by the individual layers and hence they are decoupled. This is assumed throughout the remainder of the calculation. The S-matrix $S(\beta)$ describes the evolution of the system in imaginary time and is given by

$$S(\beta) = T_\tau \exp\left[-\int_0^\beta d\tau_1 H_{12}(\tau_1)\right]. \tag{B.0.10}$$

Employing the linked cluster theorem [10] the denominator in (B.0.9) cancels all of the unconnected diagrams in the numerator and as such it may be neglected so long as only connected diagrams are included in the expansion. Recognising this,

$$\Pi_{ij}(\mathbf{x}-\mathbf{x}', \tau-\tau') = -\left\langle T_\tau\{S(\beta) j_1(\mathbf{x},\tau) j_2(\mathbf{x}',\tau)\}\right\rangle. \tag{B.0.11}$$

Expanding (B.0.10) as a power series in H_{12},

$$S(\beta) \approx 1 - T_\tau \int_0^\beta d\tau_1 H_{12}(\tau_1) + \frac{1}{2} T_\tau \int_0^\beta \int_0^\beta d\tau_1 d\tau_2 H_{12}(\tau_1) H_{12}(\tau_2) + \ldots \tag{B.0.12}$$

Since the interaction between layers is small compared to the individual subsystem Hamiltonians it is reasonable to assume that the leading order terms are the relevant ones.

Zeroth order

Substituting the zeroth order term from (B.0.12) into (B.0.11) provides

$$\Pi_{21}^{(0)}(\mathbf{x}-\mathbf{x}', \tau-\tau') = -\left\langle T_\tau\{j_1(\mathbf{x},\tau) j_2(\mathbf{x}',\tau)\}\right\rangle. \tag{B.0.13}$$

Comparing this to (B.0.2) it is clear that the zeroth order term vanishes since the current operators are decoupled and hence commute.

First order The first order term in (B.0.12) leads to

$$\begin{aligned}\Pi_{ij}(\mathbf{x}-\mathbf{x}',\tau-\tau')^{(1)} &= \int_0^\beta d\tau_1 \int d\mathbf{r_1} d\mathbf{r_2}\, \langle T_\tau\{j(\mathbf{x},\tau)\rho_1(\mathbf{r_1},\tau_1)\}\rangle \\ &\times\ U_{12}(\mathbf{r_1}-\mathbf{r_2})\,\langle T_\tau\{\rho_2(\mathbf{r_2},\tau_1)j(\mathbf{x}',\tau')\}\rangle\end{aligned} \tag{B.0.14}$$

where the correlation function has been factorised into layers since they are independent in the interaction picture. The density operators in (B.0.14) may be written in terms of current operators by considering the continuity equation

$$\bigtriangledown \cdot j(\mathbf{r},t) = -\frac{\partial \rho(\mathbf{r},t)}{\partial t} \tag{B.0.15}$$

the Fourier transform of which yields

$$\rho(\mathbf{q},i\Omega) = \frac{\mathbf{q}}{i\Omega} j(\mathbf{q},\Omega). \tag{B.0.16}$$

Making use of this leads to the first order contribution to the drag conductivity

$$\sigma_{21}\left(\mathbf{q},\Omega\right)^{(1)} = \frac{1}{ie^2\Omega}\sigma_{22}(\mathbf{q},\Omega)\mathbf{q}^2 U_{12}\left(\mathbf{q}\right)\sigma_{11}(\mathbf{q},\Omega) \tag{B.0.17}$$

It is clear that () does not give a meaningful contribution to the drag conductivity in the dc [$\Omega \to 0$] limit [7].

Second order

The second order term of equation (B.0.12) leads to

$$\begin{aligned}\Pi_{21}\left(\mathbf{x}-\mathbf{x}',\tau-\tau'\right) &= -\frac{1}{2}\int_0^\beta d\tau_1\int_0^\beta d\tau_2\int d\mathbf{r_1}\int d\mathbf{r_2}\int d\mathbf{r}_1'\int d\mathbf{r}_2' U_{12}(\mathbf{r_1}-\mathbf{r_2})U_{12}(\mathbf{r}_1'-\mathbf{r}_2') \\ &\times \left\langle T_\tau \rho_1(\mathbf{r_1},\tau_1)\rho_2(\mathbf{r_2},\tau_2)\rho_1(\mathbf{r}_1',\tau_2)\rho_2(\mathbf{r}_2',\tau_2)j_1(\mathbf{x},\tau)j(\mathbf{x}',\tau')\right\rangle . \qquad \text{(B.0.18)}\end{aligned}$$

Again, since the operators for the two layers are decoupled the expectation value in (B.0.18) can be factorised into individual layers so that

$$\begin{aligned}\Pi_{21}\left(\mathbf{x}-\mathbf{x}',\tau'-\tau\right) &= -\frac{1}{2}\int_0^\beta d\tau_1\int_0^\beta d\tau_2\int d\mathbf{r_1}d\mathbf{r_2}d\mathbf{r}_1'd\mathbf{r}_2' U_{12}(\mathbf{r_1}-\mathbf{r_2})U_{12}(\mathbf{r}_1'-\mathbf{r}_2') \\ &\times \Gamma_1(\mathbf{x}\tau,\mathbf{r_1}\tau_1,r_1'\tau_1)\Gamma_2(\mathbf{x}'\tau',\mathbf{r_2}\tau_2,\mathbf{r}_2'\tau_2). \qquad \text{(B.0.19)}\end{aligned}$$

where for brevity, the function

$$\Gamma(\mathbf{x}\tau,\mathbf{x}'\tau',\mathbf{x}''\tau'') = -\left\langle T_\tau\left\{j(\mathbf{x}\tau)\rho_i(\mathbf{x}'\tau')\rho_i(\mathbf{x}''\tau'')\right\}\right\rangle \qquad \text{(B.0.20)}$$

has been introduced. Assuming that the layers are translationally invariant (B.0.19) may be Fourier transformed so that [7]

$$\begin{aligned}\Pi(\mathbf{Q};i\Omega_n)^{(2)} &= -\frac{1}{2\upsilon}\sum_{\mathbf{q}}\frac{1}{\beta}\sum_{i\omega_n}U_{12}(\mathbf{q})U^*(\mathbf{Q}+\mathbf{q}) \qquad \text{(B.0.21)} \\ &\times \Gamma_1(\mathbf{Q}+\mathbf{q},\mathbf{q};i\Omega_n+i\omega_n,i\omega_n)\Gamma(-\mathbf{Q}-\mathbf{q},-\mathbf{q};-i\Omega_n-i\omega_n,-i\omega_n)\end{aligned}$$

where ν is the layer volume, the $i\omega_n$ sum is over Boson frequencies and the layers are assumed to be of identical size. Equation (B.0.21) corresponds to the diagram of figure B.1 where the shaded triangles represent the Γ functions.

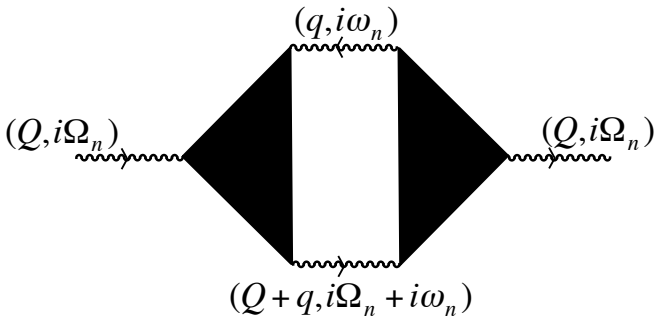

Figure B.1: Diagram corresponding to the current-current correlation function to second order in the inter-layer Coulomb interaction.

It is here that the power of the Matsubara formalism is demonstrated. Rewriting (B.0.21) as

$$\Pi_{21}(\mathbf{Q};i\Omega_n)^{(2)} = \frac{1}{2\upsilon}\sum_{\mathbf{q}} U_{12}(\mathbf{q})U^*(\mathbf{Q}+\mathbf{q})S(i\Omega_n) \tag{B.0.22}$$

where

$$S(i\Omega_n) = -\frac{1}{\beta}\sum_{i\omega_n}\Gamma_1(i\Omega_n+i\omega_n,i\omega_n)\Gamma_2(-i\Omega_n-i\omega_n,-i\omega_n) \tag{B.0.23}$$

and the momentum arguments have been suppressed, the summation over Bose frequencies may be carried out by noting that the function $\Gamma(z+i\Omega_n,z)$ has branch cuts as $Im(i\Omega_n+z)=0$ and $Im(z)=0$. The discrete frequency summation may then be converted to a contour integral (see figure B.2) by making the replacement $\frac{1}{\beta}\sum_{i\omega_n} f(i\omega_n) \to -(2\pi i)^{-1}\oint dz n_B(z)f(z)$ upon which (B.0.23) becomes

$$S(i\Omega) = \frac{1}{2\pi i}\oint dz n_B(z)\Gamma_1(i\Omega_n+z,z)\Gamma_2(-i\Omega_n-z,-z). \tag{B.0.24}$$

It can be shown [7] that only only the horizontal contours need to be considered so

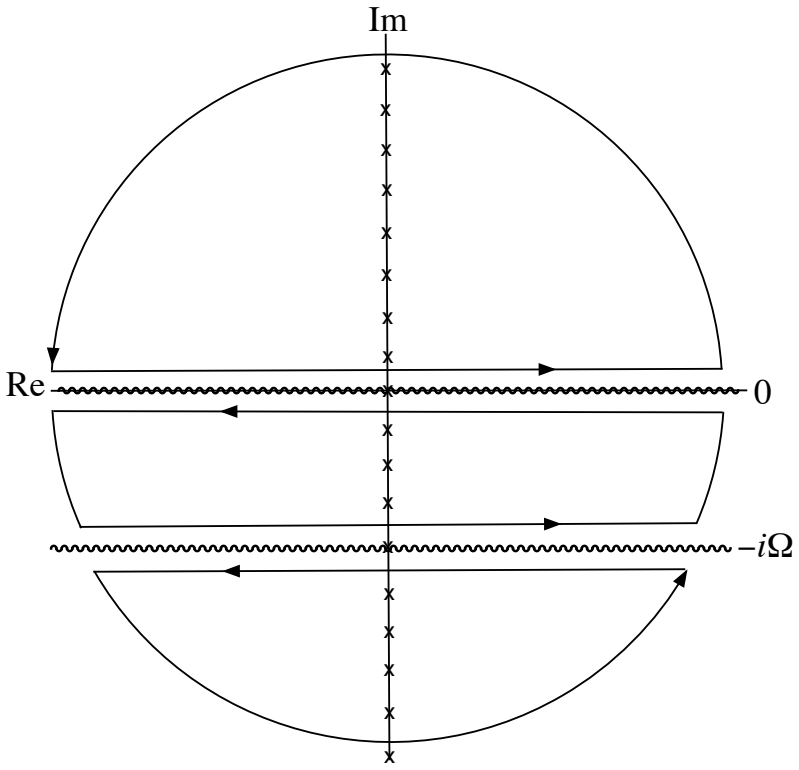

Figure B.2: Branch cuts and contour of B.0.24.

that,

$$\begin{aligned} S(i\Omega_n) &= \frac{1}{2\pi i\beta}\int_{-\infty}^{\infty} dz n_B(z)\Gamma(i\Omega_n+z, z+i\delta)\Gamma(-i\Omega_n-z,-z-i\delta) \qquad \text{(B.0.25)} \\ &+ \frac{1}{2\pi i\beta}\left[\int_{-\infty}^{\infty} dz n_B(z-i\Omega_n)\Gamma(z+i\delta, z-i\Omega_n)\Gamma(-z-i\delta,-z+i\Omega_n)-\right. \\ &- \left.\int_{-\infty}^{\infty} dz n_B(z)\Gamma(i\Omega_n+z, z-i\delta)\Gamma(-i\Omega_n-z,-z+i\delta)\right] \\ &- \frac{1}{2\pi i\beta}\int_{-\infty}^{\infty} dz n_B(z-i\Omega_n)\Gamma(z-i\delta, z-i\Omega_n)\Gamma(-z+i\delta,-z+i\Omega_n). \end{aligned}$$

Analytically continuing to real frequencies in accordance with (B.0.5) and employing the notation

$$\begin{aligned} \Gamma(\pm,\pm) &= \Gamma_1(i\Omega_n + i\omega_n \to \Omega+\omega\pm i\delta, i\omega_n \to \omega \pm i\delta) \qquad \text{(B.0.26)} \\ \Gamma(\pm,\pm) &= \Gamma_2(-i\Omega_n - i\omega_n \to -\Omega-\omega\pm i\delta, -i\omega_n \to -\omega \pm i\delta) \end{aligned}$$

(B.0.25) becomes,

$$\begin{aligned} S(\Omega) &= \frac{1}{\beta}\int_{-\infty}^{\infty}\frac{d\omega}{2\pi i}\left[n_B(\omega+\Omega)-n_B(\omega)\right]\Gamma_1\left(+,-\right)\Gamma_2\left(-,+\right) \\ &+ \frac{1}{\beta}\int_{-\infty}^{\infty}\frac{d\omega}{2\pi i}\left[n_B(\omega)\Gamma_1\left(+,+\right)\Gamma_2\left(-,-\right)-n_B\left(\omega+\Omega\right)\Gamma_1\left(-,-\right)\Gamma_2\left(+,+\right)\right]. \end{aligned} \tag{B.0.27}$$

The function $\Gamma_i\left(+,-\right)$ and $\Gamma_i\left(+,-\right)$ may be shown [7] to vanish identically in the dc limit. With this in mind and reintroducing momentum arguments the retarded correlation function is

$$\Pi_{21}^{r(2)}\left(\mathbf{Q},\Omega\right)=\frac{1}{2\beta\upsilon}\sum_{\mathbf{q}}U_{12}(\mathbf{q})U^{*}(\mathbf{Q}+\mathbf{q})\int_{-\infty}^{\infty}\frac{d\omega}{2\pi i}\left[n_B(\omega+\Omega)-n_B(\omega)\right]\Gamma_1\left(+,-\right)\Gamma_2\left(-,+\right) \tag{B.0.28}$$

Substituting the above into (B.0.1) gives for the second order contribution to the drag conductivity

$$\begin{aligned} \sigma_{12}^{(2)}(\mathbf{Q},\Omega) &= \frac{-e^2}{2\upsilon}\sum_{\mathbf{q}}U_{12}(\mathbf{q})U^{*}(\mathbf{Q}+\mathbf{q})\int_{-\infty}^{\infty}\frac{d\omega}{2\pi}\left[n_B(\omega+\Omega)-n_B(\omega)\right] \\ &\times \Gamma_1\left(\mathbf{q},\mathbf{q};\omega+i\delta,\omega-i\delta\right)\Gamma_2\left(-\mathbf{q},-\mathbf{q}'\omega-i\delta,-\omega+i\delta\right). \end{aligned} \tag{B.0.29}$$

For a uniform ($Q=0$) system in the dc limit ($\Omega\rightarrow 0$), the drag conductivity is therefore

$$\begin{aligned} \sigma_D\equiv\sigma_{12}^{(2)} &= \frac{-e^2}{2\upsilon}\sum_{\mathbf{q}}\left|U_{12}(\mathbf{q})\right|^2\int_{-\infty}^{\infty}\frac{d\omega}{2\pi}\left[\partial_\omega n_B(\omega)\right] \\ &\times \Gamma_1\left(\mathbf{q},\mathbf{q};\omega+i\delta,\omega-i\delta\right)\Gamma_2\left(-\mathbf{q},-\mathbf{q}'\omega-i\delta,-\omega+i\delta\right). \end{aligned} \tag{B.0.30}$$

This expression is exact and must be approximated in an appropriate limit in order to obtain useful results.

Appendix C

Graphene Bilayer Polarisability

The graphene polarisability derived in section 5.2 is given by

$$\chi(q,\omega) = -\frac{1}{2}\sum_{\lambda\lambda'=\pm}\sum_{\mathbf{k}}(1+\lambda\lambda'\cos 2\theta)\,\frac{n_F(\xi_{\mathbf{k},\lambda'})-n_F(\xi_{\mathbf{k}+\mathbf{q},\lambda})}{\omega+\xi_{\mathbf{k},\lambda'}-\xi_{\mathbf{k}+\mathbf{q},\lambda}+i\delta}. \tag{C.0.1}$$

C.0.3 Real Part

We will now evaluate the real part of the (C.0.1), given by

$$\mathrm{Re}\chi(\mathbf{q},\omega) = -\frac{1}{2}\sum_{\lambda,\lambda'=\pm}\sum_{\mathbf{k}'}(1+\lambda\lambda'\cos 2\theta_+)\frac{n_F(\xi_{\mathbf{k}',\lambda'})-n_F(\xi_{\mathbf{k}'+\mathbf{q},\lambda})}{\omega+\xi_{\mathbf{k}',\lambda'}-\xi_{\mathbf{k}'+\mathbf{q},\lambda}}. \tag{C.0.2}$$

where $\theta_+ = \phi_{\mathbf{k}+\mathbf{q}} - \phi_{\mathbf{k}}$ is the scattering angle.

Intraband : Starting with the intraband ($\lambda = \lambda' = +$) term,

$$\begin{aligned}\mathrm{Re}\chi^{++} &= -\frac{1}{2}\sum_{\mathbf{k}'}(1+\cos 2\theta_+)\frac{n_F(\xi_{\mathbf{k}'+})-n_F(\xi_{\mathbf{k}'+\mathbf{q}+})}{\omega+\xi_{\mathbf{k}'+}-\xi_{\mathbf{k}'+\mathbf{q}+}} \\ &= -\frac{1}{2}\sum_{\mathbf{k}'}(1+\cos 2\theta_+)\frac{n_F(\varepsilon_{\mathbf{k}'+})}{\omega+\xi_{\mathbf{k}'+}-\xi_{\mathbf{k}'+\mathbf{q}+}} + \{\omega\to-\omega\}. \end{aligned}\tag{C.0.3}$$

Using the identity $1+\cos 2\theta_+ = 2\cos^2\theta_+$ this can we written as

$$Re\chi^{++} = -\sum_{\mathbf{k}} \cos^2(\theta_+)\, \frac{n_F(\varepsilon_{\mathbf{k}'+})}{\omega + \xi_{\mathbf{k}'+} + \xi_{\mathbf{k}'+\mathbf{q}}} - \{\omega \to -\omega\}. \tag{C.0.4}$$

We can expresscos$^2(\theta_+)$ in terms of θ, the angle between the vectors as $\mathbf{k}'$ and $\mathbf{q}$ via

$$\cos(\phi_{\mathbf{k}'+\mathbf{q}} - \phi_{\mathbf{k}'}) = \frac{(\mathbf{k}'+\mathbf{q})\cdot\mathbf{k}'}{|\mathbf{k}'+\mathbf{q}|\,|\mathbf{k}'|} = \frac{q\cos\theta + k'}{\sqrt{k'^2+q^2+2kq\cos\theta}} \tag{C.0.5}$$

so that,

$$\mathrm{Re}\chi^{++} = -\sum_{\mathbf{k}'} \left(\frac{q\cos\theta + k'}{\sqrt{k'^2+q^2+2kq\cos\theta}}\right)^2 \frac{n_F(\varepsilon_{\mathbf{k}'+})}{\omega + \xi_{\mathbf{k}'+} - \xi_{\mathbf{k}'+\mathbf{q}+}} + \{\omega \to -\omega\}. \tag{C.0.6}$$

We we focus first on the first term of (C.0.4) which we shall label $\chi^{++}_{(1)}$ and later take $\omega \to -\omega$ to find the second term $\mathrm{Re}\chi^{++}_{(2)}$. Writing the sum over $\mathbf{k}$ as an integral and writing the energy terms explicitly

$$\mathrm{Re}\chi^{++}_{(1)} = \frac{1}{\pi^2}\int_0^\infty k'dk' \int_0^{2\pi} d\theta \frac{(q\cos\theta + k')^2\, n_F(\xi_{\mathbf{k}'+})}{(k^2+q^2+2k'q\cos\theta)\left(\omega + \frac{k'^2}{2m} - \frac{k'^2+q^2+2k'q\cos\theta}{2m}\right)}, \tag{C.0.7}$$

where we have taken account of the 2×2 spin and valley degeneracy and taken the . It is useful to now switch to the dimensionless variables $x = q/k_F$, $y = \omega/E_F$ and $k = k'/k_F$ so that

$$\mathrm{Re}\chi^{++}_{(1)} = \frac{2m}{\pi^2}\int_0^\infty kdk \int_0^{2\pi} d\theta \frac{(x\cos\theta + k)^2\, n_F(\varepsilon_{\mathbf{k}+})}{(k^2+x^2+2kx\cos\theta)\,(x^2 - y + 2kx\cos\theta)}. \tag{C.0.8}$$

To proceed, we split this integral up using partial fraction. Labeling $Q = 2kx\cos\theta$ we have

$$\frac{(Q/2k+k)^2}{(k^2+x^2+Q)(x^2-y+Q)} = \frac{1}{4k^2} + \frac{(2k^2+y-x^2)^2}{4k^2(k^2+y)(x^2-y+Q)} - \frac{(k^2-x^2)^2}{4k^2(k^2+y)(k^2+x^2+Q)}. \tag{C.0.9}$$

This leads to

$$\mathrm{Re}\chi^{++}_{(1)} = \frac{m}{2\pi^2}\int_0^\infty \frac{n_F(\xi_{\mathbf{k}+})}{k}dk \int_0^{2\pi} d\theta \left[\underbrace{1}_{A} + \underbrace{\frac{(2k^2+y-x^2)^2}{(k^2+y)(x^2-y+2kx\cos\theta)}}_{B} - \underbrace{\frac{(k^2-x^2)^2}{(k^2+y)(k^2+x^2+2kx\cos\theta)}}_{C} \right], \tag{C.0.10}$$

the individual terms of which we shall label A, B and C.

A : Calculating term A first,

$$A = \frac{m}{2\pi^2}\int_0^\infty \frac{n_F(\xi_{\mathbf{k}+})}{k}dk \int_0^{2\pi} d\theta = \frac{m}{\pi}\int_0^\infty \frac{n_F(\xi_{\mathbf{k}+})}{k}dk. \tag{C.0.11}$$

B :

Moving on to term B,

$$B = \frac{m}{2\pi^2}\int_0^\infty \int_0^{2\pi} \frac{n_F(\xi_{\mathbf{k}+})}{k}\frac{(2k^2+y-x^2)^2}{(k^2+y)(x^2-y+2kx\cos\theta)}dkd\theta. \tag{C.0.12}$$

We can calculate the angular integral by making use of the following identity from complex analysis

$$\int_0^{2\pi} \frac{1}{A + B\cos\theta} = \frac{2\pi sgn(A)}{\sqrt{A^2 - B^2}} \quad |A| > |B|$$

$$= 0 \qquad \text{otherwise.} \tag{C.0.13}$$

Applying (C.0.13) to (C.0.12), we get

$$B = \frac{m}{\pi}\int_0^\infty \frac{n_F(\xi_{\mathbf{k}+})}{k} \frac{(2k^2 + y - x^2)^2 \, sgn(x^2 - y)}{(k^2 + y)\sqrt{(x^2 - y)^2 - 4k^2x^2}} \theta\left((x^2 - y)^2 - 4k^2x^2\right) dk. \tag{C.0.14}$$

Employing the notation $\eta_\pm = y \pm x^2$ and $s_\pm = \eta_\pm^2/4x^2$, we can then write B, (C.0.14), as

$$B = \text{sgn}(-\eta_+)\frac{m}{\pi}\int_0^\infty \frac{n_F(\xi_{\mathbf{k}+})}{k} \frac{(2k^2 + \eta_-)^2 \, \theta\,(s - k^2)}{(k^2 + y)\sqrt{\eta_-^2 - 4k^2x^2}} dk \tag{C.0.15}$$

$$= -\text{sgn}(\eta_-)\frac{m}{2\pi x}\int_0^\infty \frac{n_F(\xi_{\mathbf{k}+})}{k} \frac{(2k^2 + \eta_-)^2 \, \theta\,(s - k^2)}{(k^2 + y)\sqrt{s_- - k^2}} dk. \tag{C.0.16}$$

C : Moving onto term C,

$$C = -\frac{m}{2\pi^2}\int_0^\infty \int_0^{2\pi} \frac{n_F(\xi_{\mathbf{k}+})}{k} \frac{(k^2 - x^2)^2}{(k^2 + y)\,(k^2 + x^2 + 2kx\cos\theta)} dk d\theta, \tag{C.0.17}$$

we can again evaluate the angular integral with the use of (C.0.13) to give

$$C = -\frac{m}{\pi}\int_0^\infty \frac{n_F(\xi_{\mathbf{k}+})}{k} \frac{(k^2 - x^2)^2 \, \theta(k^2 + x^2 - 2kx)}{(k^2 + y)\sqrt{(k^2 + x^2)^2 - 4k^2x^2}} dk. \tag{C.0.18}$$

Since $k^2 + x^2 > 2kx$ is always satisfied, there are no constraints on k. Noting that $\left(k^2+x^2\right)^2 - 4k^2x^2 = \left(k^2-x^2\right)^2$, we have finally,

$$C = -\frac{m}{\pi}\int_0^\infty \frac{n_F(\xi_{\mathbf{k}+})}{k}\frac{|k^2-x^2|}{(k^2+y)}dk. \tag{C.0.19}$$

Bringing together (C.0.11), (C.0.16) and (C.0.19), we have shown that

$$\begin{aligned}\mathrm{Re}\chi^{++}(x,y,T) &= \frac{m}{\pi}\int_0^\infty \frac{n_F(\xi_{\mathbf{k}+})}{k}dk - \mathrm{sgn}(\eta)\frac{m}{2\pi x}\int_0^\infty \frac{n_F(\xi_{\mathbf{k}+})}{k}\frac{\left(2k^2+\eta_-\right)^2\theta\left(s-k^2\right)}{(k^2+y)\sqrt{s_- - k^2}}dk \\ &\quad -\frac{m}{\pi}\int_0^\infty \frac{n_F(\xi_{\mathbf{k}+})}{k}\frac{|k^2-x^2|}{(k^2+y)}dk + \{y\to -y\}\end{aligned} \tag{C.0.20}$$

$\underline{\mathrm{Re}\chi^{--}}$: We will now calculate the $(\lambda = \lambda' = -)$ term, given by

$$\mathrm{Re}\chi^{--} = -\frac{1}{2}\sum_{\mathbf{k}'}(1+\cos 2\theta_+)\frac{n_F(\xi_{\mathbf{k}'-}) - n_F(\xi_{\mathbf{k}'+\mathbf{q}-})}{\omega + \xi_{\mathbf{k}'-} - \xi_{\mathbf{k}'+\mathbf{q}-}} \tag{C.0.21}$$

$$= -\frac{1}{2}\sum_{\mathbf{k}'}(1+\cos 2\theta_+)\frac{n_F(\xi_{\mathbf{k}'-})}{\omega + \xi_{\mathbf{k}'-} - \xi_{\mathbf{k}'+\mathbf{q}-}} + \{\omega\to -\omega\}. \tag{C.0.22}$$

Using the identity $\varepsilon_{\mathbf{k},\lambda} = -\varepsilon_{\mathbf{k},-\lambda}$, we can write this as

$$\mathrm{Re}\chi^{--} = -\frac{1}{2}\sum_{\mathbf{k}'}(1+\cos 2\theta_+)\frac{n_F(\varepsilon_{\mathbf{k}'-})}{-\omega + \xi_{\mathbf{k}'+} - \xi_{\mathbf{k}'+\mathbf{q}+}} + \{\omega\to -\omega\}, \tag{C.0.23}$$

which is just χ^{++} with $n_F(\xi_{\mathbf{k}'+})$ replaced by $n_F(\xi_{\mathbf{k}'-})$. Therefore we have

$$\begin{aligned}\mathrm{Re}\chi^{--}(x,y,T) &= \frac{m}{\pi}\int_0^\infty \frac{n_F(\xi_{\mathbf{k}-})}{k}dk - \mathrm{sgn}(\eta_-)\frac{m}{2\pi x}\int_0^\infty \frac{n_F(\xi_{\mathbf{k}+})}{k}\frac{\left(2k^2+\eta_-\right)^2\theta\left(s_- - k^2\right)}{\left(k^2+y\right)\sqrt{s_- - k^2}}dk \\ &\quad -\frac{m}{\pi}\int_0^\infty \frac{n_F(\xi_{\mathbf{k}-})}{k}\frac{|k^2-x^2|}{(k^2+y)}dk + \{y\to -y\}. \qquad \text{(C.0.24)}\end{aligned}$$

Recalling the expression for $\chi^{++}(x,y,T)$, (C.0.20):

$$\begin{aligned}\mathrm{Re}\chi^{++}(x,y,T) &= +\frac{m}{\pi}\int_0^\infty \frac{n_F(\xi_{\mathbf{k}+})}{k}dk - \mathrm{sgn}(\eta_-)\frac{m}{2\pi x}\int_0^\infty \frac{n_F(\xi_{\mathbf{k}+})}{k}\frac{\left(2k^2+\eta_-\right)^2\theta\left(s_- - k^2\right)}{\left(k^2+y\right)\sqrt{s_- - k^2}}dk \\ &\quad -\frac{m}{\pi}\int_0^\infty \frac{n_F(\xi_{\mathbf{k}+})}{k}\frac{|k^2-x^2|}{(k^2+y)}dk + \{y\to -y\}. \qquad \text{(C.0.25)}\end{aligned}$$

Combining both intraband terms we have

$$\begin{aligned}\chi^{Intra} &= \frac{m}{\pi}\int_0^\infty \frac{\left[(k^2+y)-|k^2-x^2|\right]\left[n_F(\xi_{\mathbf{k}+})-n_F(\xi_{\mathbf{k}-})\right]}{k\left(k^2+y\right)}dk \qquad \text{(C.0.26)} \\ &\quad -\mathrm{sgn}(\eta)\theta\left(s_- - k^2\right)\frac{m}{2\pi x}\int_0^\infty \frac{\left[n_F(\xi_{\mathbf{k}+})-n_F(\xi_{\mathbf{k}-})\right]\left(2k^2+\eta_-\right)^2}{k\left(k^2+y\right)\sqrt{s_- - k^2}}dk + \{y\to -y\}.\end{aligned}$$

Bringing each term in (C.0.26) under the same integral, we have

$$\begin{aligned}\chi^{Intra} &= \frac{m}{\pi}\int_0^\infty \frac{\left[n_F(\xi_{\mathbf{k}+})-n_F(\xi_{\mathbf{k}-})\right]}{k\left(k^2+y\right)}\left[k^2+y-\left|k^2-x^2\right| - \frac{sgn(\eta_-)\theta\left(s_- - k^2\right)\left(2k^2+\eta_-\right)^2}{2x\sqrt{s_- - k^2}}\right] \\ &\quad +\{y\to -y\} \qquad \text{(C.0.27)}\end{aligned}$$

Interband : We will now evaluate the intraband terms of the real part of the polarisability, starting with ($\lambda = +$, $\lambda' = -$), given by [see (C.0.2)]

$$\mathrm{Re}\chi^{+-} = -\tfrac{1}{2} \sum_{\mathbf{k}'} (1 - \cos 2\theta_+) \frac{n_F(\xi_{\mathbf{k}'-}) - n_F(\xi_{\mathbf{k}'+\mathbf{q}+})}{\omega + \xi_{\mathbf{k}'-} - \xi_{\mathbf{k}'+\mathbf{q}+}}. \tag{C.0.28}$$

By making a change of variables $k' \to -k' - q$ in the second term of (C.0.28) it can be shown that

$$\mathrm{Re}\chi^{+-} = -\frac{1}{2} \sum_{\mathbf{k}'} (1 - \cos 2\theta_+) \frac{n_F(\xi_{\mathbf{k}'-}) - n_F(\xi_{\mathbf{k}'+})}{\omega + \xi_{\mathbf{k}'-} - \xi_{\mathbf{k}'+\mathbf{q}+}}. \tag{C.0.29}$$

Using the identity $1 - \cos 2\theta_+ = 2\left(1 - \cos^2\theta_+\right)$ and then using (C.0.5) to write the Berry's phase term in terms of θ, we have

$$\mathrm{Re}\chi^{+-} = -\sum_{\mathbf{k}'} \left(1 - \frac{\left(q\cos\theta + k'\right)^2}{k'^2 + q^2 + 2k'q\cos\theta}\right) \frac{n_F(\xi_{\mathbf{k}'-}) - n_F(\xi_{\mathbf{k}'+})}{\omega + \xi_{\mathbf{k}'-} - \xi_{\mathbf{k}'+\mathbf{q}+}}, \tag{C.0.30}$$

$$= -\sum_{\mathbf{k}'} \frac{q^2\left[1 - \cos^2\theta\right]\left[n_F(\xi_{\mathbf{k}'-}) - n_F(\xi_{\mathbf{k}'+})\right]}{\left(k'^2 + q^2 + 2k'q\cos\theta\right)\left(\omega + \xi_{\mathbf{k}'-} - \xi_{\mathbf{k}'+\mathbf{q}+}\right)}. \tag{C.0.31}$$

As before, we now switch to the dimensionless variables $x = q/k_F$, $y = \omega/E_F$ and $k = k'/k_F$. Writing the sum over k' as as integral we have

$$\mathrm{Re}\chi^{+-} = -\frac{2mx^2}{\pi^2} \int_0^\infty \int_0^{2\pi} \frac{k\left[1 - \cos^2\theta\right]\left[n_F(\xi_{\mathbf{k}-}) - n_F(\xi_{\mathbf{k}+})\right]}{\left(k^2 + x^2 + 2kx\cos\theta\right)\left(y - 2k^2 - x^2 - 2kx\cos\theta\right)} d\theta dk, \tag{C.0.32}$$

where we have taken account of the 2×2 spin and valley degeneracy written the $\xi_{k,\lambda} = \frac{\lambda}{2m}|\mathbf{k}|$ terms explicitly. We proceed by applying partial fractions. Labeling

$Q = 2kx\cos\theta$ we have

$$\frac{\left(1-(Q/2kx)^2\right)^2}{\left(k^2+x^2+Q\right)\left(y-x^2-2k^2-Q\right)} = \frac{1}{4k^2}+\frac{\left(2k^2+y-x^2\right)^2}{4k^2\left(k^2+y\right)\left(x^2-y+Q\right)}-\frac{\left(k^2-x^2\right)^2}{4k^2\left(k^2+y\right)\left(k^2+x^2+Q\right)} \tag{C.0.33}$$

to write

$$\begin{aligned}\mathrm{Re}\chi^{+-} &= -\frac{mx^2}{2\pi^2}\int_0^\infty\int_0^{2\pi}\frac{\left[n_F(\xi_{\mathbf{k}-})-n_F(\xi_{\mathbf{k}+})\right]}{k}\\ &\times\left[\underbrace{1}_{A}+\underbrace{\frac{\left(k^2-2k+x^2\right)\left(k^2+2k+x^2\right)}{\left(k^2-y\right)\left(k^2+x^2+2kx\cos\theta\right)}}_{B}-\underbrace{\frac{\left(2k^2-2k-\eta_-\right)\left(2k^2+2k-\eta_-\right)}{\left(k^2-y\right)\left(2k^2-\eta_-+2kx\cos\theta\right)}}_{C}\right]d\theta dk,\end{aligned}$$

where we have employed the same notation as in the intraband band case, $\eta_\pm = y \pm x^2$, and labeled the terms A, B and C.

A : Calculating term A first,

$$A = -\frac{mx^2}{2\pi^2}\int_0^\infty\frac{\left[n_F(\xi_{\mathbf{k}-})-n_F(\xi_{\mathbf{k}+})\right]}{k}dk\int_0^{2\pi}d\theta = -\frac{mx^2}{\pi}\int_0^\infty\frac{\left[n_F(\xi_{\mathbf{k}-})-n_F(\xi_{\mathbf{k}+})\right]}{k}dk. \tag{C.0.34}$$

which is analytic at $k=0$ because the term $\left[n_F(\xi_{\mathbf{k}-})-n_F(\xi_{\mathbf{k}+})\right]\sim k$ as $k\to 0$.

B: Moving on to term B,

$$B = -\frac{mx^2}{2\pi^2}\int_0^\infty\int_0^{2\pi}\frac{\left[n_F(\xi_{\mathbf{k}-})-n_F(\xi_{\mathbf{k}+})\right]}{k}\frac{\left(k^2-2k+x^2\right)\left(k^2+2k+x^2\right)}{\left(k^2-y\right)\left(k^2+x^2+2kx\cos\theta\right)}d\theta dk. \tag{C.0.35}$$

We can calculate the angular integral by making use of (C.0.13) to yield

$$B = -\frac{mx^2}{\pi}\int_0^\infty [n_F(\xi_{\mathbf{k}-}) - n_F(\xi_{\mathbf{k}+})]\,\frac{(k^2-2k+x^2)\,(k^2+2k+x^2)}{k(k^2-y)\sqrt{(k^2+x^2)-4k^2x^2}}dk, \quad \text{(C.0.36)}$$

$$= -\frac{mx^2}{\pi}\int_0^\infty [n_F(\xi_{\mathbf{k}-}) - n_F(\xi_{\mathbf{k}+})]\,\frac{(k^2+x^2)^2-4k^2}{k(k^2-y)\,(k^2-x^2)}dk \quad \text{(C.0.37)}$$

C : Moving onto term C,

$$C = +\frac{mx^2}{2\pi^2}\int_0^\infty\int_0^{2\pi} [n_F(\xi_{\mathbf{k}-}) - n_F(\xi_{\mathbf{k}+})]\,\frac{(2k^2-2k-\eta_-)\,(2k^2+2k-\eta_-)}{k\,(k^2-y)\,(2k^2-\eta_-+2kx\cos\theta)}d\theta dk, \quad \text{(C.0.38)}$$

we can again use (C.0.5) to evaluate the angular integral and yield

$$C = +\frac{mx^2}{\pi}\int_0^\infty [n_F(\xi_{\mathbf{k}-}) - n_F(\xi_{\mathbf{k}+})]\,\frac{(2k^2-2k-\eta_-)\,(2k^2+2k-\eta_-)}{k\,(k^2-y)\,\sqrt{(2k^2-\eta_-)^2-4k^2x^2}}\theta\left(\left|2k^2-\eta_-\right|-2kx\right)dk. \quad \text{(C.0.39)}$$

Bringing together (C.0.39), (C.0.37) and (C.0.34), we have shown that

$$\mathrm{Re}\chi^{+-}(x,y,T) = -\frac{mx^2}{\pi}\int_0^\infty \frac{[n_F(\xi_{\mathbf{k}-}) - n_F(\xi_{\mathbf{k}+})]}{k(k^2-y)}\left[k^2 - y + \frac{(k^2+x^2)^2-4k^2}{(k^2-x^2)}\right.$$

$$\left. -\frac{(2k^2-2k-\eta_-)\,(2k^2+2k-\eta_-)}{\sqrt{(2k^2-\eta_-)^2-4k^2x^2}}\theta\left(\left|2k^2-\eta_-\right|-2kx\right)\right]dk. \quad \text{(C.0.40)}$$

$Re\chi^{-+}$ **:** Moving in to the ($\lambda=-1$,$\lambda'=+$) term, given by

$$\mathrm{Re}\chi^{-+} = -\frac{1}{2}\sum_{\mathbf{k}'}(1-\cos 2\theta_+)\frac{n_F(\xi_{\mathbf{k}'+}) - n_F(\xi_{\mathbf{k}'-})}{\omega + \varepsilon_{\mathbf{k}'+} - \varepsilon_{\mathbf{k}'+\mathbf{q}-}} \quad \text{(C.0.41)}$$

Using the identity $\varepsilon_{\mathbf{k},\lambda} = -\varepsilon_{\mathbf{k},-\lambda}$, we can write this as

$$\mathrm{Re}\chi^{-+} = -\frac{1}{2}\sum_{\mathbf{k}'}(1+\cos 2\theta_+)\frac{n_F(\xi_{\mathbf{k}'-}) - n_F(\xi_{\mathbf{k}'+})}{-\omega + \varepsilon_{\mathbf{k}'-} - \varepsilon_{\mathbf{k}'+\mathbf{q}+}} = Re\chi^{+-}(\omega \to -\omega)\,. \quad \text{(C.0.42)}$$

Therefore we can write the real part of the interband polarisability as

$$\begin{aligned}\mathrm{Re}\chi^{Inter}(x,y,T) &= -\frac{mx^2}{\pi}\int_0^\infty \frac{[n_F(\xi_{\mathbf{k}-}) - n_F(\xi_{\mathbf{k}+})]}{k(k^2-y)}\left[k^2 - y + \frac{(k^2+x^2)^2 - 4k^2}{(k^2-x^2)}\right. \quad \text{(C.0.43)}\\ &\left. -\frac{(2k^2-2k-\eta_-)(2k^2+2k-\eta_-)}{\sqrt{(2k^2-\eta_-)^2 - 4k^2x^2}}\theta\left(\left|2k^2-\eta_-\right| - 2kx\right)\right]dk + \{y\to -y\}\end{aligned}$$

In order to combine this expression with that for $\mathrm{Re}\chi^{Intra}$ it is easier to work with the $y \to -y$ term so that $\eta_- \to -\eta_+$. Switching the order of the Fermi functions we have

$$\begin{aligned}\mathrm{Re}\chi^{Inter}(x,y,T) &= \frac{m}{\pi}\int_0^\infty \frac{[n_F(\xi_{\mathbf{k}+}) - n_F(\xi_{\mathbf{k}-})]}{k(k^2+y)}\left[k^2 + y + \frac{(k^2+x^2)^2 - 4k^2}{(k^2-x^2)}\right. \quad \text{(C.0.44)}\\ &\left. -\frac{(2k^2-2k+\eta_+)(2k^2+2k+\eta_+)}{\sqrt{(2k^2+\eta_+)^2 - 4k^2x^2}}\theta\left(\left|2k^2+\eta\right| - 2kx\right)\right]dk + \{y\to -y\}\,.\end{aligned}$$

Therefore, we have for $\mathrm{Re}\chi^{Inter}(x,y,T)$

$$\mathrm{Re}\chi(x,y,T) = \mathrm{Re}\chi^{Inter}(x,y,T) + \mathrm{Re}\chi^{Inter}(x,y,T) \quad \text{(C.0.45)}$$

where

$$\mathrm{Re}\chi^{Intra} = \frac{m}{\pi}\int_0^\infty \frac{[n_F(\xi_{\mathbf{k}+})-n_F(\xi_{\mathbf{k}-})]}{k\,(k^2+y)}\left[k^2+y-\left|k^2-x^2\right|\right. \tag{C.0.46}$$
$$\left.-\frac{\mathrm{sgn}(\eta_-)\theta\,(s_--k^2)\,(2k^2+\eta_-)^2}{2x\sqrt{s_--k^2}}\right]dk+\{y\to -y\}\,,$$

$$\mathrm{Re}\chi^{Inter} = \frac{m}{\pi}\int_0^\infty \frac{[n_F(\xi_{\mathbf{k}+})-n_F(\xi_{\mathbf{k}-})]}{k(k^2+y)}\left[k^2+y+\left|k^2-x^2\right|\right. \tag{C.0.47}$$
$$\left.-\frac{(2k^2-2k+\eta_+)\,(2k^2+2k+\eta_+)}{\sqrt{(2k^2+\eta_+)^2-4k^2x^2}}\theta\left(\left|2k^2+\eta\right|-2kx\right)\right]dk+\{y\to -y\}\,.$$

C.0.4 Imaginary Part

We will now evaluate the imaginary part of the graphene bilayer polarisability (5.20), given by

$$\mathrm{Im}\chi(\mathbf{q},\omega)=\frac{\pi}{2}\sum_{\lambda,\lambda'=\pm}\sum_{\mathbf{k}'}(1+\lambda\lambda'\cos 2\theta_+)\,[n_F(\xi_{\mathbf{k}',\lambda'})-n_F(\xi_{\mathbf{k}'+\mathbf{q},\lambda})]\,\delta\left(\omega+\xi_{\mathbf{k}',\lambda'}-\xi_{\mathbf{k}'+\mathbf{q},\lambda}\right). \tag{C.0.48}$$

where $\theta_+=\phi_{\mathbf{k}+\mathbf{q}}-\phi_{\mathbf{k}}$ is the scattering angle.

Intraband : Starting with the intraband ($\lambda=\lambda'=+$) term, we again express the Berry's phase term in terms of $\cos\theta$ (C.0.5). We have

$$\mathrm{Im}\chi^{++} = \pi\sum_{\mathbf{k}'}[n_F(\xi_{\mathbf{k}'+})-n_F(\xi_{\mathbf{k}'+\mathbf{q}+})]\,\frac{(q\cos\theta+k')^2}{k'^2+q^2+2kq\cos\theta}\delta\left(\omega+\xi_{\mathbf{k}'+}-\xi_{\mathbf{k}'+\mathbf{q}+}\right) \tag{C.0.49}$$

A change of variable in the second term allows use to write

$$\mathrm{Im}\chi^{++} = \pi\sum_{\mathbf{k}'}\frac{n_F(\xi_{\mathbf{k}'+})\,(q\cos\theta+k')^2}{k'^2+q^2+2k'q\cos\theta}\delta\left(\omega+\xi_{\mathbf{k}'+}-\xi_{\mathbf{k}'+\mathbf{q}+}\right)-\{\omega\to\omega\} \tag{C.0.50}$$

As before, we write the sum over $\mathbf{k}'$ as an integral and then covert to the dimensionless variables $x = q/k_F$, $y = \omega/E_F$ and $k = k'/k_F$ to yield

$$\mathrm{Im}\chi^{++} = \frac{2m}{\pi}\int_0^\infty kdk \int_0^{2\pi} d\theta \frac{n_F(\xi_{\mathbf{k}+})\left(x\cos\theta + k\right)^2}{k^2 + x^2 + 2kx\cos\theta}\delta\left(y - x^2 - 2kx\cos\theta\right) - \{y \to y\}\,. \tag{C.0.51}$$

The delta function places limits on k by demanding that

$$k > \left|\frac{y - x^2}{2x}\right| \equiv \frac{|\eta_-|}{2x}. \tag{C.0.52}$$

We proceed via the change of variables $Q = 2kx\cos\theta$ so that

$$d\theta = -\frac{dQ}{\sqrt{4k^2x^2 - Q^2}} \tag{C.0.53}$$

and (C.0.51) becomes

$$\begin{aligned}\mathrm{Im}\chi^{++} &= -\frac{2m}{\pi}\int_0^\infty kdk \int dQ \frac{n_F(\xi_{\mathbf{k}+})\left(Q/2k + k\right)^2}{\left(k^2 + x^2 + Q\right)\sqrt{4k^2x^2 - Q^2}}\delta\left(y - x^2 - Q\right)\theta(k^2 - s_-) \\ &\quad - \{y \to y\} \qquad \text{(C.0.54)} \\ &= -\frac{m}{2\pi}\int_0^\infty dk \int dQ \frac{n_F(\xi_{\mathbf{k}+})\left(Q + 2k^2\right)^2}{k\left(k^2 + x^2 + Q\right)\sqrt{4k^2x^2 - Q^2}}\delta\left(y - x^2 - Q\right)\theta(k^2 - s_-) \\ &\quad - \{y \to y\} \qquad \text{(C.0.55)}\end{aligned}$$

Evaluating the angular integral by setting $Q = y - x^2 \equiv \eta_-$ yields,

$$\mathrm{Im}\chi^{++} = -\frac{m}{2\pi}\int_0^\infty dk \frac{n_F(\xi_{\mathbf{k}+})\left(\eta_- + 2k^2\right)^2}{k\left(k^2 + y\right)\sqrt{4k^2x^2 - \eta_-^2}}\theta(k^2 - s_-) - \{y \to y\}\,. \tag{C.0.56}$$

$\mathrm{Im}\chi^{--}$: Moving on to the $\lambda = \lambda' = -1$ term, we have

$$\mathrm{Im}\chi^{--} = \pi \sum_{\mathbf{k}'} \frac{n_F(\xi_{\mathbf{k}'-}) \left(q\cos\theta + k'\right)^2}{k'^2 + q^2 + 2k'q\cos\theta} \delta\left(\omega + \xi_{\mathbf{k}'-} - \xi_{\mathbf{k}'+\mathbf{q}-}\right) - \{\omega \to \omega\}\,. \quad \text{(C.0.57)}$$

Using $\xi_{\mathbf{k}',\lambda} = -\xi_{\mathbf{k}',-\lambda}$ and $\delta(\alpha x) = \frac{1}{|x|}\delta(x)$ we can write (C.0.57) as

$$\mathrm{Im}\chi^{--} = \pi \sum_{\mathbf{k}'} \frac{n_F(\xi_{\mathbf{k}'-}) \left(q\cos\theta + k'\right)^2}{k'^2 + q^2 + 2k'q\cos\theta} \delta\left(-\omega + \xi_{\mathbf{k}'+} - \xi_{\mathbf{k}'+\mathbf{q}-}\right) - \{\omega \to \omega\} \quad \text{(C.0.58)}$$

$$= -\pi \sum_{\mathbf{k}'} \frac{n_F(\xi_{\mathbf{k}'-}) \left(q\cos\theta + k'\right)^2}{k'^2 + q^2 + 2k'q\cos\theta} \delta\left(\omega + \xi_{\mathbf{k}'+} - \xi_{\mathbf{k}'+\mathbf{q}-}\right) - \{\omega \to \omega\}\,. \quad \text{(C.0.59)}$$

This is the same as $\mathrm{Im}\dot{\chi}^{++}$ (C.0.50) but with $n_F(\xi_{\mathbf{k}'-})$ replaced with $-n_F(\xi_{\mathbf{k}'+})$ and therefore

$$\mathrm{Im}\chi^{--} = \frac{m}{2\pi}\int_0^\infty dk \frac{n_F(\xi_{\mathbf{k}-}) \left(\eta_- + 2k^2\right)^2}{k\left(k^2+y\right)\sqrt{4k^2x^2 - \eta_-^2}} \theta(k^2 - s_-) - \{y \to y\}\,. \quad \text{(C.0.60)}$$

Therefore, combining (C.0.56) and (C.0.60) we have for $\mathrm{Im}\chi^{Intra} = \mathrm{Im}\chi^{++} + \mathrm{Im}\chi^{--}$,

$$\mathrm{Im}\chi^{Intra} = \frac{m}{2\pi}\int_0^\infty dk \frac{\left[n_F(\xi_{\mathbf{k}-}) - n_F(\xi_{\mathbf{k}+})\right] \left(\eta_- + 2k^2\right)^2}{k\left(k^2+y\right)\sqrt{4k^2x^2 - \eta_-^2}} \theta(k^2 - s_-) - \{y \to y\}\,. \quad \text{(C.0.61)}$$

Interband : Moving on to the interband term ($\lambda \neq \lambda'$) term we immediately notice that for the $\lambda = -$ and $\lambda' = +$ term,

$$\mathrm{Im}\chi^{-+}(\mathbf{q},\omega) = \frac{\pi}{2}\sum_{\mathbf{k}'}(1 - \cos 2\theta_+)\left[n_F(\xi_{\mathbf{k}',+}) - n_F(\xi_{\mathbf{k}'+\mathbf{q},-})\right]\delta\left(\omega + \xi_{\mathbf{k}',+} - \xi_{\mathbf{k}'+\mathbf{q},-}\right), \quad \text{(C.0.62)}$$

every term in the delta function is positive since $\omega > 0$. Therefore, $Im\chi^{-+} = 0$ and we only need to consider $\lambda = +$, $\lambda' = -$,

$$\mathrm{Im}\chi^{Inter}(\mathbf{q},\omega) = \frac{\pi}{2}\sum_{\mathbf{k}'}(1-\cos 2\theta_+)\left[n_F(\xi_{\mathbf{k}',-}) - n_F(\xi_{\mathbf{k}'+\mathbf{q},+})\right]\delta\left(\omega + \xi_{\mathbf{k}',-} - \xi_{\mathbf{k}'+\mathbf{q},+}\right). \tag{C.0.63}$$

A change of variable $\mathbf{k} \to -\mathbf{k} - \mathbf{q}$ allows us to write

$$\mathrm{Im}\chi^{Inter}(q,\omega) = \frac{\pi}{2}\sum_{\mathbf{k}'}(1-\cos 2\theta_+)\left[n_F(\xi_{\mathbf{k}',-}) - n_F(\xi_{\mathbf{k}',+})\right]\delta\left(\omega + \xi_{\mathbf{k}',-} - \xi_{\mathbf{k}'+\mathbf{q},+}\right). \tag{C.0.64}$$

As usual we write the Berry's phase term in terms of $\cos\theta$,

$$1-\cos 2\theta_+ = 2\left(1-\cos^2\theta_+\right) = 2 - \frac{2\left(q\cos\theta + k'\right)^2}{k'^2 + q^2 + 2k'q\cos\theta} = \frac{2q^2\left(1-\cos^2\theta\right)}{k'^2 + q^2 + 2k'q\cos\theta}, \tag{C.0.65}$$

so that

$$\mathrm{Im}\chi^{Inter} = \pi q^2\sum_{\mathbf{k}'}\left[n_F(\xi_{\mathbf{k}',-}) - n_F(\xi_{\mathbf{k}',+})\right]\left(\frac{1-\cos^2\theta}{k'^2 + q^2 + 2k'q\cos\theta},\right)\delta\left(\omega + \xi_{\mathbf{k}',-} - \xi_{\mathbf{k}'+\mathbf{q},+}\right). \tag{C.0.66}$$

As in the previous calculations, we now write the sum over k as an integral convert to the dimensionless variables $x = q/k_F$, $y = \omega/E_F$ and $k = k/k_F$ to yield

$$\begin{aligned}\mathrm{Im}\chi^{Inter} &= \frac{2mx^2}{\pi}\int_0^\infty kdk\int_0^{2\pi} d\theta\left[n_F(\xi_{\mathbf{k},-}) - n_F(\xi_{\mathbf{k},+})\right] \\ &\times\left(\frac{1-\cos^2\theta}{k^2 + x^2 + 2kx\cos\theta},\right)\delta\left(y - x^2 - 2k^2 - 2kx\cos\theta\right).\end{aligned} \tag{C.0.67}$$

The delta function provides the condition

$$\sqrt{2\eta_- + x^2} - x^2 < 2k < \sqrt{2\eta_- + x^2} + x^2 \tag{C.0.68}$$

where as usual $\eta_\pm = y - x^2$. We proceed by evaluating the angular integral by making he substitution $Q = 2k^2 + 2kx\cos\theta$ so that

$$d\theta = \frac{-dQ}{2kx\sqrt{1-\cos^2\theta}}, \tag{C.0.69}$$

and (C.0.67) becomes $\mathrm{Im}\chi^{Inter} =$

$$\frac{-mx}{\pi}\int_0^\infty dk \int dQ\,[n_F(\xi_{\mathbf{k},-}) - n_F(\xi_{\mathbf{k},+})]\,\frac{\sqrt{1-\cos^2\theta}}{k^2+x^2+Q-2k^2}\delta\left(y-x^2-Q\right) \tag{C.0.70}$$

$$= \frac{-m}{2\pi}\int_0^\infty \frac{dk}{k}\int dQ\,[n_F(\xi_{\mathbf{k},-}) - n_F(\xi_{\mathbf{k},+})]\,\frac{\sqrt{4k^2x^2-(Q-2k^2)^2}}{Q+x^2-k^2}\delta\left(y-x^2-Q\right).$$

Evaluating this at $Q = y - x^2$ yields,

$$\mathrm{Im}\chi^{Inter} = \frac{m}{2\pi}\int_0^\infty dk\,[n_F(\xi_{\mathbf{k},-}) - n_F(\xi_{\mathbf{k},+})]\,\frac{\sqrt{4k^2x^2-(y-x^2-2k^2)^2}}{k\,(k^2-y)} \tag{C.0.71}$$

$$= \frac{m}{2\pi}\int_0^\infty dk\,[n_F(\xi_{\mathbf{k},-}) - n_F(\xi_{\mathbf{k},+})]\,\frac{\sqrt{(\eta_- + 2kx - 2k^2)(2k^2+2kx-\eta_-)}}{k\,(k^2-y)}$$

C.0.5 Result

So we have finally for the graphene bilayer finite temperature polarisability,

$$\chi(x,y,T) = \chi^{Intra}(x,y,T) + \chi^{Inter}(x,y,T) \tag{C.0.72}$$

where

$$\mathrm{Im}\chi(x,y,T) = \mathrm{Im}\chi^{Intra} + \mathrm{Im}\chi^{Inter}, \tag{C.0.73}$$

$$\mathrm{Re}\chi(x,y,T) = \mathrm{Re}\chi^{Inter}(x,y,T) + \mathrm{Re}\chi^{Inter}(x,y,T) \tag{C.0.74}$$

and

$$\mathrm{Im}\chi^{Intra} = \frac{m}{2\pi}\int_0^\infty dk \frac{\left[n_F(\xi_{\mathbf{k}-}) - n_F(\xi_{\mathbf{k}+})\right]\left(\eta_- + 2k^2\right)^2}{k\left(k^2+y\right)\sqrt{4k^2x^2-\eta_-^2}}\theta(k^2-s_-) - \{y\to y\}\,, \tag{C.0.75}$$

$$\mathrm{Im}\chi^{Inter} = \frac{m}{2\pi}\int_0^\infty dk \left[n_F(\xi_{\mathbf{k},-}) - n_F(\xi_{\mathbf{k},+})\right]\frac{\sqrt{(\eta_- + 2kx - 2k^2)(2k^2+2kx-\eta_-)}}{k\left(k^2-y\right)}, \tag{C.0.76}$$

$$\begin{aligned}\mathrm{Re}\chi^{Intra} &= \frac{m}{\pi}\int_0^\infty \frac{\left[n_F(\xi_{\mathbf{k}+}) - n_F(\xi_{\mathbf{k}-})\right]}{k\left(k^2+y\right)}\Bigg[k^2 + y - \left|k^2-x^2\right| \\ &\quad - \frac{\mathrm{sgn}(\eta_-)\theta\left(s_- - k^2\right)\left(2k^2+\eta_-\right)^2}{2x\sqrt{s_- - k^2}}\Bigg]dk + \{y\to -y\}\,,\end{aligned} \tag{C.0.77}$$

$$\begin{aligned}\mathrm{Re}\chi^{Inter} &= \frac{m}{\pi}\int_0^\infty \frac{\left[n_F(\xi_{\mathbf{k}+}) - n_F(\xi_{\mathbf{k}-})\right]}{k(k^2+y)}\Bigg[k^2 + y + \left|k^2-x^2\right| \\ &\quad - \frac{\left(2k^2-2k+\eta_+\right)\left(2k^2+2k+\eta_+\right)}{\sqrt{\left(2k^2+\eta_+\right)^2 - 4k^2x^2}}\theta\left(\left|2k^2+\eta\right| - 2kx\right)\Bigg]dk + \{y\to -y\}\,.\end{aligned} \tag{C.0.78}$$

Bibliography

[1] M. B. Pogrebinskii, Sov. Phys. Semicond. **11**, 372 (1977)

[2] P. J. Price, Physica B **117**, 750 (1983)

[3] T. J. Gramila, J. P. Eisenstein, A. H. MacDonald, L. N. Pfeiffer and K. W. West, Phys. Rev. Lett. **66**, 1216 (1991)

[4] A. Jauho, H. Smith, Phys. Rev. B **47**, 4420 (1993)

[5] Gradshteyn and Ryzhik (Academic Press Inc., 1993)

[6] T. J. Gramila, J. P. Eisenstein, A. H. MacDonald, L. N. Pfeiffer, K. W. West, Phys. Rev. Lett. **66**, 1216 (1991)

[7] K. Flensberg *et al.*, Phys. Rev. B **52**, 14761 (1995)

[8] K. Flensberg et al., Phys. Rev. B **52**, 20 (1995)

[9] A. Kamenev, Y. Oreg, Phys. Rev. B **52**, 7516

[10] G. Mahan, Many-Particle Physics, Third Edition (Springer, 2000)

[11] Ashcroft, Mermin, Solid State Physics (Saunders College Publishing, 1976)

[12] F. Stern, Phys. Rev. Lett. **18**, 546 (1967)

[13] F. Blatt et. al., Thermoelectric Power of Metals (Plenum Press, 1976)

[14] L. D. Landau, E. M. Lifshitz, Physical Kinetics (Pergamon Press, 1989)

[15] A. G. Rojo, J. Phys. Cond. Mat. **11**, 31-52 (1999)

[16] J. P. Eisenstein, Les Houches Summer School Lecture Notes (2004)

[17] A. Fetter, J. Walecka, Quantum Theory of Many-Particle Systems (Dover Publications, 2003)

[18] J. M. Ziman, Principles of the Theory of Solids (Cambridge University Press, 1979)

[19] L. Zheng, A. MacDonald, Phys. Rev. B **48**, 8203 (1993)

[20] D. L. Maslov, Phys. Rev. B **45**, 1911 (1992)

[21] H. C. Tso & P. Vasilopoulos, Phys. Rev. B **45**, 1333 (1992)

[22] C. Zhang & Y. Takahashi, J. Phys. Cond. Mat. **68**, 2516 (1993)

[23] T. J. Gramila, J. P. Eisenstein, A. H. MacDonald, L. N. Pfeiffer and K. W. West, Phys. Rev. B. **47**, 12957 (1993)

[24] K. Flensberg, B. Y. Hu, Phys. Rev. Lett. **73**, 26 (1994)

[25] L. Swierkowski, J. Szymanski and Z. W. Gortel, Phys. Rev. Lett. **74**, 3245 (1994)

[26] H. C. Tso, P. Vasilopoulos, F. M. Peeters, Phys. Rev. Lett. **70,** 2146 (1993)

[27] T. J. Gramila, J. P. Eisenstein, A. H. MacDonald, L. N. Pfeiffer and K. W. West, Phys. Rev. B. **197**, 442 (1994)

[28] P. F. Maldague, Surf. Sci **73**, 296 (1978)

[29] N. P. R. Hill, *et al.*, J. Phys. Cond. Mat. **8**, 557 (1996)

[30] N. P. R. Hill, *et al.*, Phys. Rev. Lett. **78**, 2204 (1997)

[31] K. Guven & B. Tanatar, Solid State Commun. **104**, 439 (1997)

[32] A.Kamenev, Y.Oreg, Phys. Rev. Lett. **80**, 11 (1998)

[33] N. Giordano, J.D. Monnier, Phys. Rev. B **50**, 9363 (1994)

[34] I.V. Gornyi *et al*, Phys. Rev. Lett. **83**, 1 (1999)

[35] A. S. Price *et al*, Science **316**, 99 (2007)

[36] B. N. Narozhny, I. L. Aleiner, Phys. Rev. Lett. **84**, 5383 (2000)

[37] I.V. Lerner, Science **316**, 63 (2007)

[38] K. Flensberg and B. Hu, Phys. Rev. B **52**, 14796 (1995)

[39] R. Saito *et al.*, The Physical Properties of Carbon Nanotubes (Imperial Press, 2004)

[40] P. R. Wallace, Phys. Rev. **71**, 622 (1947)

[41] J. W. Hill and R. H. Petrucci, General Chemistry 3rd Edition (Prentice Hall, 2002)

[42] L. Pauling, The Nature of the Chemical Bond (Cornell U. P., 1960)

[43] Novoselov K.S. *et al.*, Phys. Stat. Sol. B **244**, 4106 (2007)

[44] J. Fuchs, M. Goerbig, Lecture Notes (2008)

[45] A. K. Geim, K. S. Novoselov, Nature Materials **6**, 183 (2007)

[46] R. E. Peierls, Ann. I. H. Poincare **5**, 177 (1935)

[47] L. D. Landau, , Phys. Z. Sowjetunion **11**, 26 (1937).

[48] L. D. Landau & E. M. Lifshitz, Statistical Physics Part I (Pergamon, 1980)

[49] N. D. Mermin, Phys. Rev. **176**, 250 (1968)

[50] J. A.Venables *et al.*, Rep. Prog. Phys. **47**, 399 (1984)

[51] K. S. Novoselov *et al.*, Science **306**, 666 (2004)

[52] C. Lee *et al.*, Science **321**, 385 (2008)

[53] A. Akturk & N. Goldsman, J. Appl. Phys. **103**, 53708 (2008)

[54] A. Baladin *et al.*, Nano Letters **8**, 902 (2008)

[55] K. S. Novoselov *et al.*, Proc. Nat. Acad. Sci. USA **102**, 10451 (2005)

[56] J. Meyer *et al.*, Nature **446**, 60 (2007)

[57] S. Morozov *et al.*, Phys. Rev. Lett. **96**, 16801 (2006)

[58] M. I. Katsnelson and A. K. Geim, Phil. Trans. R. Soc. A **366**, 195 (2008)

[59] B. Fauser, J. Tolksdorf, and E. Zeidler, Quantum Gravity (2007)

[60] B. Partoens & F. M. Peeters, Phys. Rev. B **74**, 75404 (2006)

[61] J. Cserti *et al.*, Phys. Rev. Lett. **99**, 66802 (2007)

[62] S. Adam & S. Das Sarma, Phys. Rev. B **77**, 115436 (2008)

[63] J. W. Evans, P.A. Thiel & M.C. Bartelt, Sur. Sci. Rep. **61**, 1 (2006).

[64] P. Blake *et al.*, Applied Physics Letters **91**, 123105 (2007)

[65] R. Nair, *et al.*, Science **320**, 1308 (2008)

[66] K.S Kim *et al.*, Nature **457**, 706 (2009)

[67] Kosynkin *et al.*, Nature **458**, 872 (2009)

[68] P. Sutter, Nature Materials **8**, 171 (2009)

[69] S. Reich *et al.*, Phys. Rev. B **66**, 35412 (2002)

[70] Katsnelson, Materials Today **10**, 1 (2007)

[71] T. Ando, *et al.*, J. Phys. Soc. Jpn **67**, 2857 (1998)

[72] M. Dresselhaus & G. Dresselhaus. Advances in Physics, **51**, 1 (2002)

[73] J. P. Hobson & W. A. Nierenberg, Phys. Rev. **89**, 662 (1953)

[74] G. W. Semenoff, Phys. Rev. Lett. **53**, 2449 (1984)

[75] E. McCann *et al.*, Phys. Rev. Lett. **97**, 146805 (2006)

[76] S. V. Vonsovsky, M. I. and Katsnelson, Quantum Solid State Physics (Springer, 1989)

[77] S. Y. Zhou, *et al.*, Nature Physics **2**, 595 (2006)

[78] A, Bostwick, *et al.*, Nature Physics **3**, 36 (2007)

[79] S. Das Sarma, E. H. Hwang and Wang-Kong Tse, Phys. Rev. B **75**, 121406 (2007)

[80] L. D. Landau, Soviet Phys. JETP **3**, 920 (1957)

[81] M. R. Ramezanali, *et al.*, J. Phys. A **42** 214015 (2009)

[82] E. H. Hwang & S. Das Sarma, Phys. Rev. B **75**, 205418 (2007)

[83] K. W. K. Shung, Phys. Rev. B **34**, 979 (1986)

[84] E. H. Hwang & S. Das Sarma, Phys. Rev. B **77**, 81412 (2007)

[85] E. McCann & V. I. Fal'ko, Phys. Rev. Lett. **96**, 086805 (2006)

[86] K. Novoselov & A. Geim, Mesoscopic Physics Group, Manchester (2004)

[87] J. Meyer, *et al.*, Nano Letters **8**, 3582 (2006)

[88] J. Nilsson, *et al.*, Phys. Rev. B **73**, 21 (2006)

[89] M. Koshino & T. Ando, Phys. Rev. B **73**, 245403 (2006)

[90] B. Partoens & F. M. Peeters, Phys. Rev. B **74**, 75404 (2006)

[91] S.B. Trickey, *et al.*, Phys. Rev. B **45**, 4460 (1992)

[92] E. H. Hwang & S. Das Sarma, Phys. Rev. Lett. **101**, 156802 (2008)

[93] K.S. Novoselov, *et al.*, Nature **438**, 201 (2005)

[94] M. I. Katsnelson, Eur. Phys. J. B **51**, 157 (2006)

[95] J. Tworzydlo, *et al.*, Phys. Rev. Lett. **96**, 246802 (2006)

[96] P. M. Ostrovsky, Phys. Rev. B **74**, 235443 (2006)

[97] K. Nomura & A. H. MacDonald, Phys. Rev. Lett. **98**, 76602 (2007)

[98] K. S. Novoselov, *et al.,* Nature Physics **2**, 177 (2006)

[99] J. Nilsson, A. H. Castro Neto, F. Guinea, N. M. R. Peres, Phys. Rev. B **78**, 45405 (2008)

[100] A. Yacoby, *et al.*, Nature Physics **4**, 144 (2008)

[101] B. Altshuler, I. L. Aleiner, V. V. Cheianov, V. I. Falko, Phys. Rev. Lett. **88**, 176801

[102] O. Klein, Z. Phys. **53**, 157 (1929)

[103] M.I. Katsnelson, K.S. Novoselov, A.K. Geim, Nature Physics **2,** 620 (2006)

[104] V.B. Berestetskii, E.M. Lifshitz, L.P. Pitaevskii, Relativistic Quantum Theory (1971)

[105] A. Savchenko, Personal Correspondence (2009)

[106] W. Tse, B. Hu & S. Das Sarma, Phys. Rev. B **76**, 081401 (2007)

[107] B. Narozhnny, Phys. Rev. B **76**, 153409 (2007)

[108] G. Mahan, Many Particle Physics (Springer, 2000)

[109] W. Tse & S. Das Sarma, Phys. Rev. B **75**, 045333 (2007)